

AD _____

Award Number: DAMD17-96-1-6143

TITLE: Exploration of Monoenergetic X-Ray Mammography with
Synchrotron Radiation

PRINCIPAL INVESTIGATOR: Richard E. Johnston, Ph.D.

CONTRACTING ORGANIZATION: University of North Carolina
Chapel Hill, North Carolina 27599-1350

REPORT DATE: June 1999

TYPE OF REPORT: Final

PREPARED FOR: U.S. Army Medical Research and Materiel Command
Fort Detrick, Maryland 21702-5012

DISTRIBUTION STATEMENT: Approved for public release;
distribution unlimited

The views, opinions and/or findings contained in this report are those of the author(s) and should not be construed as an official Department of the Army position, policy or decision unless so designated by other documentation.

DTIC QUALITY INSPECTED 4

20001019 063

REPORT DOCUMENTATION PAGE			Form Approved OMB No. 074-0188	
Public reporting burden for this collection of information is estimated to average 1 hour per response, including the time for reviewing instructions, searching existing data sources, gathering and maintaining the data needed, and completing and reviewing this collection of information. Send comments regarding this burden estimate or any other aspect of this collection of information, including suggestions for reducing this burden to Washington Headquarters Services, Directorate for Information Operations and Reports, 1215 Jefferson Davis Highway, Suite 1204, Arlington, VA 22202-4302, and to the Office of Management and Budget, Paperwork Reduction Project (0704-0188), Washington, DC 20503				
1. AGENCY USE ONLY (Leave blank)	2. REPORT DATE June 1999	3. REPORT TYPE AND DATES COVERED Final (6/1/96 - 6/30/99)		
4. TITLE AND SUBTITLE Exploration of Monoenergetic X-Ray Mammography with Synchrotron Radiation		5. FUNDING NUMBERS DAMD17-96-1-6143		
6. AUTHOR(S) Richard E. Johnston, Ph.D.				
7. PERFORMING ORGANIZATION NAME(S) AND ADDRESS(ES) University of North Carolina Chapel Hill, North Carolina 27599-1350 E-MAIL: rej@med.unc.edu		8. PERFORMING ORGANIZATION REPORT NUMBER		
9. SPONSORING / MONITORING AGENCY NAME(S) AND ADDRESS(ES) U.S. Army Medical Research and Materiel Command Fort Detrick, Maryland 21702-5012		10. SPONSORING / MONITORING AGENCY REPORT NUMBER		
11. SUPPLEMENTARY NOTES				
12a. DISTRIBUTION / AVAILABILITY STATEMENT Approved for public release; distribution unlimited			12b. DISTRIBUTION CODE	
13. ABSTRACT (Maximum 200 Words) <p>During the period of this grant we have explored the use of monoenergetic x-rays to image samples of real breast tissue comparing DEI, monoenergetic radiographs and conventional mammography. We have demonstrated that the DEI images show structures in better detail than seen with conventional x-ray image systems, and in some cases show detail that was not visualized with the conventional system. We have been able to acquire additional tissue sample images that will provide the data to determine the parameter values for optimal image acquisition.</p> <p>The Monte Carlo simulation program we have developed is a powerful tool which can be used to determine the contrast sensitivity of the imaging system to various parameters, such as beam energy or tumor density. Comparisons between real digital images and Monte Carlo based simulations showed that the effects of scatter (conventional scatter, not diffraction or refraction effects) in the synchrotron images are considerably smaller than the effects of the system modulation transfer function and can be safely ignored. The simulation also found that scattered radiation in the SenoscanTM images was appreciable and therefore must be modeled in order to simulate the images accurately.</p>				
14. SUBJECT TERMS Mammography			15. NUMBER OF PAGES 190	
			16. PRICE CODE	
17. SECURITY CLASSIFICATION OF REPORT Unclassified	18. SECURITY CLASSIFICATION OF THIS PAGE Unclassified	19. SECURITY CLASSIFICATION OF ABSTRACT Unclassified	20. LIMITATION OF ABSTRACT Unlimited	

FOREWORD

Opinions, interpretations, conclusions and recommendations are those of the author and are not necessarily endorsed by the U.S. Army.

 Where copyrighted material is quoted, permission has been obtained to use such material.

 Where material from documents designated for limited distribution is quoted, permission has been obtained to use the material.

 Citations of commercial organizations and trade names in this report do not constitute an official Department of Army endorsement or approval of the products or services of these organizations.


N/A In conducting research using animals, the investigator(s) adhered to the "Guide for the Care and Use of Laboratory Animals," prepared by the Committee on Care and use of Laboratory Animals of the Institute of Laboratory Resources, national Research Council (NIH Publication No. 86-23, Revised 1985).

X For the protection of human subjects, the investigator(s) adhered to policies of applicable Federal Law 45 CFR 46.

N/A In conducting research utilizing recombinant DNA technology, the investigator(s) adhered to current guidelines promulgated by the National Institutes of Health.

N/A In the conduct of research utilizing recombinant DNA, the investigator(s) adhered to the NIH Guidelines for Research Involving Recombinant DNA Molecules.

N/A In the conduct of research involving hazardous organisms, the investigator(s) adhered to the CDC-NIH Guide for Biosafety in Microbiological and Biomedical Laboratories.


PI Signature 9/24/99
Date

1. TABLE OF CONTENTS

	Page
FOREWORD	3
INTRODUCTION	5
BODY	5
KEY RESEARCH ACCOMPLISHMENTS	7
REPORTABLE OUTCOMES	8
CONCLUSIONS	11
REFERENCES	11
LIST OF PERSONNEL	11
APPENDICES	12

Introduction (from original grant)

Approximately 10% of clinically obvious breast cancers are not visible with mammography. This occurs most frequently in patients with large amounts of breast glandular tissue. The density of this tissue tends to obscure underlying pathology. It is desirable to increase the sensitivity of mammography in these patients so that their cancers are apparent the first time they are present. It is expected that an increase in detection is possible with improvement in mammography instrumentation.

The x-ray emission from a synchrotron provides the capability of obtaining high photon fluxes, selectable monoenergetic x-ray beams and a nearly ideal narrow beam geometry that is maintained, i.e. non divergent, over great distances from the source. Thus, the synchrotron provides the ideal x-ray imaging source particularly for imaging of soft tissues such as the breast. Scatter radiation which is present in the x-ray beam after it passes through the object being imaged, degrades the image quality and reduces the contrast between the various tissues and structures within the breast. The use of an "analyzer" placed in the beam emerging from the imaged object, provides a beam with no scatter component to the image detector. Thus, the synchrotron x-ray imaging system should provide us with the maximum detectability possible with a transmission x-ray system.

We propose that with the development of this imaging system, we will have a system that should provide improved detectability of cancer in difficult cases such as dense breasts, and that will also be a "gold standard" with which to evaluate the importance of the various components of the more conventional imaging systems and their contribution to the image quality. The unique facilities and support available at The National Synchrotron Light source (NSLS) allow us the opportunity for these experimental explorations. With regard to the potentials of synchrotron radiation for mammography, the NSLS is at the moment unique in the entire world in that its beams are not only essentially optimized in energy range, but there is a dedicated medical research facility which uses the radiation from one of the beamlines for human research (presently for coronary angiography). Thus, it is very feasible in the future of mammographic imaging at the NSLS to carry out human studies.

Body

The exploration and evaluation of using monoenergetic x-rays for mammography imaging has progressed over this grant period to the point where we believe that a new imaging method, DEI, Diffraction Enhanced Imaging, is a viable means of imaging breast tissue. We have had access to synchrotron radiation beam lines 14 different times over the course of this award period, 12 runs at NSLS (National Synchrotron Light Source, Brookhaven National Laboratory) and two runs at the Advanced Photon source, Argonne National Laboratory. We have imaged 15 samples of breast tissue, 10 samples have been followed by pathological evaluation at this time and the remaining 5 are in the process of pathology preparation.

The detailed description of the experimental methods used for our studies to explore monoenergetic x-ray imaging of breast tissues and to develop and evaluate the DEI technique of imaging is presented in Appendices A.1,2,and 3.

Appendix A.1 is a paper that has been accepted for publication by Radiology and presents the results of imaging 7 formalin-preserved human breast cancer specimens including samples containing infiltrating ductal carcinomas. This paper summarizes the results of our original experimental evaluation of monochromatic x-ray imaging using the synchrotron.

In general terms, the DEI images have shown improved visualization of calcifications (in 6/7 cases) and spiculations (or architectural distortion) (in 7/7 cases). These are mammographic features that aid radiologists in detection and classification of breast lesions. As is seen in the accompanying illustrations, this improved detail has been confirmed as representing real histologic-anatomic structures. For example, spiculations that are better visualized with the DEI method correlated with structures seen on the histologic slides by the pathologist, sometimes representing breast cancer itself extending into the surrounding breast tissue, and sometimes representing fibrosis (scarring), the breast's natural reaction to the tumor's presence. In no instance has the increased lesion detail present in the DEI images proven to be artifactual. The accompanying illustrations show the improved visualization of spiculations representing tumor extension, spiculations representing fibrosis, and calcifications seen within the DEI images that were visualized within the pathologic specimens but that could not be seen on the conventional radiographs. Clearly, this amount of improved detail is quite promising, especially when one considers the fact that we have not yet optimized this technique for breast imaging.

During the extension of the grant to year 3, we were able to obtain tissue samples and images acquired under different acquisition parameter conditions. Namely, we obtained images at 18, 22 and 30 keV, at five different locations on the "rocking curve", using two different crystal lattice configurations and under Bragg and Laue analyzer crystal configurations.. These data are presently being processed and will be available for an observer study that is funded under grant DAMD17-99-1-9330 to determine the optimal acquisition parameter values. We have also acquired image data from "thick" tissue samples at no compression, modest compression and maximum compression. An observer study and analysis of all these data will be carried out, in part, under DAMD17-99-1-9330.

Monte Carlo Simulations:

A unique approach to simulating images by the Monte Carlo method was developed under the aspeces of this grant. By calculating the unscattered and scattered image components separately on different mesh sizes and then adding them together later, full field mammographic images using realistic pixel sizes can be simulated in reasonable amounts of time. Measurements of mammographic phantoms were taken at the NSLS for comparison with the results of our Monte Carlo code.

Analysis of the contrast of the objects in the contrast detail phantom images show very good agreement between Monte Carlo and the synchrotron images. The concept of

splitting the simulation into the unscattered and scattered components is a new idea in image simulation. In fact, realistic image simulation is not done very often due to the extraordinarily large times needed. With this new concept, image simulation in many areas of medical physics will be possible in reasonable times. Please refer to publications and Appendices A.3,7,9.

Key Research Accomplishments

- Demonstrated increased contrast in images from monoenergetic x-rays.
- Demonstrated increased contrast due to “extinction” using an “analyzer crystal. This is rejection of low angle scatter (diffracted x-rays on the order of milliradians) due to structural content of the target material.
- Discovered a new imaging technique, DEI, (Diffraction Enhanced Imaging) that is based on refraction of x-rays across boundaries in the target that have different indices of refraction.
- Demonstrated the improved detection of breast cancer features in human breast tissues samples with DEI, confirmed by pathological analysis.

Reportable Outcomes

Manuscripts, abstracts, presentations.

A. Publications/Manuscripts:

1. Johnston RE, Washburn D, Pisano E, Burns C, Thomlinson WC, Chapman D, Arfelli F, Gmur NF, Zhong Z, Sayers D. Mammography Phantom Studies with Synchrotron Radiation. Radiology 1996: 200, 659-663.
2. Chapman D, Thomlinson W, Arefeli F, Gmur N, Zhong Z, Menk R, Johnston E, Washburn D, Pisano E, Sayers D. "Mammography Imaging Studies Using a Laue Analyzer Crystal". Rev.Sci. Instrum. 1996: 67(9), CD-ROM.
3. Chapman D, Thomlinson W, Johnston RE, Washburn D, Pisano E, Gmur N, Zhong Z, Menk R, Arfelli F, Sayers D. Diffraction Enhanced X-Ray Imaging. Physics in Medicine and Biology, 1997.
4. D.E. Peplow "Direction Cosines and Polarization Vectors for Monte Carlo Photon Scattering". Nuclear Science and Engineering 1999: 131, 132-136.

5. D.E. Peplow and K. Verghese "Measured Molecular Coherent Scattering Form Factors of Animal Tissues, Plastics and Human Breast Tissue".
Physics in Medicine and Biology, 1998: 43 2431-2452.
6. Chapman D, Thomlinson W, Zhong Z, Johnston RE, Pisano ED, Washburn D, Sayers D, Segre E. Diffraction enhanced imaging applied to materials science and medicine. Synchrotron Radiation News 1998;11(2):4-11.
7. Chapman D, Pisano ED, Thomlinson W, Zhong Z, Johnston RE, Washburn D, Sayers D, Malinowska K. Medical applications of diffraction enhanced imaging. Breast Disease 1998;10(3,4):197-208.
8. Pisano ED, Johnston RE, Chapman D, Geradts J, Iacocca M.V, Levasy C.A, Washburn D, Sayers D, Zhong Z, Kiss M.Z, and Thomlinson W. Diffraction Enhanced Imaging of Human Breast Cancer Specimens: Improved Conspicuity of Lesion Detail with Histologic Correlation. Radiology (In press).
9. Peplow DE, Verghese K. Digital mammography image simulation using Monte Carlo. Accepted for publication in Medical Physics, 1999.
10. Johnston RE, Washburn D, Pisano E, Thomlinson WC, Chapman D, Gmür NF, Zhong Z, Sayers D. "Preliminary Experience with Monoenergetic Photon Mammography", Medical Imaging 1995, Physics of Medical Imaging, SPIE Vol. 2432, pp. 434-441, (1996),
11. Arfell F, Burns C, Chapman D, Gmür N, Johnston RE, Menk R, Pisano E, Sayers D, Thomlinson W, Washburn D, Zhong Z. "Data Acquisition and Analysis of Mammography Images at the NSLS", NSLS, BNL, Upton, NY, BNL Informal Report 62935, (1995),
12. Thomlinson W, Chapman D, Zhong Z, Johnston RE and Sayers D. "Diffraction Enhanced X-ray Imaging", Medical Applications of Synchrotron Radiation, eds. M. Ando and C. Uyama (Springer-Verlag, Tokyo, 1998) p. 72-76,
13. DEI web page <http://ncstarl.physics.ncsu.edu>.

B. Presentations/Abstracts:

Presentations by Etta Pisano, M.D.

How Diffraction Enhanced Imaging Might Improve Breast Cancer Detection with Mammography. Illinois Institute of Technology Breast Cancer Awareness Month Celebration. Chicago, Il, October 22, 1998.

Presentations by William Thomlinson, Ph.D.

"Synchrotron Based Mammography Imaging," Physics Dept., Colby College,

November 27, 1996.

"Synchrotron Radiation in Medical Research," Materials Research Society, San Francisco CA, April 10, 1996.

"Medical Research Applications of Synchrotron Radiation," Applications of Physics in Medicine and Biology, Trieste, Italy, September 2, 1996.

"Medical Imaging with Synchrotron Radiation," Paul Scherrer Institute, Villigen, Switzerland, October 1996.

"Mammography Using Synchrotron Radiation," University of Lausanne, Switzerland, October 1996.

"Radiologic Use of Synchrotron Radiation," Meeting of Swiss Synchrotron Society, Neuchatel, Switzerland, October 27, 1996.

"Monochromatic Beam Mammography Studies Using Synchrotron Radiation," IEEE Medical Imaging Conference, Anaheim, CA, November 6-9, 1996.

"X-Ray Schlieren Imaging," IEEE Medical Imaging Conference, Anaheim, CA, November 6-9, 1996 (with D. Chapman, R. Menk, Z. Zhong).

"Monochromatic Energy Subtraction Radiography," Physics Dept., Colby College, Feb. 11, 1997.

"Applications of Synchrotron Radiation in Medical Research," Helsinki University Central Hospital, Helsinki, Finland, March 3, 1997.

"Monochromatic Beam Mammography Using Synchrotron Radiation," Radiology 97, Birmingham, England, May 19, 1997.

"Medical Applications of Synchrotron Radiation," Haga Workshop, Japan, Aug. 9, 1997.

"Diffraction Enhanced Imaging," Haga Workshop, Japan, Aug. 9, 1997.

"Medical Applications of Synchrotron Radiation at the NSLS," Harima, Japan, Aug. 11, 1997.

"Diffraction Enhanced Imaging Applied to Mammography", JRIM Toulouse, France, Feb. 4, 1998.

"Diffraction Enhanced Imaging," ESRF, March 17, 1998.

"Synchrotron Radiation in Research and Clinical Medicine", Biology and Synchrotron Radiation Conference, Argonne, IL, Aug. 7, 1998.

"Fundamentals of Synchrotron Radiation and Its Applications to Medical Research", Swiss Association of Radiation Oncology, Villigen, Switzerland, March 5, 1999.

"X-Ray Imaging: From Amplitude to Phase", International Union of Crystallography, Glasgow, Scotland, August 7, 1999.

Presentations by Dean Chapman, Ph.D.

Medical Imaging, plenary session talk at Synchrotron Radiation Instrumentation 1995, Argonne National Laboratory, August 1995.

X-ray Schlieren Imaging, IEEE Medical Imaging Conference, San Francisco, November 1995.

X-ray Refraction Imaging, Physics Colloquium, Northern Illinois University, 1996

Diffraction Enhanced X-ray Microtomography, Microscopy and Imaging Workshop, 1997 NSLS Users Meeting at Brookhaven National Laboratory, April 1996.

Diffraction Enhanced X-ray Imaging, General Electric Corporate Research and Development, Schenectady, NY, June 1997.

X-ray Refractive Index of a Rodent, APS InterCAT Technical Working Group, Oct. 1997, Advanced Photon Source, Argonne National Laboratory.

Diffraction Enhanced X-ray Imaging, American Association of Physics Teachers - Chicago Section, November 1997.

Diffraction Enhanced X-ray Imaging applied to Mammography, Seminar at Rush Memorial Hospital, Chicago, Jan. 6, 1998.

Medical and Biological Applications of Diffraction Enhanced Imaging, Biophysics in Synchrotron Radiation – 98, August 3-8, Advanced Photon Source.

A Bent Laue Analyzer for Fluorescence EXAFS Detection, Workshop, Biophysics in Synchrotron Radiation – 98, August 3-8, Advanced Photon Source.

Applications of Diffraction Enhanced Imaging, Swiss Light Source Workshop, August 1-5, Ascona, Switzerland

Medical and Biological Applications of Diffraction Enhanced Imaging, Plenary Talk, IEEE Medical Imaging Conference, November 1998, Toronto, Canada

Biological and Medical Applications of Diffraction Enhanced Imaging, Biology Colloquium, Feb. 1, 1999, Biological, Chemical, and Physical Sciences, IIT.

Recent Developments in Diffraction Enhanced Imaging Mammography, Graduate Programs in Medical Physics Seminar, University of Chicago, Feb. 16, 1999.

Applications of Diffraction Enhanced Imaging, Proctor and Gamble Corporation, Cincinnati, Ohio, Feb. 19, 1999.

Diffraction Enhanced Mammography, American Association of Physicists in Medicine Conference, Nashville, Tennessee, July 26, 1999

Patents and licenses applied for and/or issued

(I believe the existng patent was applied for prior to this grant and nothing be reported here???)

Degrees Obtained supported (in part) by this award:

Douglas E. Peplow, Ph.D. North Carolina State University, 1999.

Funding applied for based on work supported by this award:

1. USAMRMC, DAMD17-99-1-9330, Awarded July 1999.. Title: Radiologist Evaluation of DEI Breast Specimen Imaging, PI, Etta Pisano, M.D.
2. USAMRMC - Academic Research Award
DAMD 17-99-1-927 Application of Diffraction Enhanced Imaging to Medical Imaging 1 May 1999 - 1 June 2002,
PI: Dean Chapman, Ph.D.
3. NIH - R21 Award
1 R21 GM59395-01 Diffraction Enhanced Imaging Applied to Mammography
1 May 1999 - 30 April 2001,

PI: Dean Chapman, Ph.D.

4. Funding Agency: Department of Energy

Title: Image and Dose Simulation in Support of New Mammography

Modalities

Duration: 2 years - June 1, 1998 - May 31, 2000

PI: Kuruvilla Verghese

5. Educational grant from Sun Microsystems for a computing system dedicated to mammography simulations by Monte Carlo methods. 1998. The computing system was valued at \$39,000.

6. BCRP 98 pre-doctoral grant.

Title: "Integrating Digital Detectors into a Diffraction Enhanced Imaging System."

Awarded to Miklos Kiss, Physics Dept., North Carolina State University, 1999.

Conclusions

During the period of this grant we have explored the use of monoenergetic x-rays to image samples of real breast tissue comparing DEI, monoenergetic radiographs and conventional mammography. We have demonstrated that the DEI images show structures in better detail than seen with conventional x-ray image systems, and in some cases show detail that was not visualized with the conventional system. We have been able to acquire additional tissue sample images that will provide the data to determine the parameter values for optimal image acquisition.

The Monte Carlo simulation program we have developed is a powerful tool which can be used to determine the contrast sensitivity of the imaging system to various parameters, such as beam energy or tumor density. Comparisons between real digital images and Monte Carlo based simulations showed that the effects of scatter (conventional scatter, not diffraction or refraction effects) in the synchrotron images are smaller than the effects of the system modulation transfer function and can be safely ignored. The simulation also found that scattered radiation in the SenoscanTM images was appreciable and therefore must be modeled in order to simulate the images accurately.

References

Please refer to the publications listed and included in the Appendices.

Personnel Receiving Payment

R. Eugene Johnston, Ph.D. PI.

Etta D. Pisano, M.D. Co-PI

Douglas Peplow, Graduate student

Miklos Kiss, Graduate student

Suquan Zong, Graduate student

Darrin O'Connor, student

Appendices

A.1

Pisano ED, Johnston RE, Chapman D, Geradts J, Iacocca M.V, Levasy C.A, Washburn D, Sayers D, Zhong Z, Kiss M.Z, and Thomlinson W. Diffraction Enhanced Imaging of Human Breast Cancer Specimens: Improved Conspicuity of Lesion Detail with Histologic Correlation. Radiology (In press).

A.2

3.Chapman D, Thomlinson W, Johnston RE, Washburn D, Pisano E, Gmur N, Zhong Z, Menk R, Arfelli F, Sayers D. Diffraction Enhanced X-Ray Imaging. Physics in Medicine and Biology, 1997.

A.3

D.E. Peplow and K. Verghese ``Measured Molecular Coherent Scattering Form Factors of Animal Tissues, Plastics and Human Breast Tissue". Physics in Medicine and Biology, 1998: 43 2431-2452.

A.4

Johnston RE, Washburn D, Pisano E, Burns C, Thomlinson WC, Chapman D, Arfelli F, Gmur NF, Zhong Z, Sayers D. Mammography Phantom Studies with Synchrotron Radiation. Radiology 1996: 200, 659-663.

A.5

Chapman D, Thomlinson W, Arefeli F, Gmur N, Zhong Z, Menk R, Johnston E, Washburn D, Pisano E, Sayers D. "Mammography Imaging Studies Using a Laue Analyzer Crystal". Rev.Sci. Instrum. 1996: 67(9), CD-ROM.

A.6

Chapman D, Pisano ED, Thomlinson W, Zhong Z, Johnston RE, Washburn D, Sayers D, Malinowska K. Medical applications of diffraction enhanced imaging. Breast Disease 1998;10(3,4):197-208.

A.7

D.E.Peplow and K.Verghese ``Digital mammography image simulation using Monte Carlo. Accepted for publication in Medical Physics, 1999.

A.8

"Diffraction Enhanced X-ray Imaging", Medical Applications of Synchrotron Radiation, eds. M. Ando and C. Uyama (Springer-Verlag, Tokyo, 1998) p. 72-76, W. Thomlinson, D. Chapman, Z. Zhong, R. E. Johnston and D. Sayers.

A.9

D.E. Peplow "Direction Cosines and Polarization Vectors for Monte Carlo Photon Scattering". Nuclear Science and Engineering 1999: 131, 132-136.

A.10

Chapman D, Thomlinson W, Zhong Z, Johnston RE, Pisano ED, Washburn D, Sayers D, Segre E. Diffraction enhanced imaging applied to materials science and medicine. Synchrotron Radiation News 1998;11(2):4-11.

A.11

"Preliminary Experience with Monoenergetic Photon Mammography", Medical Imaging 1995, Physics of Medical Imaging, SPIE Vol. 2432, pp. 434-441, (1996), R. E. Johnston, D. Washburn, E. Pisano, W.C. Thomlinson, D. Chapman, N.F. Gmür, Z. Zhong, D. Sayers.

A.12.

"Data Acquisition and Analysis of Mammography Images at the NSLS", NSLS, BNL, Upton, NY, BNL Informal Report 62935, (1996), F. Arfelli, C. Burns, D. Chapman, N. Gmür, R.E. Johnston, R. Menk, E. Pisano, D. Sayers, W. Thomlinson, D. Washburn, Z. Zhong.

Appendix

A.1

Pisano ED, Johnston RE, Chapman D, Geradts J, Iacocca M.V, Levasy C.A, Washburn D, Sayers D, Zhong Z, Kiss M.Z, and Thomlinson W. Diffraction Enhanced Imaging of Human Breast Cancer Specimens: Improved Conspicuity of Lesion Detail with Histologic Correlation. Radiology (In press).

Diffraction Enhanced Imaging of Human Breast Cancer Specimens: Improved
Conspicuity of Lesion Detail with Histologic Correlation

Etta D. Pisano, MD*^

R. Eugene Johnston, PhD*

Dean Chapman, PhD``

Joseph Geradts, MD, MA°

Mary V. Iacocca, MD”

Chad A. Livasy, MD”

David B. Washburn, PhD*

Dale E. Sayers, PhD’

Zhong Zhong, PhD`

Miklas Z. Kiss, MS’

William Thomlinson, PhD`

The Departments of Radiology* and Pathology” and UNC-Lineberger
Comprehensive Cancer Center^ of the University of North Carolina School of
Medicine, UNC-CH;
Department of Physics and Center for Synchrotron Radiation Research and
Instrumentation, Illinois Institute of Technology``, Chicago, IL;
Nuffield Department of Pathology & Bacteriology, University of Oxford°, United
Kingdom
Department of Physics, North Carolina State University’, Raleigh, NC; and
Brookhaven National Laboratory`, Upton, NY.

Corresponding Author:

Etta D. Pisano

The Department of Radiology and UNC-Lineberger Comprehensive Cancer
Center

Manning Drive

University of North Carolina School of Medicine

Chapel Hill, NC 27599-7510

(919)966-6957

FAX: (919)966-0817

etpisano@med.unc.edu

Supported in part by US Army grant DAMD17-96-1-6143, US Department of
Energy Contract DE-AC 02-76CH00016, and by the State of Illinois Higher
Education Cooperative Agreement.

Diffraction Enhanced Imaging of Human Breast Cancer Specimens: Improved
Conspicuity of Lesion Detail with Histologic Correlation

Author's Contributions:

Guarantor of Integrity of Entire Study: EDP, REJ

Study Concepts: EDP, REJ, DC, DW, DS and WCT

Study Design: EDP, REJ, DC

Definition of Intellectual Content: EDP, REJ, DC

Literature Research: EDP, REJ, DC

Clinical Studies: Not applicable.

Experimental Studies: EDP, REJ, DC, JG, CAL, DW, DS, ZZ, MK and WCT

Data Acquisition: REJ, DC, DW, DS, ZZ, MK and WCT

Data Analysis: EDP, REJ, JG, MI and CAL

Statistical Analysis: Not applicable.

Manuscript Preparation: EDP, REJ, DC, CAL, MI, JG, and ZZ

Manuscript Editing: All co-authors.

Manuscript Review: All co-authors.

Abstract

Seven breast cancer specimens were imaged using Diffraction Enhanced Imaging at 18 keV with a silicone crystal utilizing the [333] reflection in Bragg mode. Images were compared to digital specimen radiographs and regions of increased detail were identified. Six of the seven cases (85.7%) showed enhanced visibility of surface spiculization which correlated with histopathologic information, including extension of tumor into surrounding tissue.

Key Words: Diffraction Enhanced Imaging, Breast Cancer, Synchrotron

Introduction

Overview of Previous Work

Mammographic technology has improved dramatically in the last two decades. Improvements include the development of dedicated mammography equipment with appropriate x-ray beam quality, adequate breast compression and automatic exposure control[1]. Digital mammography is the most recent development and is just now being introduced into the clinic, holding the promise of improved early detection of breast cancer[2]. All currently existing systems depend on the depiction of x-ray absorption to define the differences between normal and abnormal tissues. A new radiographic imaging method, Diffraction Enhanced Imaging, DEI, partly depends upon the refractive properties of an object in the creation of a scatter-free image[3]. This new method, which seeks to improve the x-ray beam properties for improved contrast, along with the new digital mammography detectors, could improve early detection of occult disease. See the Appendix for a complete description of the principals of DEI.

Other researchers have applied diffractive optics to imaging problems[4-7] and have observed refraction effects. There is also great interest in phase contrast imaging which makes use of the high transverse coherence of third generation synchrotron sources. However, these types of measurements are limited to materially thin objects and / or high x-ray imaging energies to obtain phase contrast images of the object[8,9]. The DEI technique works for samples of the same thickness as the human breast, and, after further development, should be achievable without the use of a synchrotron.

For this project, the mammography imaging technique under development utilizes the high intensity and collimation of synchrotron radiation to create a monoenergetic line scan imaging system which has very little scatter[10]. Synchrotron radiation is the electromagnetic radiation emitted as charged particles (electrons or positrons) change direction while passing through electromagnets. The magnets restrain the particles to a circular orbit in large accelerators called "synchrotrons", although most of the modern machines are really storage rings in which the electric currents persist for many hours at constant energy. The particles are highly relativistic, travelling at or near the speed of light, so that the radiation produced has several unique properties. The intensity of the radiation is 5 to 6 orders of magnitudes higher than a laboratory source. The energy spectrum is smooth and continuous from the infra-red to the hard x-ray range. The radiation is inherently collimated in the plane of the orbit. The radiation is taken out of the machine through metal windows and delivered to experimental stations via long vacuum vessels called beamlines. The unique radiation properties, when coupled with modern perfect crystal x-ray optics, are used to define very high intensity beams which are highly monochromatic at any selected energy and are highly collimated for medical and other applications.

In addition, this study utilized an analyzer crystal as a scatter rejection optic. Experiments performed with this scatter rejection optic revealed that DEI is also sensitive to refractive index effects within the object being imaged.

This paper describes our first results with human breast cancer specimen imaging. We have previously reported our results with phantoms[10].

Materials and Methods

The experimental setup used to apply this technique is shown in Figure 1, which shows both the synchrotron radiography system (Figure 1a) and the addition of the analyzer crystal to the DEI system (Figure 1b). The white synchrotron beam is made nearly monochromatic by a silicon double crystal monochromator. For the measurements described here the beam energy was either 18 keV or 30keV. Experiments were carried out at two separate facilities: the National Synchrotron Light Source (Brookhaven National Laboratory, Upton, NY) using the X27C Research and Development Group beamline, and at the Advanced Photon Source (Argonne National Laboratory, Argonne, IL) using the Synchrotron Radiation Instrumentation Collaborative Access Team 1-BM beamline.

The imaging beam was approximately 80 mm wide and 1 mm high at the location of the object. An ionization chamber was used to measure the radiation exposure at the surface of the object. Images taken with and without the analyzer crystal were at exposure levels comparable to conventional mammography x-ray systems. The breast specimen to be imaged was mounted on a scanning stage driven by a stepping motor. The x-ray beam transmitted through the object could be either imaged directly, as in standard radiography, or following diffraction in the vertical plane by the silicon crystal analyzer. Radiation exposure to the image plate was controlled by adjusting the scan speed and absorbers in the incident beam to maintain an exposure of about 1.3 mC/kg

(5mR) to the plate. Typical scanning times for these experiments were on the order of 4 to 200 seconds. These limits were dictated by our scanning motors and the mechanical system.

The detector was a photo-stimulative phosphor image plate, typically used for radiology (Fuji Medical Systems high resolution HR5 and standard resolution ST5 image plates, Fuji Medical Systems USA, Stamford, CT). The image recorded on the plate was digitized, stored and displayed by a Fuji Medical Systems AC3 reader and workstation or a BAS2000 reader system, also manufactured by Fuji. The image plates were read out at 2560 x 2048 matrix size, which results in an image of 100 microns per pixel ($0.1 \times 0.1 \text{ mm}^2$).

The diffraction angle of the analyzer crystal could be finely tuned using a stepper-motor driven translation stage pushing on a long bar attached to an axle to which the crystal was attached (tangent arm). The resolution limit of the tangent arm was 0.1 microradian, which was sufficient for placing the Bragg analyzer crystal at a selected position on its rocking curve.

For each sample, a “normal” radiograph with the monochromatic beam can be taken by moving the image plate to a location just downstream of the object on the sample scanning stage and scanning the combined object and image plate through the fan beam. DEI images were then acquired with the analyzer crystal tuned to various positions on the rocking curve by translating the sample and the image plate in opposite directions at the same speed through the fan beam. The change in scanning direction arises from the beam inversion from the analyzer crystal. At a scan speed of about 10 mm/s, the surface dose on the

sample was a few mGy at 18 keV and tenths of mGy at 30 keV. Rocking curves through a specific location within the specimen were obtained by fixing the specimen in the fan beam and performing a series of exposures by incrementally changing the analyzer crystal position and image plate vertical position. The rocking curve is useful for quickly visualizing the optimum analyzer position for contrast enhancement of the desired features.

Seven formalin-fixed human breast cancer specimens were imaged, three infiltrative lobular and four infiltrating ductal carcinomas. These specimens measured approximately 1 cm. in thickness. Each biological sample was sealed in a plastic bag and compressed between two Lucite plates so that the absorbing thickness was approximately 40 mm. Images were obtained at 18 keV, utilizing the [333] reflection of silicone crystals as monochromator and analyzer. The crystals were in symmetric Bragg mode, meaning that the beam makes the same angle with the crystal surface. For each sample, five images were obtained at angular positions of 0 (peak position), $\pm W/2$ and $\pm W$ on the rocking curve, where W is the full width of half maximum point on the rocking curve.

Images of the same specimens were also obtained using the Fischer SenoScan digital mammography unit. (Fischer Medical Imaging Corporation, Boulder, CO).

DEI and digital images of the specimens were subsequently evaluated by a single expert breast imager (EDP). She identified regions of interest within the DEI images that showed apparently increased lesion information. This was done

by comparing the digital radiograph and the DEI image side by side and circling areas on the DEI images. No regions of interest were identified in the standard digital radiographs.

Histologic whole mount slides of the specimens were made. With the assistance of the radiologist and direct comparison of the whole mount slides to the DEI specimen images, an expert breast pathologist (JG) evaluated the regions of interest in the specimens to determine whether the information apparent in the DEI images correlated with real histopathological structures.

This study was formally granted an exemption from review by the Institutional Review Board at the participating institutions.

Results

The DEI breast cancer specimen images have shown improved visualization of lesion spiculation and architectural distortion in 6 of 7 cases (85.7%), with the 10 regions of interest identified by the participating radiologist. These regions of interest were areas that showed increased spiculation or architectural distortion on the DEI image compared to the standard digital specimen radiograph. For these 10 areas, histopathologic review revealed the spiculations to be infiltrating ductal carcinoma (2 regions in one specimen), infiltrating lobular carcinoma (2 regions, each in a different specimen), ductal carcinoma in situ with surrounding fibrosis (1 region), fibrosis alone (3 regions in 3 separate specimens), fibrocystic change (1 region) and biopsy site changes (1

region). In every case of enhanced spiculation visualization, there was a histopathological correlate that could explain the imaging finding.

The accompanying figures show the improved visualization of spiculations corresponding with tumor extension (figures 2, 3 and 4), and spiculations corresponding to fibrosis (figure 5).

Discussion

This technique was developed using a synchrotron x-ray source. The high intensity, collimation, and tunability available using synchrotron sources make them ideal environments in which new imaging technologies, such as DEI, can be developed. An obvious drawback is then translating this technology to more conventional x-ray sources in a laboratory or clinical environment. The DEI technique delivers x-ray exposures to tissue and phantoms which is similar to that delivered by conventional x-ray mammography units. The difficulty arises in generating the highly collimated - monoenergetic imaging beam. The monochromating crystal and analyzer crystal must use the same Bragg reflection to achieve the high degree of collimation necessary to observe the refraction and scatter rejection presented earlier. Perfect single crystal silicon monochromators and analyzer are used to achieve the DEI effect. Such systems are used routinely with conventional x-ray sources, but for DEI to be applied to mammography, the source intensity and properties must be such that exposures are obtained in a few seconds to avoid image blurring due to patient motion.

Estimates of the flux from conventional x-ray sources have yielded scan time estimates of approximately 1000 to 10,000 seconds. Clearly, such long scan times to deliver a DEI image set would be unacceptable. These times are based on commercially available x-ray sources and indicate that the application of DEI with conventional sources will be challenging. However, there are reasons to believe that this will be possible.

First, conventional x-ray imaging uses the x-ray beam arising directly from the target of the x-ray tube. The spectrum may be filtered. In the implementation of DEI a monochromator must be used to collimate the imaging beam. This monochromating element allows the operational parameters of the tube to be optimized for the creation of the flux at the desired imaging energy. This eliminates concern for other parts of the spectrum that would normally deliver unnecessary dose, for example, the creation of bremsstrahlung radiation. High accelerating voltages become attractive since the flux contained in an emission line of the source is enhanced at higher accelerating voltages.

Second, the prospect of obtaining diagnostic information from the diffraction image leads to higher optimal imaging energies. Since the tissue absorption is reduced at higher energy, the transmission and thus flux requirements are reduced. However, two competing effects limit the imaging energy. First, the refraction sensitivity is reduced and secondly, the flux diffracted by the monochromator is reduced. Estimates and measurements indicate that the optimal imaging energy is in the 30keV range. An additional

benefit of this energy is reduced dose delivery (x15 less than at 18keV) and possible reduction in breast compression.

Third, multiple crystal systems can be used to use more of the source emission. Though difficult to align, a ten crystal will allow a factor of ten less scan time and scan range.

Finally, the advent of digital detectors for mammography may allow more efficient exposure utilization. A contributing element may also be the lack of scatter in the acquired image that may allow a reduction in exposure in obtaining useful diagnostic information. Perhaps this method, paired with the new more efficient detectors, will allow for the use of higher energy beams and allow for lower patient dose.

The combination of these four factors may allow a nonsynchrotron, conventional, source to be constructed. However, determining the optimal parameters for a conventional system will take time. The synchrotron with its wide flexibility in trying and modeling source parameters will play a major role in this endeavor.

These results suggest that there is potential for improved visualization of breast cancer detail by utilizing the diffraction component of the xray beam. This improved detail was achieved even without optimization of this technique for breast imaging. To obtain the maximum amount of information from DEI images for breast cancer detection and characterization, careful evaluation of image detail with histologic correlation by experts should be carried out. In this manner, the optimum crystal type, reflection type, imaging energy and rocking curve

location can be determined so that the specifications for a clinically useful (office-based) system can be developed.

Given the increased visibility of lesion features with DEI in all three cases of infiltrating lobular carcinoma that we evaluated, we wonder if this method might improve detectability of this frequently occult lesion. Infiltrating lobular carcinoma is the second most common type of invasive breast cancer, occurring in approximately 15% of women with infiltrative tumors. In fact, lobular tumors are bilateral in 10% of cases. Frequently the extent of this type of tumor is significantly underestimated by traditional imaging methods. Perhaps DEI can improve the detection of this lesion through increased visibility of subtle spiculations and architectural distortions.

This work is limited in that we have yet to evaluate any specimens predominately containing clustered calcifications. We are currently imaging breast samples that contain this type of mammographic lesion and plan to report those results in the near future.

In summary, we believe that these results suggest promise for diffraction imaging as applied to breast cancer detection and diagnosis. Further work is ongoing to determine the optimal diffraction imaging parameters for these clinical tasks.

Acknowledgements

The authors gratefully acknowledge the contributions of Anna Cleveland, N.F. Gmur, Fischer Medical Imaging Corporation (Boulder, CO), Fuji Medical Systems USA (Stamford, CT), and the Eastman Kodak Corporation (Rochester, NY).

References:

1. Haus AG. Technologic Improvements in Screen-Film Mammography. *Radiology* 1990;174(3):628-637.
2. Shtern, F. Digital mammography and related technologies: a perspective from the National Cancer Institute. *Radiology* 1992;183:629-630.
3. Chapman D, Thomlinson W, Johnston RE, Washburn D, Pisano E, Gmur N, Zhong Z, Menk R, Arfelli F, Sayers D. Diffraction enhanced x-ray imaging. *Phys. Med. Bio.* 1997;42:2015-2025.
4. Ingal VN, Beliaevsky EA. X-ray plane-wave topography observation of phase contrast from a non-crystalline object. *J. Physics D: Appl. Phys.* 1995;28:2314-2317.
5. Somenkov VA, Tklich AK, Sh. Shil'shtein S. Refraction contrast in x-ray introscopy. *Sov. Phys. Tech. Phys* 1991;36(11):1309-1311 (Brief Communication).
6. Podurets KM, Somenkov VA, Sh. Shil'shtein S. Refraction-contrast radiography, *Sov. Phys. Tech. Phys.* 1989;34:654.
7. Gureyev TE, Wilkins SW. Regimes of X-ray Phase-Contrast Imaging with Perfect Crystals. *Il Nuovo Cimento* 1997;19:545-552.
8. Davis TJ, Gureyev TE, Gao D, Stevenson AW Wilkins SW. X-Ray Image Contrast from a Simple Phase Object. *Phys. Rev. Lett.* 1995;74:3173-3175.
9. Davis TJ, Gao D, Gureyev TE, Stevenson AW, Wilkins SW. Phase-contrast of weakly absorbing materials using hard X-rays. *Nature* 1995;373:595-598.

10. Johnston RE, Washburn D, Pisano E, et al. Mammographic Phantom Studies with Synchrotron Radiation. *Radiology* 1996;200:659-663.
11. Bushuev VA, Ingal VN, Belyaevskaya EA. Dynamical Theory of Images Generated by Noncrystalline Objects for the Method of Phase-Dispersive Introscopy. *Crystallography Reports* 1966;41:766-774.
12. Zachariasen WH. *Theory of X-Ray Diffraction in Crystals*. New York, John Wiley and Sons;1945: Ch 4.
13. Guinier A, Fournet G, Walker CB, Yudowitch KL. *Small-angle scattering of x-rays*. New York, John Wiley and Sons, 1955.
14. Chapman D, Thomlinson W, Arfelli F, et al. Mammography Imaging Studies using a Laue Analyzer Crystal. *Rev. Sci. Instrum.* 1966;67(9):CD-ROM.

Figure Captions.

Figure 1

Experimental Setup. Figure 1a schematically shows the synchrotron setup used to obtain radiographs of the object. Figure 1b shows the addition of the analyzer crystal (Bragg or reflection geometry) used to implement the DEI system.

Figure 2A

This specimen contains invasive lobular carcinoma which typically grows in single files of cells. Figure 2A shows the specimen digital radiograph. Note the vague linear densities along the inferior margin of the lesion, some of which are marked with arrows. A scratch artifact lies across the top portion of the image.

Figure 2B

Figure 2B shows the diffraction image of the same specimen. Note the increased prominence and number of lines extending from the inferior border of the lesion at the arrows.

Figure 2C

Figure 2C is a high power view of the spiculations identified between the two arrows in Figure 2B. It shows a band of fibrous tissue with invasive lobular carcinoma (arrows). The other spiculations identified by a single arrow in Figure

2B proved to be both infiltrating lobular carcinoma and fibrous bands.

(Hematoxylin and Eosin (H&E) stain, 10X magnification)

Figure 3A

This invasive lobular carcinoma extends to the edge of the digital specimen radiograph. As marked by a curved white arrow, there is a suggestion of an additional focus of tumor with some evidence of spiculations extending from its surface at the edge of the specimen.

Figure 3B

The diffraction image improves the visibility of these fine lines (curved black arrow). This was identified as a region of interest for this study.

Figure 3C

Figure 3C reveals invasive lobular carcinoma (arrows) within fibrous bands corresponding to the visualized spiculations. (H & E stain, 100X magnification)

Figure 4A

Figure 4A shows the specimen digital radiograph for an infiltrating ductal carcinoma that extends to the skin. A white curved arrow in figure 4A shows an area identified as a region of interest for this study that appears as a possible

mass or satellite lesion on the digital radiograph. A straight white arrow on Figure 4A shows a small mass.

Figure 4B

Figure 4B is a diffraction image of the specimen with the area corresponding to the marked area in Figure 4A marked with a black curved arrow. This reveals subtle spiculations along the superior aspect of a definite mass. In addition, at the mass marked by a straight arrow, there are more obvious spiculations in the diffraction image. These proved to be a focus of infiltrating ductal carcinoma.

Figure 4C

Figure 4C reveals tongues of infiltrating ductal carcinoma (arrows) corresponding with the subtle spiculations visible at the tip of the curved black arrow in Figure 4B. (H & E stain, 5X magnification)

Figure 5A

A digital specimen radiograph of an infiltrating ductal cancer.

Figure 5B

This diffraction image shows fine spiculations on the surface of the lesion, lying between the two arrows, that are not identified on the digital radiograph. This area was identified as a region of interest for this study. This area represented only fibrous tissue bands pathologically, a desmoplastic reaction to the presence

of tumor. This pathologic feature is a frequent cause for spiculations and architectural distortion in mammograms.

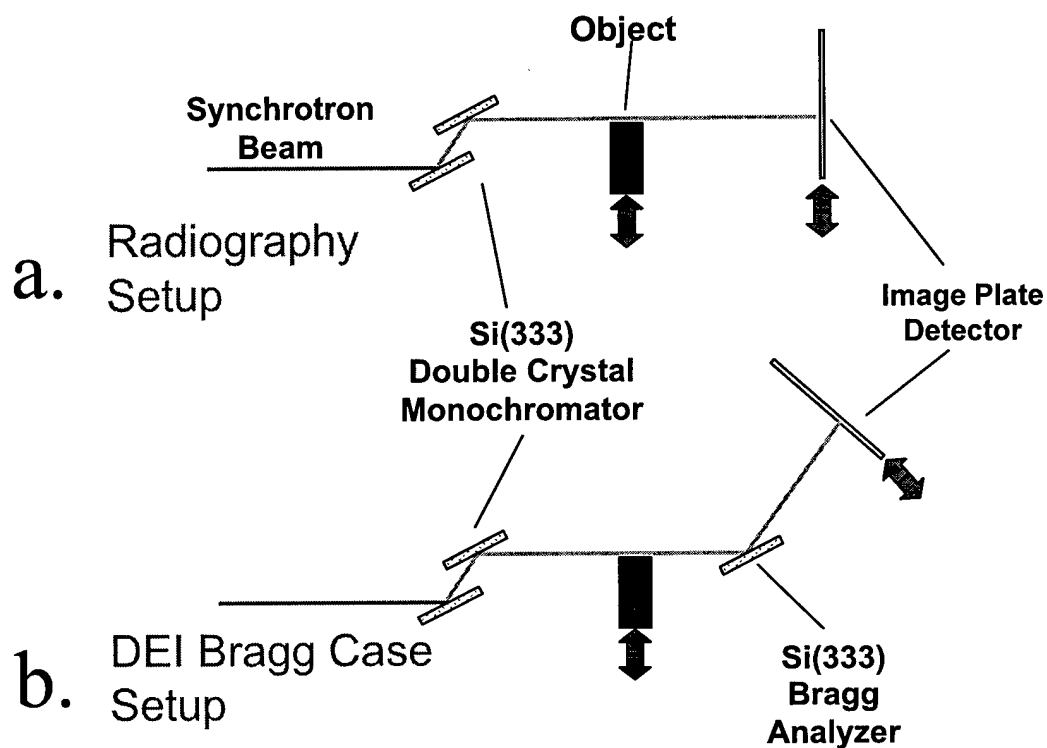


Figure 1.

Experimental Setup. Figure 1a schematically shows the synchrotron setup used to obtain radiographs of the object. Figure 1b shows the addition of the analyzer crystal (Bragg or reflection geometry) used to implement the DEI system.

Appendix

Principles of DEI

Conventional radiography uses an area beam which, after traversing and interacting with the subject, is intercepted and recorded by an area detector. The interaction of x-rays with the subject is complex, involving absorption, refraction [4-7] and scattering. The scattering may include small angle scattering [11] (scattering angles less than milliradians) which carries information about the subject's structure on the length scale up to microns. This information is lost in normal radiography because of its small angle nature. The refraction of x-rays inside the object is also not detectable in conventional radiography due to its small angle nature (on the order of microradians).

X-ray diffraction from perfect crystals, with narrow reflection angular width (on the order of a few microradians) and peak reflectivity of close to unity, provides the tools necessary to prepare and analyze x-ray beams traversing an object on the microradian scale [12]. Such crystals, typically silicon, are routinely used in the semiconductor industry to make integrated circuits and electronic devices. The purity and perfection of these crystals have allowed many advances in x-ray diffraction techniques, in particular at x-ray synchrotron sources.

The condition for x-ray diffraction from a crystal is met only when the incident beam makes the correct angle to the atomic lattice planes in the crystal for a given x-ray energy or wavelength. When this condition is met the beam

diffracts from the planes over a narrow range of incident angles, so called Bragg diffraction. As the crystal is rotated about an axis parallel to the lattice planes and perpendicular to the incident beam direction, an intensity variation observed. This is referred to as the rocking curve. The shape of this curve is roughly triangular with the peak reflectivity approaching nearly 100%.

In DEI an imaging beam is prepared by diffracting the polychromatic beam from the synchrotron to create a nearly monoenergetic imaging beam. This beam is then passed through the object being imaged as in conventional radiography. However, a matching crystal is placed between the object and the detector. This crystal is set at or near the peak of Bragg diffraction and is called the analyzer crystal. A schematic representation of a synchrotron radiography and DEI system is shown in Figure 1.

Since the condition for diffraction from this crystal limits the x-rays which can be diffracted into the detector, it automatically provides a high degree of scatter rejection resulting in improved image contrast. The range of angles accepted by the analyzer crystal is a few microradians, thus providing scatter-rejection more completely than the capabilities of conventional anti-scatter techniques such as slit collimation and grids.

The rejected scatter falls into a category referred to as small angle scattering[13], or scattering which arises from diffraction from very small organized structures. This scattering intensity, which would normally appear in the image, is missing and appears in the same way as absorption in the image. We call the improved image contrast obtained through scatter rejection of this

sort extinction contrast, drawing from a similar term used in optics and x-ray diffraction to describe intensity loss due to diffraction and scattering. Therefore, in DEI, the image which represents the absorption of the object by x-rays is referred to as the apparent absorption image, since it has contrast derived from both absorption and scatter rejection, or extinction.

The analyzer crystal rocking curve shape will introduce a sensitivity to refraction occurring within the object when the analyzer crystal is de-tuned from the peak position. Density, thickness and/or material variations in an object will refract the x-rays as they cross through the material. These small angular variations are generally in the sub-microradian range. The steep sides of the reflectivity curve will convert these subtle angle variations into intensity variations, thus making refraction effects visible in an image. We have shown that by acquiring an image pair with the analyzer crystal set to diffract on each side of the rocking curve, we can separate refraction effects from combined absorption and extinction effects[3,14].

Thus the DEI technique introduces two new sources of image contrast to radiography, refraction and extinction[3]. Each of these new image contrast sources may be further developed to apply to medical and biological imaging.

Glossary of Terms

Analyzer crystal – A crystal that is placed in the x-ray beam emerging from the target material and is used to reflect the x-ray beam at the “Bragg” angle onto the detector.

Bragg angle - The angle θ at which an electromagnetic beam is incident to and reflected from a crystal plane. The relationship between the wavelength, λ , the distance between the crystal planes, d , and the angle of reflection, θ , is given by the Bragg equation $\lambda = 2d \sin \theta$.

Diffraction – A change in direction of an x-ray when it is incident on a substance which has a periodic structure at the molecular level.

Extinction – A term used in x-ray optics to describe the loss of intensity from an x-ray beam due to photons scattering out of the beam at very small angles. Primarily because of diffraction effects.

Reflection – The changing of direction of an electromagnetic beam when it is incident on the surface of a plane. The reflection angle is equal but opposite in direction to the incident angle.

Refraction – A change in direction of the electromagnetic beam when it passes obliquely across a boundary between two materials in which the velocity of propagation is different. This can also occur in a single medium due to variations in its physical properties.

Rocking curve – The intensity of the x-ray beam that is reflected from the analyzer crystal as the analyzer angle θ is varied above and below the Bragg angle corresponding to the incident beam. The intensity of the reflected beam varies correspondingly from zero to a maximum (at the Bragg angle) and to zero again.

Synchrotron radiation – Electromagnetic radiation emitted as the path of a charged particle (an electron or positron) is bent as it passes through a magnetic field.

Appendix

A.2

3. Chapman D, Thomlinson W, Johnston RE, Washburn D, Pisano E, Gmur N, Zhong Z, Menk R, Arfelli F, Sayers D. Diffraction Enhanced X-Ray Imaging. Physics in Medicine and Biology, 1997.

Diffraction enhanced x-ray imaging

D Chapman^{†‡}, W Thomlinson[§], R E Johnston^{||}, D Washburn^{||}, E Pisano^{||},
N Gmür[§], Z Zhong[§], R Menk[¶], F Arfelli⁺ and D Sayers^{*}

[†] CSRR, Illinois Institute of Technology, 3101 South Dearborn, Chicago, IL 60616, USA

[§] National Synchrotron Light Source, Brookhaven National Laboratory, Upton, NY 11973, USA

^{||} University of North Carolina, Chapel Hill, NC 27599, USA

[¶] Universität GHS Siegen, 57068 Siegen, Germany

⁺ Società Sincrotrone Trieste e Sezione dell' INFN -Trieste, Italy

^{*} Physics Department, North Carolina State University, Raleigh, NC 27695, USA

Received 1 April 1997, in final form 4 August 1997

Abstract. Diffraction enhanced imaging is a new x-ray radiographic imaging modality using monochromatic x-rays from a synchrotron which produces images of thick absorbing objects that are almost completely free of scatter. They show dramatically improved contrast over standard imaging applied to the same phantom. The contrast is based not only on attenuation but also the refraction and diffraction properties of the sample. This imaging method may improve image quality for medical applications, industrial radiography for non-destructive testing and x-ray computed tomography.

1. Introduction

Diffraction enhanced imaging (DEI), is a new x-ray radiographic imaging modality which is a product of a research programme designed to explore a monoenergetic line scan system for radiography of thick absorbing objects (Johnston *et al* 1996). The x-ray source is from the X27C beamline at the National Synchrotron Light Source. Synchrotron radiation provides x-rays which are intense, vertically collimated, polarized and continuous over a wide energy range (Margaritondo 1988). These highly desirable qualities allow a wide variety of imaging research to be performed at a synchrotron (Thomlinson 1992, 1994).

For this study a crystal monochromator is used to select a small energy band from the incident synchrotron radiation which forms the imaging beam which strikes the object. One aspect of this programme has been the use of an additional crystal similar to the type used in the monochromator as a scatter rejection optic that diffracts the beam which is transmitted through the object being imaged. This additional crystal is called an analyser crystal or just analyser. Experiments performed with the analyser revealed that this system was sensitive to refractive index effects within the object in addition to the x-ray absorption and scattering by the object. The early experiments indicated that from two images acquired using an analyser crystal a simple algorithm could be used to separate refractive index effects from the absorption effects (Chapman *et al* 1996). These pilot experiments were performed using a transmission case (Laue geometry) analyser to simultaneously obtain a transmission image and a diffracted image.

[‡] E-mail address: chapman@sparky.csrr.iit.edu

Definitive experiments and analysis have now been performed to explore the use of a reflection case (Bragg geometry) analyser crystal arrangement to decompose two diffracted images into an independent refraction image and an apparent absorption image. Apparent absorption means the combined absorption and extinction processes. Extinction is the loss of intensity due to diffraction occurring as the beam traverses the object. The type of extinction referred to is commonly called secondary extinction (Zachariasen 1963). Images taken with the new system are presented which show contrast at least an order of magnitude greater than the measured values for synchrotron x-ray images of the same object acquired using the conventional transmission imaging modality. These images are of thick objects containing at least a 36 mm acrylic plastic thickness. In fact, images from this new modality show additional information that is not available with standard radiography.

An algorithm is presented here for the case of a Bragg analyser which can be used to decompose the images into separate refraction and apparent absorption components. The same algorithm can be applied to the diffracted images in the Laue case. The diffracted images are essentially scatter free, since the crystal prevents much of the scatter from reaching the detector. The refraction image is shown to have high sensitivity for delineating the boundaries of those regions in the object which have different refractive indices. An explanation of the sources of the enhanced image contrast is also given which shows that the increased contrast is a result of extinction effects. This opens new opportunities for imaging based on these properties. Since the contrast of an image based on extinction can be much higher than contrast based on x-ray attenuation, detection of smaller inhomogeneities like tumours in medical images or microfractures in industrial parts should be feasible.

The ability of the monochromator and analyser system to resolve refraction effects does not depend on the imaging energy. However, the scattering properties of various elements are energy dependent, which may allow optimization of the imaging system energy to maximize contrast due to extinction while maintaining refraction contrast. Thus, the new modality may be optimally applied at higher x-ray energies, which would allow for better penetration in non-destructive testing or lower doses in medical imaging.

Other researchers have applied diffractive optics to imaging problems (Beliaevsky *et al* 1991, Somenkov *et al* 1996, Podurets *et al* 1989) and have observed refraction effects. However, the method described here quantifies and produces images of the refraction and absorption independently for the first time. Recently, there has been interest in phase contrast imaging which makes use of the high transverse coherence of third-generation synchrotron sources. Phase contrast images are limited to either thin objects or high x-ray imaging energies (Davis *et al* 1995, Nugent *et al* 1996, Wilkins *et al* 1996). The DEI technique in the present work does not depend on phase contrast and works with thick samples.

2. Physical principles of DEI

A radiograph using monoenergetic x-rays contains several components: a coherently scattered component, an incoherently scattered component, and the transmitted beam. Part of the transmitted beam may be refracted in the sample through a very small angle (microradians) due to refractive index gradients in the object. In the x-ray range refractive index gradients arise from variations in ρt along the beam path, where ρ is the density and t is the thickness. A fraction of the transmitted beam may also be diffracted by organized structures within the sample through angles of the order of milliradians (small-angle scattering). I_C , I_I , and I_D are the portions of the coherent scattering, incoherent scattering and diffraction intensity which arrive on the detector along with I_R . I_R is the portion of the incident beam which has only been affected by refraction and attenuated by

absorption and extinction. The recorded intensity, I_N , in a radiograph can be expressed as

$$I_N = I_R + I_D + I_C + I_I. \quad (1)$$

Variations in I_N across the field of view of the detector are the sources of contrast in normal radiography (formally $\Delta I_N/I_N$). The DEI modality will separate I_R from the other components and will show contrast based on refraction, absorption and extinction.

The scattering components, I_C and I_I , contribute to loss of contrast and spatial resolution. Some improvement can be obtained by using synchrotron radiation and a monochromator to select the energy (Johnston *et al* 1996, Burattini *et al* 1994). However, it has been shown that considerable additional gain in contrast can be realized by adding crystal diffraction optics between the object and the imaging system. This refinement almost completely removes the scatter contribution to the image since only x-rays aligned within the angular acceptance of a crystal analyser will be diffracted onto the detector. I_C and I_I are eliminated as contributions to the image. The angular acceptance is called the rocking curve of the crystal (Zachariasen 1945). For the x-ray energies and crystal reflections used here, the width of this curve is a few microradians.

Since the diffraction angles in the sample being imaged are typically a few milliradians (small-angle scattering), most of I_D is rejected by the crystal. It is this rejection of small-angle scattering in particular which gives rise to the sensitivity to the loss of direct beam intensity which has been 'small-angle scattered'. In diffraction research, the term used for the loss of direct beam intensity due to scattering is secondary extinction (Zachariasen 1945, 1963). Normally, the small-angle scattered x-rays will not be distinguished from the direct beam and will appear in a radiograph of the object. Thus in normal radiography there will be no extinction contrast.

The rejection of the scattered x-rays leaves only I_R , the intensity of x-rays transmitted through the sample with a direction very close to the initial direction of the beam. This beam may have been refracted slightly as it passes through the sample (of the order of microradians).

In DEI two images are acquired, one on each side of the rocking curve of the Bragg analyser. Each image contains information about the object's apparent absorption and refraction. Since the analyser crystal orientation is chosen to diffract the beam in the vertical plane, it is sensitive only to the vertical component, $\Delta\theta_Z$, of the refracted x-rays.

The intensity diffracted by the analyser set at a relative angle θ from the Bragg angle θ_B where $\theta_B + \theta$ is the angle between the incident beam and diffraction planes and is given by

$$I_B = I_R R(\theta_B + \theta) \quad (2)$$

where $R(\theta)$ is the analyser reflectivity.

For DEI the analyser is set to $\theta = \pm\Delta\theta_D/2$ where $\Delta\theta_D$ is the full width at half maximum of the rocking curve (Darwin width). This is the point of steepest slope of the rocking curve. For an incident x-ray which is not deviated in passing through the sample and incident upon the analyser at this angle the reflectivity will be 0.5. If the x-ray emerging from the object is refracted by $\Delta\theta_Z$ then the diffracted intensity will be

$$I_B = I_R R\left(\theta_B \pm \frac{\Delta\theta_D}{2} + \Delta\theta_Z\right). \quad (3)$$

For refracted x-rays there will be a variation in intensity due to the slope of the rocking curve. For example, with $\Delta\theta_D/2$ positive (high-angle side) a beam refracted with $\Delta\theta_Z > 0$ is diffracted by the analyser with reflectivity less than 0.5. A beam refracted with $\Delta\theta_Z < 0$ is diffracted by the analyser with reflectivity greater than 0.5. If the alignment of the

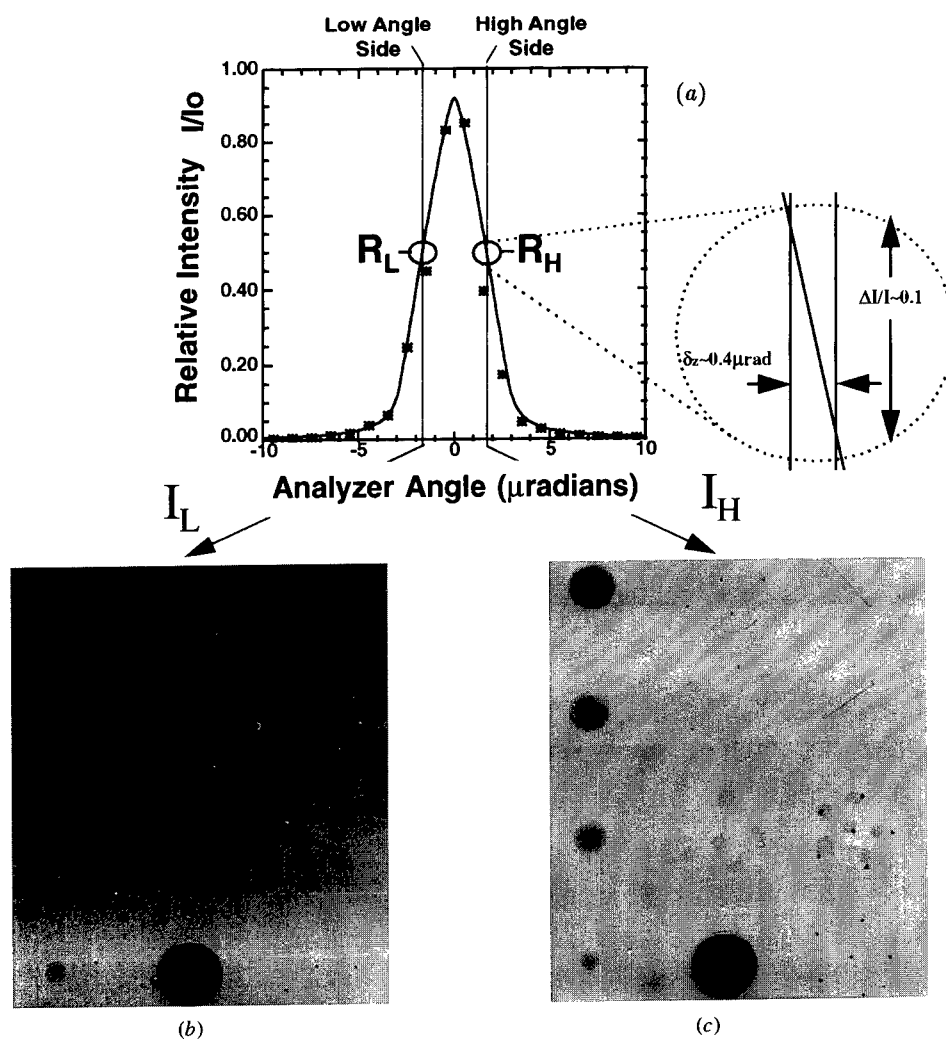


Figure 1. (a) The Si (3, 3, 3) analyser rocking curve at 18 keV (full curve, calculated; stars, measured points). The calculation includes the effects of the beam diffracted by the double-crystal monochromator. An image is taken on each side of the peak, shown by the vertical lines. Any refraction near these vertical lines is varied in intensity due to the slope of the rocking curve, as shown in the inset. The range of refraction angles occurring in the ACR phantom is $\pm 0.2 \mu\text{rad}$, creating intensity variations of $\pm 5\%$. (b) The intensity recorded on the image plate using the low-angle side of the rocking curve. (c) The high-angle side image. Notice that the contrast of the fibrils has switched between the two images.

analyser crystal was such that $\Delta\theta_D/2$ was negative (low-angle side) this effect would be reversed since the derivative of the rocking curve, $dR/d\theta$, is of opposite sign. The steeper the slope, the greater the intensity variation due to refraction effects in the two images. For a deviation of more than $\Delta\theta_D/2$ the reflectivity will not be unique and refraction effects cannot be resolved. This is shown in figure 1(a) which shows the locations on the rocking curve where the images are taken. Also shown in figure 1 are images taken on the high- and low-angle sides of the rocking curve which will be discussed

later. In the regions of the phantom which were imaged, the refraction angles were within $\pm 0.2 \mu\text{rad}$, placing all possible angles within a limited region of the rocking curve (about $5 \mu\text{rad}$).

At $\pm \Delta\theta_D/2$ where the slope of the rocking curve is fairly constant and for small values of $\Delta\theta_Z$, $R(\theta_0 + \Delta\theta_Z)$ can be expressed as a two-term Taylor series approximation

$$R(\theta_0 + \Delta\theta_Z) = R(\theta_0) + \frac{dR}{d\theta}(\theta_0)\Delta\theta_Z. \quad (4)$$

The intensity of the images taken on the low-angle side (θ_L) and the high-angle side (θ_H) of the rocking curve are

$$I_L = I_R \left(R(\theta_L) + \frac{dR}{d\theta}(\theta_L)\Delta\theta_Z \right) \quad (5a)$$

$$I_H = I_R \left(R(\theta_H) + \frac{dR}{d\theta}(\theta_H)\Delta\theta_Z \right). \quad (5b)$$

These two equations can be solved for the intensity affected by apparent absorption, I_R , and for the refraction angle image, $\Delta\theta_Z$, the angle through which I_R is refracted in the z direction in traversing the object. The solutions are

$$I_R = \frac{I_L \left(\frac{dR}{d\theta} \right)(\theta_H) - I_H \left(\frac{dR}{d\theta} \right)(\theta_L)}{R(\theta_L) \left(\frac{dR}{d\theta} \right)(\theta_H) - R(\theta_H) \left(\frac{dR}{d\theta} \right)(\theta_L)} \quad (6a)$$

$$\Delta\theta_Z = \frac{I_H R(\theta_L) - I_L R(\theta_H)}{I_L \left(\frac{dR}{d\theta} \right)(\theta_H) - I_H \left(\frac{dR}{d\theta} \right)(\theta_L)}. \quad (6b)$$

This algorithm is applied on a pixel-by-pixel basis to the diffracted images from the high- and low-angle side of the rocking curve.

3. Methods

The experiments were performed at the X27C beamline at the National Synchrotron Light Source (NSLS) at Brookhaven National Laboratory. The experimental set-up is shown in figure 2. The white synchrotron beam was made nearly monochromatic by a silicon double-crystal monochromator which is located approximately 22 m from the source of

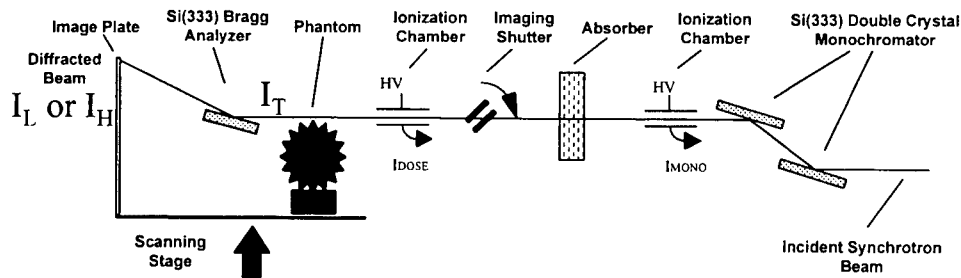


Figure 2. A schematic diagram of the Bragg geometry set-up in the X27C experimental hutch at the NSLS. The image in figure 1(b) was made using a similar set-up, only without the Bragg crystal analyser in place. Not shown in the diagram are the sets of collimators just before the sample and just before the image plate, which help to reduce air scatter and scatter from the sample reaching the detector.

radiation. The tunable energy range of this system was 16–25 keV. For the measurements described here the beam energy was 18 keV with an energy width of about 1.5 eV. The monochromator crystals used the silicon (3, 3, 3) lattice planes. This choice of lattice planes increased the sensitivity to refraction effects by a factor of five from the previous experiments that used the (1, 1, 1) lattice planes because of the narrower rocking curve of the (3, 3, 3) reflection (Chapman *et al* 1996). The imaging beam was approximately 80 mm wide and 0.1 mm high at the location of the object. The beam passed through a gas ionization chamber, used for monitoring the intensity of the direct beam, and a set of Lucite absorbers that reduced the beam intensity. A rotary shutter was used to control the exposure and limit unnecessary scatter at the detector position. A second ion chamber was used to measure the radiation exposure at the surface of the object. Images taken with and without the analyser were at exposure levels comparable to conventional mammography x-ray systems. The object to be imaged was mounted on a scanning stage that was driven by a stepping motor. The x-ray beam transmitted through the object could be either imaged directly as in normal radiography or following diffraction in the vertical plane by the silicon Bragg analyser. Radiation exposure to the image plate was controlled by adjusting the scan speed to maintain an exposure of about $1.3 \mu\text{C kg}^{-1}$ (5 mR) to the plate. Typical scanning times for these experiments were on the order of 4 to 200 s. These limits were dictated by our scanning motors and mechanical system.

The synchrotron images were obtained by maintaining a nearly constant exposure ($\sim 1.3 \mu\text{C kg}^{-1}$) to the image plate. In acquiring the DEI images the phantom was exposed to four times the exposure of the non-analyser synchrotron radiographs. A factor of two in increased exposure compensates for the 0.5 reflectivity of the Bragg analyser crystal and another factor of two increased exposure compensates for the two images on each side of the rocking curve.

The detector was a photo stimulative phosphor image plate, typically used for radiology (Fuji Medical Systems high-resolution HR5 and standard resolution ST5 image plates). The image recorded on the plate was digitized, stored and displayed by a Fuji Medical Systems AC3 reader and workstation. The image plates were read out at 2560×2048 matrix size which results in an image of $100 \mu\text{m}$ per pixel ($0.1 \times 0.1 \text{ mm}^2$).

The diffraction angle of the analyser crystal could be finely tuned using a stepper-motor driven translation stage pushing on a long bar attached to an axle to which the crystal was attached (tangent arm). The resolution limit of the tangent arm was $1 \mu\text{rad}$ which was sufficient for placing the Bragg analyser crystal at a selected position on its rocking curve.

Because the initial interest was in studying the use of synchrotron imaging for early detection of breast cancers, a mammography phantom was used as the test object to be radiographed. The standard phantom used for quality control in mammography is the American College of Radiology (ACR) phantom manufactured by Gammex RMI: Model 156. It contains features which simulate lesions commonly found in breast tissue, namely tumour-like masses (lens-shaped objects of different thicknesses and diameters), simulated microcalcifications arranged as vertices of five-point stars and cylindrical nylon fibrils (Johnston *et al* 1996, Arfelli *et al* 1995). The features are fixed in a wax block contained in a thick acrylic base. This phantom approximates a 40 to 45 mm thick compressed breast. Since the x-ray beam is a fan in the horizontal plane (x – y plane), the object and the image plate were simultaneously translated in the vertical direction (z -direction). This scanning was accomplished by a computer-controlled stepper-motor translation stage which held both the phantom support and a mount for the image plate cassette.

4. Results

Images taken of the ACR phantom for a conventional x-ray tube source and a monoenergetic synchrotron beam without the analyser are shown in figures 3(a) and 3(b) respectively. The synchrotron radiographs typically showed an increase in contrast compared with images from the conventional system (Johnston *et al* 1996). The conventional radiographs were taken with a Siemens Mammomat 2 using Fuji mammography film (UM MA-HC), Fuji screen (UM Fine), and grid (4:1 ratio 27 lines/cm). The ACR image was obtained at 25 kVp, phototimed, 60 mA s. The synchrotron radiograph, figure 3(b), was obtained with the synchrotron set-up described in section 3 above, except that the analyser crystal was removed to allow a radiograph to be taken of the ACR phantom and the vertical beam size was increased to 0.5 mm. The image was taken at 18 keV x-ray energy, with $43 \mu\text{C kg}^{-1}$ exposure to the phantom. The scanning speed was 5.33 mm s^{-1} with an exposure time of 16.7 s. A Fuji ST5 image plate was used to record the image.

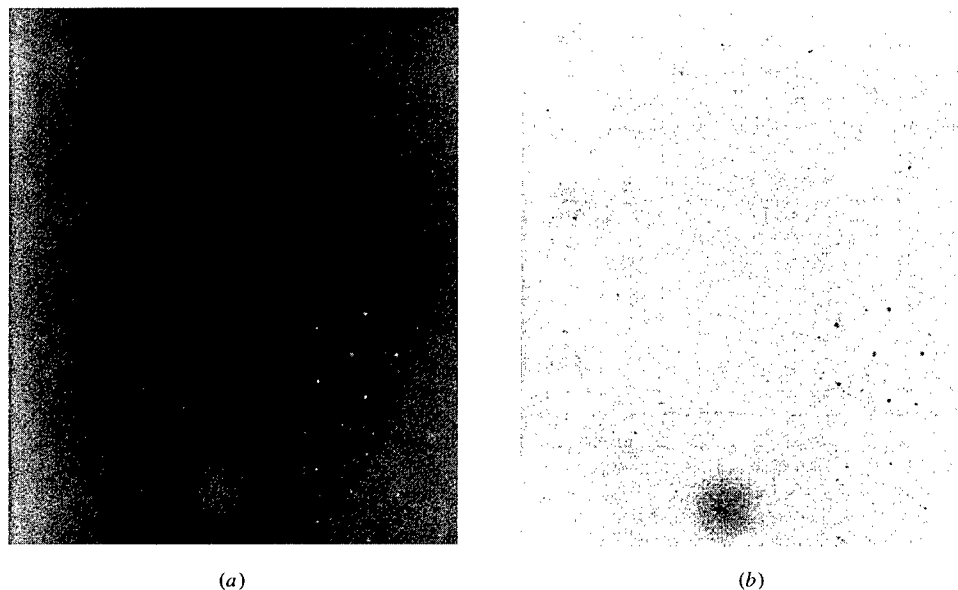


Figure 3. Images of the ACR phantom. (a) A conventional image taken with a Siemens Mammomat II (Siemens Medical Systems, Iselin, NJ) mammography x-ray machine operated at 25 kVp. (b) An image taken using monoenergetic synchrotron radiation at 18 keV without an analyser crystal in place.

The low- and high-angle Bragg analyser images are shown in figures 1(b) and 1(c) respectively. Each of these images were taken with an increased exposure to the phantom of $84 \mu\text{C kg}^{-1}$ to maintain the same exposure to the image plate due to the half-reflectivity of the analyser crystal. Variations in the exposure to the image plate occur due to our inability to achieve exactly the half-reflectivity point in the rocking curve. These images were acquired at a scan speed of 0.54 mm s^{-1} with an exposure time of 165 s. The exposures were made onto a Fuji HR5 image plate.

Careful inspection of the images in figure 1 show that the edges of features in the images are enhanced and highlighted as if a shadow is cast on a three-dimensional surface. This shadowing effect is reversed between the images. This is most visible from the two

fibrils at the top right corners of the images. This effect is due to the images being taken on opposite slopes of the rocking curve. Coherent, incoherent and small-angle scattering outside the rocking curve (I_D diffraction) are not present in these images, leaving only the beam affected by apparent absorption and refraction (I_R from equation (1)). Any rays which deviate by even a few μrad from the incident direction and/or which deviate in energy by more than a few eV from the energy of the incident beam will not be diffracted by the analyser. It is clear that the images in figure 1 taken with the analyser have vastly superior contrast compared with the images in figures 3(a) and (b).

Figures 4(a) and (b) show the apparent absorption image, I_R , and the refraction angle image, $\Delta\theta_Z$, calculated from the decomposition algorithm (equations (6a) and (6b) applied to the images shown in figures 1(b) and (c). Since these images are derived from the two Bragg images, they are also scatter free.

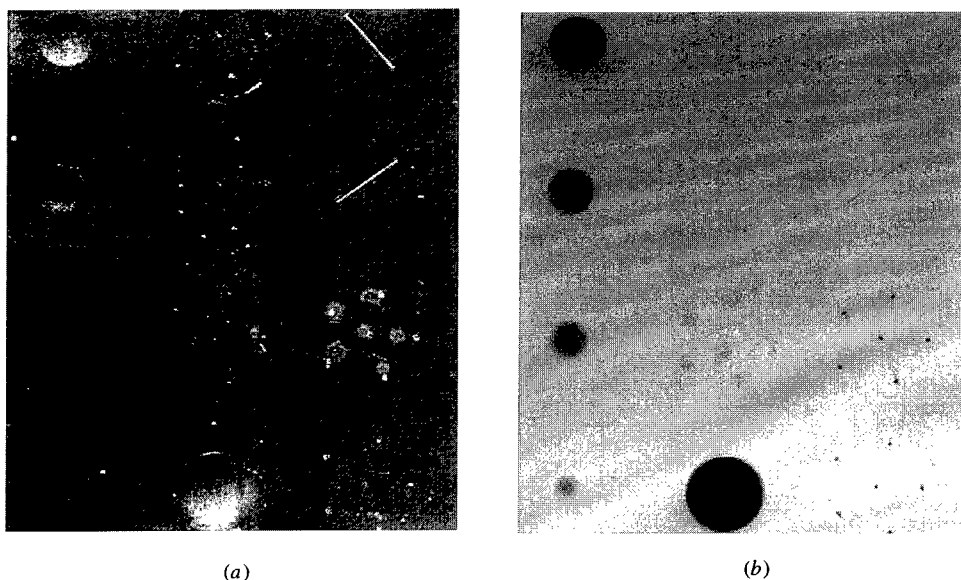


Figure 4. The decomposed images obtained from the images in figures 1(b) and (c) using equations (6a) and (6b). (a) The refraction angle image. (b) The apparent absorption image.

The refraction image is, in effect, an image of the gradient of the refractive index of the object and hence capable of delineating very clearly the boundaries of regions in the object where the refractive index changes sharply. In effect, this produces an image edge enhancement in the Bragg images. Contrast in the refraction image arises from refractive index gradients along the beam path. This explains the three-dimensional shadowed look of the image. A good example of the refraction is to inspect the fibril simulation in the upper right-hand corner of figure 4(a). This object is a right circular cylinder and acts like a cylindrical lens. Thus the upper half will refract the x-rays in the opposite sense from the lower half. The refraction image is very useful in highlighting boundaries or edges in heterogeneous regions within the object. One may thus expect the refraction image to be highly useful in non-destructive examination of microcracks or other types of minute flaws.

The I_R image is a map of the intensity remaining after all the loss mechanisms have been taken out. Virtually all scatter is missing except for a small portion which falls within the angular acceptance of the analyser. The image is dominated by the apparent absorption

Table 1. Conventional and DEI contrast determination for a tumour simulation and a microcalcification from the American College of Radiology Quality Assurance Phantom.

Image	Exposure to phantom $\mu\text{C kg}^{-1}$	Embedded object	Signal ^a			Noise ^a	
			I	ΔI	$\Delta I/I$	δI	$\delta I/I$
Synchrotron radiograph (figure 3(b))	43	Tumour simulation	16.6	0.25	0.015	± 0.10	± 0.006
		Microcalcification	16.3	1.55	0.095	± 0.09	± 0.006
Synchrotron DEI (low-angle image, figure 1(c))	84	Tumour simulation	9.5	3.9	0.41	± 0.28	± 0.030
		Microcalcification	11.5	3.72	0.33	± 0.17	± 0.015
Apparent absorption image (combined image, figure 4(b))	168	Tumour simulation	18.8	7.6	0.40	± 0.25	± 0.013
		Microcalcification	21.3	5.13	0.24	± 0.26	± 0.012

^a Values are taken from image plate data with no background subtraction. Data have been linearized using $I_{\text{LINEAR}} = \exp(N_{\text{RAW}}/255.0)$ where N_{RAW} is the raw data value.

which is normal absorption plus extinction. The ACR phantom is a good example of a material whose absorption and scatter are such that the sum in a normal transmission image (figure 3(a)) significantly degrades the contrast of the objects. For example, consider the simulated tumour mass in the upper left-hand corner of figure 3(b) and figure 4(b). The measured contrast of this 1.0 mm thick mass is summarized in table 1. The exposures used to obtain the images and the relative intensities measured from the images are shown. The relative intensities shown result from raw image plate data and are linearized since the raw data appear in 10-bit logarithmic form. The equation used to obtain the relative intensities is shown in the note to the table. The factor of 255 which divides the raw data value represents the gain setting of the logarithmic amplifier of the image plate reader. The relative intensities will then range from 1 to e^4 (~ 55). The I column values arise from the average background intensity in the vicinity of the embedded object. ΔI is the average change in intensity from the background in the middle of the object. Contrast is the ratio of these two values. The noise level, δI , is the standard deviation of the intensity, I (from the same region over which I has been averaged). The contrast measured from the synchrotron radiograph taken without an analyser in figure 3(b) gives a measured contrast of 1.5% $\Delta I_N/I_N$. However, the same mass in figure 1(b) taken on the low-angle side of the rocking curve gives a measured contrast of 41% $\Delta I_R/I_R$. The contrast of the apparent absorption image shown in figure 4(b) calculated using equation (6a) has a contrast of 40%. The diffracted beam images from the analyser alone have produced a contrast which is about 27 times greater than that in a synchrotron radiograph taken without an analyser! The apparent absorption image has similar contrast, but has a lower noise level since it results from a combination of two images.

The contrast has also been measured for the 0.54 mm diameter microcalcification simulation (largest of the star pattern dots above and to the right of the largest tumour simulation at the bottom of figures 1, 3 and 4). This microcalcification has a measured contrast of 9.5% in the synchrotron radiograph shown in figure 3(b). The image taken with the analyser, figure 1(b), has a measured contrast of 33%.

This startling contrast cannot be explained by normal absorption but is due to intensity loss caused by extinction. The mass created a significant amount of small-angle scatter which was removed from the Bragg diffracted images. This loss of intensity will appear as an apparent absorption within the object and hence as highly enhanced contrast in the image. It is suggested that this contrast enhancement effect be called extinction contrast.

The images in figure 4 demonstrate the usefulness of DEI for imaging objects based on their refraction properties and their ability to diffract (based on the spatial order or structure within the object). This raises the possibility of distinguishing between objects of the same elemental composition, but whose scattering properties are different based on structural order.

5. Conclusion

We believe that this new imaging technique may provide significant improvements in mammography and other areas of radiology, medical or non-medical. The unique ability of this system to provide an essentially scatter-free image of the object's apparent absorption as well as an image of the refraction effects may provide radiologists with sufficient additional information to allow detection of malignancies at an earlier stage than currently possible, even in patients with dense breasts. Since the ability of the monochromator and analyser system to resolve refraction effects and reject scattering does not depend on the imaging energy, there is a possibility that DEI may be optimally applied at higher x-ray energies, thus allowing dose reduction and in the case of mammography, less breast compression.

More studies using real tissues and anthropomorphic phantoms must be done to come to the conclusion that this technique can lead to a better method of breast imaging. There is the possibility that the enhanced contrast may detract from the ability to detect cancerous tissue due to the complexity of the structures involved. These issues will be the topic of future research.

Acknowledgments

The authors would like to thank Fuji Medical Systems for the loan of the AC3 image plate reader system and technical support in setting up and operating the unit. Also, we would like to thank Dr D Peter Siddons for the use of the X27C beamline and Ms B Dowd for assistance in setting up and operating the beamline. We thank Dr I Ivanov for preparing the analyser crystals used in these experiments. This work was supported in part by the State of Illinois Higher Education Cooperative Agreement, US Army grant DAMD17-96-1-6143 and at the National Synchrotron Light Source by US Department of Energy Contract DE-AC02-76CH00016 and ARPA contract AOB227.

References

- Arfelli F, Burns C, Chapman D, Gmür N, Johnston R E, Menk R, Pisano E, Sayers D, Thomlinson W, Washburn D and Zhong Z 1995 *Brookhaven National Laboratory Informal Report* BNL-62935
- Beliaevsky E A, Epfanov V P and Ingal V N 1991 Method for obtaining the image of the internal structure of an object *Soviet Patent* 4934958
- 1992 Method for obtaining the image of the internal structure of an object *US Patent* 5319694
- Burattini E, Cossu E, DiMaggio C, Gambaccini M, Indovina P, Marziani M, Porek M, Simeoni S and Simonetti G 1994 X-ray mammography with synchrotron radiation: a new high resolution technique valid for clinical application *Radiology* **195** 239–44
- Chapman D, Thomlinson W, Arfelli F, Gmür N, Zhong Z, Menk R, Johnston R E, Washburn D, Pisano E and Sayers D 1996 Mammography imaging studies using a Laue crystal analyzer *Rev. Sci. Instrum.* **67** (published on CD-ROM)
- Davis T J, Gao D, Gureyev T E, Stevenson A W and Wilkins S W 1995 Phase-contrast of weakly absorbing materials using hard X-rays *Nature* **373** 595–8
- Davis T J, Gureyev T E, Gao D, Stevenson A W and Wilkins S W 1995 X-ray image contrast from a simple phase object *Phys. Rev. Lett.* **74** 3173–5

- Johnston R E, Washburn D, Pisano E, Burns C, Thomlinson W C, Chapman L D, Arfelli F, Gmür N, Zhong Z and Sayers D 1996 Mammographic phantom studies with synchrotron radiation *Radiology* **200** 659–63
- Margaritondo 1988 *Introduction to Synchrotron Radiation* (New York: Oxford University Press)
- Nugent K A, Gureyev T E, Cookson D F, Paganin D and Barnea Z 1996 Quantitative phase imaging using hard x rays *Phys. Rev. Lett.* **77** 2961–4
- Podurets K M, Somenkov V A and Shil'shtein S Sh 1989 Refraction-contrast radiography *Sov. Phys.-Tech. Phys.* **34** 654–7
- Somenkov V A, Tkalic A K and Shil'shtein S Sh 1991 Refraction contrast in x-ray introscopy *Sov. Phys.-Tech. Phys.* **36** 1309–11
- Thomlinson W 1992 Medical applications of synchrotron radiation *Nucl. Instrum. Methods A* **319** 295–304
- 1994 Medical applications of synchrotron radiation at the National Synchrotron Light Source *Synchrotron Radiation in the Biosciences* ed B Chance *et al* (New York: Oxford University Press) pp 674–80
- Wilkins S W, Gureyev T E, Gao D, Pogany A and Stevenson A W 1996 Phase-contrast imaging using polychromatic hard x-rays *Nature* **384** 335–8
- Zachariasen W H 1945 *Theory of X-Ray Diffraction in Crystals* (New York: Wiley) ch 4
- 1963 The secondary extinction correction *Acta Crystallogr.* **16** 1139–44

Appendix

A.3

D.E. Peplow and K. Verghese ``Measured Molecular Coherent Scattering Form Factors of Animal Tissues, Plastics and Human Breast Tissue".
Physics in Medicine and Biology, 1998: 43 2431-2452.

Measured molecular coherent scattering form factors of animal tissues, plastics and human breast tissue

Douglas E Peplow† and Kuruvilla Verghese

Department of Nuclear Engineering, NC State University, Raleigh, NC 27695-7909, USA

Received 23 January 1998, in final form 14 May 1998

Abstract. Photon scattering angular distributions from various animal tissues were measured at two energies of a monochromatic synchrotron x-ray beam. Two plastics and human breast tissue were also measured. From these two measurements, the molecular coherent scattering form factor of each material was extracted. A new data analysis technique that uses Monte Carlo based corrections for air scattering, incoherent scattering and multiple scattering was used. The form factors of the 16 materials are presented in tabular form, suitable for use in computer calculations.

1. Introduction

As part of a team studying a new mammographic imaging modality using linearly polarized monoenergetic photons (Chapman *et al* 1997, Johnston *et al* 1996), we are interested in performing some design analysis using Monte Carlo calculations. In order to simulate the radiographic image, both the coherent and incoherent angular scattering distributions must be known in detail.

Narten (1970) and Narten and Levy (1971) measured the scattering distribution of water at various temperatures. These measurements used a molybdenum tube source with a characteristic x-ray energy of 17.4 keV. Measurements of this type are expressed as functions of x , related to the momentum transfer of the interaction, $x = (E/hc) \sin(\theta/2)$ where E is the photon energy, h is Planck's constant, c is the speed of light and θ is the angle of scatter. Their measurements included data from $x = 0.4$ to $x = 12.7$ per nm. The value at $x = 0$ was calculated using thermodynamic properties of water.

Johns and Yaffe (1983) showed that the atomic form factors, which dominate the angular distribution for coherent scattering, do not correctly predict the angular scattering distribution for photons in water. They showed that the measured molecular form factor must be used in order to obtain a reasonable agreement between calculation and measurement. The most significant difference in the theoretical and measured coherent scattering distributions is that the peak of the measured data is not at an angle of zero degrees.

Kosanetzky *et al* (1987) used a powder diffraction machine with a cobalt anode to measure the scattering distributions of various pig tissues and several plastics used in the AAPM mammographic phantoms. They found that most tissues appeared similar to water in their coherent scattering distributions. The distributions obtained by this group cover only up to $x = 4.28$ per nm due to the low energy, 6.935 keV, of the characteristic x-ray used in the measurements.

† E-mail address: depeplow@eos.ncsu.edu

Evans *et al* (1991) measured the coherent scattering distribution in many tissues, including adipose, fibroglandular, benign tumour, carcinoma, fibrocystic disease/benign mammary dysplasia and blood. They used a copper anode x-ray tube source operating at 60 kVp for the measurements. The photon distribution was calculated to have a mean energy of 46 keV with a full width at half maximum of 18 keV. They only tabulated the angle of the main peak in the scattering distributions of each material. They did not tabulate the angular distribution.

Leliveld *et al* (1996) refer to a set of tables of molecular form factors made using the data from Kosanetzky *et al* (1987). Of course, these tables cover only a small range of x and have the influence of a tube source spectrum.

Tartari *et al* (1997b) presented the molecular form factors of Lucite and pork fat in tabular form. The measurements were made with a powder diffraction machine up to $x = 6.4$ per nm. Monte Carlo calculations were used to find transmission factors and self-absorption corrections but overall the analysis was simple (Tartari *et al* 1997a).

What is needed, by our group and by others modelling photon transport problems where coherent scattering becomes important, is a set of tables of molecular coherent scattering form factors that can be used in Monte Carlo calculations. This paper provides that for several animal tissues, two plastics and human breast tissue. The method used to obtain these tables, a unique approach using a combination of two monoenergetic measurements, is described here as well. The tables are evaluated at the same x values as the tables by Hubbell and Øverbø (1979) in order to make it easier for modellers to incorporate these data sets into their calculations.

2. Theory

The differential cross sections for coherent and incoherent scattering of polarized x-rays of energy E to scatter to polar angle θ and azimuthal angle ϕ (measured from the direction of polarization) from an atom with atomic number Z are

$$\frac{d}{d\Omega}\sigma_{\text{coh}}(\theta, \phi, E) = r_e^2(1 - \sin^2\theta \cos^2\phi)F^2(x, Z) \quad (1)$$

$$\frac{d}{d\Omega}\sigma_{\text{inc}}(\theta, \phi, E) = \frac{r_e^2}{2}\left(\frac{\alpha'}{\alpha}\right)^2\left(\frac{\alpha'}{\alpha} + \frac{\alpha}{\alpha'} - 2\sin^2\theta \cos^2\phi\right)S(x, Z) \quad (2)$$

where $F(x, Z)$ is the atomic form factor, $S(x, Z)$ is the incoherent scattering factor, x may be written as $(E/1.239\,852 \text{ keV nm}) \sin(\theta/2)$, α is $E/m_e c^2$, α' is $E'/m_e c^2 = \alpha/[1 + \alpha(1 - \cos\theta)]$ and $r_e = e^2/4\pi\epsilon_0 m_e c^2$ is the classical electron radius. The charge of an electron is e , $m_e c^2$ is the rest energy of an electron and ϵ_0 is the permittivity of free space. The total cross sections for elements can be found by integrating these distributions.

The coherent scattering form factor F and the incoherent scattering factor S account for the interference between the electrons of the atom. Non-relativistic values for F and S were tabulated for elements 1 to 100 by Hubbell *et al* (1975, 1977) and a set of relativistic form factors were tabulated by Hubbell and Øverbø (1979).

Our measurements were carried out using monochromatic synchrotron radiation. This beam of radiation is completely linearly polarized in the horizontal direction. For measurements in the vertical plane ($\phi = 90^\circ$), the term $\cos^2\phi$ reduces to 0 in the above differential cross sections.

When considering a molecule, F_{mol}^2 is often calculated (Chan and Doi 1983) by adding the squares of the individual atomic form factors, weighted by their respective atomic abundances n_i . Correspondingly, the molecular incoherent scattering factor is calculated by

adding the atomic scattering factors, again weighted by the atomic abundances

$$F_{\text{mol}}^2(x) = \sum_i n_i F^2(x, Z_i) \quad (3)$$

$$S_{\text{mol}}(x) = \sum_i n_i S(x, Z_i). \quad (4)$$

For most composite materials, the atomic abundances are not known so the composite scattering factor can be expressed without knowing the molecular formula as

$$\frac{F_{\text{mol}}^2(x)}{W} = \sum_i \frac{w_i}{M_i} F^2(x, Z_i) \quad (5)$$

where w_i is the mass fraction of element i , M_i is the atomic mass of element i and W the molecular weight. A similar expression can be written for $S_{\text{mol}}(x)/W$.

Since each atom is considered without regard to its neighbours, this is called the 'free-gas' model. This, however, does not include intramolecular effects or intermolecular effects caused by the close spacing of molecules in real materials. The use of atomic form factors for real materials is not adequate at low energies and/or small scattering angles. For accurate results, $F_{\text{mol}}(x)$ must be measured. Amorphous materials such as plastics and water show broad peaks oscillating around the free-gas model. For strongly ordered materials such as crystals, the free-gas model completely breaks down and the true molecular form factor would be essentially zero for most values of x with many sharp diffraction peaks, corresponding to the crystal lattice planes.

At large values of x (i.e. either high energies or large scatter angles) the free-gas model and the true molecular coherent scattering form factor become the same. This fact is exploited in the extraction of the form factors from scattering data.

3. Methods

3.1. Samples

A total of 16 samples were measured for this study. These were: plastics commonly used in phantoms (Lucite and Lexan), Kapton, deionized water, five pork samples, five beef samples, formaline (10% formaldehyde in water) and human breast tissue fixed in formaline. Fresh pork and beef tissues were used due to the difficulty of obtaining fresh human tissues. These samples were kept refrigerated and never frozen. They were allowed to warm up to room temperature before measurement. The human breast tissue was fixed in formaline and stored at room temperature. A sample of formaline was measured as a check—to ensure that the measurement of the breast tissue was not just measuring formaline. Kapton was measured so that its effects could be removed from measurements of tissues that were held by a Kapton foil.

3.2. Scattering distribution measurement

Measurements of the angular scattering distributions were made on line X3B1 of the National Synchrotron Light Source at Brookhaven National Laboratory. This beamline can produce a monoenergetic beam from 5 keV to 30 keV with a full width at half maximum of less than 6 eV at 9 keV. The beam is nearly parallel and very close to completely polarized.

The beam size was 8 mm horizontal by 2 mm vertical. Between the sample and the detector was a set of Söller slits which allowed only a range of about 0.03° around the desired scatter angle to reach the detector. An NaI detector was used with only minimal

energy discrimination, allowing both coherent and incoherent scatter to be fully counted at any angle.

Tissue samples and liquids were contained in a plastic sample holder (Lucite) with a thin Kapton cover. The container was placed in the beam with the Kapton film at the centre of rotation. The sample size was $2.54 \times 1.91 \times 0.95$ cm. Measurements were made in reflection mode, with the sample container at an angle $\theta/2$ when the detector was at angle θ , as shown in figure 1. As seen in the figure, at low angles the side walls of the container would be in the beam, contributing scatter into the detector.

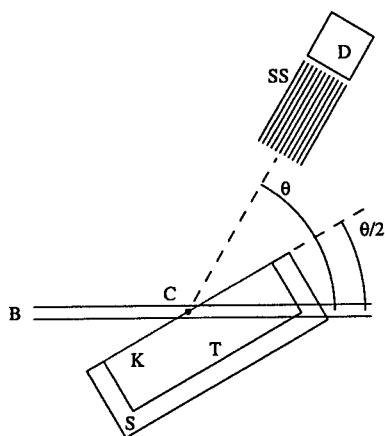


Figure 1. Cross-sectional view of the sample container in reflection mode. Tissue (T) is held by the sample container (S) and the Kapton foil (K). The monoenergetic beam of photons (B) from the synchrotron enter from the left. The sample container is rotated to an angle $\theta/2$ about the centre of rotation (C). This configuration is used to measure the scattering at angle θ , where the Soller slits (SS) and the detector (D) are positioned.

Solid samples (plastics and Kapton) were measured in transmission mode, which was less susceptible to alignment errors. The samples were held at angle $\theta/2$ when the detector was at angle θ to reduce the attenuation thickness and maximize signal to the detector. Every sample was measured at two different x-ray energies. Lexan and Lucite were measured at a thickness of 1.59 cm for the high-energy run, and for the low-energy run 0.16 cm was used.

The choice of beam energy affects the range of x that is measured. To provide data at large x where the atomic form factor calculation matches molecular form factor calculations, a high beam energy is required. But at this higher beam energy, the interesting details in the molecular form factor are crowded down in the low- x range, where low-angle geometry effects appear. Using a low beam energy will move the interesting details away from the geometry effects but will not provide the data at large x . For these reasons, both high- and low-energy beams were used and the results were combined in the final determination of the form factors.

Measurements of the scattered x-rays from the samples were made at 20 keV at intervals of 0.25° for angles from 1° to 110° resulting in a range of x from 0.14 to 13 per nm. The low-energy measurements were made at 8 keV at every 0.25° from 1° to 60° ($x = 0.056$ to 3.2 per nm). A computer precisely controlled the motion of the sample and the detector and also collected the data. Data collection times varied from 20 min to 2 h, depending on the beam energy and synchrotron photon flux. The data were corrected for detector dead time

and the synchrotron photon flux, which decayed with ring current. Except for Kapton, data were collected to a statistical uncertainty ($1/\sqrt{\text{counts}}$) of less than 1%. Kapton, which was a very thin sample, had an average uncertainty of 4% and 2% respectively for the 20 keV and 8 keV photon energies.

3.3. Data analysis procedure

The analysis is based on the fact that the oscillations in the molecular form factor damp out at high x values. A Monte Carlo calculation using atomic form factors should match the measured data in this high x -range. Once the model and the data are fitted, the molecular form factor can be extracted from the data. The effects of the sample holder, Kapton cover and air can also be accounted for in the model and then subtracted out of the data. This procedure uses both the high-energy and low-energy measurements to provide more details in the low- x region.

Modelling the entire response expected from radiation scattered from anywhere in the experiment is a much more rigorous approach than reported in the literature (Kosanetzky *et al* 1987, Tartari *et al* 1997b). Attempting to subtract the measured scattering distribution of an empty sample container from the scattering distribution of a container plus sample is inaccurate since this problem is definitely not linear.

3.3.1. Solid samples. First the Lucite, Lexan and Kapton samples were analysed since their molecular form factors would be needed in the Monte Carlo simulations of the sample holder which held the tissues. The first step in extracting a molecular form factor from a data set was to perform a Monte Carlo calculation of the expected response using the atomic form factors in a free-gas model. This was done using an in-house code. The code has been compared with both Chan and Doi (1983) and Boone (1992) and found to match their results well. The Monte Carlo code followed particles through the geometry and at each interaction site calculated the probability of coherent and incoherent scatter through the Söller slits and into the detector. The model calculated the expected response at the same angles that were used in the experimental measurements.

For these three samples, x-ray interactions in only two materials were considered: the sample and the surrounding air. The response was tabulated into different tallies depending on the type of scatter (coherent or incoherent) and which material was the scatterer. A tally was also kept for multiple scatter, which included any photon that was scattered more than once in any combination of materials.

The total Monte Carlo predicted response, R , at each angle was then

$$R = C_{\text{sam}} + C_{\text{air}} + I_{\text{sam}} + I_{\text{air}} + M \quad (6)$$

where C_i and I_i represent the amount of coherent and incoherent single scatter respectively from material i (sample or air) and M represents the multiple scatter component. What the Monte Carlo code actually calculated was

$$C_i = \int_V \exp(-\mu s_1) \frac{\rho_i N_A}{W_i} r_e^2 F_i^2(x) \exp(-\mu s_2) dV \quad (7)$$

$$I_i = \int_V \exp(-\mu s_1) \frac{\rho_i N_A}{W_i} r_e^2 \left(\frac{\alpha'}{\alpha} \right)^2 \left(\frac{\alpha'}{\alpha} + \frac{\alpha}{\alpha'} \right) S(x, Z) \exp(-\mu' s_2) dV \quad (8)$$

at each scatter angle where μ and μ' represent the attenuation coefficients for the entering and exiting photon, s_1 and s_2 the lengths of the entrance path and exit path and V the volume of region i . N_A is Avogadro's number, ρ_i is the density of material i and W_i is the

molecular weight of material i . Since the Söller slits allowed only one scatter angle to be detected, the first integral was reduced to

$$C_i = r_e^2 \frac{\rho_i N_A}{W} F_i^2(x) \int_V \exp(-\mu s_1) \exp(-\mu s_2) dV \quad (9)$$

$$= F_i^2(x) G_i \quad (10)$$

where G_i contains the information about the geometry, the self-attenuation correction and the constant term. The two single scatter components calculated by the Monte Carlo code completely matched the analytic forms of equations (7) and (8).

The Monte Carlo calculation for 20 keV photons, R_{20} , was fit by linear least squares to the experimental data, D_{20} , in the region $x = 9$ to 13 per nm

$$D_{20} = a_1 R_{20} \quad (11)$$

$$= a_1 (C_{\text{sam}} + C_{\text{air}} + I_{\text{sam}} + I_{\text{air}} + M) \quad (12)$$

to find the coefficient a_1 . Once a_1 was fixed, the experimental data were then set equal to the coherent scatter term using the true molecular form factor, $F_{\text{mol},20}$, plus all of the other calculated components.

$$D_{20} = a_1 (F_{\text{mol},20}^2(x) G_{\text{sam}} + C_{\text{air}} + I_{\text{sam}} + I_{\text{air}} + M). \quad (13)$$

Of course, the G_{sam} was easily found by dividing the Monte Carlo data by the square of the atomic form factor, $C_{\text{sam}}/F_{\text{sam}}^2$. Inserting this and solving for the molecular form factor gave

$$D_{20} = a_1 \left(F_{\text{mol},20}^2(x) \frac{C_{\text{sam}}}{F_{\text{sam}}^2(x)} + C_{\text{air}} + I_{\text{sam}} + I_{\text{air}} + M \right) \quad (14)$$

$$F_{\text{mol},20}^2(x) = \frac{F_{\text{sam}}^2(x)}{C_{\text{sam}}} \left(\frac{D_{20}}{a_1} - C_{\text{air}} - I_{\text{sam}} - I_{\text{air}} - M \right). \quad (15)$$

This was now an approximation to the molecular form factor of the sample.

To get more detail in the low- x region, the process was repeated with the 8 keV data, D_8 , and 8 keV Monte Carlo run, R_8 . The data were fitted to the Monte Carlo responses except for the term C_{sam} , where the approximate form factor was used in place of the atomic form factor that was used in the calculation

$$D_8 = a_2 R_8 \quad (16)$$

$$= a_2 \left(C_{\text{sam}} \frac{F_{\text{mol},20}^2(x)}{F_{\text{sam}}^2(x)} + C_{\text{air}} + I_{\text{sam}} + I_{\text{air}} + M \right). \quad (17)$$

The fit was over the highest portion of the 8 keV data, $x > 0.275$, to find a_2 . Once this was found, the molecular form factor was found by

$$D_8 = a_2 \left(F_{\text{mol},8}^2(x) \frac{C_{\text{sam}}}{F_{\text{sam}}^2(x)} + C_{\text{air}} + I_{\text{sam}} + I_{\text{air}} + M \right) \quad (18)$$

$$F_{\text{mol},8}^2(x) = \frac{F_{\text{sam}}^2(x)}{C_{\text{sam}}} \left(\frac{D_8}{a_2} - C_{\text{air}} - I_{\text{sam}} - I_{\text{air}} - M \right). \quad (19)$$

The values of $F_{\text{mol},8}$ at low x were combined with values of $F_{\text{mol},20}$ at high x to generate the final molecular form factor.

3.3.2. Liquids and tissue samples. The analysis of the other samples followed a similar procedure to that of the solid samples. The difference was that there were four materials to consider in the Monte Carlo calculation: the sample itself, the Lucite sample container, the Kapton cover and the surrounding air. The Monte Carlo calculations used the molecular form factors for the Lucite and Kapton and used atomic form factors for the sample and for air. Compositions for the various animal tissues were assumed to correspond to human tissue compositions, taken from ICRU Report 46 (ICRU 1992). An example of the tallies from the Monte Carlo calculation for water at 8 keV is shown in figure 2. As seen in the figure, multiple scatter is 10–20% of the total detected. For 20 keV, multiple scatter is about 6–9% of the total.

The 20 keV Monte Carlo response, R_{20} , was fitted to the 20 keV experimental data, D_{20} , over the range $x = 9$ to 13 per nm to find the fit coefficient a_1 . This fit for water is shown in figure 3(a). The data were then set equal to the Monte Carlo responses from the other regions (i) plus a coherent scattering term containing the molecular form factor of the

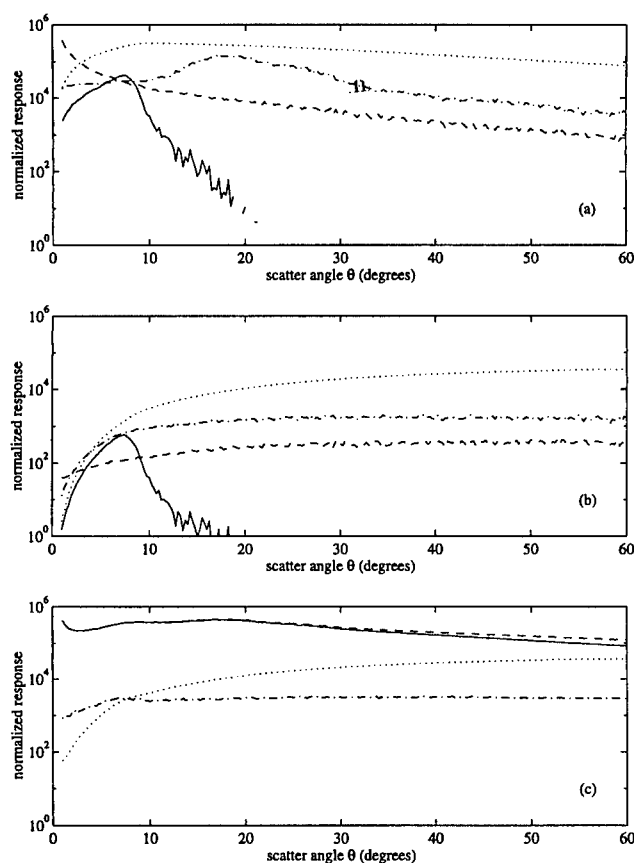


Figure 2. Monte Carlo predicted response for water using atomic form factors at 8 keV showing (a) single coherent scatter from the water (.....), the Kapton foil (— · —), the surrounding air (---) and the sample holder (—); (b) single incoherent scatter from the water (.....), the Kapton foil (— · —), the surrounding air (---) and the sample holder (—); and (c) the grand total (---), total coherent (—), total incoherent (.....) and multiple scatter (— · —).

sample (j). The molecular form factor was then found

$$D_{20} = a_1 \left(F_{\text{mol},20}^2(x) \frac{C_j}{F_j^2(x)} + \sum_{i \neq j} C_i + \sum_{i=1}^4 I_i + M \right) \quad (20)$$

$$F_{\text{mol},20}^2(x) = \frac{F_j^2(x)}{C_j} \left(\frac{D_{20}}{a_1} - \sum_{i \neq j} C_i - \sum_{i=1}^4 I_i - M \right). \quad (21)$$

The approximate molecular form factor from the 20 keV data for water is shown in figure 3(b). As seen in the figure, most of the interesting details are in the range of $x < 3$ per nm. These details are difficult to extract due to the peak from the sample holder, which occurs at low angles, independent of the photon energy.

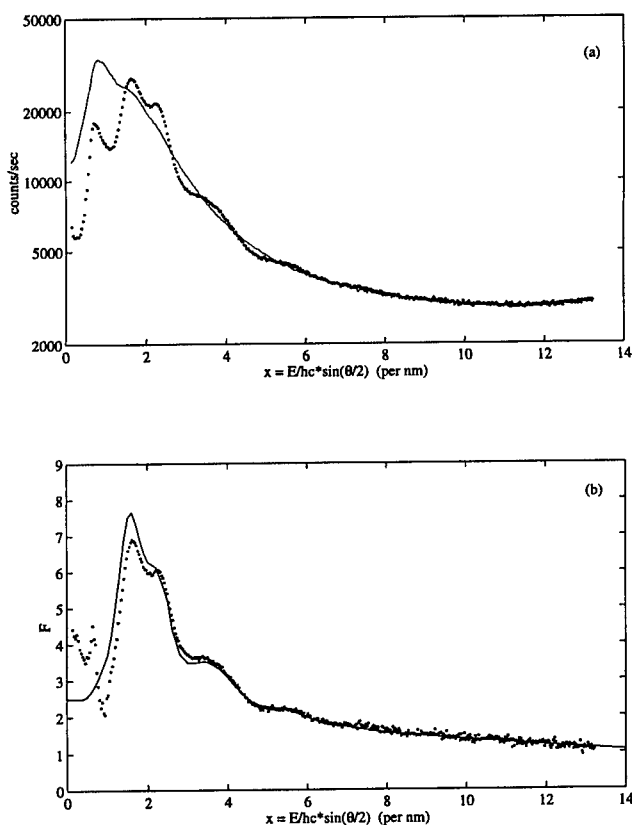


Figure 3. The extraction process (data shown here are for water): (a) the Monte Carlo calculation (—) using atomic form factors and the 20 keV data (·) for $x = 9$ to 13 per nm. (b) An approximation of the molecular form factor (·) as described in the text and Narten's data (1970) using a polyenergetic source (—).

Also shown in figure 3(b) is Narten's measured molecular form factor for 25 °C water. It is apparent from this figure that the scattering from the sample container and the air was not completely accounted for in the process of obtaining the form factor. Slight variations in alignment and slight curvatures of the Kapton foil too small to be taken into account in the Monte Carlo model are the causes. This was confirmed by experiment (forcing large curvatures in the Kapton) and by multiple Monte Carlo runs (beam alignment changes).

Reiterating, to provide more details at the low- x range, the 8 keV data were used. First, the coherent scatter tally from the sample (region j) was modified by the approximate molecular form factor found from the 20 keV data. Using this and all of the other tallies (i), a fit coefficient, a_2 , was found. The 8 keV fit for water is shown in figure 4(a). The molecular form factor was then extracted by

$$D_8 = a_2 \left(F_{\text{mol},8}^2(x) \frac{C_j}{F_j^2(x)} + \sum_{i \neq j} C_i + \sum_{i=1}^4 I_i + M \right) \quad (22)$$

$$F_{\text{mol},8}^2(x) = \frac{F_j^2(x)}{C_j} \left(\frac{D_8}{a_2} - \sum_{i \neq j} C_i - \sum_{i=1}^4 I_i - M \right). \quad (23)$$

The molecular form factor $F_{\text{mol},8}$ for water is also shown in figure 4(b) with Narten's measurement. As with the solid samples, the values of $F_{\text{mol},8}$ at low x were combined with values of $F_{\text{mol},20}$ at high x to generate the final molecular form factor.

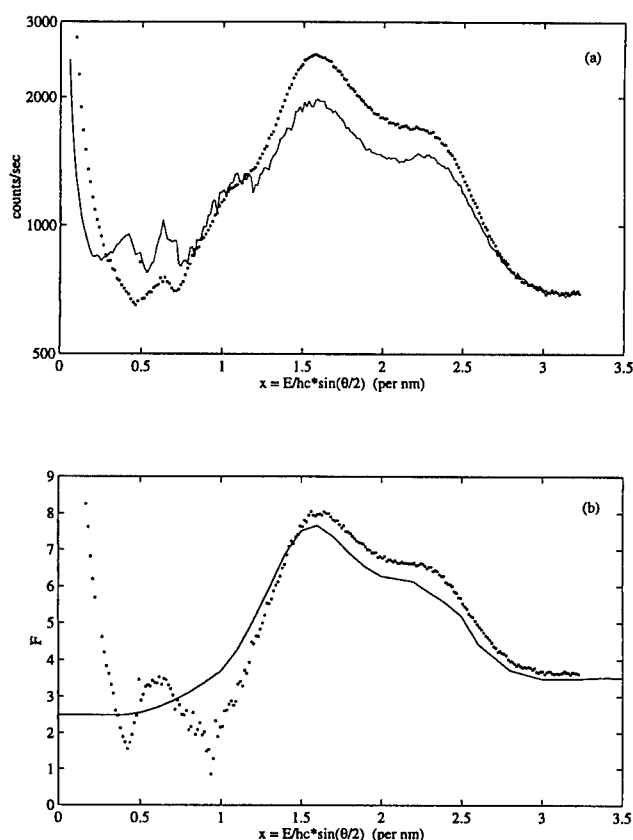


Figure 4. The extraction process continued (data shown here are for water): (a) the 8 keV Monte Carlo calculation (—), modified by the approximate form factor from the 20 keV data, and the 8 keV measured data (·) for $x > 2.75$ per nm. (b) Form factor using both the 8 and 20 keV data and Narten's molecular form factor (—).

3.4. Extrapolation at very low x

After obtaining the form factors from a few samples, it was noticed that the fit at low angles was not good. Again, this is believed to be caused by small alignment errors, slight curvatures in the sample holder cover and effects of the primary beam from the synchrotron which were not modelled. To remedy this, one of two approaches was used. The first approach replaced the tainted values at low x with Narten's (1970) value for water at $x = 0$, which was calculated from bulk thermodynamic principles. Narten's value was used up to some x_{crit} corresponding to the rise of the main peak. This method was used for most of the tissues, since they consist mostly of water and their distributions appear similar to water. The second approach simply used the lowest value of F before the drastic rise near $x = 0$ from air scatter. From $x = 0$ to some x_{crit} , where F is a minimum, the value of $F(x_{\text{crit}})$ was used. This method was used for the plastics, adipose and breast tissue. Examples of each method are shown in figure 5. Table 1 lists each sample and which approach was used.

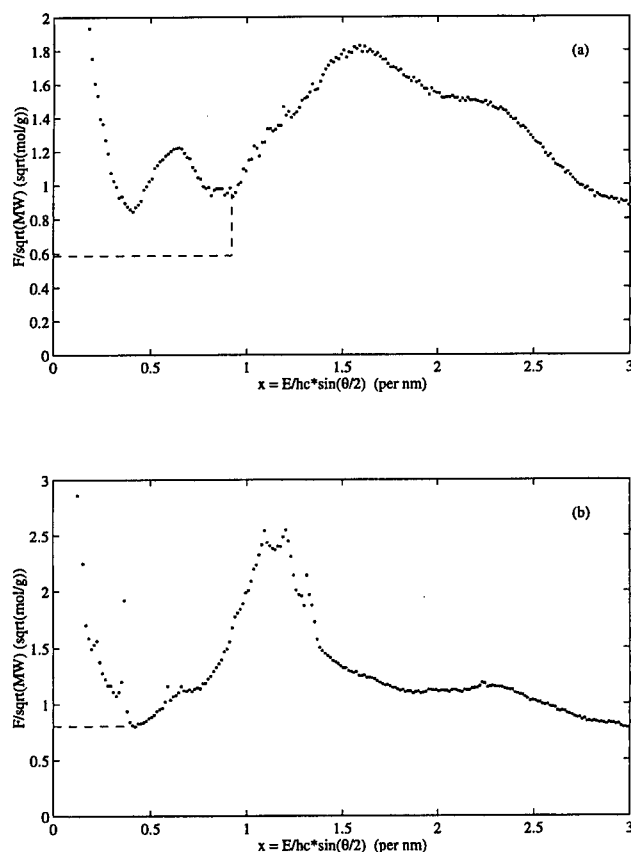


Figure 5. Example of extrapolation at very low x values: (a) the calculated value of water for water based tissues (this example is beef liver) or (b) the lowest value in the low- x region for non-water based materials (this example is pork adipose). The extrapolations are shown as (---).

Table 1. Method of extrapolation to $x = 0$ and relative error of the final molecular form factor F_{mol} .

Sample material	Low- x extrapolation		Relative error in F	
	Method	x_{crit} (per nm)	Highest	Average
Lucite	Low point	0.18	0.049	0.013
Lexan	Low point	0.15	0.053	0.013
Kapton	Low point	0.32	0.344	0.044
Water	Water value	1.01	0.048	0.017
Pork adipose	Low point	0.42	0.053	0.015
Beef adipose	Low point	0.42	0.051	0.015
Pork muscle	Water value	0.92	0.048	0.013
Beef muscle	Water value	0.92	0.046	0.013
Pork kidney	Water value	0.92	0.360	0.015
Beef kidney	Water value	0.92	0.053	0.014
Pork liver	Water value	0.92	0.039	0.014
Beef liver	Water value	0.92	0.042	0.014
Pork heart	Water value	0.93	0.064	0.014
Beef blood	Water value	1.08	0.047	0.017
Human breast tissue	Low point	0.42	1.118	0.067
Formaline	Water value	0.99	0.052	0.017

3.5. Molecular form factor tables

In order to make the molecular form factors useful, they have been interpolated and tabulated at the same x values as the tables by Hubbell and Øverbø (1979). The form factors were smoothed using a five point average in the range of $x = 5$ to 10 per nm. Four examples are shown in figure 6. Hubbell and Øverbø's relativistic atomic form factors, combined using the free-gas approximation, are used in the tables above $x = 10$ per nm. By interpolating values of the molecular form factors only at the x values of Hubbell and Øverbø, some fine details seen in the figures in this paper will be missed.

Units of the table are the form factor per square root of molecular weight. This was used since the tissues have no molecular formula to speak of, only a composition by mass fractions. Individual users have probably found different ways to handle this and the units of the table should fit everyone. The values are all listed in tables 2–4. Table 1 lists the highest relative error in the form factor and the average relative error over the range of $x = x_{\text{crit}}$ to 10 per nm for each sample. This error takes into account the counting statistics from the high- and low-energy measurements and the stochastic error from the high- and low-energy Monte Carlo calculations.

The tables shown in this paper and a set of more detailed tables may be obtained from the first author, through his web site at <http://www4.ncsu.edu/~depeplow>.

4. Results and discussion

The molecular form factor of water is compared with Narten's measurement in figure 6(b). The peak in our form factor is sharper, possibly due to the use of a monoenergetic beam instead of a tube source. The close agreement of the two curves implies that the measurements and data analysis of the other tissues are valid.

The form factors of the animal tissues all appear similar in shape to water. This is consistent with the composition of these tissues. The adipose tissue from pork and

Table 2. Molecular coherent scattering form factors.

x (per nm)	Lucite	Lexan	Kapton	Water
0.00E + 00	0.9220E + 00	0.9827E + 00	0.8556E + 00	0.5871E + 00
0.10E + 00	0.9220E + 00	0.9827E + 00	0.8556E + 00	0.5871E + 00
0.20E + 00	0.9367E + 00	0.9881E + 00	0.8556E + 00	0.5871E + 00
0.30E + 00	0.1018E + 01	0.1052E + 01	0.8556E + 00	0.5871E + 00
0.40E + 00	0.1188E + 01	0.1134E + 01	0.9293E + 00	0.5871E + 00
0.50E + 00	0.1486E + 01	0.1169E + 01	0.1013E + 01	0.5871E + 00
0.60E + 00	0.1861E + 01	0.1187E + 01	0.1200E + 01	0.5871E + 00
0.70E + 00	0.2340E + 01	0.1403E + 01	0.1485E + 01	0.5871E + 00
0.80E + 00	0.2419E + 01	0.1814E + 01	0.2161E + 01	0.5871E + 00
0.90E + 00	0.2173E + 01	0.2434E + 01	0.2658E + 01	0.5871E + 00
0.10E + 01	0.1902E + 01	0.2498E + 01	0.3095E + 01	0.5871E + 00
0.11E + 01	0.1633E + 01	0.2225E + 01	0.3156E + 01	0.7338E + 00
0.12E + 01	0.1430E + 01	0.1855E + 01	0.2939E + 01	0.1048E + 01
0.13E + 01	0.1287E + 01	0.1592E + 01	0.2671E + 01	0.1299E + 01
0.14E + 01	0.1256E + 01	0.1508E + 01	0.2581E + 01	0.1568E + 01
0.15E + 01	0.1314E + 01	0.1423E + 01	0.2483E + 01	0.1800E + 01
0.16E + 01	0.1389E + 01	0.1285E + 01	0.2104E + 01	0.1876E + 01
0.17E + 01	0.1414E + 01	0.1167E + 01	0.1786E + 01	0.1840E + 01
0.18E + 01	0.1352E + 01	0.1080E + 01	0.1576E + 01	0.1758E + 01
0.19E + 01	0.1263E + 01	0.1001E + 01	0.1405E + 01	0.1667E + 01
0.20E + 01	0.1146E + 01	0.9553E + 00	0.1395E + 01	0.1600E + 01
0.22E + 01	0.1105E + 01	0.9808E + 00	0.1274E + 01	0.1560E + 01
0.24E + 01	0.1084E + 01	0.1021E + 01	0.1191E + 01	0.1451E + 01
0.25E + 01	0.9855E + 00	0.1019E + 01	0.1199E + 01	0.1324E + 01
0.26E + 01	0.8875E + 00	0.9694E + 00	0.1168E + 01	0.1167E + 01
0.28E + 01	0.7845E + 00	0.8165E + 00	0.1087E + 01	0.9384E + 00
0.30E + 01	0.7317E + 00	0.6919E + 00	0.9445E + 00	0.8699E + 00
0.32E + 01	0.6827E + 00	0.6273E + 00	0.9224E + 00	0.8600E + 00
0.34E + 01	0.6389E + 00	0.5743E + 00	0.8561E + 00	0.8571E + 00
0.35E + 01	0.6291E + 00	0.5660E + 00	0.8222E + 00	0.8515E + 00
0.36E + 01	0.6128E + 00	0.5620E + 00	0.7401E + 00	0.8305E + 00
0.38E + 01	0.6042E + 00	0.5796E + 00	0.7278E + 00	0.8022E + 00
0.40E + 01	0.5959E + 00	0.6126E + 00	0.7754E + 00	0.7354E + 00
0.42E + 01	0.5978E + 00	0.6293E + 00	0.7684E + 00	0.6701E + 00
0.44E + 01	0.6190E + 00	0.6292E + 00	0.8115E + 00	0.6150E + 00
0.45E + 01	0.6137E + 00	0.6184E + 00	0.7909E + 00	0.5769E + 00
0.46E + 01	0.6016E + 00	0.5949E + 00	0.7741E + 00	0.5558E + 00
0.48E + 01	0.5492E + 00	0.5743E + 00	0.7583E + 00	0.5226E + 00
0.50E + 01	0.5056E + 00	0.5401E + 00	0.7050E + 00	0.5222E + 00
0.55E + 01	0.4645E + 00	0.4643E + 00	0.6283E + 00	0.5166E + 00
0.60E + 01	0.4549E + 00	0.4500E + 00	0.5848E + 00	0.4744E + 00
0.65E + 01	0.4707E + 00	0.4513E + 00	0.5443E + 00	0.4316E + 00
0.70E + 01	0.4492E + 00	0.4605E + 00	0.5067E + 00	0.4196E + 00
0.80E + 01	0.4119E + 00	0.4225E + 00	0.4592E + 00	0.3793E + 00
0.90E + 01	0.3534E + 00	0.3716E + 00	0.4369E + 00	0.3522E + 00
0.10E + 02	0.3160E + 00	0.3169E + 00	0.3190E + 00	0.3244E + 00
0.11E + 02	0.2912E + 00	0.2904E + 00	0.2925E + 00	0.3058E + 00
0.12E + 02	0.2674E + 00	0.2649E + 00	0.2671E + 00	0.2877E + 00
0.13E + 02	0.2448E + 00	0.2408E + 00	0.2431E + 00	0.2698E + 00
0.14E + 02	0.2234E + 00	0.2182E + 00	0.2204E + 00	0.2521E + 00
0.15E + 02	0.2038E + 00	0.1976E + 00	0.1998E + 00	0.2349E + 00
0.16E + 02	0.1855E + 00	0.1785E + 00	0.1807E + 00	0.2182E + 00
0.17E + 02	0.1686E + 00	0.1613E + 00	0.1633E + 00	0.2019E + 00
0.18E + 02	0.1532E + 00	0.1455E + 00	0.1474E + 00	0.1866E + 00

Table 2. (Continued)

x (per nm)	Lucite	Lexan	Kapton	Water
0.19E + 02	0.1393E + 00	0.1315E + 00	0.1333E + 00	0.1722E + 00
0.20E + 02	0.1266E + 00	0.1188E + 00	0.1204E + 00	0.1588E + 00
0.22E + 02	0.1046E + 00	0.9717E - 01	0.9852E - 01	0.1343E + 00
0.24E + 02	0.8671E - 01	0.7981E - 01	0.8093E - 01	0.1135E + 00
0.25E + 02	0.7904E - 01	0.7244E - 01	0.7346E - 01	0.1044E + 00
0.26E + 02	0.7211E - 01	0.6582E - 01	0.6675E - 01	0.9596E - 01
0.28E + 02	0.6021E - 01	0.5456E - 01	0.5533E - 01	0.8124E - 01
0.30E + 02	0.5049E - 01	0.4547E - 01	0.4611E - 01	0.6891E - 01
0.33E + 02	0.3909E - 01	0.3492E - 01	0.3540E - 01	0.5412E - 01
0.35E + 02	0.3313E - 01	0.2945E - 01	0.2985E - 01	0.4625E - 01
0.36E + 02	0.3055E - 01	0.2710E - 01	0.2747E - 01	0.4281E - 01
0.39E + 02	0.2415E - 01	0.2131E - 01	0.2159E - 01	0.3414E - 01
0.40E + 02	0.2239E - 01	0.1972E - 01	0.1998E - 01	0.3172E - 01
0.42E + 02	0.1929E - 01	0.1694E - 01	0.1716E - 01	0.2747E - 01
0.46E + 02	0.1449E - 01	0.1266E - 01	0.1282E - 01	0.2081E - 01
0.50E + 02	0.1105E - 01	0.9616E - 02	0.9729E - 02	0.1597E - 01
0.54E + 02	0.8550E - 02	0.7413E - 02	0.7497E - 02	0.1242E - 01
0.55E + 02	0.8034E - 02	0.6961E - 02	0.7039E - 02	0.1168E - 01
0.58E + 02	0.6698E - 02	0.5791E - 02	0.5855E - 02	0.9770E - 02
0.60E + 02	0.5956E - 02	0.5143E - 02	0.5198E - 02	0.8704E - 02
0.62E + 02	0.5311E - 02	0.4581E - 02	0.4630E - 02	0.7775E - 02
0.66E + 02	0.4260E - 02	0.3666E - 02	0.3705E - 02	0.6253E - 02
0.70E + 02	0.3452E - 02	0.2966E - 02	0.2996E - 02	0.5080E - 02
0.74E + 02	0.2823E - 02	0.2422E - 02	0.2447E - 02	0.4163E - 02
0.80E + 02	0.2123E - 02	0.1818E - 02	0.1836E - 02	0.3138E - 02
0.90E + 02	0.1371E - 02	0.1172E - 02	0.1183E - 02	0.2034E - 02
0.10E + 03	0.9227E - 03	0.7870E - 03	0.7942E - 03	0.1372E - 02
0.11E + 03	0.6425E - 03	0.5474E - 03	0.5522E - 03	0.9568E - 03
0.12E + 03	0.4604E - 03	0.3918E - 03	0.3953E - 03	0.6865E - 03
0.14E + 03	0.2540E - 03	0.2159E - 03	0.2177E - 03	0.3796E - 03
0.16E + 03	0.1512E - 03	0.1284E - 03	0.1294E - 03	0.2262E - 03
0.18E + 03	0.9546E - 04	0.8099E - 04	0.8165E - 04	0.1429E - 03
0.20E + 03	0.6318E - 04	0.5357E - 04	0.5400E - 04	0.9469E - 04
0.22E + 03	0.4346E - 04	0.3684E - 04	0.3713E - 04	0.6517E - 04
0.25E + 03	0.2629E - 04	0.2227E - 04	0.2245E - 04	0.3944E - 04
0.28E + 03	0.1682E - 04	0.1425E - 04	0.1436E - 04	0.2526E - 04
0.31E + 03	0.1126E - 04	0.9536E - 05	0.9611E - 05	0.1692E - 04
0.35E + 03	0.6980E - 05	0.5907E - 05	0.5953E - 05	0.1049E - 04
0.40E + 03	0.4124E - 05	0.3488E - 05	0.3515E - 05	0.6199E - 05
0.45E + 03	0.2592E - 05	0.2192E - 05	0.2208E - 05	0.3897E - 05
0.50E + 03	0.1712E - 05	0.1447E - 05	0.1458E - 05	0.2575E - 05
0.70E + 03	0.4561E - 06	0.3852E - 06	0.3881E - 06	0.6869E - 06
0.10E + 04	0.1130E - 06	0.9534E - 07	0.9603E - 07	0.1705E - 06
0.10E + 05	0.2127E - 10	0.1767E - 10	0.1774E - 10	0.3273E - 10
0.10E + 08	0.1126E - 19	0.9192E - 20	0.9197E - 20	0.1769E - 19
0.10E + 11	0.1151E - 28	0.9383E - 29	0.9384E - 29	0.1809E - 28

beef samples appeared similar to each other and both showed some sharp peaks as if from diffraction in crystalline materials. Form factors for the adipose samples appear very different from water.

Human breast tissue had peaks corresponding to the peaks of water and adipose, which is consistent with the composition of breast tissue. Since this tissue was not fresh, the

Table 3. Molecular coherent scattering form factors.

x (per nm)	Pork fat	Beef fat	Pork muscle	Beef muscle
0.00E + 00	0.8004E + 00	0.9064E + 00	0.5871E + 00	0.5871E + 00
0.10E + 00	0.8004E + 00	0.9064E + 00	0.5871E + 00	0.5871E + 00
0.20E + 00	0.8004E + 00	0.9064E + 00	0.5871E + 00	0.5871E + 00
0.30E + 00	0.8004E + 00	0.9064E + 00	0.5871E + 00	0.5871E + 00
0.40E + 00	0.8004E + 00	0.9064E + 00	0.5871E + 00	0.5871E + 00
0.50E + 00	0.8798E + 00	0.9746E + 00	0.5871E + 00	0.5871E + 00
0.60E + 00	0.1075E + 01	0.1097E + 01	0.5871E + 00	0.5871E + 00
0.70E + 00	0.1128E + 01	0.1178E + 01	0.5871E + 00	0.5871E + 00
0.80E + 00	0.1224E + 01	0.1287E + 01	0.5871E + 00	0.5871E + 00
0.90E + 00	0.1499E + 01	0.1555E + 01	0.5871E + 00	0.5871E + 00
0.10E + 01	0.1991E + 01	0.2043E + 01	0.9541E + 00	0.1012E + 01
0.11E + 01	0.2486E + 01	0.2555E + 01	0.1178E + 01	0.1208E + 01
0.12E + 01	0.2533E + 01	0.2166E + 01	0.1330E + 01	0.1381E + 01
0.13E + 01	0.1871E + 01	0.1878E + 01	0.1461E + 01	0.1514E + 01
0.14E + 01	0.1467E + 01	0.1537E + 01	0.1593E + 01	0.1643E + 01
0.15E + 01	0.1328E + 01	0.1439E + 01	0.1725E + 01	0.1749E + 01
0.16E + 01	0.1248E + 01	0.1382E + 01	0.1745E + 01	0.1769E + 01
0.17E + 01	0.1187E + 01	0.1321E + 01	0.1714E + 01	0.1738E + 01
0.18E + 01	0.1121E + 01	0.1242E + 01	0.1634E + 01	0.1655E + 01
0.19E + 01	0.1109E + 01	0.1211E + 01	0.1559E + 01	0.1572E + 01
0.20E + 01	0.1116E + 01	0.1195E + 01	0.1503E + 01	0.1518E + 01
0.22E + 01	0.1141E + 01	0.1211E + 01	0.1473E + 01	0.1490E + 01
0.24E + 01	0.1107E + 01	0.1165E + 01	0.1379E + 01	0.1377E + 01
0.25E + 01	0.1031E + 01	0.1085E + 01	0.1252E + 01	0.1253E + 01
0.26E + 01	0.9722E + 00	0.1007E + 01	0.1141E + 01	0.1138E + 01
0.28E + 01	0.8411E + 00	0.8671E + 00	0.9360E + 00	0.9311E + 00
0.30E + 01	0.7825E + 00	0.7884E + 00	0.8672E + 00	0.8658E + 00
0.32E + 01	0.7093E + 00	0.7303E + 00	0.8562E + 00	0.8438E + 00
0.34E + 01	0.6797E + 00	0.7212E + 00	0.8514E + 00	0.8479E + 00
0.35E + 01	0.6798E + 00	0.7111E + 00	0.8461E + 00	0.8294E + 00
0.36E + 01	0.6801E + 00	0.7064E + 00	0.8380E + 00	0.8237E + 00
0.38E + 01	0.6730E + 00	0.6999E + 00	0.8154E + 00	0.7957E + 00
0.40E + 01	0.6895E + 00	0.6996E + 00	0.7773E + 00	0.7615E + 00
0.42E + 01	0.6679E + 00	0.6837E + 00	0.7239E + 00	0.7127E + 00
0.44E + 01	0.6397E + 00	0.6478E + 00	0.6774E + 00	0.6638E + 00
0.45E + 01	0.6197E + 00	0.6207E + 00	0.6592E + 00	0.6483E + 00
0.46E + 01	0.6013E + 00	0.6076E + 00	0.6413E + 00	0.6273E + 00
0.48E + 01	0.5666E + 00	0.5704E + 00	0.5995E + 00	0.5944E + 00
0.50E + 01	0.5453E + 00	0.5436E + 00	0.5848E + 00	0.5755E + 00
0.55E + 01	0.4943E + 00	0.5036E + 00	0.5618E + 00	0.5568E + 00
0.60E + 01	0.4819E + 00	0.4840E + 00	0.5218E + 00	0.5188E + 00
0.65E + 01	0.4839E + 00	0.4863E + 00	0.4909E + 00	0.4848E + 00
0.70E + 01	0.4677E + 00	0.4719E + 00	0.4686E + 00	0.4628E + 00
0.80E + 01	0.4290E + 00	0.4332E + 00	0.4346E + 00	0.4214E + 00
0.90E + 01	0.3634E + 00	0.3658E + 00	0.3947E + 00	0.3884E + 00
0.10E + 02	0.3084E + 00	0.3084E + 00	0.3310E + 00	0.3310E + 00
0.11E + 02	0.2837E + 00	0.2837E + 00	0.3102E + 00	0.3102E + 00
0.12E + 02	0.2601E + 00	0.2601E + 00	0.2901E + 00	0.2901E + 00
0.13E + 02	0.2377E + 00	0.2377E + 00	0.2705E + 00	0.2705E + 00
0.14E + 02	0.2165E + 00	0.2165E + 00	0.2514E + 00	0.2514E + 00
0.15E + 02	0.1972E + 00	0.1972E + 00	0.2331E + 00	0.2331E + 00
0.16E + 02	0.1791E + 00	0.1791E + 00	0.2156E + 00	0.2156E + 00
0.17E + 02	0.1626E + 00	0.1626E + 00	0.1987E + 00	0.1987E + 00
0.18E + 02	0.1474E + 00	0.1474E + 00	0.1830E + 00	0.1830E + 00

Table 3. (Continued)

x (per nm)	Pork fat	Beef fat	Pork muscle	Beef muscle
0.19E + 02	0.1338E + 00	0.1338E + 00	0.1684E + 00	0.1684E + 00
0.20E + 02	0.1215E + 00	0.1215E + 00	0.1548E + 00	0.1548E + 00
0.22E + 02	0.1001E + 00	0.1001E + 00	0.1303E + 00	0.1303E + 00
0.24E + 02	0.8281E - 01	0.8281E - 01	0.1097E + 00	0.1097E + 00
0.25E + 02	0.7541E - 01	0.7541E - 01	0.1007E + 00	0.1007E + 00
0.26E + 02	0.6873E - 01	0.6873E - 01	0.9246E - 01	0.9246E - 01
0.28E + 02	0.5729E - 01	0.5729E - 01	0.7807E - 01	0.7807E - 01
0.30E + 02	0.4798E - 01	0.4798E - 01	0.6608E - 01	0.6608E - 01
0.33E + 02	0.3708E - 01	0.3708E - 01	0.5176E - 01	0.5176E - 01
0.35E + 02	0.3139E - 01	0.3139E - 01	0.4417E - 01	0.4417E - 01
0.36E + 02	0.2893E - 01	0.2893E - 01	0.4085E - 01	0.4085E - 01
0.39E + 02	0.2285E - 01	0.2285E - 01	0.3253E - 01	0.3253E - 01
0.40E + 02	0.2117E - 01	0.2117E - 01	0.3021E - 01	0.3021E - 01
0.42E + 02	0.1823E - 01	0.1823E - 01	0.2614E - 01	0.2614E - 01
0.46E + 02	0.1368E - 01	0.1368E - 01	0.1977E - 01	0.1977E - 01
0.50E + 02	0.1042E - 01	0.1042E - 01	0.1516E - 01	0.1516E - 01
0.54E + 02	0.8057E - 02	0.8057E - 02	0.1178E - 01	0.1178E - 01
0.55E + 02	0.7570E - 02	0.7570E - 02	0.1108E - 01	0.1108E - 01
0.58E + 02	0.6308E - 02	0.6308E - 02	0.9257E - 02	0.9257E - 02
0.60E + 02	0.5608E - 02	0.5608E - 02	0.8244E - 02	0.8244E - 02
0.62E + 02	0.4999E - 02	0.4999E - 02	0.7362E - 02	0.7362E - 02
0.66E + 02	0.4008E - 02	0.4008E - 02	0.5918E - 02	0.5918E - 02
0.70E + 02	0.3247E - 02	0.3247E - 02	0.4805E - 02	0.4805E - 02
0.74E + 02	0.2655E - 02	0.2655E - 02	0.3937E - 02	0.3937E - 02
0.80E + 02	0.1995E - 02	0.1995E - 02	0.2966E - 02	0.2966E - 02
0.90E + 02	0.1288E - 02	0.1288E - 02	0.1921E - 02	0.1921E - 02
0.10E + 03	0.8665E - 03	0.8665E - 03	0.1295E - 02	0.1295E - 02
0.11E + 03	0.6032E - 03	0.6032E - 03	0.9032E - 03	0.9032E - 03
0.12E + 03	0.4322E - 03	0.4322E - 03	0.6480E - 03	0.6480E - 03
0.14E + 03	0.2384E - 03	0.2384E - 03	0.3581E - 03	0.3581E - 03
0.16E + 03	0.1418E - 03	0.1418E - 03	0.2134E - 03	0.2134E - 03
0.18E + 03	0.8954E - 04	0.8954E - 04	0.1348E - 03	0.1348E - 03
0.20E + 03	0.5926E - 04	0.5926E - 04	0.8929E - 04	0.8929E - 04
0.22E + 03	0.4076E - 04	0.4076E - 04	0.6145E - 04	0.6145E - 04
0.25E + 03	0.2465E - 04	0.2465E - 04	0.3718E - 04	0.3718E - 04
0.28E + 03	0.1578E - 04	0.1578E - 04	0.2381E - 04	0.2381E - 04
0.31E + 03	0.1056E - 04	0.1056E - 04	0.1595E - 04	0.1595E - 04
0.35E + 03	0.6544E - 05	0.6544E - 05	0.9884E - 05	0.9884E - 05
0.40E + 03	0.3866E - 05	0.3866E - 05	0.5842E - 05	0.5842E - 05
0.45E + 03	0.2429E - 05	0.2429E - 05	0.3672E - 05	0.3672E - 05
0.50E + 03	0.1605E - 05	0.1605E - 05	0.2427E - 05	0.2427E - 05
0.70E + 03	0.4274E - 06	0.4274E - 06	0.6472E - 06	0.6472E - 06
0.10E + 04	0.1059E - 06	0.1059E - 06	0.1606E - 06	0.1606E - 06
0.10E + 05	0.1987E - 10	0.1987E - 10	0.3072E - 10	0.3072E - 10
0.10E + 08	0.1048E - 19	0.1048E - 19	0.1655E - 19	0.1655E - 19
0.10E + 11	0.1071E - 28	0.1071E - 28	0.1692E - 28	0.1692E - 28

question of how formaline affects the measured form factor arises. The form factor for formaline was measured separately and it appears very similar to that of water (which is 90% of formaline). Since formaline is mostly water and it replaces water in the tissue, the overall form factor of the breast tissue should not be changed too much by the presence of

Table 4. Molecular coherent scattering form factors.

x (per nm)	Pork kidney	Beef kidney	Pork liver	Beef liver
0.00E + 00	0.5871E + 00	0.5871E + 00	0.5871E + 00	0.5871E + 00
0.10E + 00	0.5871E + 00	0.5871E + 00	0.5871E + 00	0.5871E + 00
0.20E + 00	0.5871E + 00	0.5871E + 00	0.5871E + 00	0.5871E + 00
0.30E + 00	0.5871E + 00	0.5871E + 00	0.5871E + 00	0.5871E + 00
0.40E + 00	0.5871E + 00	0.5871E + 00	0.5871E + 00	0.5871E + 00
0.50E + 00	0.5871E + 00	0.5871E + 00	0.5871E + 00	0.5871E + 00
0.60E + 00	0.5871E + 00	0.5871E + 00	0.5871E + 00	0.5871E + 00
0.70E + 00	0.5871E + 00	0.5871E + 00	0.5871E + 00	0.5871E + 00
0.80E + 00	0.5871E + 00	0.5871E + 00	0.5871E + 00	0.5871E + 00
0.90E + 00	0.5871E + 00	0.5871E + 00	0.5871E + 00	0.5871E + 00
0.10E + 01	0.9287E + 00	0.9711E + 00	0.1082E + 01	0.1104E + 01
0.11E + 01	0.1144E + 01	0.1173E + 01	0.1284E + 01	0.1296E + 01
0.12E + 01	0.1305E + 01	0.1328E + 01	0.1422E + 01	0.1427E + 01
0.13E + 01	0.1472E + 01	0.1481E + 01	0.1502E + 01	0.1514E + 01
0.14E + 01	0.1624E + 01	0.1656E + 01	0.1649E + 01	0.1663E + 01
0.15E + 01	0.1785E + 01	0.1799E + 01	0.1775E + 01	0.1790E + 01
0.16E + 01	0.1830E + 01	0.1831E + 01	0.1795E + 01	0.1797E + 01
0.17E + 01	0.1779E + 01	0.1775E + 01	0.1743E + 01	0.1759E + 01
0.18E + 01	0.1712E + 01	0.1707E + 01	0.1667E + 01	0.1683E + 01
0.19E + 01	0.1633E + 01	0.1630E + 01	0.1595E + 01	0.1616E + 01
0.20E + 01	0.1562E + 01	0.1564E + 01	0.1528E + 01	0.1544E + 01
0.22E + 01	0.1534E + 01	0.1515E + 01	0.1486E + 01	0.1498E + 01
0.24E + 01	0.1421E + 01	0.1404E + 01	0.1368E + 01	0.1389E + 01
0.25E + 01	0.1296E + 01	0.1294E + 01	0.1261E + 01	0.1267E + 01
0.26E + 01	0.1157E + 01	0.1153E + 01	0.1136E + 01	0.1143E + 01
0.28E + 01	0.9574E + 00	0.9529E + 00	0.9450E + 00	0.9613E + 00
0.30E + 01	0.8881E + 00	0.8805E + 00	0.8790E + 00	0.8867E + 00
0.32E + 01	0.8613E + 00	0.8580E + 00	0.8399E + 00	0.8557E + 00
0.34E + 01	0.8670E + 00	0.8657E + 00	0.8461E + 00	0.8647E + 00
0.35E + 01	0.8661E + 00	0.8642E + 00	0.8404E + 00	0.8571E + 00
0.36E + 01	0.8603E + 00	0.8474E + 00	0.8328E + 00	0.8458E + 00
0.38E + 01	0.8209E + 00	0.8094E + 00	0.7891E + 00	0.8107E + 00
0.40E + 01	0.7736E + 00	0.7735E + 00	0.7706E + 00	0.7776E + 00
0.42E + 01	0.7225E + 00	0.7243E + 00	0.7163E + 00	0.7366E + 00
0.44E + 01	0.6783E + 00	0.6850E + 00	0.6670E + 00	0.6962E + 00
0.45E + 01	0.6458E + 00	0.6471E + 00	0.6456E + 00	0.6625E + 00
0.46E + 01	0.6258E + 00	0.6304E + 00	0.6183E + 00	0.6416E + 00
0.48E + 01	0.5935E + 00	0.5945E + 00	0.5724E + 00	0.5953E + 00
0.50E + 01	0.5735E + 00	0.5751E + 00	0.5673E + 00	0.5829E + 00
0.55E + 01	0.5547E + 00	0.5532E + 00	0.5470E + 00	0.5574E + 00
0.60E + 01	0.5190E + 00	0.5217E + 00	0.5092E + 00	0.5255E + 00
0.65E + 01	0.4823E + 00	0.4806E + 00	0.4792E + 00	0.4827E + 00
0.70E + 01	0.4646E + 00	0.4702E + 00	0.4631E + 00	0.4687E + 00
0.80E + 01	0.4285E + 00	0.4330E + 00	0.4300E + 00	0.4353E + 00
0.90E + 01	0.3902E + 00	0.3863E + 00	0.3853E + 00	0.3976E + 00
0.10E + 02	0.3275E + 00	0.3275E + 00	0.3285E + 00	0.3285E + 00
0.11E + 02	0.3064E + 00	0.3064E + 00	0.3070E + 00	0.3070E + 00
0.12E + 02	0.2861E + 00	0.2861E + 00	0.2865E + 00	0.2865E + 00
0.13E + 02	0.2665E + 00	0.2665E + 00	0.2667E + 00	0.2667E + 00
0.14E + 02	0.2476E + 00	0.2476E + 00	0.2477E + 00	0.2477E + 00
0.15E + 02	0.2295E + 00	0.2295E + 00	0.2295E + 00	0.2295E + 00
0.16E + 02	0.2123E + 00	0.2123E + 00	0.2122E + 00	0.2122E + 00
0.17E + 02	0.1958E + 00	0.1958E + 00	0.1957E + 00	0.1957E + 00
0.18E + 02	0.1804E + 00	0.1804E + 00	0.1803E + 00	0.1803E + 00

Table 4. (Continued)

x (per nm)	Pork kidney	Beef kidney	Pork liver	Beef liver
0.19E + 02	0.1661E + 00	0.1661E + 00	0.1660E + 00	0.1660E + 00
0.20E + 02	0.1529E + 00	0.1529E + 00	0.1528E + 00	0.1528E + 00
0.22E + 02	0.1290E + 00	0.1290E + 00	0.1291E + 00	0.1291E + 00
0.24E + 02	0.1091E + 00	0.1091E + 00	0.1092E + 00	0.1092E + 00
0.25E + 02	0.1003E + 00	0.1003E + 00	0.1005E + 00	0.1005E + 00
0.26E + 02	0.9232E - 01	0.9232E - 01	0.9251E - 01	0.9251E - 01
0.28E + 02	0.7838E - 01	0.7838E - 01	0.7864E - 01	0.7864E - 01
0.30E + 02	0.6678E - 01	0.6678E - 01	0.6710E - 01	0.6710E - 01
0.33E + 02	0.5292E - 01	0.5292E - 01	0.5331E - 01	0.5331E - 01
0.35E + 02	0.4557E - 01	0.4557E - 01	0.4599E - 01	0.4599E - 01
0.36E + 02	0.4236E - 01	0.4236E - 01	0.4279E - 01	0.4279E - 01
0.39E + 02	0.3427E - 01	0.3427E - 01	0.3472E - 01	0.3472E - 01
0.40E + 02	0.3202E - 01	0.3202E - 01	0.3247E - 01	0.3247E - 01
0.42E + 02	0.2803E - 01	0.2803E - 01	0.2849E - 01	0.2849E - 01
0.46E + 02	0.2176E - 01	0.2176E - 01	0.2220E - 01	0.2220E - 01
0.50E + 02	0.1715E - 01	0.1715E - 01	0.1756E - 01	0.1756E - 01
0.54E + 02	0.1371E - 01	0.1371E - 01	0.1409E - 01	0.1409E - 01
0.55E + 02	0.1299E - 01	0.1299E - 01	0.1336E - 01	0.1336E - 01
0.58E + 02	0.1110E - 01	0.1110E - 01	0.1144E - 01	0.1144E - 01
0.60E + 02	0.1003E - 01	0.1003E - 01	0.1035E - 01	0.1035E - 01
0.62E + 02	0.9092E - 02	0.9092E - 02	0.9390E - 02	0.9390E - 02
0.66E + 02	0.7519E - 02	0.7519E - 02	0.7782E - 02	0.7782E - 02
0.70E + 02	0.6276E - 02	0.6276E - 02	0.6506E - 02	0.6506E - 02
0.74E + 02	0.5280E - 02	0.5280E - 02	0.5481E - 02	0.5481E - 02
0.80E + 02	0.4128E - 02	0.4128E - 02	0.4292E - 02	0.4292E - 02
0.90E + 02	0.2825E - 02	0.2825E - 02	0.2942E - 02	0.2942E - 02
0.10E + 03	0.1996E - 02	0.1996E - 02	0.2080E - 02	0.2080E - 02
0.11E + 03	0.1447E - 02	0.1447E - 02	0.1508E - 02	0.1508E - 02
0.12E + 03	0.1073E - 02	0.1073E - 02	0.1118E - 02	0.1118E - 02
0.14E + 03	0.6245E - 03	0.6245E - 03	0.6504E - 03	0.6504E - 03
0.16E + 03	0.3864E - 03	0.3864E - 03	0.4021E - 03	0.4021E - 03
0.18E + 03	0.2512E - 03	0.2512E - 03	0.2612E - 03	0.2612E - 03
0.20E + 03	0.1701E - 03	0.1701E - 03	0.1768E - 03	0.1768E - 03
0.22E + 03	0.1191E - 03	0.1191E - 03	0.1237E - 03	0.1237E - 03
0.25E + 03	0.7358E - 04	0.7358E - 04	0.7639E - 04	0.7639E - 04
0.28E + 03	0.4786E - 04	0.4786E - 04	0.4966E - 04	0.4966E - 04
0.31E + 03	0.3246E - 04	0.3246E - 04	0.3367E - 04	0.3367E - 04
0.35E + 03	0.2040E - 04	0.2040E - 04	0.2115E - 04	0.2115E - 04
0.40E + 03	0.1223E - 04	0.1223E - 04	0.1267E - 04	0.1267E - 04
0.45E + 03	0.7774E - 05	0.7774E - 05	0.8054E - 05	0.8054E - 05
0.50E + 03	0.5186E - 05	0.5186E - 05	0.5371E - 05	0.5371E - 05
0.70E + 03	0.1426E - 05	0.1426E - 05	0.1476E - 05	0.1476E - 05
0.10E + 04	0.3668E - 06	0.3668E - 06	0.3789E - 06	0.3789E - 06
0.10E + 05	0.1034E - 09	0.1034E - 09	0.1058E - 09	0.1058E - 09
0.10E + 08	0.8282E - 19	0.8282E - 19	0.8363E - 19	0.8363E - 19
0.10E + 11	0.9385E - 28	0.9385E - 28	0.9412E - 28	0.9412E - 28

formaline. In fact, a sum of the form factors of about one part water and two parts beef adipose gives a shape very similar to that measured for the breast tissue form factor.

Some work is needed to improve the data collection, especially in the low-angle range where the effects of the sample container are strong. For example, some of the materials, like water and beef blood, had a slight but noticeable inward curvature of the Kapton film

Table 5. Molecular coherent scattering form factors.

x (per nm)	Pork heart	Beef blood	Breast tissue	Formaline
0.00E + 00	0.5871E + 00	0.5871E + 00	0.8191E + 00	0.5871E + 00
0.10E + 00	0.5871E + 00	0.5871E + 00	0.8191E + 00	0.5871E + 00
0.20E + 00	0.5871E + 00	0.5871E + 00	0.8191E + 00	0.5871E + 00
0.30E + 00	0.5871E + 00	0.5871E + 00	0.8191E + 00	0.5871E + 00
0.40E + 00	0.5871E + 00	0.5871E + 00	0.8191E + 00	0.5871E + 00
0.50E + 00	0.5871E + 00	0.5871E + 00	0.9665E + 00	0.5871E + 00
0.60E + 00	0.5871E + 00	0.5871E + 00	0.1134E + 01	0.5871E + 00
0.70E + 00	0.5871E + 00	0.5871E + 00	0.1250E + 01	0.5871E + 00
0.80E + 00	0.5871E + 00	0.5871E + 00	0.1247E + 01	0.5871E + 00
0.90E + 00	0.5871E + 00	0.5871E + 00	0.1464E + 01	0.5871E + 00
0.10E + 01	0.9336E + 00	0.5871E + 00	0.1813E + 01	0.6872E + 00
0.11E + 01	0.1124E + 01	0.6910E + 00	0.2073E + 01	0.8685E + 00
0.12E + 01	0.1322E + 01	0.9595E + 00	0.1890E + 01	0.1118E + 01
0.13E + 01	0.1504E + 01	0.1227E + 01	0.1706E + 01	0.1307E + 01
0.14E + 01	0.1672E + 01	0.1445E + 01	0.1670E + 01	0.1563E + 01
0.15E + 01	0.1844E + 01	0.1649E + 01	0.1710E + 01	0.1782E + 01
0.16E + 01	0.1878E + 01	0.1723E + 01	0.1708E + 01	0.1836E + 01
0.17E + 01	0.1831E + 01	0.1695E + 01	0.1648E + 01	0.1792E + 01
0.18E + 01	0.1759E + 01	0.1625E + 01	0.1553E + 01	0.1685E + 01
0.19E + 01	0.1657E + 01	0.1551E + 01	0.1486E + 01	0.1585E + 01
0.20E + 01	0.1594E + 01	0.1488E + 01	0.1438E + 01	0.1546E + 01
0.22E + 01	0.1550E + 01	0.1463E + 01	0.1409E + 01	0.1500E + 01
0.24E + 01	0.1426E + 01	0.1350E + 01	0.1323E + 01	0.1416E + 01
0.25E + 01	0.1317E + 01	0.1235E + 01	0.1220E + 01	0.1285E + 01
0.26E + 01	0.1161E + 01	0.1110E + 01	0.1096E + 01	0.1150E + 01
0.28E + 01	0.9638E + 00	0.9187E + 00	0.9061E + 00	0.9281E + 00
0.30E + 01	0.8914E + 00	0.8455E + 00	0.8443E + 00	0.8622E + 00
0.32E + 01	0.8656E + 00	0.8215E + 00	0.7942E + 00	0.8381E + 00
0.34E + 01	0.8732E + 00	0.8178E + 00	0.7964E + 00	0.8336E + 00
0.35E + 01	0.8670E + 00	0.8074E + 00	0.7930E + 00	0.8275E + 00
0.36E + 01	0.8604E + 00	0.8009E + 00	0.8021E + 00	0.8289E + 00
0.38E + 01	0.8249E + 00	0.7608E + 00	0.7664E + 00	0.7831E + 00
0.40E + 01	0.7809E + 00	0.7069E + 00	0.7370E + 00	0.7280E + 00
0.42E + 01	0.7299E + 00	0.6410E + 00	0.7095E + 00	0.6729E + 00
0.44E + 01	0.6866E + 00	0.5978E + 00	0.6654E + 00	0.6083E + 00
0.45E + 01	0.6546E + 00	0.5654E + 00	0.6406E + 00	0.5825E + 00
0.46E + 01	0.6339E + 00	0.5507E + 00	0.6119E + 00	0.5478E + 00
0.48E + 01	0.6047E + 00	0.5272E + 00	0.5851E + 00	0.5279E + 00
0.50E + 01	0.5848E + 00	0.5018E + 00	0.5654E + 00	0.5104E + 00
0.55E + 01	0.5632E + 00	0.4929E + 00	0.5441E + 00	0.5087E + 00
0.60E + 01	0.5228E + 00	0.4649E + 00	0.5133E + 00	0.4673E + 00
0.65E + 01	0.4808E + 00	0.4264E + 00	0.4889E + 00	0.4282E + 00
0.70E + 01	0.4664E + 00	0.4100E + 00	0.4722E + 00	0.4093E + 00
0.80E + 01	0.4317E + 00	0.3746E + 00	0.4282E + 00	0.3793E + 00
0.90E + 01	0.3849E + 00	0.3375E + 00	0.3967E + 00	0.3450E + 00
0.10E + 02	0.3273E + 00	0.3275E + 00	0.3144E + 00	0.3230E + 00
0.11E + 02	0.3061E + 00	0.3067E + 00	0.2921E + 00	0.3028E + 00
0.12E + 02	0.2858E + 00	0.2867E + 00	0.2707E + 00	0.2833E + 00
0.13E + 02	0.2661E + 00	0.2673E + 00	0.2502E + 00	0.2643E + 00
0.14E + 02	0.2471E + 00	0.2485E + 00	0.2305E + 00	0.2457E + 00
0.15E + 02	0.2290E + 00	0.2305E + 00	0.2121E + 00	0.2280E + 00
0.16E + 02	0.2117E + 00	0.2133E + 00	0.1947E + 00	0.2109E + 00
0.17E + 02	0.1952E + 00	0.1968E + 00	0.1784E + 00	0.1945E + 00
0.18E + 02	0.1799E + 00	0.1814E + 00	0.1633E + 00	0.1792E + 00

Table 5. (Continued)

x (per nm)	Pork heart	Beef blood	Breast tissue	Formaline
0.19E+02	0.1656E+00	0.1671E+00	0.1495E+00	0.1649E+00
0.20E+02	0.1524E+00	0.1538E+00	0.1367E+00	0.1517E+00
0.22E+02	0.1286E+00	0.1299E+00	0.1142E+00	0.1278E+00
0.24E+02	0.1087E+00	0.1098E+00	0.9556E-01	0.1077E+00
0.25E+02	0.9995E-01	0.1009E+00	0.8746E-01	0.9884E-01
0.26E+02	0.9198E-01	0.9289E-01	0.8010E-01	0.9077E-01
0.28E+02	0.7809E-01	0.7883E-01	0.6734E-01	0.7667E-01
0.30E+02	0.6654E-01	0.6712E-01	0.5679E-01	0.6493E-01
0.33E+02	0.5274E-01	0.5312E-01	0.4429E-01	0.5088E-01
0.35E+02	0.4543E-01	0.4569E-01	0.3769E-01	0.4343E-01
0.36E+02	0.4223E-01	0.4245E-01	0.3483E-01	0.4018E-01
0.39E+02	0.3418E-01	0.3427E-01	0.2766E-01	0.3200E-01
0.40E+02	0.3194E-01	0.3199E-01	0.2567E-01	0.2973E-01
0.42E+02	0.2797E-01	0.2797E-01	0.2218E-01	0.2572E-01
0.46E+02	0.2173E-01	0.2164E-01	0.1673E-01	0.1946E-01
0.50E+02	0.1714E-01	0.1699E-01	0.1281E-01	0.1493E-01
0.54E+02	0.1371E-01	0.1353E-01	0.9931E-02	0.1160E-01
0.55E+02	0.1300E-01	0.1281E-01	0.9338E-02	0.1091E-01
0.58E+02	0.1111E-01	0.1091E-01	0.7798E-02	0.9119E-02
0.60E+02	0.1004E-01	0.9844E-02	0.6941E-02	0.8121E-02
0.62E+02	0.9102E-02	0.8902E-02	0.6195E-02	0.7253E-02
0.66E+02	0.7531E-02	0.7335E-02	0.4976E-02	0.5831E-02
0.70E+02	0.6288E-02	0.6100E-02	0.4038E-02	0.4735E-02
0.74E+02	0.5291E-02	0.5114E-02	0.3306E-02	0.3880E-02
0.80E+02	0.4137E-02	0.3979E-02	0.2489E-02	0.2924E-02
0.90E+02	0.2832E-02	0.2704E-02	0.1611E-02	0.1894E-02
0.10E+03	0.2000E-02	0.1900E-02	0.1085E-02	0.1277E-02
0.11E+03	0.1450E-02	0.1370E-02	0.7564E-03	0.8905E-03
0.12E+03	0.1075E-02	0.1012E-02	0.5424E-03	0.6389E-03
0.14E+03	0.6249E-03	0.5851E-03	0.2996E-03	0.3531E-03
0.16E+03	0.3864E-03	0.3604E-03	0.1785E-03	0.2104E-03
0.18E+03	0.2510E-03	0.2335E-03	0.1127E-03	0.1329E-03
0.20E+03	0.1699E-03	0.1576E-03	0.7464E-04	0.8806E-04
0.22E+03	0.1189E-03	0.1102E-03	0.5136E-04	0.6060E-04
0.25E+03	0.7343E-04	0.6789E-04	0.3108E-04	0.3667E-04
0.28E+03	0.4775E-04	0.4407E-04	0.1990E-04	0.2348E-04
0.31E+03	0.3238E-04	0.2985E-04	0.1332E-04	0.1573E-04
0.35E+03	0.2034E-04	0.1873E-04	0.8257E-05	0.9749E-05
0.40E+03	0.1218E-04	0.1121E-04	0.4880E-05	0.5762E-05
0.45E+03	0.7746E-05	0.7117E-05	0.3067E-05	0.3622E-05
0.50E+03	0.5166E-05	0.4743E-05	0.2027E-05	0.2394E-05
0.70E+03	0.1420E-05	0.1300E-05	0.5403E-06	0.6384E-06
0.10E+04	0.3646E-06	0.3329E-06	0.1340E-06	0.1584E-06
0.10E+05	0.1021E-09	0.9112E-10	0.2550E-10	0.3033E-10
0.10E+08	0.8100E-19	0.7125E-19	0.1366E-19	0.1635E-19
0.10E+11	0.9134E-28	0.7998E-28	0.1397E-28	0.1673E-28

once they were loaded into the container. Other materials had a slight outward curvature of the Kapton film after loading. Care was taken to try to minimize these problems but they could not be completely eliminated. This and the changes in response caused by slight alignment changes led to problems at low values of x . The remedies presented in this paper to these problems are not rigorous and are somewhat cumbersome to use.

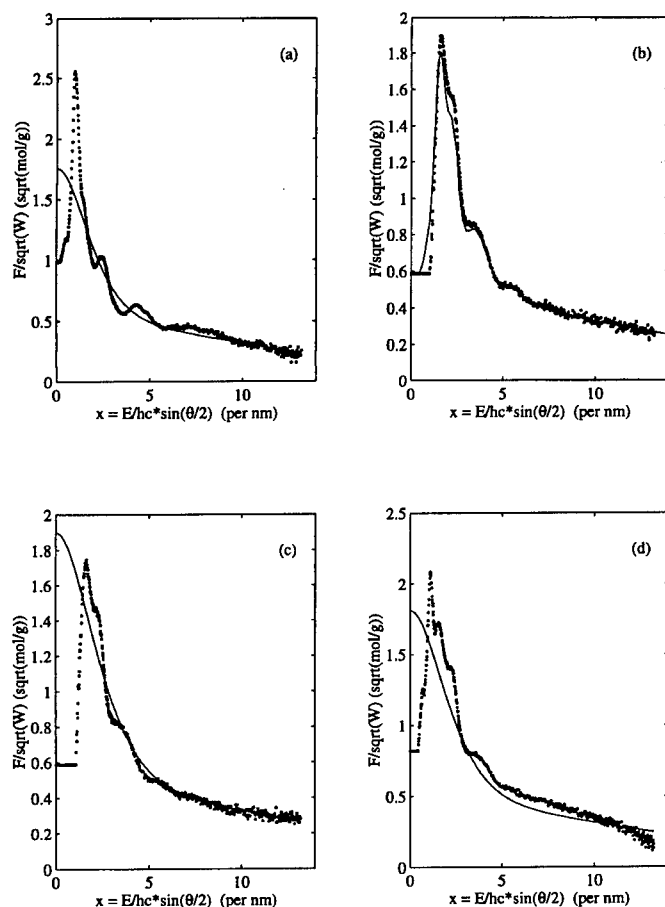


Figure 6. Free gas model (—) and the molecular coherent scattering form factor (·) reduced from scattering distribution measurements for (a) Lexan, (b) water (in this case, Narten's measurement is shown instead of the free gas model), (c) beef blood and (d) breast tissue.

It was assumed in this procedure that only the coherent scatter form factor was affected by intramolecular and intermolecular interferences. As in almost all reported literature, incoherent scatter for molecules was calculated using atomic scattering factors. However, Guy *et al* (1992) measured the incoherent scattering distributions of several metals and showed some differences compared with Hubbell's incoherent scattering factors. Their work implied that the incoherent scattering factors may need to include molecular and solid state electron binding effects. This is, however, not expected to be a significant error in the data presented since incoherent scatter is only a minor component, as shown in figure 2(c).

The molecular form factors of Lucite and pork adipose from this study and from Tartari *et al* (1997b), shown in figure 7, agree quite well given the different quality of beams and analysis techniques. The molecular form factors also agree in shape with other powder diffraction studies (Kosanetzky *et al* 1987, Evans *et al* 1991, Leliveld 1996). However, this study stands apart from others with its use of monoenergetic x-rays and its unique approach to extraction of the form factors using dual-energy measurements and detailed Monte Carlo modelling.

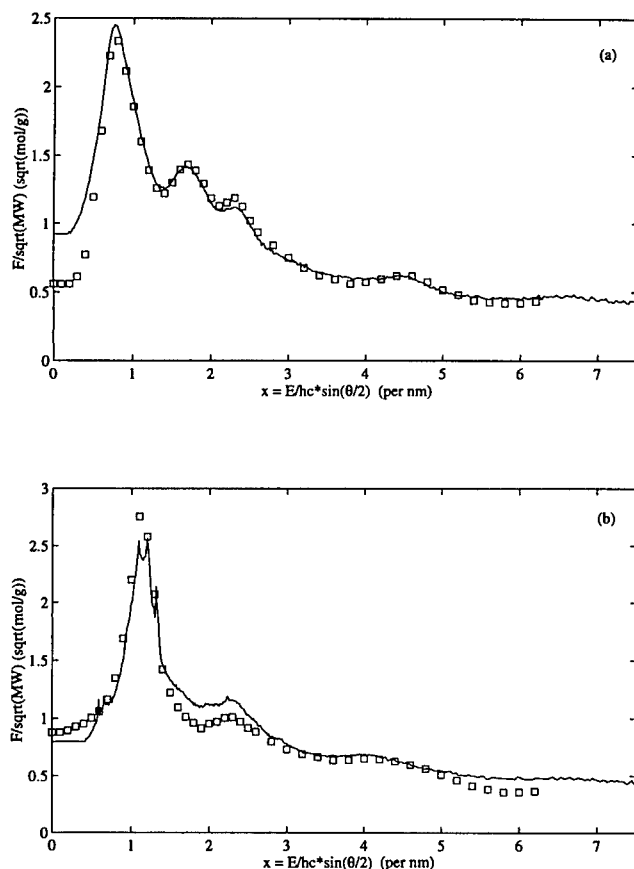


Figure 7. Molecular form factors for (a) Lucite and (b) pork adipose compared for this study (—) and Tartari *et al* (1997b) (\square).

5. Summary

Molecular form factors were measured and tabulated for two plastics, five pork tissues, five beef tissues, water, Kapton, formaline and human breast tissue. The final values were constructed by combining measurements at two different source energies made with monoenergetic polarized synchrotron radiation. The x values listed in the tables match those of Hubbell and Øverbø's work and should be able to be easily implemented into codes.

We believe that these tables will be most useful to those in the medical physics community, especially in a low-energy application, such as mammographic imaging.

Acknowledgments

Research was carried out in part at the National Synchrotron Light Source, Brookhaven National Laboratory, which is supported by the US Department of Energy, Division of Materials Sciences and Division of Chemical Sciences. Many thanks to Dr Peter W Stephens for allowing this work to be done on beamline X3B1. Thanks also to Dr David Cox of beamline X7A where some preliminary measurements were made.

Monte Carlo simulations and the analysis of the experimental data were performed on a Sun Ultra 2/2200 donated by Sun Microsystems, through their Academic Equipment Grant. Many thanks to Sun Microsystems.

Financial support of the first author (DEP) was provided by Dr R Eugene Johnston, University of North Carolina, through his Breast Cancer Research Grant from the US Army Medical Research and Material Command.

Animal tissue samples were obtained from McLamb's Abattoir of Benson, NC.

References

- Boone J M 1992 Parameterized x-ray absorption in diagnostic radiology from Monte Carlo calculations: implications for x-ray detector design *Med. Phys.* **19** 1467-73
- Chan H P and Doi K 1983 Energy and angular dependence of x-ray absorption and its effect on radiographic response in screen-film systems *Phys. Med. Biol.* **28** 565-79
- Chapman D, Thomlinson W, Johnston R E, Washburn D, Pisano E, Gmür N, Zhong Z, Menk R, Arfelli F and Sayers D 1997 Diffraction enhanced x-ray imaging *Phys. Med. Biol.* **42** 2015-25
- Evans S H, Bradley D A, Dance D R, Bateman J E and Jones C H 1991 Measurement of small-angle photon scattering for some breast tissues and tissue substitute materials *Phys. Med. Biol.* **35** 7-18
- Guy L P, Taylor R B and Whittingham I B 1992 Incoherent scattering function at small momentum transfer *Nucl. Instrum. Methods B* **69** 174-7
- Hubbell J H and Øverbø I 1979 Relativistic atomic form factors and photon coherent cross sections *J. Phys. Chem. Ref. Data* **8** 69-105
- Hubbell J H, Veigele W J, Briggs E A, Brown R T, Cromer D T and Howerton R J 1975 Atomic form factors, incoherent scattering functions, and photon cross sections *J. Phys. Chem. Ref. Data* **4** 471-538
- 1977 Erratum: atomic form factors, incoherent scattering functions, and photon cross sections *J. Phys. Chem. Ref. Data* **6** 615-16
- ICRU 1992 Photon, electron, proton, and neutron interaction data for body tissues *ICRU Report 46* (Bethesda, MD: ICRU)
- Johns P C and Yaffe M J 1983 Coherent scattering in diagnostic radiology *Med. Phys.* **10** 40-50
- Johnston R E, Washburn D, Pisano E, Burns C, Thomlinson W, Chapman L D, Arfelli F, Gmür N F, Zhong Z and Sayers D E 1996 Mammographic phantom studies with synchrotron radiation *Radiology* **200** 659-63
- Kosanetzky J, Knoerr B, Harding G and Neitzel U 1987 X-ray diffraction measurements of some plastic materials and body tissues *Med. Phys.* **14** 526-32
- Leliveld C J, Maas J G, Bom V R and van Eijk C W E 1996 Monte Carlo modelling of coherent scattering: influence of interference *IEEE Trans. Nuc. Sci.* **43** 3315-21
- Narten A H 1970 X-ray diffraction data on liquid water in the temperature range 4 to 200°C *Report ORNL-4578* (Oak Ridge, TN: Oak Ridge National Laboratory)
- Narten A H and Levy H A 1971 Liquid water: molecular correlation functions from x-ray diffraction *J. Chem. Phys.* **55** 2263-9
- Tartari A, Casnati E, Bonifazzi C and Baraldi C 1997b Molecular differential cross sections for x-ray coherent scattering in fat and polymethyl methacrylate *Phys. Med. Biol.* **42** 2551-60
- Tartari A, Casnati E, Bonifazzi C and Paganetto G 1997a Photon scattering by compounds: an assessment of the validity of the independent atomic model approximation *X-Ray Spectrom.* **26** 169-73

Appendix

A.4

Johnston RE, Washburn D, Pisano E, Burns C, Thomlinson WC, Chapman D, Arfelli F, Gmur NF, Zhong Z, Sayers D. Mammography Phantom Studies with Synchrotron Radiation. Radiology 1996: 200, 659-663.

R. Eugene Johnston, PhD • David Washburn, PhD • Etta Pisano, MD • Charles Burns, MS
William C. Thomlinson, PhD • L. Dean Chapman, PhD • Fulvia Arfelli, PhD
Nicholas F. Gmur, PhD • Zhong Zhong, MS • Dale Sayers, PhD

Mammographic Phantom Studies with Synchrotron Radiation¹

PURPOSE: To explore the potential improvement in image contrast for breast imaging with use of monoenergetic photons.

MATERIALS AND METHODS: The x-ray energy available from the National Synchrotron Light Source is from 5 to over 50 keV. A specific energy is selected with a tunable crystal monochromator. The object is scanned with a narrow beam of 80.0×0.5 mm. Mammography phantoms were imaged with plate and film as the imaging detectors. Phantom images were obtained at 16–24 keV and compared with images obtained with a conventional mammographic unit.

RESULTS: Preliminary findings indicate improved image contrast of the monoenergetic images compared with that obtained from the conventional x-ray source, particularly at 18 keV and below.

CONCLUSION: Pilot results are encouraging, and the authors presently continue to explore monoenergetic photon imaging with improved instrumentation, scatter rejection, and use of tissue samples.

SCREENING mammography has proved to be an effective procedure for identifying early breast cancer. The results of several large randomized trials have demonstrated that the mortality rate from breast cancer among women older than 50 years who have undergone screening can be reduced at least 30% when compared with control subjects who have not undergone screening (1–3). The cancers found with mammography tend to be smaller and of less advanced stages than those found with breast physical examination or breast self-examination (4–6). Detection and removal of smaller and lower stage breast cancers result in improved 5-, 10-, and 20-year survival rates (7–10).

Mammographic technology has improved dramatically in the past 2 decades. These improvements include the development of dedicated mammographic equipment with appropriate x-ray beam quality, grid capability, adequate breast compression, and automatic exposure control. In addition, magnification techniques with a very small focal spot size have become widely available. Better screen-film systems and appropriate film processing have also been developed to improve image contrast. Over the same time period, the average glandular radia-

tion dose from mammography has dropped, generally because of the development of faster screen-film combinations.

Unfortunately, approximately 10% of clinically obvious breast cancers are not visible with mammography (4). This occurs most frequently in patients with large amounts of breast glandular tissue (4,11). The density of this tissue tends to obscure underlying abnormalities. It is desirable to increase the sensitivity of mammography in these patients so that their cancers become apparent at the earliest possible stage. Further improvement in detection is expected with the advent of digital mammography (12,13), which uses better x-ray beam geometry and improved sensitivity of the detector systems.

The conventional source of x rays for medical imaging is the x-ray tube, which generates a mixture of bremsstrahlung and characteristic x rays. In modern mammographic x-ray tubes, the target material usually used is molybdenum ($Z = 42$). The characteristic peaks at 17 and 19 keV are reported to contribute about 25% of the photon flux, the remainder being a continuum of energies (14). Other investigators (15) have experimented with different target-filter materials (ie, molybdenum

Index terms: Breast radiography, technology, 00.119 • Phantoms • Synchrotron

Abbreviations: ACR = American College of Radiology, NSLS = National Synchrotron Light Source.

Radiology 1996; 200:659–663

¹ From the Department of Radiology, University of North Carolina, Chapel Hill, NC 27599 (R.E.J., D.W., E.P., C.B.); National Synchrotron Light Source, Brookhaven National Laboratory, Upton, NY (W.C.T., L.D.C., F.A., N.F.G., Z.Z.); Department of Physics, North Carolina State University, Raleigh (D.S.); Illinois Institute of Technology, Chicago (L.D.C.); and Istituto Nazionale de Fisica Nucleare di Trieste and Università di Trieste, Italy (F.A.). From the 1995 RSNA scientific assembly. Received November 28, 1995; revision requested January 23, 1996; revision received April 8; accepted April 22. Supported in part by National Institutes of Health grant no. RO1 CA60193 and the Department of Radiology, University of North Carolina; work at the National Synchrotron Light Source was supported by the U.S. Department of Energy under contract no. DE-AC02-76CH00016. Address reprint requests to R.E.J.

© RSNA, 1996

target-molybdenum filter, Mo-Mo; molybdenum target-rhodium filter, Mo-Rh; and rhodium target-rhodium filter, Rh-Rh) to improve the image contrast of the dense breast. However, there are trade-offs in contrast as the effective energies are increased for better penetration of dense breast tissues. Inherent in the geometry of the conventional x-ray image is degradation of the image by scattered radiation.

The key features of a synchrotron radiation beam of x rays are (a) the energy spectrum is smooth and continuous from the far infrared to the hard x-ray ends of the spectrum, (b) the intensities are orders of magnitude higher than conventional x-ray tube sources at the energies used for mammography (16–20 keV), (c) perfect crystal optics allow the selection of any energy with very high monochromaticity (bandwidths less than 10 eV at 10 keV), (d) the beams are planar fan beams with extremely high inherent collimation of a few tenths of a milliradian—ideal for line-scan, low-scatter imaging, (e) polarization of the beam is intrinsic in the plane of the storage ring and can be used in certain imaging modalities, and (f) the fan beams can be very wide and can be scanned vertically by scanning optics, or the sample can be scanned through the beams. Thus, from a theoretic perspective, the synchrotron provides the ideal x-ray imaging source particularly for imaging of soft tissues such as the breast.

A small number of experimenters have explored the use of monoenergetic x rays for medical imaging other than mammography (16–18). Carroll et al (19) have shown that there are statistically significant differences in attenuation between normal and cancerous tissues for monoenergetic x rays in the range of 14 to 18 keV. Boone and Seibert (20) did a computer simulation to compare the performance of monoenergetic x rays with that of polyenergetic x rays from tungsten anode systems with regard to imaging. Their conclusion was that monoenergetic sources exhibited a 40%–200% improvement in tissue contrast when imaging the chest with different contrast targets. Admittedly, soft-tissue contrast benefited the least. Burattini et al (21,22) recently published their work with use of synchrotron radiation to image both breast phantoms and specimens. They conclude that the images obtained with monoenergetic x rays have higher contrast, better resolution, and similar, or less, radiation dose than that of conventional

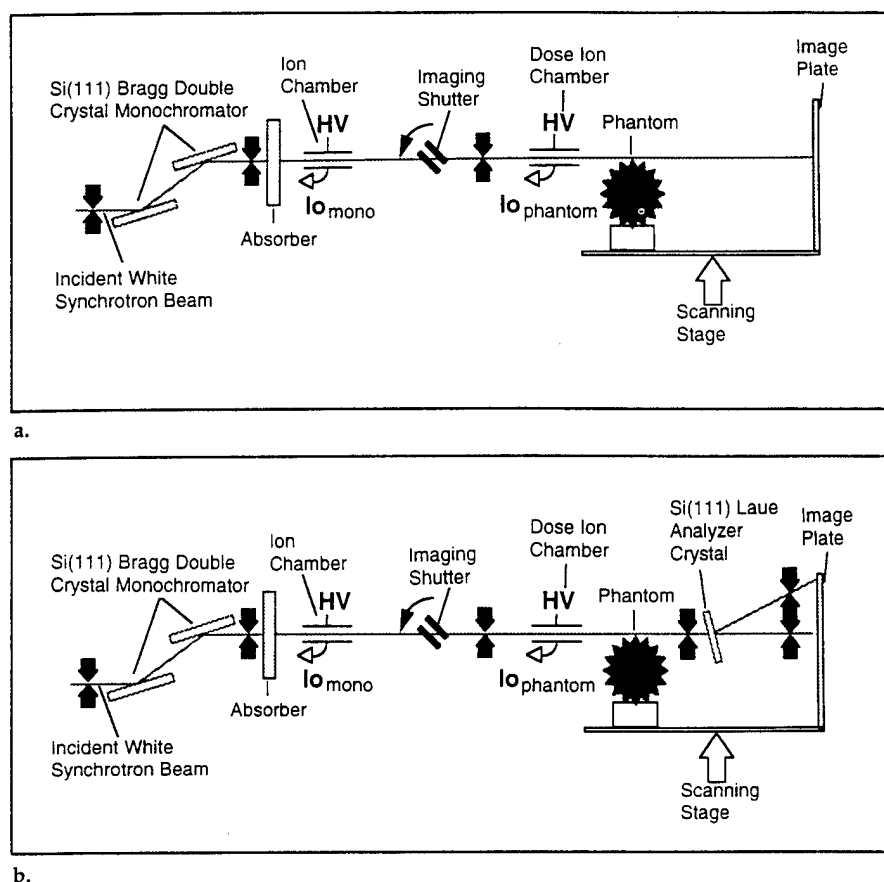


Figure 1. Schematic diagram of the experimental setup used for the preliminary mammography experiments at the NSLS on beam line X27C. (a) Experimental arrangement for imaging the transmitted x-ray beam. (b) Addition of the "analyzer" crystal to obtain simultaneously diffracted and directly transmitted images.

polyenergetic x-ray images. Recently, Mantykentta-Pramanick and Carr (unpublished data, 1996) made calculations showing that there is improvement in contrast and signal-to-noise ratio on monoenergetic images that leads to improved resolution of microcalcifications. The results of our preliminary experiments (23) indicate that we could obtain image contrast somewhat superior to that from conventional x-ray images, but due to instrumentation problems, we had very noisy images with streaking due to nonuniform transport in the vertical direction and nonuniform intensity in the horizontal direction due to impurity buildup on the beam port beryllium window. In the current study, we used a dual-crystal monochromator, instead of the single-crystal monochromator, an improved sample transport system, and a cleaned beam port window.

MATERIALS AND METHODS

During the past year, we embarked on a pilot project with use of a monoenergetic x-ray beam from the X27C beamline at the National Synchrotron Light Source (NSLS),

Brookhaven National Laboratory, to explore the potential of monoenergetic photons for mammographic imaging. The following is a summary of our experience to date.

Monochromator-Beam Scanning System

Figure 1 shows the experimental apparatus and setup used in the preliminary experiments. The monochromatic beam is produced by a double crystal Si-111 Laue monochromator. This monochromator produces a beam with a bandwidth of about 5–10 eV in the energy range used here (16–24 keV). The energy is set by the angle the crystal makes with the incident synchrotron beam (the Bragg angle). The vertical position of the beam is essentially fixed over the small energy range used in these experiments, thus shielding and component alignment do not have to change when the energy is changed. Changing energies is accomplished by driving the angle of the monochromator to the Bragg angle and adjusting the second crystal to give a maximum response. The energy calibration of the monochromator is set by measuring the K-absorption edges of materials such as molybdenum. A beam collimator is placed at the exit of the monochromator to shield against stray radiation,

Table 1
Percentage of Contrast Measured for a 1-mm-thick Lucite Disk in the Contrast-Detail Phantom with Monoenergetic X Rays

Energy (keV)	Thickness* (mm)	Percentage of Contrast	
		Calculated	Measured
17	65	8.9	8.4
18	55	7.9	7.8
19	65	6.9	6.5
20	65	6.4	6.0
22	75	5.4	5.1
24	95	4.6	4.3

Note.—For the well-collimated, monoenergetic synchrotron radiation beam, which has minimal scatter, contrast is independent of phantom thickness.

* Total thickness of Lucite in the photon beam including the 15-mm thickness of the contrast-detail phantom.

Table 2
Percentage of Contrast Measured for a 1-mm-thick Lucite Disk in the Contrast-Detail Phantom with Polyenergetic X Rays

Peak Kilovoltage	Phantom Thickness (mm)	Percentage of Contrast
24	15	7.8
25	45	6.6
30	75	4.5

another slit is located approximately 110 cm in front of the object to be imaged, and a final slit between the object and the imaging plate serves as an antiscatter slit. Because of the high beam intensity, an aluminum absorber is placed in the monochromator beam to reduce the intensity to a level that can be handled by the detector after the beam has passed through the phantom. It is necessary to attenuate the beam by a factor of more than 100. This was accomplished by using the absorber and by working with a vertical beam size of 0.5 mm. The overall length of the system from monochromator to detector plate is 2.8 m. To form an image, the image plate and the object are scanned through the beam. The total scan field is 85 × 85 mm. This is large enough to image phantoms and tissue samples. The drive system is a stepping motor translation stage with a speed that is varied under computer control to limit the radiation dose to the detector to a predetermined level.

The Laue crystal analyzer is a thin Si-111 crystal placed in the beam between the object being imaged and the imaging detector. A portion of the beam is diffracted and imaged on the image receptor. The importance of the Laue-diffracted image is that it is essentially free of scatter from the sample. That is because the scattered x rays are at lower energy and travel in directions different from that of the primary monochromator beam. The scattered rays

are not diffracted by the Laue crystal, which is set at the Bragg angle for the primary beam energy and direction. The Laue crystal analyzer is thus an ideal scatter rejection optic. Since the Laue analyzer also transmits a fraction of the incident beam, a nondiffracted image is obtained simultaneously on the imaging receptor.

Two NSLS-design ion chambers that are placed in the beamline are used to determine the dose to the sample (or entrance dose). Although the chambers perform close to the theoretic limit in their response, initial experiments were performed to verify the response by using thermoluminescent dosimeters. The first ion chamber (in front of the imaging shutter) measures the strength of the monochromatic beam. The experiment control computer calculates the proper rate of vertical translation of the sample for a predetermined exposure to the image detector on the basis of the measured monochromatic beam intensity. The second ion chamber is behind the slits and directly in front of the sample. Since it accepts all of the beam that actually strikes the sample, the second ion chamber is used, along with the known translation rate, to calculate the actual exposure dose to the sample.

Detectors

The image detector used to obtain digital image data is a model STIII photostimulable storage phosphor plate (Fuji Medical Systems, Stamford, Conn). This is a high-sensitivity plate and the only one that could be read with the available reader, model BAS 2000 (Fuji Medical Systems). A manual "latitude" control allowed four possible selections, from "1," which uses the 10 bits of acquired data to display a narrow window of the recorded intensity range, to "4," which is a wide window and displays the entire range of recorded intensities. A sensitivity of 400 was used to read the plates since this is the lowest sensitivity available on the reader. The plates are read out at a 2,560 × 2,048 matrix (100 mm per pixel) resolution. Images are also recorded with a conventional mammographic cassette with mammographic film (UM MA-HC; Fuji Medical Systems) and a mammographic screen (UM Fine; Fuji Medical Systems). The films are processed by using a tabletop film processor (Film Quick-CT; Imaging Marketing, Mesa, Ariz). Film speed and contrast are monitored sensitometrically. The conventional mammography system is a model Mammat 2 (Siemens Medical Systems, Iselin, NJ). Fuji mammography film (UM MA-HC) and screen (UM Fine) are used as a Bucky grid with a 4:1 grid ratio and 27 lines per centimeter. Processor chemistry used was 3-7-90 type S developer (Picker International, Cleveland, Ohio) and Spectre fixer (Picker International).

Samples

For quantitative measurements of contrast, a model 180 contrast-detail phantom

(Gammex RMI, Middleton, Wis) is used that has target Lucite disks with thicknesses varying from 1.0 to 0.06 mm and diameters varying from 7.0 to 0.3 mm machined into a Lucite substrate. The phantom is 15-mm thick; to obtain greater thickness, Lucite slabs are added to the phantom. For subjective assessment, the American College of Radiology (ACR) phantom and a Gammex RMI model 165 anthropomorphic phantom were used. Only one real-tissue sample so far in these preliminary studies has been imaged. Since the tissue sample had no abnormalities, its only value was to confirm that a high-quality synchrotron image of real tissue could be obtained. Future plans are to acquire tissue samples with tumors.

Contrast

For the images recorded on the Fuji plate, radiation exposure to the plate is controlled by adjusting the scan speed of the phantom and detector system to maintain a consistent exposure of about 1.3 $\mu\text{C/kg}$ (5 mR) to the detector. From the digital information recorded with the Fuji plate, contrast is calculated of the largest diameter 1-mm-thick target disk in the contrast-detail phantom. Image contrast is defined by the following equation: $(I_t - I_s)/I_s$, where I_t is the average intensity within the image of the 1-mm-thick disk and I_s is the average intensity of the immediate surround. Thus, percentage of contrast = $100(I_t - I_s)/I_s$. The standard deviation for the percentage of contrast measurements is less than or equal to $\pm 0.06\%$. For the images obtained from the conventional x-ray machine, the phantom was imaged at three different thicknesses with use of automatic exposure control. The average optical density of the film images was 1.5 for the 15- and 45-mm phantoms and 1.25 for the 75-mm phantom. The images were digitized with a Lumiscan model 100 film digitizer (Lumisys, Sunnyvale, Calif) at 50 μm per pixel and 12 bits grey scale. From the digital data, contrast was calculated by using the same methods described above.

Dose

The mean glandular dose was calculated, in the case of the monoenergetic images, by using the ion chamber to measure the entrance exposure dose at each phantom thickness and each energy. We assumed 50% adipose and 50% glandular tissue and simple exponential attenuation in the tissue by using the model outlined in NCRP Report no. 85 (24). An estimate of the mean glandular dose for the polyenergetic source was made by measuring the entrance exposure dose to each of the three different thickness phantoms, measuring the half-value layer, and using the values for mean glandular dose per unit exposure in air versus the breast thickness published in table 3.3 of NCRP Report no. 85 (24). The values from table 3.3 extend from 30- to 70-mm thickness. To estimate the dose at 15 and 75 mm, a smooth curve

was fit to the data and extrapolated to the thicknesses used in our experiments. The error due to extrapolation could contribute on the order of a 10% error in the calculated mean glandular dose. However, we suggest that these calculated dose values give a reasonable estimate for comparison purposes.

RESULTS

The results of the contrast measurements are shown in Tables 1 and 2. Clearly, the contrast decreases with increasing energy, as would be expected. The average difference of about 0.3% less in the measured value compared with the calculated value could be due to the presence of some scatter in the actual image not considered in the calculated contrast, or more likely, the detailed atomic composition of the actual phantom differing from that assumed for the calculation. The fact that the beam is narrow, does not spread over distance, and is collimated before and after the target material means that there is very little scatter within the beam. A qualitative estimate of the scatter was made by visually comparing the image from the Laue analyzer with the nonanalyzed image; this estimate indicated that very little of the nonanalyzed beam was due to scatter. A quantitative measurement was not done in this preliminary experiment but will be carried out in later experiments. Without scatter and with a monoenergetic beam, the contrast is independent of phantom thickness. Therefore, with the monoenergetic source, one has the opportunity to customize the energy for imaging different breast thicknesses to obtain the highest contrast image.

A comparison of the mean glandular dose from the monoenergetic source shows that as the energy increases the dose decreases (less absorption of the photon beam) (Table 3). For any given energy, the dose increases as the target tissue thickness increases. In general, the radiation dose from the two sources was similar (Table 4).

A qualitative assessment of the images from the ACR phantom was made by scoring the images according to ACR criteria. The synchrotron images in the energy range of 16–18 keV typically show an increase of one-half to one additional target detected in each category compared with images from a conventional system. An example is the ACR phantom imaged at 16 keV shown in Figure 2. The use of the Laue crystal analyzer was first postulated for scatter rejection. How-

ever, during the course of these preliminary experiments, it became evident that another property of the optical arrangement is potentially even more important. When an optical beam traverses a transparent medium that contains refractive index inhomogeneities (and, therefore, gradients), it will be deviated through an angle. The deviation is based on the concept of schlieren optics in which refractive index inhomogeneities can be quantified and imaged. The schlieren imaging system depends on an optical element that modulates the transmitted intensity according to the angle that a given ray makes with an undeviated ray. In the case of x rays, a Laue crystal can be used as the optical element.

In the x-ray energy range, there are no completely transparent objects, so the refractive index effects cannot be determined independently from absorption effects. In the present experimental setup, the problem was solved by simultaneously acquiring a transmitted beam image and a diffracted beam image on the image plate. A simple mathematic transform was then applied to the images to produce an image of the refractive index gradient and an image of the absorption. The refractive index gradient image is extremely sensitive to boundaries between materials (high refractive index gradients). This property could be used as a sensitive indicator of boundaries in tissues. Preliminary experiments have confirmed this effect and the interpretation (25). Future experiments are planned to optimize the sensitivity and imaging energy for mammographic applications.

DISCUSSION

On the basis of preliminary experiments with synchrotron-generated monoenergetic radiation, we have shown increased contrast in phantom images. As expected, the lower the energy used, the better the contrast. The advantage of the tunable energy from the monochromator is that one can use the lowest feasible energy for a given thickness of tissue.

Because of the geometry of the photon beam, and the fact that the energy flux is considerably higher than that from conventional x-ray tubes, the limiting factor is the radiation dose to the breast. We have shown that the radiation dose from monoenergetic photon beams is comparable to the dose from conventional x-ray systems, and for thin samples, in which one can use the lowest mono-

Table 3
Calculated Mean Glandular Dose from the Monoenergetic Source

Phantom Thickness (mm)	Energy (keV)				
	17	18	19	20	22
15	20	18	17	16	15
45	181	123	85	72	51
75	2,271	1,059	508	367	125

Note.—Glandular doses are in centigray. Monoenergetic x rays were normalized to an exposure dose of 2.1 $\mu\text{C/kg}$ (8 mR) to the film.

Table 4
Mean Glandular Dose from the Polyenergetic Source

Peak Kilovoltage	Phantom Thickness (mm)	Mean Glandular Dose (cGy)
24	15	22
25	45	107
30	75	373

Note.—Polyenergetic x rays were normalized to an exposure dose of 2.1 $\mu\text{C/kg}$ (8 mR) to the film.



Figure 2. Image of the ACR phantom taken with 16-keV monoenergetic x rays from the synchrotron. Noise streaks are from contamination on the beryllium window and mechanical artifacts from the drive system.

chromatic energy, the contrast could be improved with reduced radiation dose. As the breast thickness increases, the radiation dose in all cases increases. With the monoenergetic source, one can increase energy to compensate for thickness but with a decrease in radiation dose while maintaining the same exposure to the detector.

There is much room for improvement in the imaging system used. It is necessary to reduce the artifactual noise content of the images by making improvements in the mechanical transport system and the nonuniformities in the beam due to contamina-

tion of the beryllium window. The next step is to more fully explore the use of the "analyzer" crystal and to use tissue samples with known cancers. ■

References

1. Shapiro S, Venet W, Strax P, et al. Ten to fourteen year effect of screening on breast cancer mortality. *J Natl Cancer Inst* 1982; 69:349-355.
2. Tabar L, Fagerberg G, Duffy SW, et al. The Swedish two county trial of mammographic screening for breast cancer: recent results and calculation of benefit. *J Epidemiol Community Health* 1989; 43:107-114.
3. Shapiro S, Venet W, Strax P, et al. Ten to fourteen year effect of screening. In: Shapiro S, Venet W, Strax P, Venet L, eds. *Periodic screening for breast cancer*. Baltimore, Md: Johns Hopkins Press, 1988.
4. Baker LH. Breast cancer detection demonstration project: five-year summary report. *CA* 1982; 32:194-225.
5. Saltzstein SL. Potential limits of physical examination and breast self-examination in detecting small cancers of the breast: an unselected population-based study of 1302 cases. *Cancer* 1984; 54:1443-1446.
6. Fletcher SW, O'Malley MS, Bunce LA. Physicians abilities to detect lumps in silicone breast models. *JAMA* 1985; 253:2224-2228.
7. Fisher B, Slack NH, Bross I. Cancer of the breast: size of neoplasm and prognosis. *Cancer* 1969; 24:1071.
8. Wanebo HJ, Huvos AG, Urban JA. Treatment of minimal breast cancer. *Cancer* 1974; 33:349-357.
9. Gallager HS, Martin JE. An orientation to the concept of minimal breast cancer. *Cancer* 1971; 28:1519-1526.
10. Frazier TG, Copeland EM, Gallager HS, et al. Prognosis and treatment in minimal breast cancer. *Am J Surg* 1977; 133:697-701.
11. Stomper PC, Gelman RS. Mammography in symptomatic and asymptomatic patients. *Hematol Oncol Clin North Am* 1989; 3:611-640.
12. Rosenthal MS, Sashin D, Herron J, et al. Evaluation of a moving slit technique for mammography. *Proc SPIE* 1991; 1443:132-138.
13. Maidment ADA, Yaffee MJ. Scanned-slot digital mammography. *SPIE* 1990; 1231:316-326.
14. Boone JM, Seibert JA. A comparison of mono- and poly-energetic x-ray beam performance for radiographic and fluoroscopic imaging. *Med Phys* 1994; 21:1853-1863.
15. Wu X, Gingold EL, Tucker DM, et al. X-ray spectral effects on contrast and dose in mammography (abstr). *Med Phys* 1994; 21:1006.
16. Thomlinson W. Medical applications of synchrotron radiation. *Nucl Instr Meth* 1992; 319:295-304.
17. Luccio A. Synchrotron radiation and biomedical imaging. *Phys Med* 1988; 4(suppl 1):87-117.
18. Mori H, Hyodo K, Tobita K, et al. Visualization of penetrating transmural arteries in situ by monoenergetic synchrotron radiation. *Circulation* 1994; 89:863-871.
19. Carroll F, Waters J, Andrews W, et al. Attenuation of monochromatic x-rays by normal and abnormal breast tissues. *Invest Radiol* 1994; 29:266-272.
20. Boone JM, Seibert JA. Monte Carlo simulation of the scattered radiation distribution in diagnostic radiology. *Med Phys* 1988; 15:713-720.
21. Burattini E, Gambaccini M, Indovina PL, et al. Synchrotron radiation: a new source in x-ray mammography. *Radiol Med* 1992; 4:181-188.
22. Burattini E, Cossu E, Di Maggio C, et al. Mammography with synchrotron radiation. *Radiology* 1995; 195:239-244.
23. Johnston RE, Washburn D, Pisano P, et al. Preliminary experience with monoenergetic photon mammography. *Proc SPIE* 1995; 2432:434-441.
24. Mammography: a user's guide. NCRP Report no. 85. Washington, DC: Government Printing Office, 1986.
25. Chapman D, Thomlinson W, Arfelli F, et al. Mammography imaging studies using a Laue crystal analyzer. *Rev Sci Instrum* (in press).

Appendix

A.5

Chapman D, Thomlinson W, Arefeli F, Gmur N, Zhong Z, Menk R, Johnston E, Washburn D, Pisano E, Sayers D. "Mammography Imaging Studies Using a Laue Analyzer Crystal". Rev.Sci. Instrum. 1996: 67(9), CD-ROM.

Mammography imaging studies using a Laue crystal analyzer

D. Chapman (1), W. Thomlinson (2), F. Arfelli (2,4), N. Gmür (2), Z. Zhong (2), R. Menk (2), R.E. Johnson (3), D. Washburn (3), E. Pisano (3), and D. Sayers (5)

(1) CSRR, Illinois Institute of Technology, 3301 S. Dearborn, Chicago, IL 60616 USA

(2) National Synchrotron Light Source, Brookhaven National Laboratory, Upton, NY 11973 USA

(3) University of North Carolina, Chapel Hill, NC 27599 USA

(4) INFN di Trieste and Università di Trieste, Trieste, Italy

(5) North Carolina State University, Raleigh, NC 27695 USA

(Presented on 18 October 1995)

Synchrotron-based mammography imaging experiments have been performed with monochromatic x-rays in which a Laue crystal placed after the object being imaged has been used to split the beam transmitted through the object. The X27C R&D beamline at the National Synchrotron Light Source was used with the white beam monochromatized by a double crystal Si(111) monochromator tuned to 18keV. The imaging beam was a thin horizontal line approximately 0.5mm high by 100mm wide. Images were acquired in line scan mode with the phantom and detector both scanned together. The detector for these experiments was an image plate. A thin Si(111) Laue analyzer was used to diffract a portion of the beam transmitted through the phantom before the image plate detector. This "scatter free" diffracted beam was then recorded on the image plate during the phantom scan. Since the thin Laue crystal also transmitted a fraction of the incident beam, this beam was also simultaneously recorded on the image plate. The imaging results are interpreted in terms of an x-ray schlieren or refractive index inhomogeneities. The analyzer images taken at various points in the rocking curve will be presented. © 1996 American Institute of Physics.

I. INTRODUCTION

Synchrotron-based mammography imaging experiments have been performed with monochromatic x-rays in which a Laue crystal placed after the object being imaged has been used to split the beam transmitted through the object. The imaging beam was a thin horizontal line approximately 0.5mm high by 100mm wide. Images were acquired in line scan mode with the phantom and detector both scanned together. The detector for these experiments was an image plate. A thin Si(111) Laue analyzer was used to diffract a portion of the beam transmitted through the phantom before the image plate detector. This "scatter free" diffracted beam was then recorded on the image plate during the phantom scan. Since the thin Laue crystal also transmitted a fraction of the incident beam, this beam was also simultaneously recorded on the image plate.

The imaging results are interpreted in the context of schlieren optics in which refractive index inhomogeneities of a transparent media can be quantified and imaged. These techniques rely on an optical element that modulates the transmitted intensity according to a deviation angle of rays through a media. The crystal analyzer in the x-ray imaging system is the equivalent of such an element.

The X27C R&D beamline at the National Synchrotron Light Source (NSLS) was used for these experiments. This is a large general purpose white beam hutch. A double crystal Bragg case monochromator was installed in the hutch to prepare a wide horizontal imaging beam at a photon energy of 16-25keV. An energy of 18keV was chosen for these experiments. This imaging beam was then monitored by an ionization chamber to measure the skin entry dose to the various phantoms used to characterize the imaging system.

Plastic absorbers were used to control the dose to the phantom. A fast shutter system was used to begin and end the exposure on the image plate. The shutter was opened when the scanning stage was at a constant velocity and was closed at the end of the scan range before the stage was slowed to a stop. The dose was controlled by a combination of incident beam plastic absorbers and the scanning speed. The phantom thickness was typically in the 4-8cm thickness range to simulate the attenuation of compressed breast tissue as would be the case in a conventional mammographic imaging procedure.

Exposures were made onto a 20×25cm image plate and were subsequently read on a Fuji BAS 2000 reader. Typical reading parameters were a sensitivity of 1000, a latitude of 4, and a resolution size of 100 μ m.

Imaging experiments were performed with and without a crystal analyzer. The arrangements are shown in Figure 1. Only the experiments with the analyzer are presented here. Nonanalyzer results will be discussed elsewhere.¹ The top arrangement in the figure is the nonanalyzer setup, while bottom shows the setup with the analyzer. The analyzer was placed in the beam after it had passed through the phantom. The crystal was set in the Laue arrangement in which the beam is incident on one side of the crystal plate and the diffracted beam emerges from the other side and was set in the parallel crystal geometry with respect to the monochromator. The crystal was approximately one absorption length thick ($\mu t=1.04$, $t=0.74$ mm) at the 18 keV imaging energy and had an asymmetry angle of 26° . This is the thickness range referred to as the thin crystal Laue case in dynamical theory.² Figure 2 shows the theoretical and measured relative intensities from the crystal. Note the relatively large

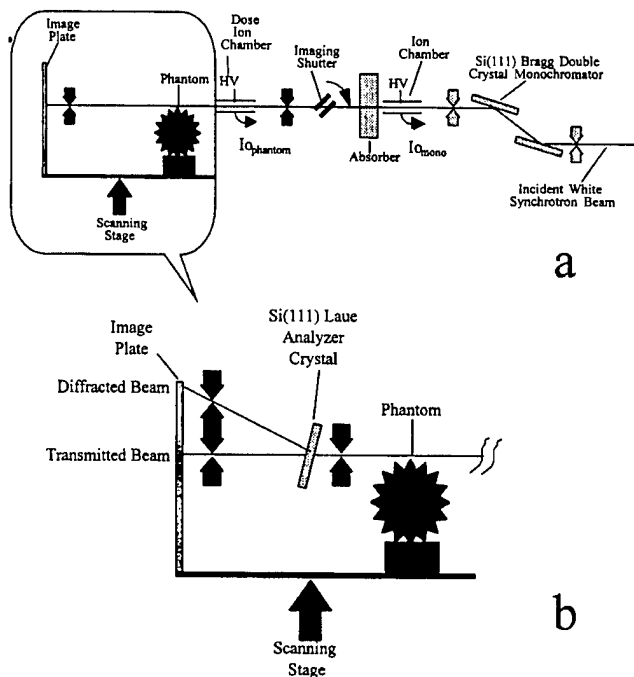


FIG. 1. Schematic of experimental setup in the X27C hutch. a) shows the arrangement without the analyzer crystal, b) shows additions to the setup for imaging with the Laue crystal analyzer.

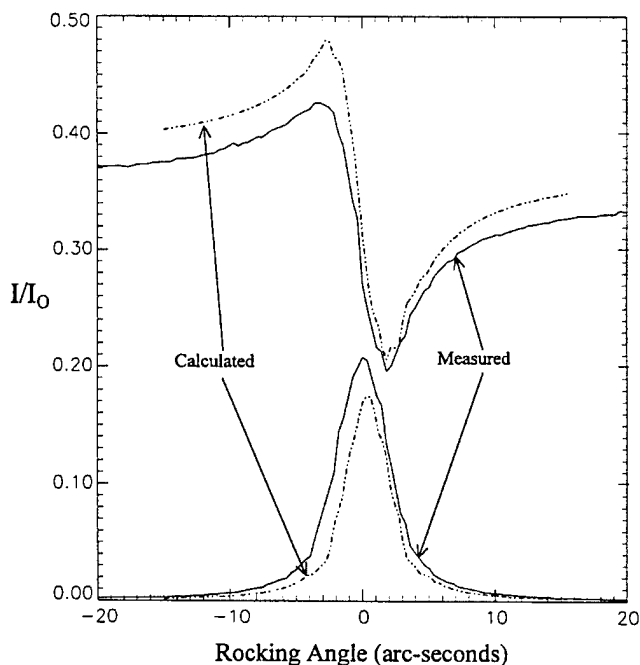


FIG. 2. Measured and calculated Laue crystal rocking curves. Measured rocking curve obtained with ionization chambers at the location of the imageplate. Calculated curves based on a Si(111) Laue crystal 0.7mm thick with an asymmetry angle of 26° at 18keV photon energy.

transmission directly through the crystal. The agreement between the calculation and measurement is quite good.

Since the crystal is semitransparent, this feature allows two simultaneous exposures to be performed on the image plate. The separation between the analyzer and the image plate was

set so that these two images could be recorded over the scanning range without overlap or spilling over the edges of the image plate. Thus two images were recorded in each scan; a 'direct' beam image and a diffracted beam image.

There are three regions of particular interest when using such an analyzer crystal to create images. Those regions are the left and right slopes of the diffracted beam rocking curve and the center peak position. As can be seen from the complex shape of the transmitted beam rocking curve, the low and high angle sides of the diffracted beam rocking curve are not equivalent for the transmitted beam. The half intensity point on the low angle side corresponds to a peak in the transmitted beam (the anomalous transmission side), while the half intensity point on the high angle side corresponds to a minima in the transmission (anomalous absorption side).² The peak of the diffracted beam corresponds to the high slope region of the transmission.

This behavior results in various imaging possibilities depending on the setting of the analyzer. Images were acquired (as much as the stability of the analyzer would allow) at the following points in the diffracted beam rocking curve: at 1/2 peak intensity on the low and high angle side and at the peak.

These images for both the diffracted and transmitted beams are interpreted in the context of these rocking curves (i.e., their intensity values and the dependence of the intensity vs angle).

II. ANALYSIS

The transmitted and diffracted beam images are a composite of two (sometimes competing) effects: absorption and refraction. The refractive part is based on calculating the very small angle deflections in the media due to thickness, density, or material composition variations. The propagation of light through such an inhomogeneous media is called "schlieren". These angle deflections alter the intensity transmitted or diffracted by the analyzer according to the rocking curve. This is very similar to an optical system used to visualize and measure gradients in the refractive index, Töpler's schlieren method.³

The optical schlieren effect results when there is an effective gradient in the refractive index in a transparent media. The complication in the x-ray regime is that there will always be an attenuation of the beam as it traverses the object.

The gradient direction, in this case, is in the vertical direction or the projection of the diffraction vector onto the plane perpendicular to the transmitted beam. This direction is referred to as z . The beam path direction through the media is the x direction. Note that the imaging plane is the y - z plane. Assume that the media is composed of a single material with a varying refractive index and thickness, then the schlieren angle, δ , is:

$$\delta_z = \int_0^{t(y,z)} \frac{1}{n(x,y,z)} \frac{\partial n(x,y,z)}{\partial z} dx \quad (1)$$

The refractive index in the x-ray energy range is slightly less than one and is given approximately by:⁴

$$n(x, y, z) = 1 - \frac{r_0 \lambda^2 Z}{2\pi V}(x, y, z), \quad (2)$$

where r_0 is the classical electron radius (2.81×10^{-13} cm), λ is the x-ray wavelength, and Z is the number of electronic charges in the volume V . The latter quantity, Z/V , depends on the spatial coordinates, x , y and z , and is related to the material density, ρ , by $Z/V = (Z/A)\rho/m_{AMU}$, where A is the atomic number and m_{AMU} is the mass of a nucleon (1.66×10^{-24} g). Then the schlieren angle is approximately:

$$\delta_z \equiv -\frac{r_0 \lambda^2}{2\pi m_{AMU}} \int_0^{t(y,z)} \frac{Z}{A}(x, y, z) \frac{\partial \rho(x, y, z)}{\partial z} dx, \quad (3)$$

where the $1/n(x, y, z)$ term has been approximated by one to keep terms to first order in ρ . If equation 3 is simplified by assuming that the quantity Z/A is a constant and that all of the spatial dependence is in the density and thickness and that the gradient of density is constant with x , then the equation can be rewritten as:

$$\begin{aligned} \delta_z &\equiv -\frac{r_0 \lambda^2}{2\pi m_{AMU}} \frac{Z}{A} \frac{\partial \rho t(y, z)}{\partial z} \\ &\equiv -(2.69 \times 10^{10} \text{ cm/g}) \frac{Z}{A} \lambda^2 \frac{\partial \rho t(y, z)}{\partial z} \end{aligned} \quad (4)$$

This equation gives the deviation angle of the transmitted beam through the object being imaged. In practice this angle is too small ($\delta \approx 10^{-6}$ radian) to result in spatially displaced beams in an image given the source size at the NSLS. Interference of the refracted beam with the direct beam would not be visible in this measurement.⁵ The distance from the phantom to the image plate in our experiments is approximately 1m. This displacement is expected to be then $\sim 10^{-5}$ m or ~ 10 μ m. This angle is however sufficient to cause a intensity change with the analyzer in place. Angles in this range (10^{-6} radian, 1 μ radian or 0.2 arc-seconds) can result in intensity variations of several percent (see the rocking curve in Figure2).

If the special case of a fixed density object with just thickness variations, a mean density of water (1 g/cm³), an imaging energy of 18 keV and an effective Z/A of 0.5 is considered, then equation 4 can be further reduced to:

$$\delta_z \equiv -(0.64 \mu\text{radians}) \frac{\partial t(y, z)}{\partial z}. \quad (5)$$

This gives an indication of the scale of the deviation angles resulting from a thickness gradient.

The schlieren deflection angle results in a modulation of intensity since the reflectivity and transmissivity of the Laue crystal is a function of the incident beam angle.

The intensity is also affected by the normal transmission through the object via:

$$\begin{aligned} \frac{I}{I_0} &= \exp \left\{ - \int_0^{t(y,z)} \frac{\mu}{\rho}(x, y, z) \rho(x, y, z) dx \right\} \\ &\equiv \exp \left\{ - \frac{\mu}{\rho} \rho t(y, z) \right\}, \end{aligned} \quad (6)$$

where μ/ρ is the mass absorption coefficient and ρ the mass density of the material. Therefore the image recorded on the image plate is proportional to:

$$\begin{bmatrix} I_R \\ I_T \end{bmatrix} \equiv I_0 \exp \left\{ - \frac{\mu}{\rho} \rho t(y, z) \right\} \begin{bmatrix} R(\theta_0 + \delta_z) \\ T(\theta_0 + \delta_z) \end{bmatrix}, \quad (7)$$

where I_R and I_T are the diffracted and transmitted beams onto the image plate, respectively, and the analyzer is set to θ_0 relative to the peak position, and δ_z is the schlieren angle. Since the deviation angle, δ_z , is presumed small, the reflectivity and the transmissivity can be expanded as:

$$\begin{bmatrix} R(\theta_0 + \delta_z) \\ T(\theta_0 + \delta_z) \end{bmatrix} \equiv \begin{bmatrix} R(\theta_0) + \frac{\partial R}{\partial \theta} \delta_z \\ T(\theta_0) + \frac{\partial T}{\partial \theta} \delta_z \end{bmatrix}. \quad (8)$$

Substituting equation 8 into equation 7 gives:

$$\begin{aligned} \begin{bmatrix} I_R \\ I_T \end{bmatrix} &\equiv I_0 \exp \left\{ - \frac{\mu}{\rho} \rho t(y, z) \right\} \\ &\times \left\{ \begin{bmatrix} R(\theta_0) \\ T(\theta_0) \end{bmatrix} + \begin{bmatrix} \frac{\partial R(\theta_0)}{\partial \theta} \\ \frac{\partial T(\theta_0)}{\partial \theta} \end{bmatrix} \delta_z(y, z) \right\}. \end{aligned} \quad (9)$$

Thus there are two contributions to the intensity in the diffracted and transmitted beams through the analyzer crystal: 1) the "normal" transmission given by the absorption coefficient and modified by the transmissivity and reflectivity of the analyzer, and 2) the schliere given by the product of the normal transmission, the slope of the reflectivity or transmissivity curve, and the schlieren angle.

This equation can be easily solved for the absorption map, $\rho t(y, z)$, and the schlieren angle map, $\delta_z(y, z)$:

$$\rho t(y, z) = -\frac{1}{\frac{\mu}{\rho}} \ln \left\{ \frac{I_T(y, z) \frac{\partial R}{\partial \theta}(\theta_0) - I_R(y, z) \frac{\partial T}{\partial \theta}(\theta_0)}{I_0 \left[T(\theta_0) \frac{\partial R}{\partial \theta}(\theta_0) - R(\theta_0) \frac{\partial T}{\partial \theta}(\theta_0) \right]} \right\} \quad (10)$$

$$\delta_z(y, z) = \frac{I_R(y, z) T(\theta_0) - I_T R(\theta_0)}{I_T(y, z) \frac{\partial R}{\partial \theta}(\theta_0) - I_R(y, z) \frac{\partial T}{\partial \theta}(\theta_0)} \quad (11)$$

* These equations will now be used to interpret images acquired with the Laue analyzer.

III. RESULTS

The use of equations 10 and 11 requires that the rocking curve angle, θ_0 , at which the images were taken is known. This was determined by setting the analyzer angle to achieve the expected ionization chamber reading for the diffracted beam. This procedure could establish the region on the rocking curve but, due to instrumental drifts occurring in the time between the tuning of the analyzer and the acquisition of image data, could not be relied upon to give a precise rocking angle, θ_0 . The best estimation of the rocking angle comes from the data from the image plate. There is generally a region of the image that is known to have no structure in the imaging beam. In this region, the schlieren angle must be zero. The rocking angle can be calculated using the reflected and transmitted intensities from the image. This procedure works very well and matched quite closely the desired analyzer setting.

To confirm the refractive index effects, images were acquired of a phantom that had known linear thickness variations, referred to as a "wedge" phantom. A full image of this phantom is shown in Figure 3. The upper image is the diffracted beam image, I_R , and the bottom is the transmitted beam image, I_T . This full image was acquired at the peak of the diffracted beam, i.e., $\theta_0=0$. The sensitivity to a refractive index gradient occurs along a line from the transmitted beam image to the diffracted beam image. A small region of the image was used to confirm a sensitivity to the gradient. This is a region with a Plexiglas sawtooth phantom. This phantom was composed of parallel Plexiglas prisms. These prisms had a profile shown in Figure 4 with a rising thickness gradient of $\tan(60^\circ)=1.73$ and a falling gradient of $\tan(30^\circ)=0.56$. The maximum height of the prisms is 1.14mm with a repeat distance of 2.63mm. Figure 5 is a composite showing the diffracted and transmitted beam images as well as the resulting schlieren angle, δ_z , and thickness, pt , images. These images are taken at three settings of the analyzer corresponding to the locations shown on the rocking curve. The far left set from the low angle side of the rocking curve at $\theta_0=-4.9$ μ rad, the middle set near the peak at $\theta_0=+1.5$ μ rad, and the right set on the high angle side at $\theta_0=+10.7$ μ rad.

Averaged sections of each schlieren angle and thickness images were taken and plotted in Figure 6 along with the expected theoretical values. The expected or theoretical values are based on the material parameters for Plexiglas ($\mu/\rho=0.69$ cm^2/g , $\rho=1.19$ g/cm^3) and the use of equation 6 for the refraction angle.

One noticeable feature in the image as well as the section line plot is that the image taken at the peak has little sensitivity to the gradient. This results from the use of equation 11 in a region where the reflectivity slope can

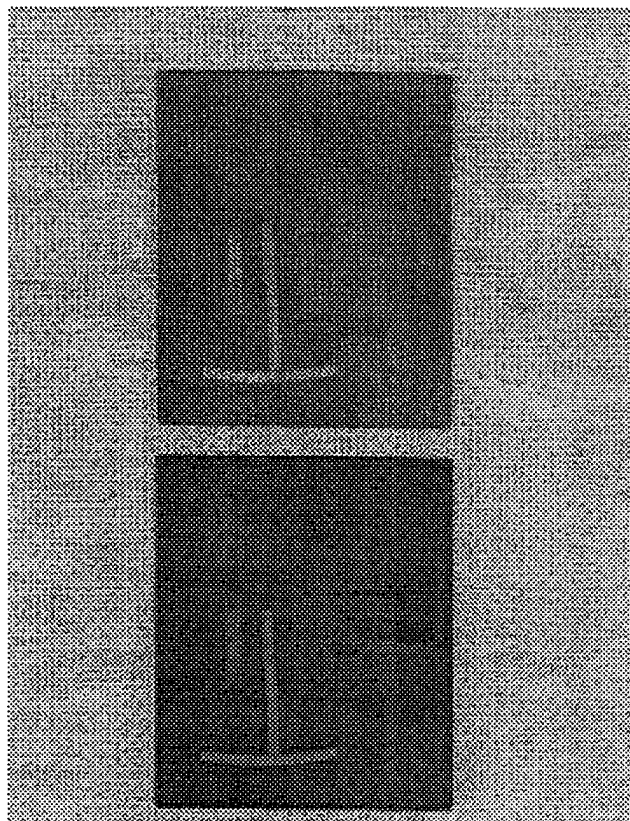


FIG. 3. Image of "wedge" phantom as read from image plate. Upper image is the diffracted beam image; lower image is the transmitted beam image. Image was taken with the analyzer set at the diffraction peak.



FIG. 4. Cross-sectional view of the Plexiglas sawtooth phantom.

change sign. A more complex equation should be used here or a self-consistent solution using the rocking curve. The agreement becomes more tolerable away from the Bragg peak. The best agreement between the measured and expected values occurs for the image taken at -4.9 μ rad below the peak. At this position, the measured Δpt is approximately 25% below the expected value. The schlieren angle has the correct value for the low gradient sides of the prisms at approximately -0.5 μ rad, however, on the high gradient side, the measured angle is approximately 34% below the expected value of 1.3 μ rad.

As was expected for the images taken at the Bragg peak, there may be a failure of the equation to handle the relatively large deviation angles when there are large gradients in the index or material thickness.

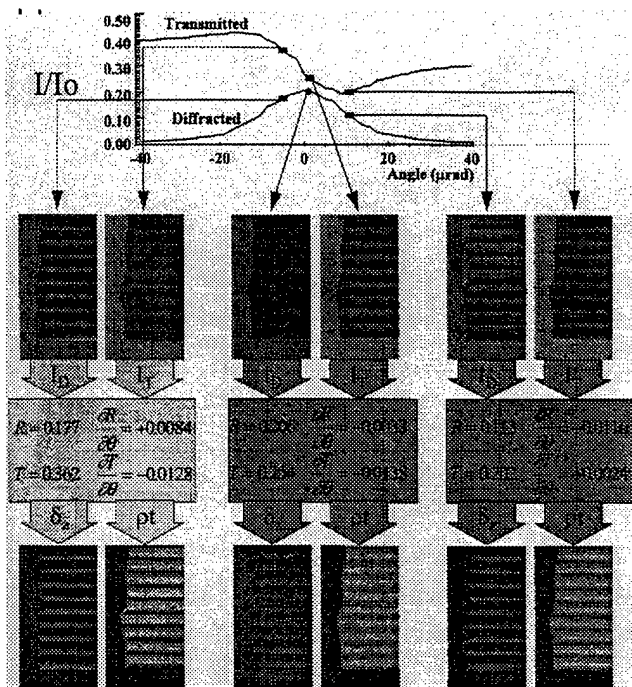


FIG. 5. Composite figure showing a section of the sawtooth phantom acquired at various analyzer angle settings and the δ_z and pt images derived from the measured diffracted, I_d , and transmitted, I_T , beam images. The quantities in the boxes are the reflectivity, transmissivity and their angular gradients required to transform the images. The left image set was taken at $\theta_0 = -4.9 \mu\text{radians}$, the middle image at $\theta_0 = +1.5 \mu\text{radians}$ and the right image at $\theta_0 = +10.7 \mu\text{radians}$.

IV. CONCLUSION

Images of phantoms have been taken of phantoms using a Laue crystal analyzer to create two images of the same object. Approximate equations have been derived to describe these images in terms of the analyzer rocking curve and the object being imaged. These two images can be combined to give an image of the absorption of the object (pt image) and an image of the refractive index gradient or schlieren angle image (δ_z image). The analysis of these images in these terms looks promising. There is satisfactory agreement between the measured and expected thicknesses and refraction angles.

Future measurements are planned to investigate the use of diffraction optics to enhance the features in mammographic imaging.

ACKNOWLEDGMENTS

The authors would like to thank Dr. Jerry Hastings and Dr.D.P. Siddons for many useful discussions regarding the use of an analyzer crystal for imaging and Dr. Siddons for the beam time on the X27C beamline without which these experiments would not have been possible. This work is supported by NIH R01 CA60193, the Dept. of Radiology, UNC and US DOE DE-AC02-76CH00016.

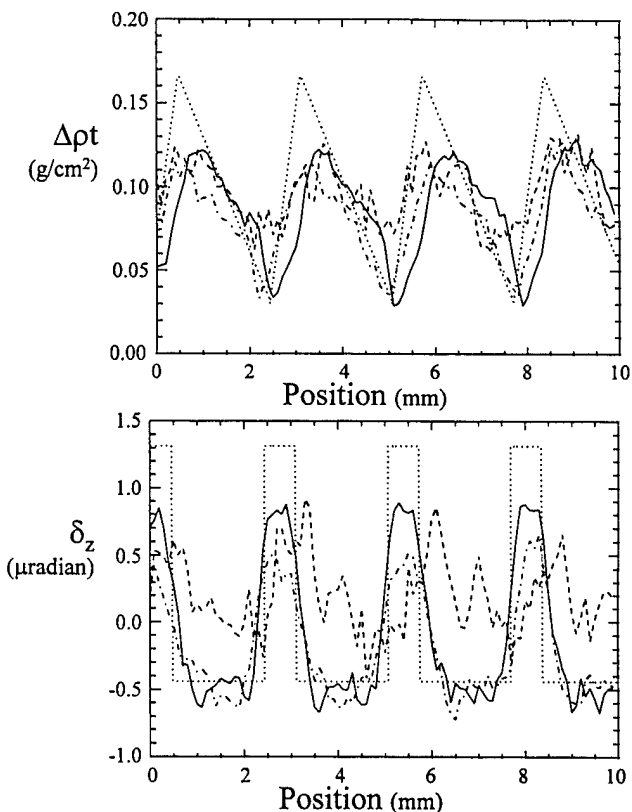


FIG. 6. Averaged line plots of a section of the sawtooth phantom image. The upper plot is the thickness image, Δpt , and the lower plot is the schlieren angle image, δ_z . The dotted line is the expected values based on the dimensions and composition of the phantom. The solid line is the measured value from the data at $\theta_0 = -4.9 \mu\text{radians}$, the dashed line at $\theta_0 = +1.5 \mu\text{radians}$, and the dot-dash at $\theta_0 = +10.7 \mu\text{radians}$.

- 1 N. Gmür, W. Thomlinson, R.E. Johnson, D. Washburn, E. Pisano, F. Arfelli, L.D. Chapman, Z. Zhong, R. Menk, and D. Sayers, A37, these proceedings.
- 2 B.W. Batterman and H. Cole, Rev. Mod. Phys. **36**, 681 (1964).
- 3 c.f. J.R. Meyer-Arendt, *Introduction to Classical and Modern Optics* (Prentice-Hall, Englewood Cliffs, New Jersey, 1972), Section 3.3, p. 315.
- 4 R.W. James, *The Optical Principles of the Diffraction of X-Rays* (Ox Bow Press, Woodbridge, Connecticut 1982), Chapter 2, p. 54.
- 5 C. Raven, A. Snigirev, I. Snigireva, P. Spanne, and A. Suvrov, A35, these proceedings.

Appendix

A.6

Chapman D, Pisano ED, Thomlinson W, Zhong Z, Johnston RE, Washburn D, Sayers D, Malinowska K. Medical applications of diffraction enhanced imaging. *Breast Disease* 1998;10(3,4):197-208.

Medical Applications of Diffraction Enhanced Imaging

D. Chapman^{a,*}, E. Pisano^b,
W. Thomlinson^c, Z. Zhong^c,
R.E. Johnston^b, D. Washburn^b,
D. Sayers^d and K. Malinowska^a

^a CSRRI, Illinois Institute of Technology,
3101 South Dearborn, Chicago, IL 60616,
USA

^b Department of Radiology, University of
North Carolina, Chapel Hill, NC 27599, USA

^c National Synchrotron Light Source,
Brookhaven National Laboratory, Upton, NY
11973, USA

^d Department of Physics, North Carolina
State University, Raleigh, NC 27695, USA

ABSTRACT: We have developed a new X-ray imaging technique, diffraction enhanced imaging (DEI), which can be used to independently visualize the refraction and absorption of an object. The images are almost completely scatter-free, allowing enhanced contrast of objects that develop small angle scattering. The combination of these properties has resulted in images of mammography phantoms and tissues that have dramatically improved contrast over standard imaging techniques. This technique potentially is applicable to mammography and other fields of medical X-ray imaging and to radiology in general, as well as possible use in nondestructive testing and X-ray computed tomography.

Images of various tissues and materials are presented to demonstrate the wide applicability of this technique to medical and biological imaging.

*Corresponding author: Dean Chapman, Center for Synchrotron Radiation Research and Instrumentation, Illinois Institute of Technology, 3101 South Dearborn, Chicago, IL 60616, USA. Tel.: +1 312 567-3575; Fax: +1 312 567-3576; E-mail: chapman@sparky.csrri.iit.edu.

INTRODUCTION

Screening mammography has proven to be an effective procedure in identifying early breast cancer. Screening trials have demonstrated that breast cancer mortality among women can be reduced when compared with unscreened controls (1-4). The cancers found by mammography tend to be smaller and of less advanced stages than those found by breast physical examination or breast self-examination (5-7). Smaller and lower stage breast cancers have better survival rates (8-11). Unfortunately, approximately 10% of clinically obvious breast cancers are not visible with mammography (5). This occurs most frequently in patients with large amounts of breast glandular tissue (5,12). The density of this tissue tends to obscure underlying pathology. Premenopausal women and women undergoing estrogen replacement therapy are more likely to have dense glandular breasts. Increasing the sensitivity of mammography in women with dense breasts is an important goal. Earlier detection may result in significantly reduced mortality in this population.

Mammographic technology has improved dramatically in the last two decades. These improvements include the development of dedicated mammography equipment with appropriate X-ray beam quality, adequate breast compression, and automatic exposure control (13). Digital mammography, the most recent development, is just being introduced into the clinic and holds promise of improved early detection of breast cancer (14). However, all of these currently existing systems depend on the depiction of X-ray absorption

to define the differences between normal and abnormal tissues. This paper describes a new method, diffraction enhanced imaging (DEI), that partly depends upon the refractive properties of an object in the creation of a scatter-free image. This new method, which seeks to improve the X-ray beam properties and analysis for improved contrast, along with the new digital mammography detectors, could improve early detection of occult disease.

Other researchers have applied diffractive optics to imaging problems (15-18) and have observed refraction effects. Also, there is great interest in phase contrast imaging that uses high transverse coherence of third generation synchrotron sources. However, these measurements are limited to materially thin objects and/or high X-ray imaging energies to obtain phase contrast images of the object (19,20). The DEI technique works for thick samples and does not require the use of a synchrotron.

The mammography imaging technique under development utilizes the high intensity and collimation of synchrotron radiation to create a monoenergetic line scan imaging system that has very little scatter (21). One aspect of this program has been to study the use of an analyzer crystal as a scatter rejection optic. Experiments performed with this scatter rejection optic revealed an imaging system that is sensitive to refractive index effects within the object being imaged as well.

PRINCIPLES OF DEI

Conventional radiography uses an area beam that, after traversing and interacting with the subject, is intercepted and recorded by an area detector. The interaction of X-rays with the subject is complex, involving absorption, refraction (15-18) and scattering. The scattering may include small angle scattering (22) (scattering angles less than milliradians) that carries information about the subject's structure on the length scale up to microns. This

information is lost in normal radiography because of its small angle nature. The refraction of X-rays inside the object also is not detectable in conventional radiography due to its small angle nature (on the order of microradians).

X-ray diffraction from perfect crystals, whose narrow reflection angular width (on the order of a few microradians) and peak reflectivity of close to unity, provides the tools necessary to prepare and analyze X-ray beams traversing an object on the microradian scale (23). Such crystals, typically silicon, routinely are used in the semiconductor industry to make integrated circuits and electronic devices. The purity and perfection of these crystals have allowed many advances in X-ray diffraction techniques and in particular at X-ray synchrotron sources.

The condition for X-ray diffraction from a crystal is met only when the incident beam makes the correct angle to the atomic lattice planes in the crystal for a given X-ray energy or wavelength. When this condition is met, the beam "Bragg" diffracts from the planes over a narrow range of incident angles. As the crystal is rotated about an axis parallel to the lattice planes and perpendicular to the incident beam direction, the intensity variation observed is referred to as the rocking curve. The shape of this curve is roughly triangular with the peak reflectivity approaching nearly 100%.

In DEI, an imaging beam is prepared by diffracting the polychromatic beam from the synchrotron to create a nearly monoenergetic imaging beam. This beam is then passed through the object being imaged as in conventional radiography. However, a matching crystal is placed between the object and the detector. This crystal, which is called the analyzer crystal, is set at or near the peak of Bragg diffraction.

Since the condition for diffraction from this crystal limits the X-rays that can be diffracted into the detector, it automatically provides a high degree of scatter rejection, resulting

in improved image contrast. The acceptable range of angles is a few microradians; therefore, the analyzer provides scatter rejection at the microradian level that is below the capabilities of conventional antiscatter techniques such as slit collimation and grids. The scatter rejected falls into a category referred to as small angle scattering (24), which arises from diffraction from organized structures with dimensions up to micron sizes. This scattering intensity, which would normally appear in the image, is missing and appears in the same way as absorption in the image. This scatter rejection contrast is called extinction contrast, drawing from a similar term used in optics and X-ray diffraction to describe intensity loss due to diffraction and scattering. Therefore, in DEI, the image representing the absorption of the object by X-rays is referred to as the apparent absorption image since it has contrast derived from both absorption and scatter rejection, or extinction.

The analyzer rocking curve shape will introduce a sensitivity to refraction occurring within the object when the analyzer is detuned from the peak position. Density, thickness and/or material variations in an object will refract the X-rays as they cross through the material. These small, angular variations are generally in the submicroradian range. The steep sides of the reflectivity curve will convert these subtle angle variations into intensity variations, thus making refraction effects visible in an image. By acquiring an image pair with the analyzer set to diffract on each side of the rocking curve, we can separate refraction effects from combined absorption and extinction effects (25,26).

With the DEI technique, we have introduced two new sources of image contrast to radiography: refraction and extinction (26). Each of these new image contrast sources have been found to apply to medical and biological imaging.

EXPERIMENTAL SETUP

The experimental setup used to apply this technique is shown in Figure 1. The white synchrotron beam is made nearly monochromatic by a silicon double crystal monochromator. For the measurements described here, the beam energy was either 18keV or 30keV. The pilot experiments were carried out at the National Synchrotron Light Source (Brookhaven National Laboratory, Upton, NY) using the X27C Research and Development Group beamline. Subsequent experiments were performed at the Advanced Photon Source (Argonne National Laboratory, Argonne, IL) using the Synchrotron Radiation Instrumentation Collaborative Access Team 1-BM beamline. The imaging beam was approximately 80mm wide and 1mm high at the location of the object. An ionization chamber was used to measure the radiation exposure at the surface of the object. Images taken with and without the analyzer were at exposure levels comparable to conventional mammography X-ray systems. The object to be imaged was mounted on a scanning stage that was driven by a stepping motor. The X-ray beam transmitted through the object could be either imaged directly as in normal radiography or following diffraction in the vertical plane by the silicon crystal analyzer. Radiation exposure to the image plate was controlled by adjusting the scan speed and absorbers in the incident beam to maintain an exposure of about $1.3\mu\text{C/kg}$ (5mR) to the plate. Typical scanning times for these experiments were on the order of 4 to 200 seconds. These limits were dictated by our scanning motors and mechanical system.

In acquiring the DEI apparent absorption and refraction images the phantom was exposed to approximately four times the exposure compared to the nonanalyzer synchrotron radiographs. A factor of two in increased exposure compensates for the 0.5 reflectivity of the Bragg analyzer crystal, and another factor of two in increased exposure compensates

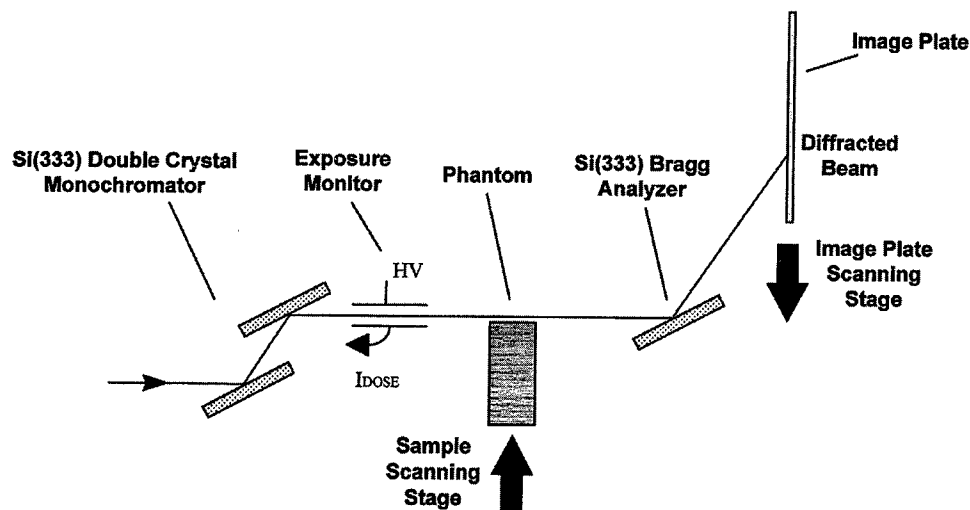


Fig. 1. A simplified schematic diagram of the DEI setup.

for the two images on each side of the rocking curve.

The detector was a photo-stimulative phosphor image plate, typically used for radiology (Fuji Medical Systems high resolution HR5 and standard resolution ST5 image plates, Fuji Medical Systems USA, Stamford, CT). The image recorded on the plate was digitized, stored, and displayed by a Fuji Medical Systems AC3 reader and workstation or a Fuji BAS2000 reader system. The image plates were read out at 2560×2048 matrix size, which resulted in an image of 100 microns per pixel ($0.1 \times 0.1 \text{ mm}^2$).

The diffraction angle of the analyzer crystal could be finely tuned using a stepper-motor driven translation stage pushing on a long bar attached to an axle to which the crystal was attached (tangent arm). The resolution limit of the tangent arm was 0.1 microradian, which was sufficient for placing the Bragg analyzer crystal at a selected position on its rocking curve.

For each sample, a "normal" radiograph with the monochromatic beam was taken by moving the analyzer out of the beam and scanning the image plate and sample through the fan beam in the same direction and at the same speed. DEI images then were acquired

with the analyzer tuned to various positions on the rocking curve by translating the sample and the image plate in opposite directions at the same speed through the fan beam. The change in scanning direction arises from the beam inversion from the analyzer crystal. At a scan speed of about 10mm/s, the surface dose on the sample was a few mGy at 18keV and tenths of mGy at 30keV. Rocking curves through a line on the phantom were obtained by fixing the phantom in the fan beam and performing a series of exposures by incrementally changing the analyzer position and image plate vertical position. The rocking curve is useful for quickly visualizing the optimum analyzer position for contrast enhancement of the desired features.

AMERICAN COLLEGE OF RADIOLOGY (ACR) PHANTOM RESULTS

Because the initial interest was in studying the use of this new method for early detection of breast cancers, a mammography phantom was used as the test object. The standard phantom used for quality control in mammography is the American College of Radiology (ACR) phantom manufactured by Gam-

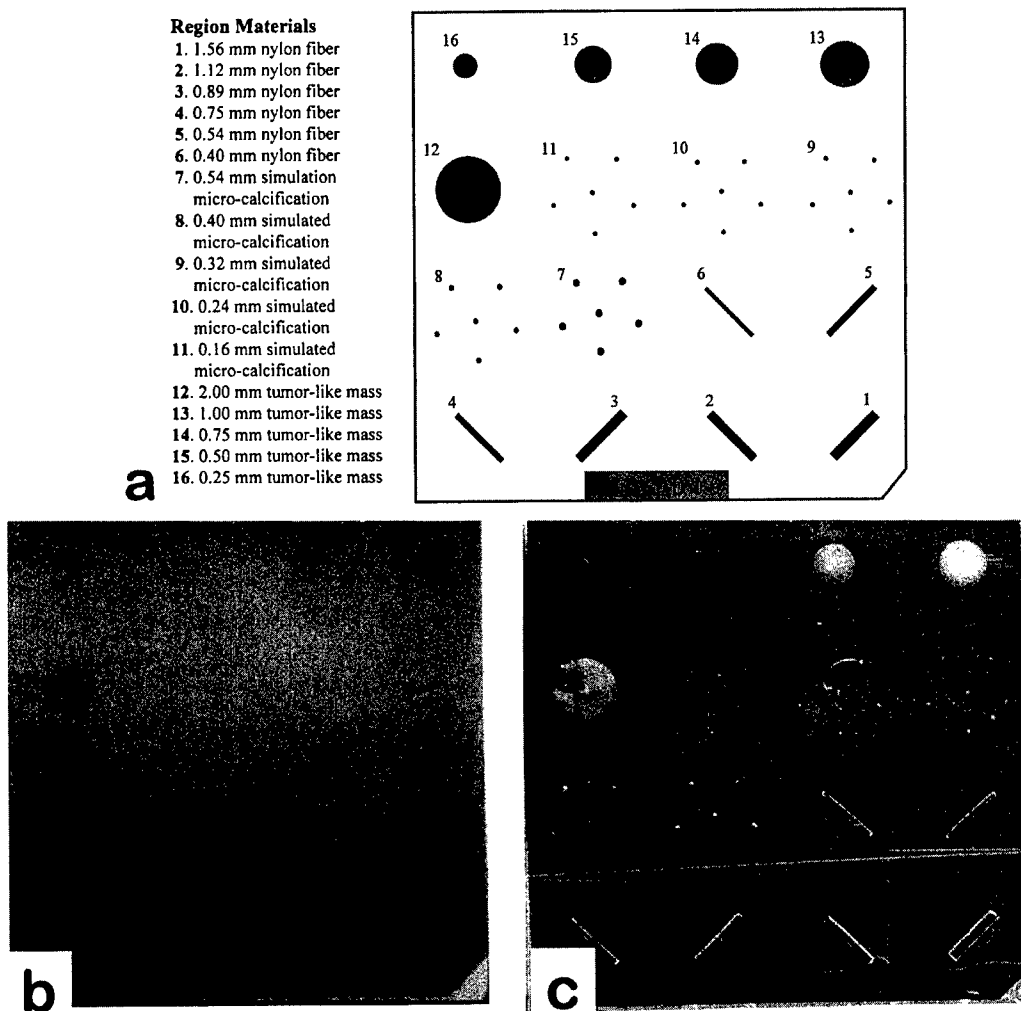


Fig. 2. The American College of Radiology quality assurance phantom for mammography. Figure 2a is a schematic of the phantom with each feature identified. Figure 2b is a conventional radiograph of this phantom taken with a Siemens Mammomat II system. Figure 2c is a DEI image taken at 18keV with the analyzer in place and at 3 microradians from the peak position.

mex RMI: Model 156 (Gammex RMI, Middleton, WI). It contains features that simulate lesions commonly found in breast tissue, namely tumor-like masses (lens-shaped objects of different thicknesses and diameters), simulated microcalcifications arranged as vertices of five-point stars, and cylindrical nylon fibrils (21, 27). A schematic of this test object is shown in Figure 2a. The features are fixed in a wax block contained in a thick acrylic base. This phantom approximates a 40 to 45mm thick compressed breast. Figure 2b is a conventional radiograph of the ACR phantom taken with a Siemens Mammomat II system at the

University of North Carolina, Chapel Hill. Figure 2c is a DEI image taken with the analyzer set 3 microradians from the peaked position. Note that all the features of the phantom are visible in the image, as is some tape used to hold the phantom to a Lucite holder. Also note that the tumor simulations have excess intensity compared to the surrounding area. This is a result of the analyzer diffracting the small angle scattering from the simulations at the 3 microradian offset angle.

Figure 3 shows the ACR phantom imaged at 18 and 30keV. The use of higher X-ray energy to image soft-tissue may be tenable with

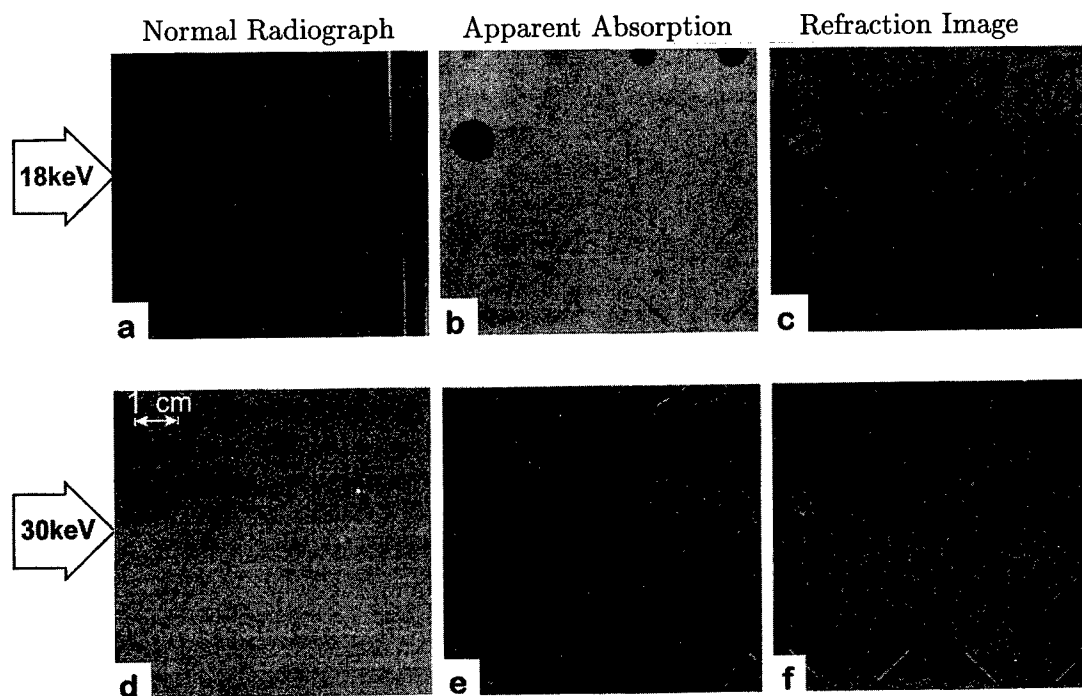


Fig. 3. Images taken of the ACR phantom at 18 and 30keV. The upper row of images are acquired at 18keV; the lower row at 30keV. Figures 3a and 3d are synchrotron radiographs taken without the analyzer in place. Figures 3b and 3e are apparent absorption images resulting from images taken with the analyzer in place and the DEI analysis. Figures 3c and 3f are the matching refraction images.

DEI since there are substantial differences between the DEI sources of contrast and absorption and those available with conventional radiography.

Conventional radiography depends on the absorption of X-rays by an object to create the radiograph. In DEI, the energy dependence of the refraction and extinction effects differ from that of absorption. Also, the sensitivity of the analyzer crystal to these effects depends on the imaging energy. In general, for a feature in an object that refracts X-rays, the DEI sensitivity will be proportional to $1/E$. For extinction features, the ability of the system to reject scatter will be energy independent, while the scattering intensity from the object will decrease with energy. Therefore, sensitivity of the DEI technique to refraction and extinction is decreased as the imaging energy is increased. Since the X-ray transmission through an object is a very strong function of imaging energy in the photoelectric range, the net effect on the DEI refraction and extinction

signal-to-noise is to skew the optimal imaging energy to higher energies when compared to an optimal absorption contrast energy. For example, in mammography, the optimal absorption imaging energy is near 18keV for 5cm of soft tissue. With DEI, the optimal imaging energy for refraction is near 30keV. The transmission through the tissue increases dramatically over this energy range, and the skin entry exposure drops by a factor of 15 while maintaining the same exposure to the detector. Obviously, lower patient glandular radiation doses might be possible if this technique could be optimized at a higher beam kVp than is used with conventional mammography.

Figures 3a-c are ACR phantom images taken at 18keV, while Figures 3d-f are taken at 30keV. Figures 3a and 3d are radiographs taken with the analyzer removed; 3b and 3e are the DEI apparent absorption images; and 3c and 3f are DEI refraction images. At 30keV, note that the radiograph shows very little contrast for any of the ACR features,

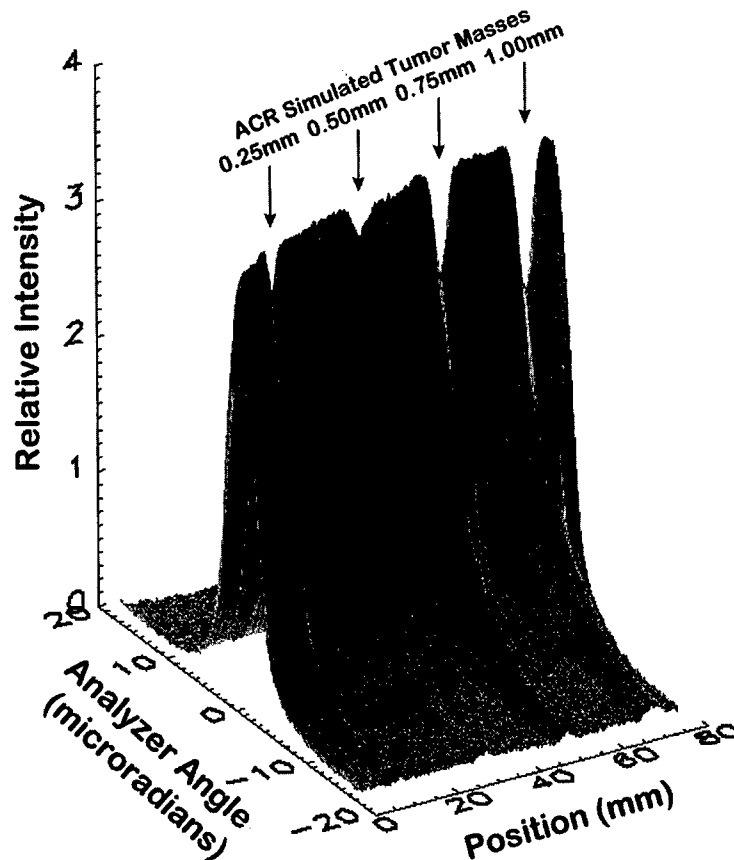


Fig. 4. Rocking curve of a fixed X-ray beam striking the row of four tumor simulations in the ACR phantom. Each simulation is identified at the top of the figure. The analyzer crystal is rotated in angle through the peak position while the intensity is recorded on the image plate.

while the DEI images at 30keV retain much of the information.

A series of images at various settings of the analyzer crystal could be acquired to determine if extinction contrast exists in a particular material. As illustrated in Figure 4, this data was acquired for fixed position of the ACR phantom, with the X-ray beam centered over the row of four mass simulations. The image plate then was moved in coordination with the analyzer angle to obtain a "rocking curve" profile. The locations of the tumor simulations are marked above. When the analyzer is at or near the peak position, there is a marked decrease in intensity at the tumor simulation positions. The contrast obtained is approximately 25 times higher than the radiographic value for this analyzer setting (26).

As the analyzer is moved from the peak position, the deficit of intensity will become excess intensity (this is the effect observed in Figure 2c). This is the small angle scattering created by the tumor simulations. In a normal radiograph, this small angle scattering is indistinguishable from the normal transmission through the simulations, and each pixel will record the sum.

EXCISED BREAST TISSUE IMAGING

Various formalin-preserved human breast tissue samples were imaged, including samples containing infiltrating ductal carcinomas. Each biological sample was sealed in a plastic bag and compressed between two Lucite

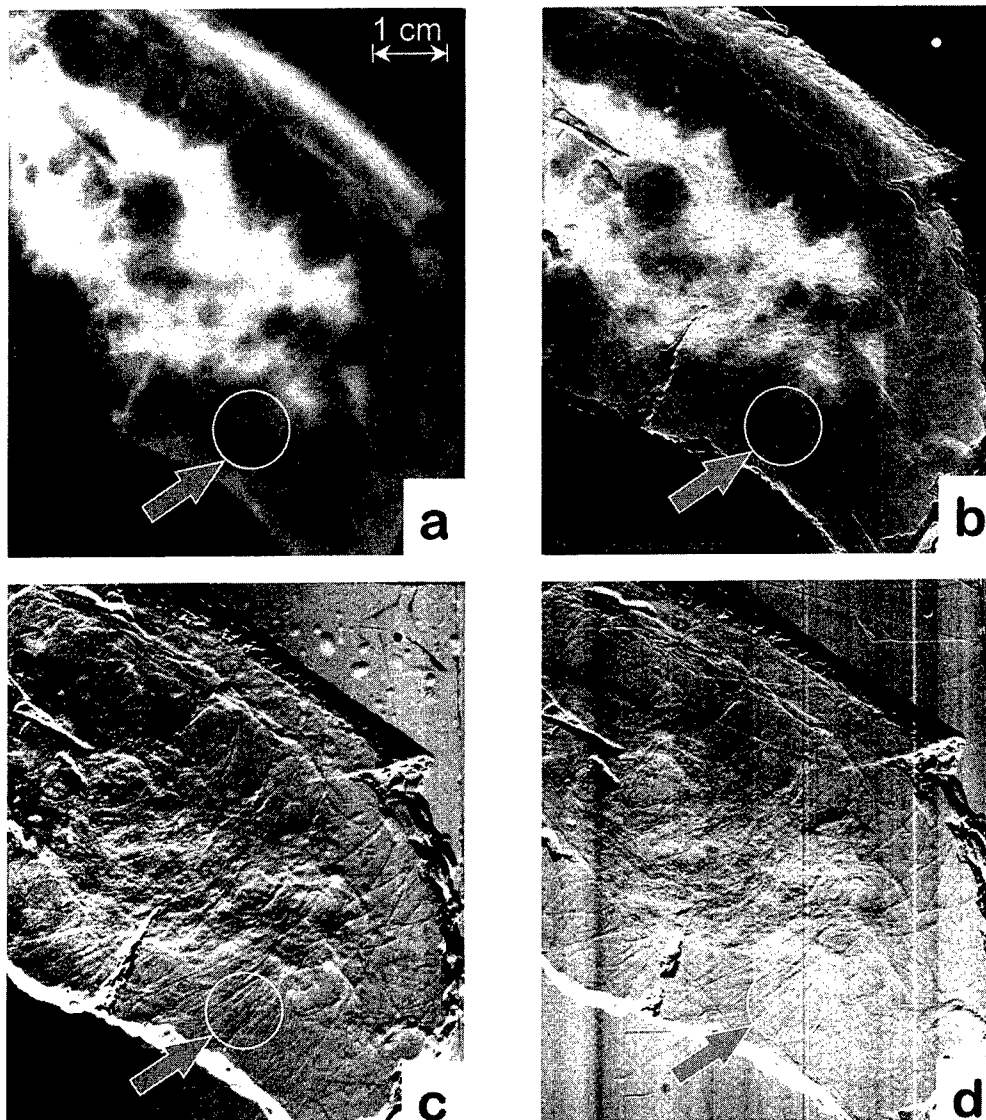


Fig. 5. Images taken of an excised breast tissue sample with infiltrating ductal carcinoma. Figure 5a shows an image taken of this sample with a Fischer digital mammography unit at the University of North Carolina, Chapel Hill. Figure 5b shows the DEI apparent absorption image, and 5c shows the refraction image. Figure 5d show a DEI refraction image taken at 30keV. The circled regions indicate refraction from spiculations (Figures 5c and 5d) which is not readily apparent in the radiograph or apparent absorption images (Figures 5a and 5b).

plates. Additional Lucite plates were added during the imaging to make the absorbing thickness on the order of 30–50mm.

Images of a breast tissue acquired at 18keV are shown in Figure 5. Figure 5a shows a “normal” specimen radiograph; Figures 5b and 5c show the apparent absorption and refraction images, respectively, of the sample. These images are derived from the images taken at ± 1.5 microradians on each side of the analyzer

rocking curve. Compared to the “normal” radiographs, the apparent absorption image (Figure 5b) shows more contrast for the tumor when compared to the background normal breast tissue. The DEI apparent absorption image shows clearer calcifications (clusters of white dots in the image) than does normal radiography. The most striking feature is the refraction image (Figure 5c) that shows small spiculations not observable in the

conventional image. As seen in the circled regions, these likely indicate extension of tumor or fibrosis into surrounding breast tissue.

An image of the tissue sample at a 30keV imaging energy is shown in Figure 5d. This is the refraction image from a DEI image pair. Note that the image content at 30keV is similar to that obtain at 18keV, even though the exposure to the sample is somewhat less than that of the 18keV image. By comparison, the apparent absorption image at 30keV (not shown) shows very little structure due to the weak absorption of the sample.

POTENTIAL FUTURE FOR CLINICAL APPLICABILITY

This technique was developed using a synchrotron X-ray source. The availability of high intensity, collimation, and tunability using synchrotron sources creates an ideal environment in which to develop new imaging technologies, such as DEI. An obvious drawback is the translation of this technology to more conventional X-ray sources in a laboratory or clinical environment. The DEI technique delivers X-ray exposures to tissue and phantoms, similar to that delivered by conventional X-ray mammography units. The difficulty arises in generating the highly collimated-monoenergetic imaging beam. The monochromating crystal and analyzer crystal must use the same Bragg reflection to achieve the high degree of collimation necessary to observe the refraction and scatter rejection presented earlier. Perfect, single crystal silicon monochromators and analyzer are used to achieve the DEI effect. Such systems are used routinely with conventional X-ray sources; however, for DEI to be applied to mammography, the source intensity and properties must be such that exposures are obtained in a few seconds to avoid image blurring due to patient motion.

The flux from conventional X-ray sources have yielded scan time estimates of approximately 1,000 to 10,000 seconds. Clearly, such

long scan times required to deliver a DEI image set would be unacceptable. Presently, investigations are underway to enhance the source and optics throughput sufficiently to make such imaging practical.

CONCLUSION

We believe that this new imaging technique may provide significant improvements in image contrast, both in soft tissue imaging in mammography and in other areas of medical and nonmedical radiology. This system's unique ability to provide an essentially scatter-free image of the object's apparent absorption, as well as an image of the refraction effects, may provide radiologists with sufficient additional information to allow detection of malignancies at an earlier stage than is presently possible, even in patients with dense breasts. Since the new sources of contrast, refraction, and extinction do not depend on absorption, DEI may be applied optimally at higher X-ray energies, thus allowing dose reduction and, in the case of mammography, less breast compression.

More studies using real tissue samples and patients are needed before concluding that this technique can lead to improved breast imaging. A clinically useful device that can function separately from a synchrotron facility must be developed for this technique to be a practical benefit to women.

FUTURE RESEARCH

This work will be extended to a wide variety of biological and materials samples at the X15A beamline at the National Synchrotron Light Source (Brookhaven National Laboratory, Upton, NY), and in future work at the Advanced Photon Source (Argonne National Laboratory, Argonne, IL). Many questions need to be answered concerning the applicability of DEI to soft-tissue differentiation, optimization of energy and analyzer position, the

advantages and disadvantages of imaging at higher energies, and the role of DEI in nondestructive materials testing. The future of DEI in clinical mammography will depend on the results of the synchrotron-based studies and on the development of compact DEI system for the clinical environment.

ACKNOWLEDGEMENTS

We would like to thank D.P. Siddons and B. Dowd at the National Synchrotron Light Source for support and beamtime at the X27C R&D beamline, and G. Srajer and D. Mills for support and beamtime at the Advanced Photon Source SRICAT 1-BM beamline. We would also like to thank Fuji Medical Systems (in particular I. Pipkin and L. Sawyer) for the loan of the AC3 image plate reader system and support in setting up and operating the unit. This work was supported in part by US ARMY grant DAMD17-96-1-6143, US Department of Energy Contract DE-AC02-76CH00016, ARPA contract AOB227 and by the State of Illinois Higher Education Cooperative Agreement.

REFERENCES

1. Shapiro S, Venet W, Strax P, et al. Ten to fourteen year effect of screening on breast cancer mortality. *J Natl Cancer Inst* 1982; 69:349-355.
2. Tabar L, Fagerberg G, Duffy SW, et al. The Swedish two county trial of mammographic screening for breast cancer: recent results and calculation of benefit. *J Epidemiol Community Health* 1989; 43:107-114.
3. Shapiro S, Venet W, Strax P, et al. Ten to fourteen year effect of screening. In: Shapiro S, Venet W, Strax P, Venet L, eds. *Periodic screening for breast cancer*. Baltimore, Johns Hopkins Press; 1988.
4. Thurfjell EL, Lindgren JA. Breast cancer survival rates with mammographic screening: similar favorable survival rates for women younger and those older than 50 years. *Radiology* 1996 Nov; 201(2): 309-316.
5. Baker LH. Breast cancer detection demonstration project: five-year summary report. *CA Cancer J Clin* 1982; 32(4):194-225.
6. Saltzstein SL. Potential limits of physical examination and breast self-examination in detecting small cancers of the breast: an unselected population-based study of 1302 cases. *Cancer* 1984; 54:1443-1446.
7. Fletcher SW, O'Malley MS, Bunce LA. Physicians abilities to detect lumps in silicone breast models. *JAMA* 1985; 253:2224-2228.
8. Fisher B, Slack NH, Bross ID. Cancer of the breast: size of neoplasm and prognosis. *Cancer* 1969; 24:1071-1080.
9. Wanebo HJ, Huvos AG, Urban JA. Treatment of minimal breast cancer. *Cancer* 1974; 33:349-357.
10. Gallager HS, Martin JE. An orientation to the concept of minimal breast cancer. *Cancer* 1971; 28:1519-1526.
11. Frazier TG, Copeland EM, Gallager HS, et al. Prognosis and treatment in minimal breast cancer. *Am J Surg* 1977; 133:697-701.
12. Stomper PC, Gelman RS. Mammography in symptomatic and asymptomatic patients. *Hematol Oncol Clin North Am* 1989; 3(4):611-640.
13. Haus AG. Technologic improvements in screen-film mammography. *Radiology* 1990; 174(3):628-637.
14. Shtern, F. Digital mammography and related technologies: a perspective from the National Cancer Institute. *Radiology* 1992; 183:629-630.
15. Ingal VN, Beliaevsky EA. X-ray plane-wave topography observation of phase contrast from a non-crystalline object. *J Physics D: Appl Phys* 1995; 28:2314-2317.
16. Somenkov VA, Tkachik AK, Sh. Shil'shtein S. Refraction contrast in X-ray microscopy. (Brief Communication). *Sov Phys Tech Phys* 1991; 36(11):1309-1311.
17. Podurets KM, Somenkov VA, Sh. Shil'shtein S. Refraction-contrast radiography. *Sov Phys Tech Phys* 1989; 34:654.
18. Gureyev TE, Wilkins SW. Regimes of X-ray phase-contrast imaging with perfect crystals. *Il Nuovo Cimento* 1997; 19:545-552.
19. Davis TJ, Gureyev TE, Gao D, Stevenson AW, Wilkins SW. X-ray image contrast from a simple phase object. *Phys Rev Lett* 1995; 74:3173-3175.
20. Davis TJ, Gao D, Gureyev TE, Stevenson AW, Wilkins SW. Phase-contrast of weakly absorbing materials using hard X-rays. *Nature* 1995; 373:595-598.
21. Johnston RE, Washburn D, Pisano E, et al. Mammographic phantom studies with synchrotron radiation. *Radiology* 1966; 200:659-663.
22. Bushuev VA, Ingal VN, Belyaevskaya EA. Dynamical theory of images generated by noncrystalline objects for the method of phase-dispersive microscopy. *Crystallogr Rep* 1966; 41:766-774.
23. Zachariasen WH. *Theory of X-ray diffraction in crystals*. New York, John Wiley and Sons 1945; Ch 4.

24. Guinier A, Fournet G, Walker CB, Yudowitch KL. Small-angle scattering of X-rays. New York, John Wiley and Sons; 1955.
25. Chapman D, Thomlinson W, Arfelli F, et al. Mammography imaging studies using a laue analyzer crystal. Rev Sci Instrum 1966; 67(9):CD-ROM.
26. Chapman D, Thomlinson W, Johnston RE, et al. Diffraction enhanced X-ray imaging. Phys Med Biol 1997; 42:2015-2025.
27. Arfelli F, Burns C, Chapman D, et al. Data acquisition and analysis of mammography images at the NSLS: June - August 1995. Brookhaven National Laboratory Informal Report, 1995; BNL-62935.

Appendix

A.7

D.E.Peplow and K.Verghese ``Digital mammography image simulation using Monte Carlo. Accepted for publication in Medical Physics, 1999.

Digital mammography image simulation using Monte Carlo

Douglas E. Peplow and Kuruvilla Verghese

Department of Nuclear Eng., NC State University, Box 7909, Raleigh, NC 27695

(July 26, 1999)

Abstract

Monte Carlo simulations of digital images of the contrast detail phantom and the ACR phantom are presented for two different x-ray digital mammography modalities: a synchrotron mammography system and a next-generation scanning slot clinical system. A combination of variance reduction methods made it possible to simulate accurate images using real pixel dimensions within reasonable computation times. The complete method of image simulation, including noise and system effects (MTF), is presented. The simulated images of the phantoms show excellent agreement with images measured on the two systems.

keywords: digital mammography, image simulation, Monte Carlo

02.70.Lq, 87.59.Ek

Typeset using REVTeX

I. INTRODUCTION

A rapidly expanding area in medical applications of x rays from synchrotrons^{1,2} is synchrotron mammography. Several groups worldwide (for example, in Italy^{3,4} and the National Synchrotron Light Source (NSLS) at Brookhaven National Laboratory (BNL) in the US⁵) have been generating exciting results in synchrotron mammography using monoenergetic, parallel, plane-polarized x rays, with a high degree of collimation, long air gaps to reduce x-ray scatter contribution and even crystal analyzers to virtually eliminate image degradation due to scatter. Diffraction of the transmitted beam from the object using a Bragg or Laue analyzer has been shown to produce images that are unparalleled in clarity and contrast⁶. A group in Russia has been doing similar investigations using x-ray tubes instead of synchrotron beams and generating high quality images⁷. Chapman *et al*⁶ have shown that the transmitted and diffracted images can be coupled to obtain a pure absorption image with imaging details smaller than ever seen before. Simultaneously with the development of synchrotron mammography, next generation clinical mammography systems with slot geometry and digital detectors⁸ have been undergoing clinical trials. Scatter contribution is reduced through the use of a narrow collimator slot and detector array scanned across the object. To quantify the amount of scatter in these two types of modalities, a Monte Carlo study was proposed. This paper presents the results of a code designed to create very accurate simulated images for the study of scatter contributions.

Most of the previous Monte Carlo studies⁹⁻¹¹ have attempted to evaluate mammography systems based on simple studies which quantify the scattered radiation striking the image plane from a slab of material, usually water or Lucite. These studies may show trends with energy or slab thickness correctly but they do not include the full three dimensional effects, such as air scatter or edge effects. Recently, Jing, Huda and Walker¹² studied scanning slot systems using a 3-D model. However, they only focused on the average scatter-to-primary ratio (S/P) observed in a strip located at the center of the image. Spyrou *et al*¹³ has recently performed some Monte Carlo image simulations but using an analog code which required 18

days to run¹, even for a very simple phantom and system. What is really needed is a way to determine whether or not objects of certain sizes and densities can be seen in the image produced by the mammography system in question. To answer this, a full 3-D model and an entire accurate simulated image are required.

Full field image simulation for realistic pixel sizes (50 or 100 μm) using standard Monte Carlo techniques would require prohibitively long computing times. Larger pixel sizes could be used for the purpose of modeling to reduce the times but the clinical relevancy would be lost. Small objects, such as fibrils or calcifications, would not be discernible when using large pixel sizes. In order to simulate images with accurate pixel sizes in reasonable times, a combination of three variance reduction techniques are implemented.

Section III of the paper describes the methods used in the Monte Carlo simulation code written to generate images from the synchrotron-based system and from the Fischer SenoscanTM, a new digital scanning-slot system that is representative of the next generation of clinical mammography machines. The code is verified by comparison to a large set of published computational results and also to images measured on both systems. The concepts presented in this paper should be applicable also to image simulations using general purpose codes such as MCNPTM. In fact, Los Alamos National Laboratory^{14,15} is currently investigating the incorporation of image simulation capability within a future version of MCNPTM.

By comparing real digital images taken by the synchrotron and the SenoscanTM, this paper will demonstrate that image simulation by Monte Carlo is possible within reasonable computing times. Hopefully this modeling ability will prove as valuable to mammography and other imaging problems in medical physics as it has proven in many other fields.

¹G. Panayiotakis, private communication (1998).

II. DIGITAL MAMMOGRAPHY SYSTEMS

A. Synchrotron Imaging

The new synchrotron-based digital mammography system is still in its early experimental phase of development. The concept is being developed in the United States at the NSLS (BNL) and at the Advanced Photon Source at Argonne National Lab. The basic system consists of a plane-polarized, parallel, monoenergetic source of radiation collimated into a rectangular beam. Since the beam is fixed in position by the monochromator, the object and the imaging plate are scanned through the beam. Since the beam is parallel, there is no geometric magnification and large air gaps are used in addition to various collimators to reduce the amount of scatter. A schematic diagram is shown in Fig. 1.

The system used to take images for this project was on the X15A beamline of the NSLS. The energy of the beam can be selected to be between 18 keV and 42 keV and the beam size is 13×0.1 cm. The air gap between the target and the image plate is 26 cm. Currently, the image is recorded by a Fuji HR-III image plate and developed by a Fuji BAS2000 image plate reader.

B. Fischer SenoscanTM

The Fischer SenoscanTM system, shown schematically in Fig. 2, is a scanning slot system which uses a linear CsI/CCD detector array. The tungsten anode is well-collimated and rotates at the same rate as the detector, scanning the breast with a fan beam of x rays in five seconds. Like conventional systems, the x-ray source spectrum consists of bremsstrahlung and it is polyenergetic. The machine can be operated at various kVp settings and has a choice of three filter materials, which greatly reduce the L-lines from tungsten.

The machine used for this study was at the University of North Carolina Hospitals as part of the clinical trials for FDA approval, which are currently ongoing at several sites in

the US. This machine and other digital mammography units are expected to replace the film/screen systems used in clinics today.

C. Mammography Phantoms

To compare the two systems, digital images were taken of two very common mammography phantoms – the contrast detail (CD) phantom and the American College of Radiologists (ACR) phantom. The CD phantom is a 1.5 cm thick slab of Lucite with embedded discs of Lucite of varying thicknesses and diameters. Thicknesses range from 0.1 cm down to 0.0063 cm, representing density changes of 7% down to 0.45%. Radii vary from 0.35 cm to 0.016 cm. Mammography systems are graded on how many objects can be seen in the image. The ACR phantom is a 4.9 cm thick block of Lucite containing a rectangular wax insert with embedded nylon fibers (fibril simulations), aluminum oxide spheres (calcification simulations) and the top portions of plastic balls (tumor simulations). Information pertaining to the placement and composition of the materials of the objects was obtained from the manufacturer, Gammex RMI. Schematics of the two phantoms are shown in Fig. 3.

III. DESCRIPTION OF THE CODE

MCMIS (Monte Carlo Mammography Image Simulation) is a detailed code specifically for the simulation of digital mammography systems, including scanning slot systems. This code was written so that three variance reduction techniques can be used together. These are source rastering, separation of the scattered and unscattered image and the point-detector scheme. The code uses four input decks describing the problem, various cross section tables and outputs several image files, image files describing stochastic uncertainty, and tables describing dose and exposure. The code contains four source models, three detector geometries and three detector types. These models and all of their parameters are listed in one of the input decks. The geometry of the object being imaged and a list of materials are listed in other input decks. The last input deck contains information for the Monte Carlo run –

number of histories, variance reduction methods to use, etc. In addition to the image, this code also calculates for each region the energy deposited, the total flux, the exposure and the dose.

A. Source Models

Four types of monoenergetic sources can be modeled with MCMIS. Polyenergetic sources can be simulated by adding together a set of monoenergetic images weighted by the polyenergetic spectrum, which allows the user to use the same monoenergetic runs to simulate different polyenergetic source spectra. The code is designed in a manner such that sources are at a high z location, pointed down at some target plane. The detector lies on a lower z plane and the image is viewed as a picture with x and y coordinates.

The four source models are:

1. A polarized parallel beam, from a rectangular source rastered over a rectangular target, with a scanning slot oriented in the x direction moving in the y direction. (synchrotron system)
2. An isotropic point source rastered over a target which is curved in the x direction, with a scanning slot oriented in the y direction moving in the x direction. (Fischer system)
3. A polarized pencil beam, for comparing to other Monte Carlo studies.
4. An isotropic point source rastered over a flat rectangular target, with a scanning slot oriented in the y direction moving in the x direction. This is also for comparing to other work in the literature.

“Rastering” refers to the use of a stratified sampling routine used to evenly sample the source over the target area. This is a common variance reduction technique and helps eliminate quantum mottle in the image.

B. Basic Transport

The geometry package of MCMIS handles six basic shapes commonly found in phantoms and imaging systems. These are: spheres, cylinders (in any orientation), rectangular boxes, boiler plates (curved detector systems), spherical chords (the top of a sphere cut by a plane), and compressed breast shapes (half of a right elliptical cylinder). Geometry regions can be nested to any level. This arrangement makes description of complex phantoms very simple.

Materials are described by a list of elements, the mass fractions (w_i) of those elements and the density (ρ) of the material. Cross sections are calculated for an energy range of 1 to 300 keV for any material consisting of elements with $Z = 1$ to 20. Photoelectric cross sections are taken from the ITS¹⁶ library and scattering cross sections are calculated by integrating the form factors for the materials. MCMIS has the ability to use either the free-gas atomic form factors¹⁷ or measured molecular form factors¹⁸ for coherent scatter. Incoherent scatter was modeled using atomic incoherent scattering factors.

Interactions modeled in this code include the photoelectric effect, coherent scatter and incoherent scatter. Implicit capture (forcing a scatter and reducing the weight to account for the fraction that would have been absorbed) and the last-flight estimator variance reduction techniques are available as options. Both of these are well known and will not be discussed here. The code does model polarization effects, if that option is selected by the user, in the scattering interactions. K x-ray fluorescence can be modeled by MCMIS but this option is not available when using implicit capture since photoelectric events are not simulated.

C. Detector Models

In addition to a perfectly absorbing detector designed for use in testing and benchmark problems, two more realistic detectors are modeled by MCMIS. The Fischer SenoscanTM detector is modeled as a CsI plate, 0.015 cm thick. The density and thickness are left to the user as variable inputs and the nominal values used for this report were supplied by

Fischer Imaging². The second detector is a photostimulable phosphor imaging plate by Fuji. It is made of $\text{BaFBr}_{0.85}\text{I}_{0.15}$. Fuji literature with the imaging plate reports values of density thickness of 0.033 g/cm^2 for the HR (high resolution) plate and 0.048 g/cm^2 for ST (standard) plate. Fuji literature also reports a thickness of 0.0150 cm for the phosphor layer.

In order to account for energy deposition across neighboring pixels, energy is deposited along the photon path through the detector layer, weighted by the probability of the photon surviving up to that point in the layer. This is a simple model but more complex than most, which do not consider the spatial distribution of energy at all. Instead of continuing the Monte Carlo game in the detector model, a ray-trace approach is taken. The distance traveled through each pixel is calculated and the probabilities of interaction in those lengths are found. Energy is then distributed according to those probabilities in the pixels the path crosses. A total of $E(1 - e^{-\mu t})$ energy is deposited, where μ is the total linear attenuation and t is the total distance through the detector layer. This model does not take into account x-ray fluorescence or electron motion, since that would be contained in the system MTF.

Three types of detector grids are available: a flat plate, a plate curved in the one direction and a detector made of concentric rings. The synchrotron system uses the flat plate, the Fischer SenoscanTM uses the curved detector and concentric ring model is used for some test problems. Each detector grid type has many parameters set by the user. Scores are split into two images, one for scattered photons and one for unscattered (source) photons.

MCMIS has the unique feature of modeling scanning slot detector motion. Both the synchrotron system and the Fischer SenoscanTM move the source and detector relative to the object being imaged. This motion is modeled by MCMIS by defining a detector slot width (w) and a beam size (b). At the production of each source photon, a line is marked on the detector and the center of the slot is placed randomly within $\pm b/2$ about this line, in the scan direction. Photons that strike the detector region outside the slot are not scored.

²M. Tesic, private communication, 1998.

This scanning slot option may be easily turned off by defining the slot to encompass the entire detector.

D. Variance Reduction

For an image of 10 cm by 10 cm with 100 μm pixels (a 1000×1000 array) using 10^7 histories, the number of photons striking any one pixel will be $10 \pm \sqrt{10}$. This would be seen in the image as quantum mottle and this amount would completely mask any details in the imaged object. To reduce this mottle to 1%, a total of 10^{10} histories would be needed. Instead, simulating 10 histories per pixel (weighted by the angular distribution probability for source emission) will give an image with considerably reduced mottle. This stratified sampling scheme used in Monte Carlo is what we call source rastering. An amount of noise for the imaging system modeled can then be added to accurately reflect the true mottle.

The path of a photon through a material is picked stochastically from the basic scattering and transport models. At each interaction of the photon there is a small chance of the photon scattering towards a given pixel in the detector, surviving through the material in between the interaction site and that pixel, and then interacting in that pixel. The point-detector scheme calculates this probability for every pixel in the scanning slot of the detector at each interaction that the photon has along its stochastic path. This way, each pixel in the image receives some score with every history instead of just one pixel where the simulated particle actually strikes. This helps to eliminate mottle in the image from scatter. The scheme can also be thought of as a splitting game where the photon is split into many pieces: many that are forced to interact in the pixels of the detector and one that is prevented from striking the detector (the fraction that continues on in the simulation). When the weight of the surviving photon becomes low enough, Russian Roulette is played. Keeping the number of histories per pixel constant, the time required for a simulation is inversely proportional to pixel size raised to the fourth power. Using this scheme for 100 μm pixels in a realistically sized image would result in a prohibitively large simulation time.

To use the point-detector scheme without excessively large times, the separation of the scattered and unscattered images can be used. For the unscattered image, a Monte Carlo simulation is not even necessary. It can be calculated simply by the exponential attenuation of every material in a line between the source and the target pixel. This is very fast and can be done in minutes for a full-field image using $100\text{ }\mu\text{m}$ pixels, allowing the smallest details of the object to be seen in the image. The scattered image does not show small scale structure and can be modeled using larger pixel sizes – sizes up to 0.5 cm were used in this study – which drastically reduces the time required by the point-detector scheme. The fine mesh unscattered image and the coarse mesh scattered image can then be added together.

IV. TRANSPORT MECHANICS BENCHMARKS

A series of comparisons of the basic parts of our Monte Carlo code package were made against previously published works. This was done to ensure that the fundamental transport, tracking, interaction and scoring mechanisms in our code worked properly. This section will briefly review the comparisons. Detailed graphs and tables of each comparison would require more space than allotted in a journal article and interested readers are referred to the first author's dissertation.¹⁹

A. Transmission, Backscatter and Absorption

For an infinite slab of water, Boone²⁰ calculated the primary transmission, the total absorption, forward scatter emission and backward scatter emission of a monoenergetic pencil beam of photons. This was done for at a variety of slab thicknesses and primary photon energies. MCMIS was also used to calculate the same quantities and the results agree very closely with Boone's values.

Another check of the transport mechanics used in MCMIS is Boone's calculation of the mean number of scattering events for photons which have escaped the slab. These numbers calculated by MCMIS also compare very well with those from Boone.

B. Scattering Distributions

Chan and Doi¹⁰ computed the following for monoenergetic pencil beams of photons hitting a slab of water: angular distributions of scattered photons, as a function of incident photon energy and slab thickness; mean exit angle of scattered photons, as a function of incident photon energy and slab thickness; spectral distributions of scattered photons, as a function of incident photon energy, slab thickness and exit angle; mean energy of scattered photons, as a function of incident photon energy, slab thickness and exit angle; spectral distributions of scattered photons, as a function of incident photon energy and slab thickness for all exit angles combined; mean energy of photons emerging at any angle, as a function of incident photon energy and slab thickness; numbers of transmitted primary and scattered photons as a function of incident photon energy and slab thickness; and other quantities. MCMIS was also used to calculate the items listed above and they all agreed very closely with the results of Chan and Doi. Re-running MCMIS using the measured molecular coherent scattering form factor of water slightly changed the distributions at low angles and low energies.

C. Dose

MCMIS calculates dose by taking the energy deposited in a geometric region and dividing by the mass of the material in that region. Exposure is calculated using a path-length tally (similar to a total flux tally) but weighted by the energy of the photon and the energy absorption coefficient for air. The code then reports dose or exposure in rads or roentgen, respectively, per photon.

Liu, Goodsitt and Chan²¹ have reported the dose per unit skin entrance exposure for various combinations of kVp settings and spectral HVL's. (Half value layer is the amount of material required to reduce the exposure in half. This is used as a description of beam hardness.) The paper focuses on magnification mammography but it still provides a useful

check. The model used by Liu *et al* included a divergent point source located 65 cm above the breast support. The breast phantom simulated was a semi-elliptical right cylinder with a 0.4 cm skin, made of the same material as the breast. Liu *et al* calculated the dose per unit entrance exposure as a function of breast thickness for two cases, a standard mammogram and a magnification image. The magnification shot gives the patient a lower dose for the same skin exposure. The ratios computed with MCMIS are 5-20% lower than those of Liu *et al* . Considering that different cross sections, energy absorption coefficients for air, and different tube spectra were employed, this difference is reasonable. These cases were for 28 kVp without a compression paddle for a 50/50 adipose/glandular tissue breast. Liu reported that their spectrum had a HVL of 0.31 mm Al while the spectrum used in the analysis of the MCMIS data had a HVL of 0.334 mm Al.

MCMIS was also used to calculate the dose per unit entrance exposure for a magnification image on a 100% glandular tissue breast at 30 kVp. Two calculations were made, one without a compression paddle, using a spectrum with an HVL of 0.33 mm Al, and one with a 5 mm Lexan compression paddle, after which the spectrum then had an HVL of 0.42 mm Al. Agreement with the calculation of Liu *et al* was similar to the above cases.

D. Scanning Slot Systems S/P

Jing, Huda and Walker¹² reported in 1998 on the S/P ratio of scanning slot mammography systems. They used the EGS4 Monte Carlo code package to calculate the ratio of energy from scattered radiation absorbed in the detector to energy from the unscattered (primary) radiation. Simulations were for point sources above a Lucite slab (20×20 cm² area) and a planar detector (60 cm from source). Only the center slit was considered. They investigated four parameters: source energy, slab thickness, airgap size between the slab and the detector, and the width of the slot. The molecular coherent scattering form factor reported by Leliveld²² was used for Lucite. Most simulations were done for a perfectly absorbing detector but a few were performed using a Gd₂O₂S:Tb 36.7 mg/cm² plate. They

then calculated the S/P ratio over the entire slot for many cases of the four parameters, all to a reported 1% stochastic error. Their paper also reports values for polyenergetic spectra.

MCMIS was used to simulate 79 of the monoenergetic cases reported by Jing *et al.* The point-detector scheme was turned off and the detector was defined to have one pixel, corresponding to the slot. Scanning motion of the detector and the slot was not used. All the S/P ratios were calculated to a stochastic error of 1% or less. The results from MCMIS match those of Jing *et al* very well, typically within 3% of each other and for a few cases at low energies and small slot widths to within 8%.

V. IMAGE PROCESSING

One run of MCMIS will produce five images – one unscattered image on a fine mesh and four images on a coarse mesh, with both mesh sizes as specified by the user. The four coarse mesh images are an unscattered image, a scattered image, and the stochastic uncertainties from these images. From these images, several steps must be taken to form the final simulated image.

A. Simulation of Synchrotron Images

The images taken by the synchrotron are not from a truly monoenergetic source and this must be taken into account in simulating an image. Since Bragg reflection of a particular order through a crystal is used to select the energy of the synchrotron beam, reflections of other orders are also present in the beam. For example, for a 26 keV beam selected using the $[3, 3, 3]$ reflection from a Si crystal, there is a component at 34.67 keV (19% of the intensity of the 26 keV) and a 43.33 keV component (1.6% of the primary intensity). This is easily accounted for in the Monte Carlo calculations by running each component energy and then adding the results weighted by the intensities. The intensities were supplied by the X15A

beamline personnel³ and are shown in Table I.

For each synchrotron image, four monoenergetic components are simulated. The four unscattered images on the fine mesh are added together and the four scattered images on the coarse mesh are added together. The total scattered image is then interpolated using the fine mesh and then added to the total unscattered image creating the total Monte Carlo image. The stochastic uncertainties in the final image were calculated by propagating the stochastic uncertainties in the image components.

To simulate the quantum mottle produced by photon statistics, an appropriate amount of noise (see next section) is added to the Monte Carlo image. The amount of relative noise for each simulated image was determined by the total flux recorded by the ionization chamber for the corresponding experimental image. The values of relative noise are typically one percent or less.

The next step in the image simulation process is to smear the image with the system MTF. The MTF (modulation transfer function) is the norm of the Fourier transform of the point spread function and describes the spatial resolution of a system. Applying the MTF to an image smears it slightly, taking energy from one pixel and depositing it in the neighboring pixels. This accounts for the smear of the laser light which liberates small amounts of energy from neighboring pixels. In reality, we did not have access to MTF data on this system but we did measure the square-wave response (SWR) with a standard line-pair phantom. Since the SWR and the system MTF are so similar²³, the SWR was used in place of the MTF. This will not smear the image quite as much as the MTF but the difference is very slight.

The energy liberated by the laser is in the visible range and there is a quantum mottle associated with it. So, more noise is added to the smeared image making the final simulated image. An example of each stage in this process is shown in Fig. 4. A note about the scattered image - the amount of scatter across this portion of the image is very constant,

³Z. Zhong, private communication (1998).

not showing any detail. The figure is shown with the contrast maximized, which highlights the statistical variation of a few percent.

B. Synchrotron Imaging Noise Model

For a good simulation process for the synchrotron, the image noise also needs to be modeled. The simulations are not very useful if one has to take a real image to determine the amount of noise to complete the simulation. By analyzing the noise observed in the fourteen synchrotron images and the ionization chamber readings (related to photon flux) for each, a simple noise model was developed.

Noise coming from each step in the image formation process needs to be considered but the exact amounts and forms are unknown. These steps include the uncertainty associated with the number of photons striking a pixel, the amount of energy deposited in the plate, the number of photons liberated by the laser reading the plate, etc. From the ionization chamber readings before the target, the amount of energy striking the image plate, E , can be found. From this, the number of photons is found and then the expected noise from quantum mottle, σ_E can also be found. When this noise is added to the Monte Carlo image (scattered plus unscattered), the MTF tends to smear it, reducing the relative amount by a factor k . The difference in the relative noise observed in the image and $k\sigma_E/E$ is due to the process of reading the plate, which converts the stored energy into visible photons, which are then converted to an electronic signal.

A simple model for the total relative noise (uncertainty) observed in the final image was constructed by proposing that the relative variance of the final image, $(\sigma_I/I)^2$, could be described by the sum of three terms:

$$\left(\frac{\sigma_I}{I}\right)^2 = \left(\frac{k\sigma_E}{E}\right)^2 + \left(\frac{K_1}{E}\right)^2 + (K_2)^2 \quad (1)$$

where the first term represents the amount of quantum mottle (as discussed above); the second term represents processes with a Poisson-type error related to the energy deposited in

the plate E (for example, the number of light photons generated); and third term represents processes with a constant relative variance.

The two constants K_1 and K_2 were found by fitting the model to the amounts of relative noise observed in the fourteen synchrotron images listed in Table II. The results of this noise model are shown in Fig. 5. This model also predicted very well the relative noise in eight other synchrotron images of Lucite and wax phantoms that were not used in finding the two model constants. The measured relative noise levels in these images were between 1 and 1.5% and the model predicted values that followed the trends well and were typically within 10% of the measured values.

C. Simulation of SenoscanTM Images

To simulate polyenergetic images from tube anode systems like the SenoscanTM, many monoenergetic runs of MCMIS are required. These runs, made from 5 keV to 40 keV in 1 keV intervals, are added together, weighted by the tube spectra. For this project, tube spectra from Boone²⁴ were used.

Quantum mottle noise is added to the image and the system MTF is applied. The MTF accounts for the focal spot size, scanning motion wobble and noise in the detector. The MTF was supplied by Fischer Imaging Corporation and checked by an edge-phantom measurement. Of course, the MTF effects and the noise effects are not in reality separate – the best we can do is apply them in steps. The Fischer detector system is more complex than what was used for the synchrotron images and the noise was considerably less (see Table III). So, we did not attempt to model the noise for this system. Instead, we used an amount of noise typically seen in the SenoscanTM images of 0.5%.

Real Fischer images are corrected for the flux fall-off towards the nipple by dividing the entire image by the whiteness profile which is the flux profile recorded at a standard kVp and extra-large filter thickness. This is also done for the simulated image, dividing by a profile determined by a separate Monte Carlo run matching the specifications of the Fischer

whiteline image.

VI. RESULTS AND DISCUSSION

A. Synchrotron Imaging

Seven images of each phantom were taken using the X15A synchrotron imaging system at the NSLS. Images were made at 18, 26, 34 and 42 keV. Several collimator sizes were used at 18 keV in order to observe the effects of increased scattered radiation in the image. Noise in the images was typically very low, in the 1% range. The details of each measurement are listed in Table II. The image plates were read by the Fuji BAS2000 using a 100 μm pixel size.

Monte Carlo simulations were performed with MCMIS for the same conditions as the experimental images from X15A. Pixel size in the fine mesh image was 100 μm and in the coarse mesh image was 0.5 cm. Monte Carlo images were smeared with the measured system MTF and then had noise added in the same amount as in the corresponding synchrotron image, as described above. The scatter-to-primary ratios for a 2×2 cm area in the middle of the image as well as over the entire image are listed in Table II. Computing times for the entire Monte Carlo simulations (up to four monoenergetic calculations) are also listed for the Sun Ultra 60 (300 MHz).

Examples of the measured image and the simulated image matching the measurement for both the CD phantom and the ACR phantom are shown in Figs. 6 and 7. Although one image may exhibit a greater degree of darkening than the other in each set, the discernibility of the objects in each phantom is very nearly the same in the measured and simulated images, implying that the contrast values of the two images match. The Monte Carlo images are, of course, cleaner because they do not contain the experimental artifacts caused by defects in the monochromators and in the image plate.

Contrast of an object in the CD phantom is calculated by finding the difference in levels

inside and outside of a detail divided by the average level. For example, if the average pixel value inside the detail is a and the average pixel value just outside the detail is b , the contrast c is

$$c = \frac{|a - b|}{\frac{1}{2}(a + b)} \quad (2)$$

Fig. 8 shows the contrast from the first four columns (same thickness in each column) of the CD phantom shown in Fig. 6. In a perfect imaging system, the contrast would only decrease for thinner details, not for smaller diameter details. In real systems, the decrease in contrast that is observed for smaller objects of the same thickness is due to the scatter component, the MTF of the system and noise. Fig. 8 also shows the contrast calculated from the Monte Carlo image before the MTF and noise were applied, and it does not decrease with decreasing detail radius, indicating that scatter component is small in synchrotron images and only the MTF of the system (image plate and image plate reader) and noise degrades the contrast. The spread in the measured contrast values is mainly due to artifacts in the image.

For images taken with different collimator sizes, there was no significant change in the observed contrast. The results from MCMIS show average S/P ratios for the center of the CD phantom images of 0.5%, 0.6%, 1.4% and 4% for the four different collimator sizes of 3 mm, 5 mm, 10 mm and infinite (no collimators) used in the X15A images. Even the image where the S/P was 4%, scatter did not decrease the calculated contrast in the Monte Carlo image. Synchrotron imaging is essentially scatter free and it appears that the analytically calculated unscattered image, with MTF applied and noise, would be sufficient to model the images.

B. Fischer SenoscanTM

Eight images were taken on the Fischer SenoscanTM – five images of the contrast detail phantom at various kVp settings and filters and three images of the ACR phantom using

the aluminum filter. Before comparisons to the Monte Carlo images, the SenoscanTM images were reduced in resolution due to large file size, from 54 μm pixel size to 108 μm pixel size. The parameters of the SenoscanTM images are listed in Table III along with the measured noise level of the reduced images. These values were typically around 0.5%.

Monte Carlo simulations were performed using MCMIS for the same conditions as the SenoscanTM images. Pixel size in each fine mesh image was 100 μm and in the coarse mesh image was 0.5 cm. The scatter-to-primary ratios for a 2×2 cm area in the middle of the image as well as over the entire image are listed in Table III. Computer times are not listed for each image since the same monoenergetic images were used in making the different simulations at different kVp settings and different filters. The total times for all 36 monoenergetic contrast detail phantom images were 12 hours for the fine mesh unscattered and 72 hours for the coarse mesh scattered images. For the ACR phantom, the total fine mesh unscattered images took 6 hours and the coarse mesh scattered images took 99 hours. These times are for the Sun Ultra 60.

The simulations compare very nicely to the real SenoscanTM images. An example of each phantom image taken by the SenoscanTM and its Monte Carlo simulation are shown in Figs. 9 and 10. The simulated images appear very similar to the SenoscanTM images in the level of detail that is visible.

The computed contrast for the two CD phantom images, as well as the contrast from the Monte Carlo image before the MTF was used (to show contrast degradation from scatter alone) are shown in Fig. 11. Unlike the synchrotron images, the contrast of the SenoscanTM images are slightly degraded by the scatter contribution ($S/P \sim 9\%$). Being a scanning slot system, this degradation is still less than in today's conventional mammography units. After applying the MTF to the Monte Carlo image, the calculated contrast matches the contrast measured in the SenoscanTM image fairly well. Since the scatter degrades the contrast, modeling the SenoscanTM does require a calculation of the scatter component.

VII. SUMMARY

Accurate Monte Carlo simulation of complex imaging problems is possible by using a combination of three variance reduction techniques: rastering, point detectors and the separation of the unscattered and scattered components. Simulated images from two new mammography systems, the Fischer SenoscanTM and the synchrotron based system compared very well to real images, both in the level of detail visible in the images and the calculated contrast of standard details. Full 3-D simulation, generating a complete image, should be able to provide more information to system designers compared to simple pencil-beam simulations.

This study also determined that the amount of scatter in synchrotron images is so small, scatter can safely be left out of the simulation process. For scanning slot systems like the Fischer SenoscanTM, even though the amount of scatter is small compared to conventional mammography systems, the scatter does play an important role in the image formation process and needs to be modeled.

VIII. ACKNOWLEDGMENTS

Research was carried out in part at the National Synchrotron Light Source, Brookhaven National Laboratory, which is supported by the US Department of Energy, Division of Materials Sciences and Division of Chemical Sciences. Many thanks to Dr. W. C. Thomlinson and Dr. Z. Zhong for allowing this work to be done on beamline X15A.

Dr. R. Eugene Johnston of the University of North Carolina, Chapel Hill, provided assistance in both the synchrotron imaging and SenoscanTM imaging aspects of this study. We thank him for all of his valuable help.

Fischer Imaging Corporation supplied a great deal of technical information and help in modeling the SenoscanTM. Special thanks to Dr. M. M. Tesic for his time and energy in helping us.

Mr. Peplow, a doctoral student, was supported by Dr. R. Eugene Johnston, UNC-Chapel Hill, through his US Army Medical Research and Material Command Breast Cancer Research Grant. He is currently supported by a Nuclear Engineering Education Research (NEER) Grant from the Department of Energy, Idaho Operations Office.

Thanks also to the referees who helped make this a better article.

REFERENCES

- ¹ W. Thomlinson, "Medical applications of synchrotron radiation at the National Synchrotron Light Source" in *Synchrotron Radiation in the Biosciences* edited by B. Chance. Oxford:Clarendon (1994).
- ² R. Lewis, "Medical applications of synchrotron radiation x-rays" *Physics in Medicine and Biology*, **42**, 1213-1243 (1997).
- ³ F. Arfelli, G. Barbiellini, V. Bonvicini, A. Bravin, G. Cantatore, E. Castelli, L. Dalla Palma, M. Di Michiel, R. Longo, A. Olivo, S. Pani, D. Pontoni, P. Poropat, M. Prest, R. Rosei, M. Sessa, G. Tromba and A. Vacchi, "Digital mammography at the Trieste Synchrotron Light Source," *IEEE Transactions on Nuclear Science* **43**, 2061-2067 (1996).
- ⁴ E. Burattini, E. Cossu, C. Di Maggio, M. Gambaccini, P. L. Indovina, M. Marziani, M. Poeck, S. Simeoni and G. Simonetti, "Mammography with synchrotron radiation," *Radiology* **195**, 239-244 (1995).
- ⁵ R. E. Johnston, D. Washburn, E. Pisano, C. Burns, W. Thomlinson, L. D. Chapman, F. Arfelli, N. F. Gmür, Z. Zhong and D. E. Sayers, "Mammographic phantom studies with synchrotron radiation," *Radiology* **200**, 659-663 (1996).
- ⁶ D. Chapman, W. Thomlinson, R. E. Johnston, D. Washburn, E. Pisano, N. F. Gmür, Z. Zhong, R. Menk, F. Arfelli and D. E. Sayers, "Diffraction enhanced x-ray imaging," *Physics in Medicine and Biology* **42**, 2015-2025 (1997).
- ⁷ V. N. Ingal, E. A. Beliaevskaya, A. P. Brianskaya and R. D. Merkurieva, "Phase mammography - a new technique for breast investigation," *Physics in Medicine and Biology* **43**, 2555-2567 (1998).
- ⁸ M. J. Yaffe M J and J. A. Rowlands, "X-ray detectors for digital radiography" *Physics in Medicine and Biology* **42**, 1-39 (1997).

- ⁹ J. M. Boone and J. A. Seibert, "Monte Carlo simulation of the scattered radiation distribution in diagnostic radiology," *Medical Physics* **15**, 713-720 (1988).
- ¹⁰ H. P. Chan and K. Doi, "Physical characteristics of scattered radiation in diagnostic radiology: Monte Carlo simulation studies," *Medical Physics* **12**, 152-165 (1985).
- ¹¹ D. R. Dance and G. J. Day, "The computation of scatter in mammography by Monte Carlo methods," *Physics in Medicine and Biology* **29**, 237-247 (1994).
- ¹² Z. Jing, W. Huda and J. K. Walker, "Scattered radiation in scanning slot mammography," *Medical Physics* **25**, 1111-1117 (1998).
- ¹³ G. Spyrou, G. Tzanakos, A. Bakas, and G. Panayiotakis, "Monte Carlo generated mammograms: development and validation," *Physics in Medicine and Biology* **43**, 3341-3357 (1998).
- ¹⁴ E. C. Snow, "MCNPTM radiography patch," Los Alamos National Laboratory memorandum XTM:96-169(U) (1996).
- ¹⁵ G. P. Estes and W. M. Taylor, "Computational radiology and imaging with the MCNPTM Monte Carlo code," in *Computational Medicine, Public Health and Biotechnology: Building a Man in the Machine*, edited by M. Whitten (World Scientific Publishing Co., River Edge, NJ, 1995), pp. 832-845.
- ¹⁶ J. A. Halbleib, R. P. Kensek, T. A. Mehlhorn, G. D. Valdez, S. M. Seltzer and M. J. Berger, *ITS Version 3.0: The Integrated TIGER Series of coupled electron/photon Monte Carlo transport codes* SAND91-1634 (Sandia National Laboratories, Albuquerque, NM, 1992).
- ¹⁷ J. H. Hubbell and I. Øverbø, "Relativistic atomic form factors and photon coherent cross sections," *Journal of Physical and Chemical Reference Data* **8**, 69-105 (1979).
- ¹⁸ D. E. Peplow and K. Verghese, "Measured molecular coherent scattering form factors of

- animal tissues, plastics and human breast tissue,” *Physics in Medicine and Biology* **43**, 2431-2452 (1998).
- ¹⁹ D. E. Peplow, *Monte Carlo Mammography Image Simulation with Measured Coherent Scattering Form Factors and Differential Sampling*, doctoral dissertation at North Carolina State University, available through UMI (Bell & Howell) (1999).
- ²⁰ J. M. Boone, “Parameterized x-ray absorption in diagnostic radiology from Monte Carlo calculations: implications for x-ray detector design,” *Medical Physics* **19**, 1467-1473 (1992).
- ²¹ B. Liu, M. Goodsitt and H. P. Chan, “Normalized average glandular dose in magnification mammography,” *Radiology* **197**, 27-32 (1995).
- ²² C. J. Leliveld, J. G. Maas, V. R. Bom and C. W. E. van Eijk, “Monte Carlo modeling of coherent scattering: influence of interference,” *IEEE Transactions on Nuclear Science* **43**, 3315-3321 (1996).
- ²³ International Commission on Radiation Units and Measurements, “Modulation transfer function of screen-film systems” Report 41, p 21 (1986).
- ²⁴ J. M. Boone, T. R. Fewell and R. J. Jennings, “Molybdenum, rhodium, and tungsten anode spectral models using interpolating polynomials with application to mammography” *Medical Physics* **24**, 1863-1874 (1997).

TABLES

TABLE I. Energies and intensities (without any filtration) from the monochromator on NSLS beamline X15A. It should be noted that the 1.5 to 4.5 mm of added aluminum used in the synchrotron images preferentially reduced the low energy components of the beam.

desired energy (keV)	[111] reflection		[333] reflection		[444] reflection		[555] reflection	
	E_i	I_i	E_i	I_i	E_i	I_i	E_i	I_i
	(keV)		(keV)		(keV)		(keV)	
18	18	1	54	0.00065	72	1.7e-6	90	1.9e-7
26	8.67	0.008	26	1	34.67	0.19	43.33	0.016
34	11.33	4.26	34	1	45.33	0.099	56.67	0.0046
42	14	92.80	42	1	56	0.058	70	0.0017

TABLE II. Parameters of the real and simulated synchrotron images.

#	phantom	energy	slit	Real Image	Monte Carlo Simulations			
		(keV)	width	Relative Uncertainty (Noise)	S/P_{mid}	S/P	Unscat. Time (hours)	Scat. Time (hours)
1	CD	18	3 mm	0.0096	0.0047	0.0037	0.095	2.8
2	CD	26	3 mm	0.0079	0.0036	0.0032	0.064	2.6
3	CD	34	3 mm	0.0070	0.0031	0.0030	0.069	2.7
4	CD	42	3 mm	0.0058	0.0030	0.0027	0.065	2.8
5	CD	18	5 mm	0.0083	0.0063	0.0057	0.060	3.2
6	CD	18	10 mm	0.0091	0.014	0.012	0.039	6.5
7	CD	18	none	0.0078	0.040	0.034	0.008	23.0
8	ACR	18	3 mm	0.0094	0.011	0.010	0.046	4.4
9	ACR	26	3 mm	0.0089	0.010	0.0094	0.044	4.0
10	ACR	34	3 mm	0.0073	0.0092	0.0085	0.038	4.1
11	ACR	42	3 mm	0.0092	0.0090	0.0080	0.037	4.9
12	ACR	18	5 mm	0.0118	0.019	0.018	0.046	6.0
13	ACR	18	10 mm	0.0096	0.040	0.035	0.027	10.5
14	ACR	18	none	0.0119	0.11	0.095	0.016	30.4

TABLE III. Parameters of the real and simulated SenoscanTM images.

#	phantom	kVp	filter	Real Image	M C Simulations	
				Relative Uncertainty (Noise)	S/P_{mid}	S/P
1	CD	25	Al	0.00529	0.095	0.092
2	CD	30	Al	0.00382	0.092	0.087
3	CD	35	Al	0.00393	0.089	0.084
4	CD	30	Rh	0.00463	0.094	0.090
5	CD	30	Mo	0.00644	0.096	0.093
6	ACR	30	Al	0.00651	0.22	0.20
7	ACR	35	Al	0.00509	0.21	0.19
8	ACR	40	Al	0.00454	0.19	0.18

FIGURES

FIG. 1. Imaging with a monoenergetic beam from the synchrotron. The white radiation from the synchrotron (W) passes through the double monochromator (M) to select a single energy of photons. The fan beam is collimated by horizontal slits (C) and the dose is measured by ionization chambers (IC). An absorber (A) is used to attenuate the beam. The stage (S) holding the target object (T) and the image plate (P) are scanned through the fixed beam. Exposure to the plate is regulated by the speed of the stage, which is controlled by the current from the second ionization chamber. (Figure not to scale.)

FIG. 2. The Fischer SenoscanTM scanning slot digital mammography unit. The anode and CCD detector array move together scanning the breast with a well-collimated fan beam. (Figure not to scale.)

FIG. 3. Schematics of the two common mammography phantoms used in the real and simulated images. The upper drawing is the contrast detail phantom (10.8×14.9×1.5 cm thick) and the lower drawing is the American College of Radiologists phantom (10.16×10.16×4.88 cm thick).

FIG. 4. Image processing for simulating the synchrotron images: (a) the unscattered image and the (b) scattered image calculated by Monte Carlo are added together (c). Quantum mottle noise is then added (d). The image is smeared using the measured system MTF (e) and image plate reader noise is added creating the final image (f). Each image is scaled to maximize visual contrast.

FIG. 5. Predicted relative uncertainty in each synchrotron image using the three-term noise model compared to the observed relative uncertainty in each real image. The fourteen images are those listed in Table II.

FIG. 6. Images of the contrast detail phantom. Top – real image obtained with the synchrotron system at 18 keV with no collimators. Bottom – Monte Carlo simulation.

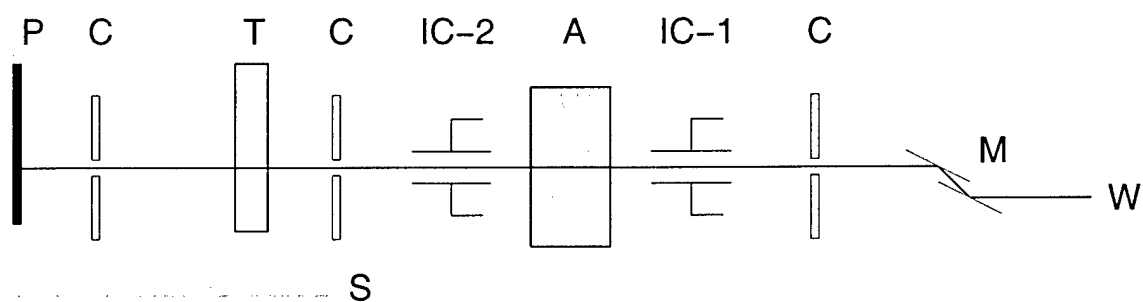
FIG. 7. Images of the ACR phantom. Top – real image obtained with the synchrotron system at 18 keV with 5 mm collimators. Bottom – Monte Carlo simulation.

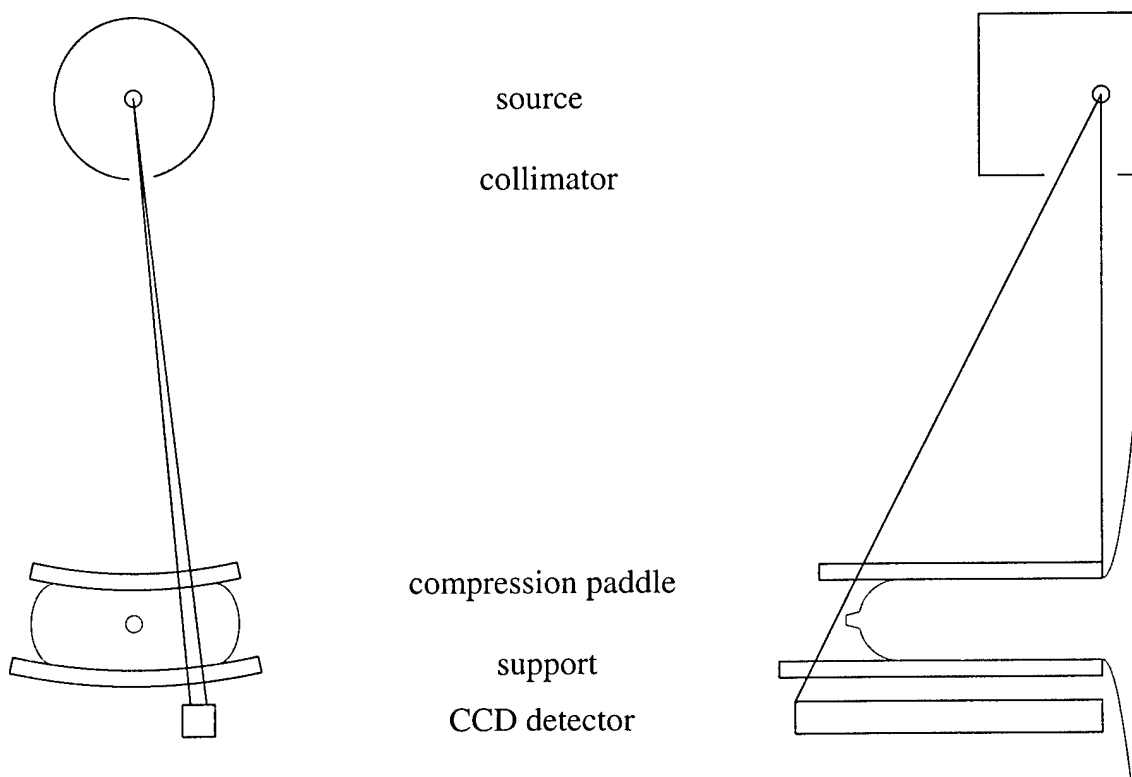
FIG. 8. Contrast of the details in the CD phantom as a function of detail radius. Each series of points is from a column of details of the same thickness. Data from the real synchrotron image appear as points and the contrast values calculated from the simulated image appear as lines: solid lines from the raw Monte Carlo images and dashed lines after the MTF and noise have been added.

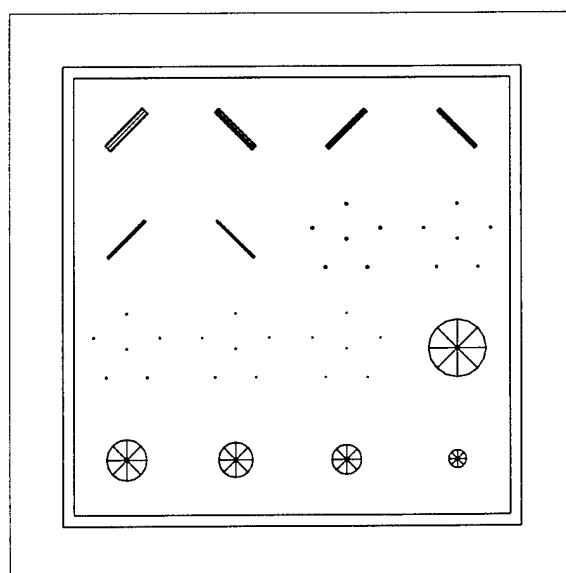
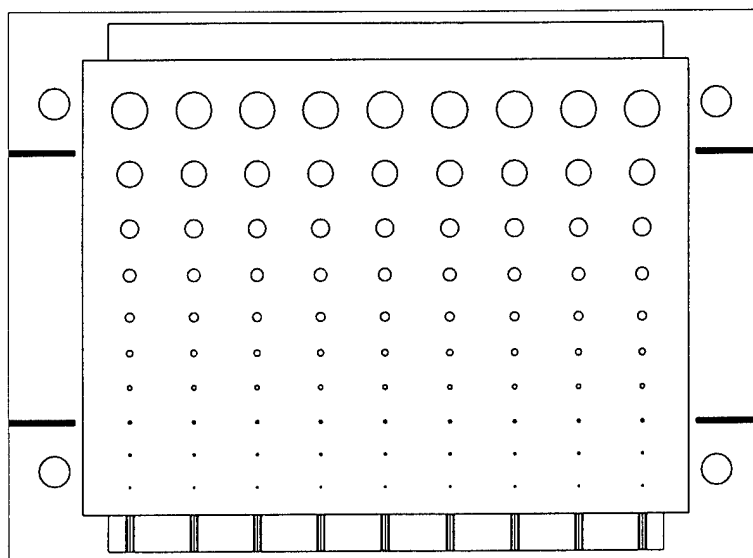
FIG. 9. Images of the contrast detail phantom. Top – real image obtained with the Fischer SenoscanTM at 25 kVp with an aluminum filter. Bottom – Monte Carlo simulation.

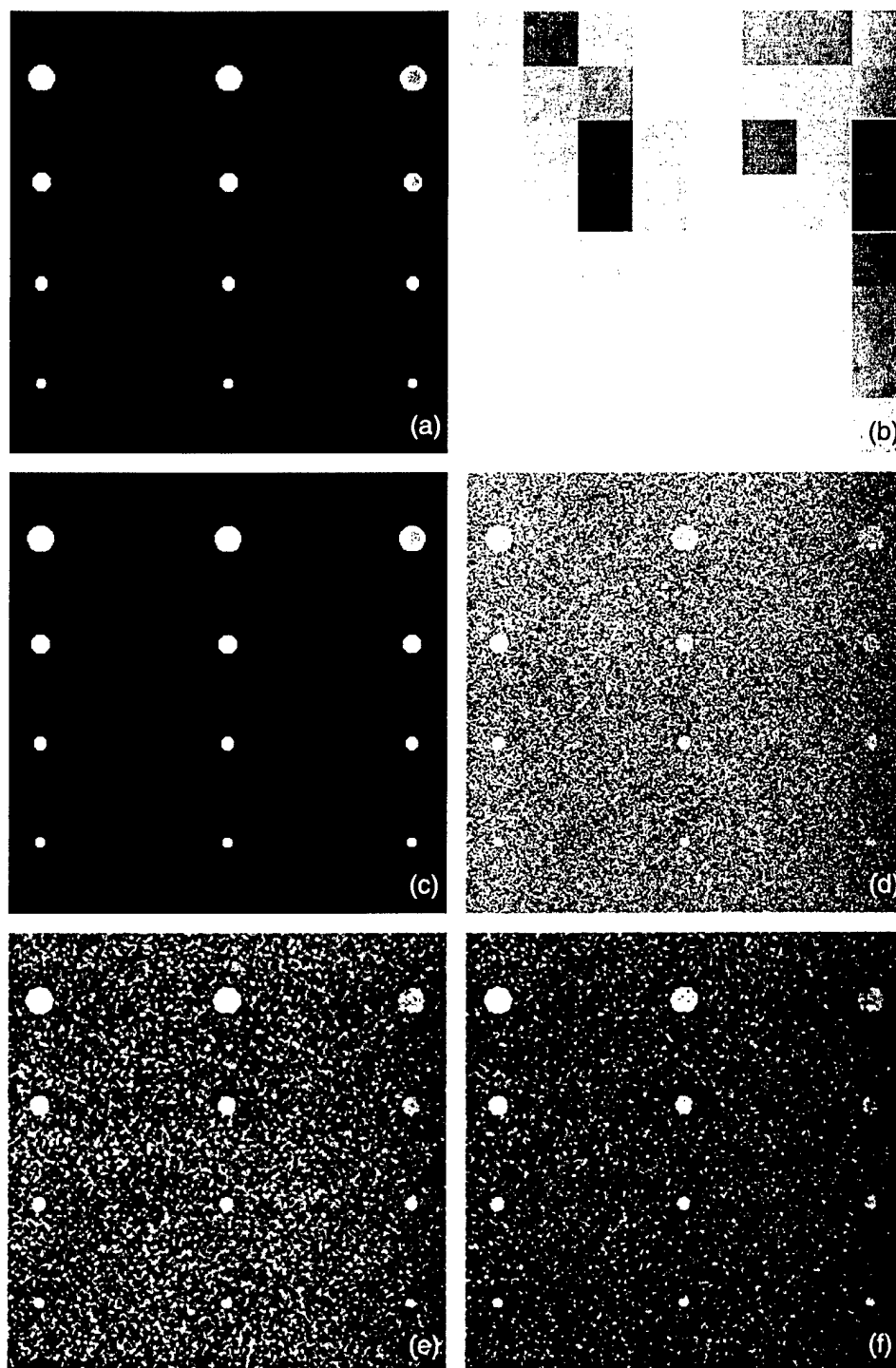
FIG. 10. Images of the ACR phantom. Top – real image obtained with the Fischer SenoscanTM at 30 kVp with an aluminum filter. Bottom – Monte Carlo simulation.

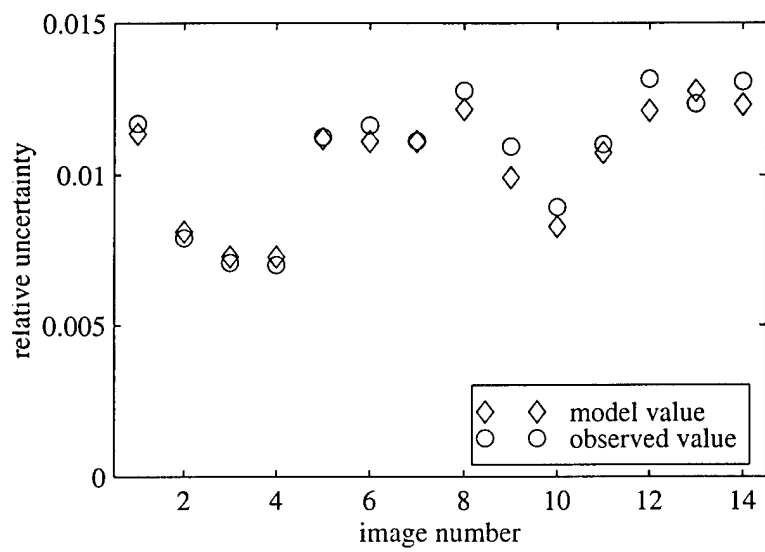
FIG. 11. Contrast of the details in the CD phantom as a function of detail radius. Each series of points is from a column of details of the same thickness. Data from the Fischer SenoscanTM appear as points and the contrast values calculated from the simulated image appear as lines: solid lines from the raw Monte Carlo images and dashed lines after the MTF and noise have been added.

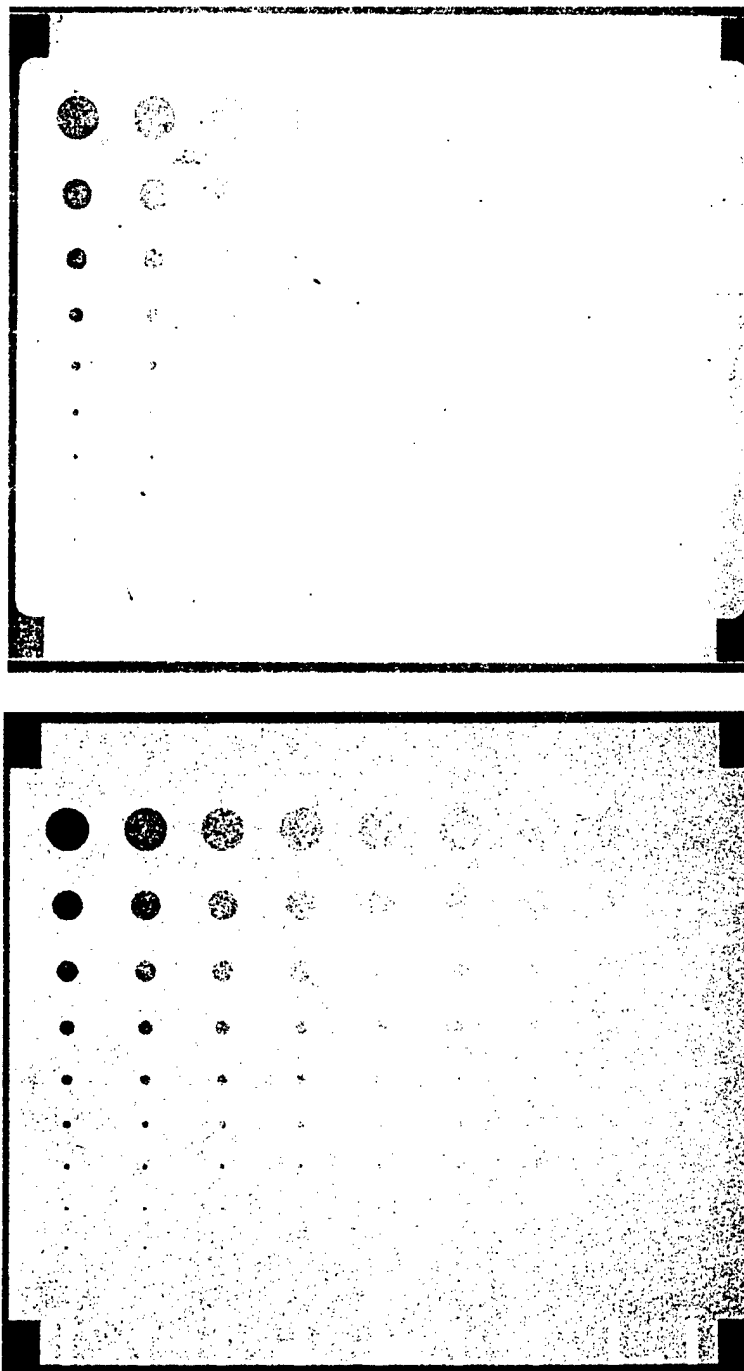


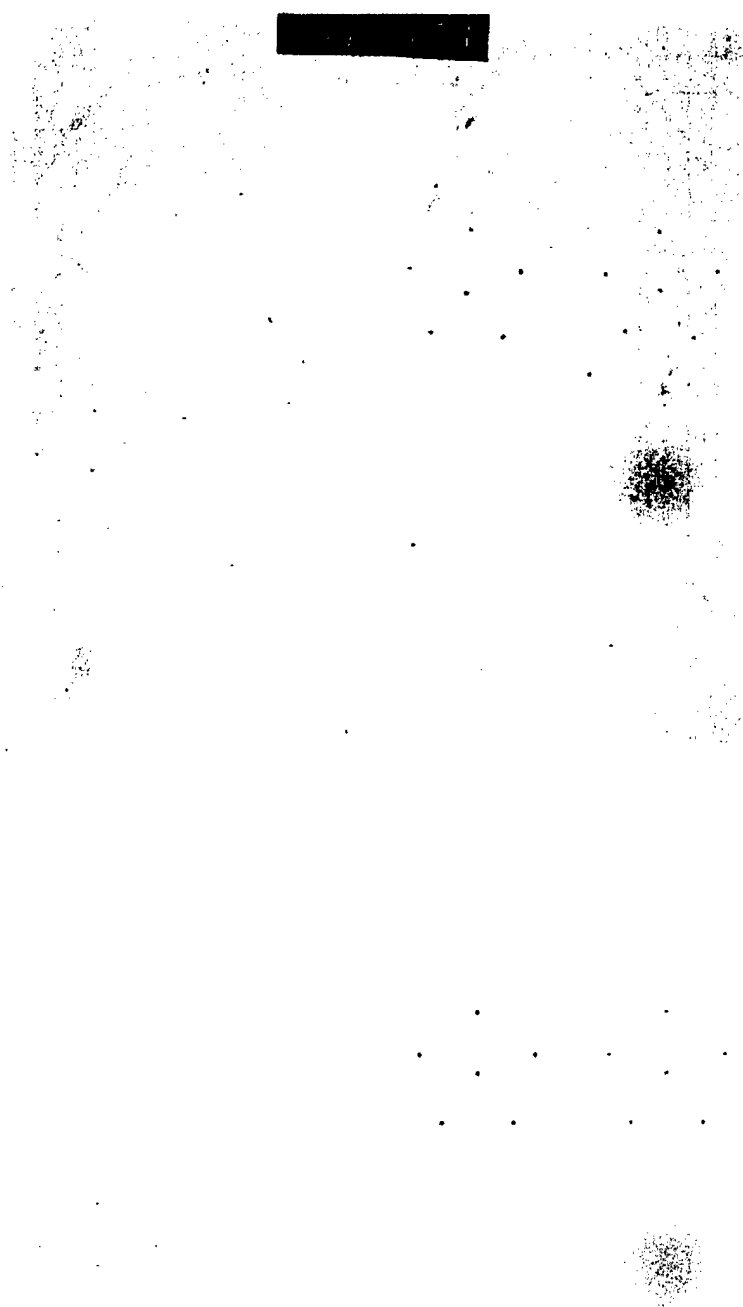


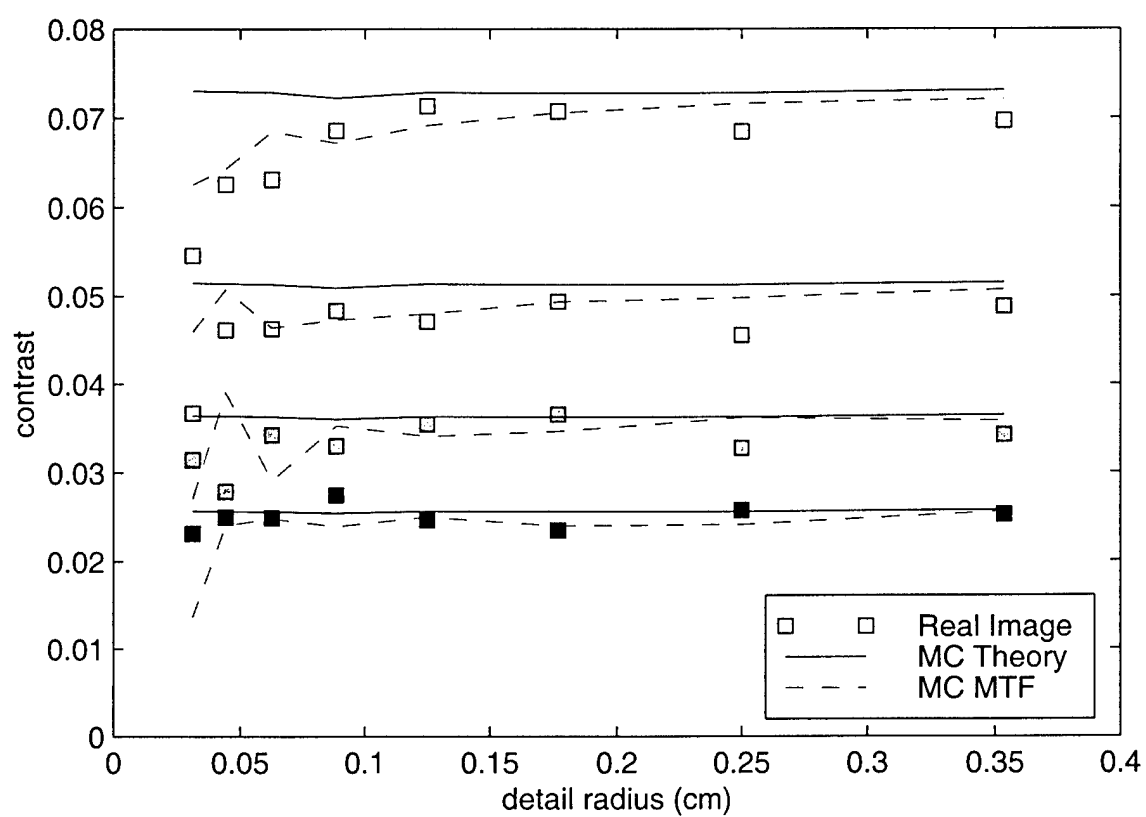


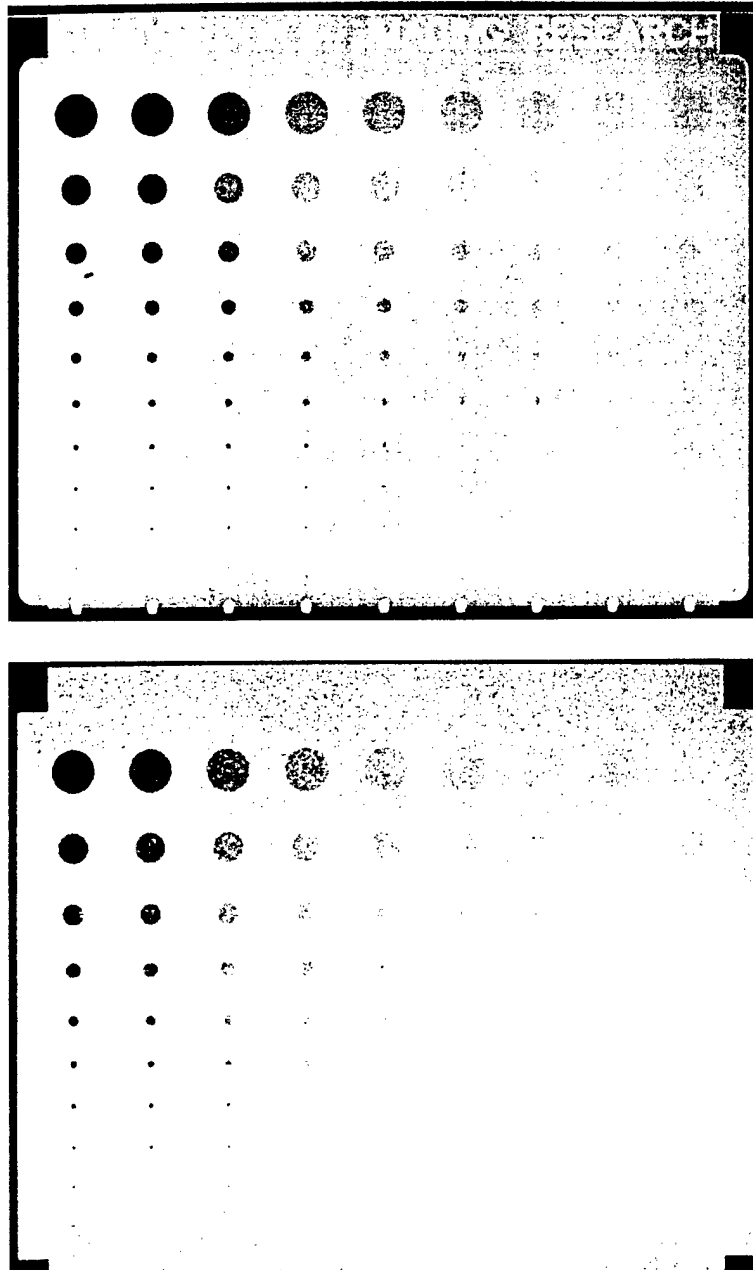


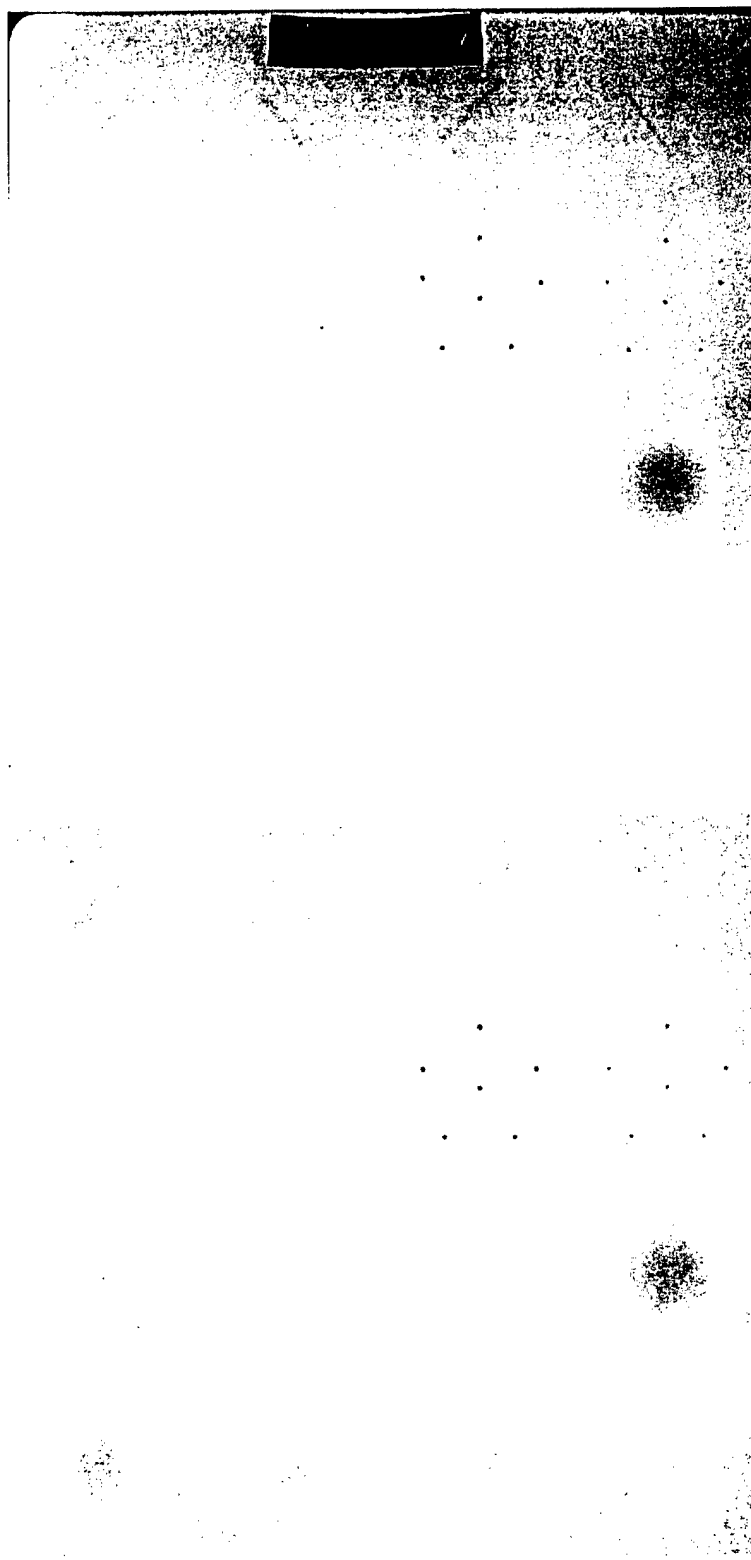


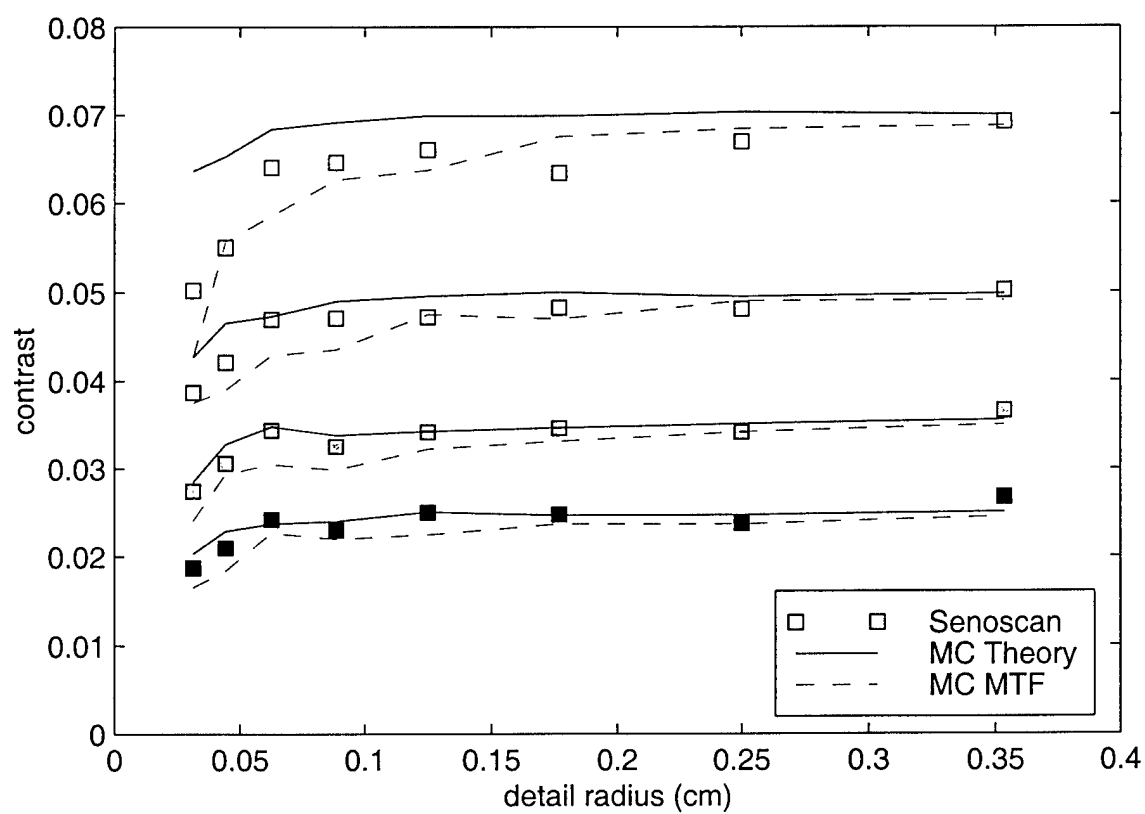












Appendix

A.8

"Diffraction Enhanced X-ray Imaging", Medical Applications of Synchrotron Radiation, eds. M. Ando and C. Uyama (Springer-Verlag, Tokyo, 1998) p. 72-76, W. Thomlinson, D. Chapman, Z. Zhong, R. E. Johnston and D. Sayers.

Diffraction Enhanced X-ray Imaging

W. Thomlinson¹, D. Chapman², Z. Zhong¹, R. E. Johnston³ and D. Sayers⁴

¹National Synchrotron Light Source, Brookhaven National Laboratory, Upton, NY 11973, USA

²CSRRI, Illinois Institute of Technology, 3101 South Dearborn, Chicago, IL 60616, USA

³Department of Radiology, University of North Carolina, Chapel Hill, NC 27599, USA

⁴Department of Physics, North Carolina State University, Raleigh, NC 27695, USA

SUMMARY. Diffraction enhanced imaging (DEI) is a new x-ray radiographic imaging modality using synchrotron x-rays which produces images of thick absorbing objects that are almost completely free of scatter. They show dramatically improved contrast over standard imaging applied to the same phantoms. The contrast is based not only on attenuation but also the refraction and diffraction properties of the sample. The diffraction component and the apparent absorption component (absorption plus extinction contrast) can each be determined independently. This imaging method may improve the image quality for medical applications such as mammography.

KEY WORDS: synchrotron, mammography, diffraction enhanced imaging, DEI

INTRODUCTION

Normal medical x-ray radiography uses an area beam which, after traversing and interacting with the subject, is detected by an area detector. The interaction of x-rays with the subject is complex, involving absorption, refraction [1-2] and scattering. The scattering includes small angle scattering [3] (scattering angles less than mrad) which carries information about the subject's structure on the length scale up to microns. This information is lost in normal radiography because of its small angle nature. X-ray diffraction of perfect crystals, with its narrow reflection angular width (on the order of a few microradians) and peak reflectivity of close to unity (for Bragg diffraction), provides a mechanism for rejecting or accepting small angle scattering, thus providing additional information about the subject.

An imaging method called Diffraction Enhanced Imaging (DEI) has been reported [4] which utilizes a perfect crystal analyzer and centers around the concept of taking digital images at different analyzer positions and combining them to produce apparent absorption and refraction images of the object. It was demonstrated in experiments at the National Synchrotron Light Source that one can separate the refraction effects from the absorption by taking images at two positions on either side of the rocking curve. Objects which have different small angle scattering characteristics from their surroundings can be enhanced by taking images at suitable analyzer positions [5]. These experiments were done with standard mammography phantoms which, although suggesting the potential applicability of DEI to mammography, do not directly prove this due to anticipated differences between the phantom tumor simulation and real tumors. A new set of experiments was performed at the Advanced Photon Source (APS) to study the tissue characterization capability of DEI with biological phantoms consisting of imbedded tumors. This paper reports the preliminary results obtained in that experiment. A more detailed analysis of the results is in preparation and will be submitted for publication soon.

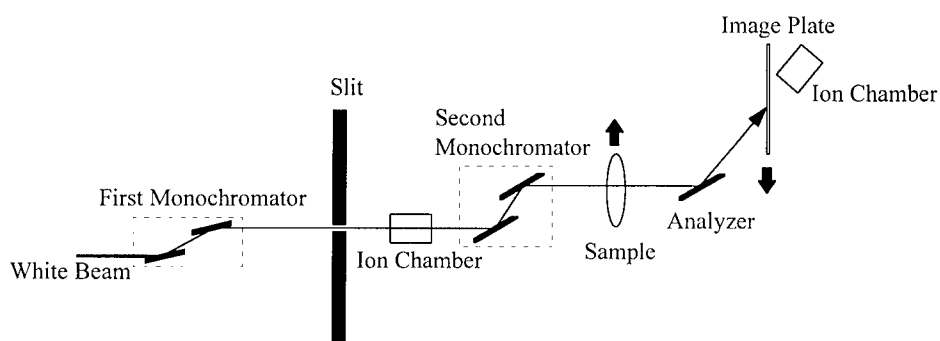


Fig.1. The setup of the experiment with an analyzer crystal

EXPERIMENTAL METHOD

The experiment was performed at the Synchrotron Radiation Instrumentation Collaborative Access Team (SRICAT) sector 1-BM-B (a bending magnet beamline) of the APS. The experimental setup is shown in Fig.1. Perfect silicon crystals in Bragg geometry were used for producing the monochromatic beam and as the analyzer. The first double-crystal monochromator was the beamline monochromator located upstream of the experimental hut in the beamline. The [111] reflection was used for this monochromator to pre-monochromize the white beam to 18 keV and to deliver the beam into the experimental hut. The second monochromator crystals were set to the [333] reflection. Because of the dispersion mismatch between the two monochromators and the vertical divergence of the incident beam, the tuning curve of the second monochromator unit with respect to the first monochromator was much wider than the Darwin width of the [333] reflection. Thus the beam intensity on the sample was stable against relative changes of angle between the two monochromators (which was hard to avoid in this prototype set-up due to vibrations).

The analyzer, also [333], was non-dispersive with respect to the second monochromator. The analyzer was mounted on a tangent arm with 1 meter arm length driven by a linear translator of 0.1 micrometer resolution. This provides an angular resolution of 0.1 microradians which is sufficient to tune the analyzer to any location on the analyzer rocking curve which has a FWHM of around 5 microradians for 18 keV x-rays. The tangent arm was mounted on the same optical table as the second monochromator to minimize intensity modulation due to relative angle changes between them caused by vibrations. The beam intensity at the APS was strong enough to provide a surface dose on the order of a few mGy to the sample at a sample scan speed of about 10 mm/s.

Various phantoms and biological samples were imaged. The biological samples studied included a mouse with an implanted tumor and beef tissue with an implanted subcutaneous dog tumor. Each biological sample was preserved in formalin, sealed in a plastic bag and compressed between two Lucite plates. Additional Lucite plates were added during the imaging to make the absorbing thickness on the order of 30-40 mm.

For each sample, a "normal" radiograph with the monochromatic beam at 18 keV was taken by moving the analyzer out of the beam and scanning the image plate and sample through the fan beam in the same direction and at the same speed. DEI tissue characterization studies were performed in several ways: a) With the analyzer tuned to various positions on the rocking curve, the entire phantom and the image plate were translated in opposite directions at the same speed

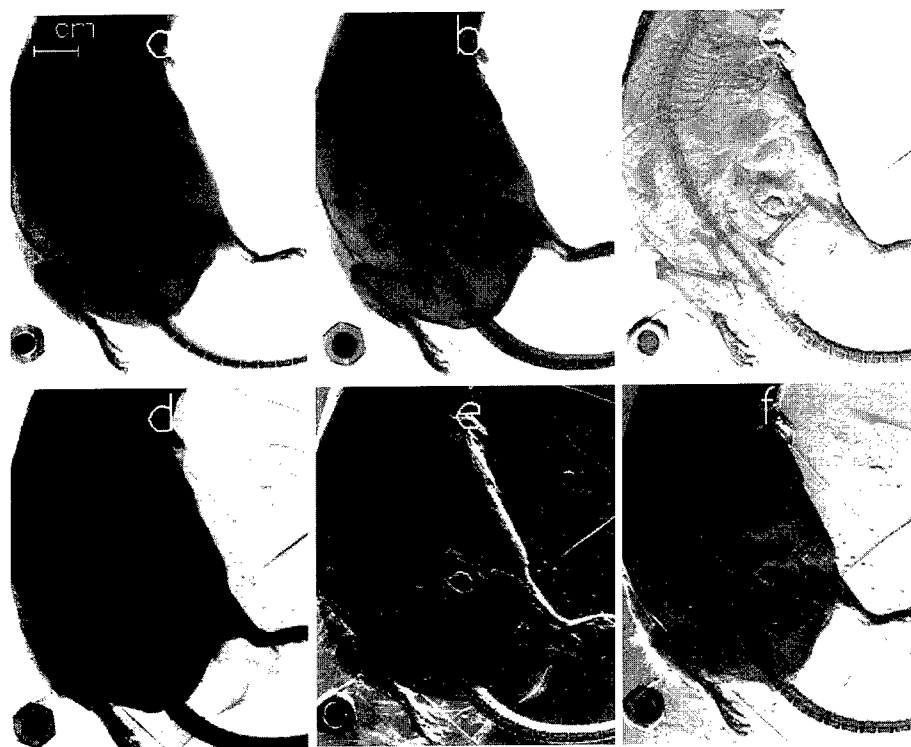


Fig. 2. Images of mouse with imbedded tumor. **a**, "Normal" radiograph taken with analyzer removed. **b**, Apparent absorption image by summing up the images taken with analyzer at ± 1.5 micro radians. **c**, Refraction image represented by the difference of the ± 1.5 micro radians images. **d**, Image taken with analyzer at the peak of the rocking curve. **e**, Image with analyzer at -3 microradians. **f**, Analyzer at $+3$ microradians.

through the fan beam; b) Multi-scans: with the analyzer tuned to each of a series of predefined positions on the rocking curve, a short scan of a region of sample was performed as in a). The image plate was repositioned after each scan so that images did not overlap on the image plate; c) Rocking curves through a line on the phantom were obtained by fixing the phantom in the fan beam and performing a series of exposures with incrementing analyzer position and image plate vertical position.

RESULTS AND ANALYSIS

The images of the mouse are shown in Fig.2. Fig.2a shows a "normal" radiograph. Fig.2b and Fig.2c show the apparent absorption and refraction images, respectively, of the mouse. These images are derived from the images taken at ± 1.5 microradians on each side of the analyzer rocking curve. It is clear from the refraction image that the tumor (about 5 mm in diameter) has been "implanted" in the leg of the mouse. The refraction image shows the "crater" (not present in the "normal" radiograph) formed when the tumor was pushed into the tissue. Compared to the

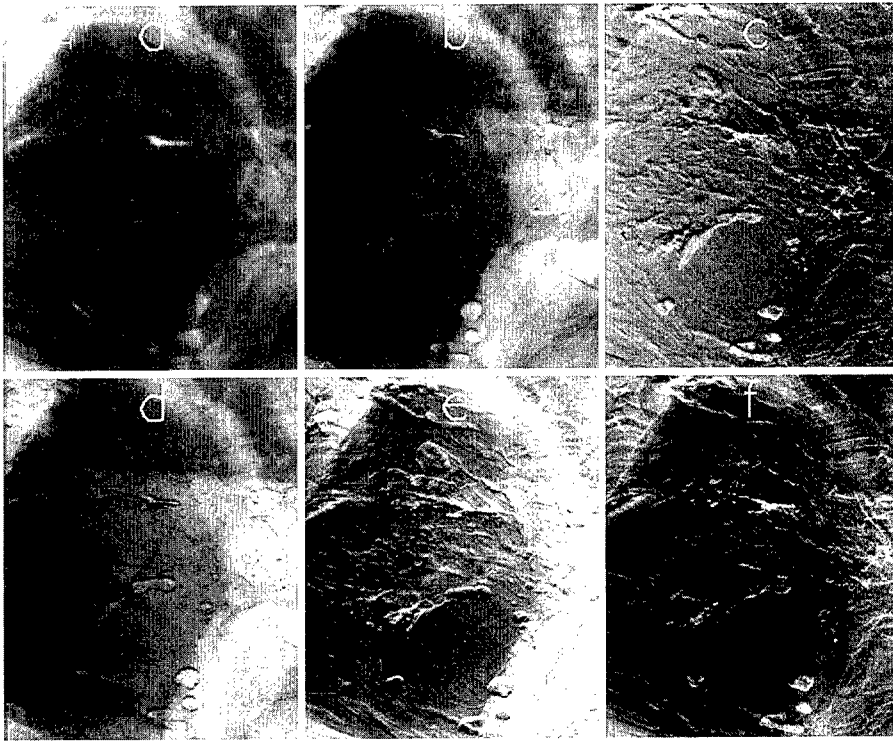


Fig. 3. Images of beef with an imbedded dog tumor. **a.** "Normal" radiograph taken with the analyzer removed. **b.** Apparent absorption image represented by sum of the images taken with the analyzer at ± 1.5 microradians. **c.** Refraction image represented by the difference of the ± 1.5 micro-radians images. **d.** Image taken with the analyzer at the peak of the rocking curve. **e.** Image with the analyzer at -3 microradians. **f.** Image with the analyzer at +3 microradians.

"normal" radiograph, the apparent absorption image (Fig.2b) shows more contrast for the tumor. This demonstrates DEI's ability to enhance tissues whose small angle scattering is different than the surrounding tissues. Fig.2e and 2f show images taken further in the wings of the analyzer rocking curve at plus/minus 3 microradians.

The images of the beef with the imbedded dog tumor are shown in Fig.3. Fig.3a shows a "normal" radiograph. The tumor is the roughly circular object with about 2 cm diameter close to the bottom of the image. Fig.3b and Fig.3c show the apparent absorption and refraction images, respectively. It is clear from the refraction image that the tumor has been "implanted" in the beef. The refraction image shows the "crater" formed when the tumor was pushed into the tissue. The crater is not present in the "normal" radiograph. This clearly demonstrates DEI's ability to enhance edges of features in biological objects. Since DEI is not sensitive to refraction when the analyzer is on top of the peak, the apparent absorption image (Fig.3b) is comparable to the image taken with the analyzer at the peak of the rocking curve (Fig.3d). Figs.3e and 3f show images taken farther out on the wings of the analyzer rocking curve at ± 3 micro-radians. It appears that the dog tumor may have a lack of small angle scattering and a lack of complex refraction at large analyzer rocking

curve angles due to smoother morphology of the tumor as compared to beef tissue. There is a reversal in the contrast of the tumor relative to the beef when the analyzer angle is changed from the peak (Fig.3d) to +3 (Fig.3f) micro-radians. This is due to the different relative small angle scattering distributions of the tumor and the beef, and suggests that the tumor can be selectively highlighted. This indicates that DEI may be sensitive to the extinction and refraction contrast in cancerous tissue. In all cases, it is clear that new information is obtained by the DEI technique and that DEI at different analyzer positions on the rocking curve can enhance different features of the sample.

DISCUSSION

The consequence of the two sources of contrast (refraction and extinction contrast) is of importance to mammography and medical imaging in general. These contrast sources are largely energy independent effects as opposed to absorption. Conventional radiography depends on the absorption of x-rays by an object to create the radiograph, thus a compromise must be made between the contrast, signal to noise ratio and the absorbed dose. Refraction and scattering is expected to remain the same as the imaging energy is increased. This raises the possibility of successfully applying this technique at higher x-ray energies. This will be the focus of further investigation.

ACKNOWLEDGMENTS

We would like to thank Fuji Medical Systems for the loan of the AC3 image plate reader system and technical support in setting up and operating the unit. We would like to also thank the staff members at APS SRICAT for technical support and beamtime. This work was supported in part by US ARMY grant DAMD17-96-1-6143 and at the National Synchrotron Light Source by US Department of Energy Contract DE-AC02-76CH00016 and ARPA contract AOB227.

REFERENCES

1. Bushuev VA, Ingal VN, Belyaevskaya EA (1996) Dynamical theory of images generated by noncrystalline objects for the method of phase-dispersive introscopy. *Crystallography Reports* 41(5): 766-774
2. Podurets KM, Somenkov VA, Shilstein SS (1989) Neutron radiography with refraction contrast. *Physica B* 156&157: 691-693
3. Guinier A, Fournet G, Walker CB Yudowitch KL (1955) *Small-angle scattering of x-rays*. Wiley, New York.
4. Chapman D, Thomlinson W, Arfelli F, Gmür N, Zhong Z, Menk R, Johnston RE, Washburn D, Pisano E, Sayers D (1996) Mammography imaging studies using a Laue crystal analyzer. *Rev Sci Instrum* 67(9): CD-ROM
5. Chapman D, Thomlinson W, Johnston RE, Washburn D, Pisano E, Gmür N, Zhong Z, Menk R, Arfelli F, Sayers D (1997) Diffraction enhanced x-ray imaging. *Phys Med Bio*, Accepted for publication

Appendix

A.9

D.E. Peplow ``Direction Cosines and Polarization Vectors for Monte Carlo Photon Scattering". Nuclear Science and Engineering 1999: 131, 132-136.

Direction Cosines and Polarization Vectors for Monte Carlo Photon Scattering

Douglas E. Peplow*

*North Carolina State University, Department of Nuclear Engineering, Box 7909
Raleigh, North Carolina 27695*

Received April 2, 1998

Accepted June 16, 1998

Abstract—New ways to calculate the direction cosines and polarization vectors for Monte Carlo photon scattering are developed and presented. The new approach for direction cosines is more physical, easier to understand, straightforward to implement, and—for simulations involving polarized photons—slightly faster than the traditional approach. The polarization vector after scatter is also presented.

I. TRADITIONAL METHOD FOR DIRECTION COSINES

Carter and Cashwell¹ presented a scheme, which is used in many Monte Carlo codes, for finding the direction cosines of a photon after a scatter. For a photon with unit direction vector $\mathbf{\Omega} = \langle u, v, w \rangle$ that is then scattered with polar angle θ and azimuthal angle ϕ , the scattered direction vector is

$$\mathbf{\Omega}' = \begin{bmatrix} u' \\ v' \\ w' \end{bmatrix} = \begin{cases} \begin{bmatrix} \sqrt{1-\mu^2} \cos \phi \\ \sqrt{1-\mu^2} \sin \phi \\ \frac{\mu w}{|w|} \end{bmatrix} & \text{if } |w| \sim 1 \\ \begin{bmatrix} u\mu + (uw \cos \phi - v \sin \phi) \frac{\sqrt{1-\mu^2}}{\sqrt{1-w^2}} \\ v\mu + (vw \cos \phi + u \sin \phi) \frac{\sqrt{1-\mu^2}}{\sqrt{1-w^2}} \\ w\mu - \cos \phi \sqrt{1-\mu^2} \sqrt{1-w^2} \end{bmatrix} & \text{otherwise,} \end{cases} \quad (1)$$

using $\mu = \cos \theta$ and $\sqrt{1-\mu^2} = \sin \theta$. These relationships come from a transformation of coordinates so that the original photon direction is on the z axis, scattering with angles θ and ϕ , and then the coordinates are transformed back to the laboratory frame. These expressions were originally derived from rotations through angles expressed as complex numbers by Cashwell and Everett.²

The same result can be found without a coordinate transformation. The direction $\phi = 0$ is defined to be a unit vector lying on the plane perpendicular to $\mathbf{\Omega}$ and also lying in a plane that contains the projection of $\mathbf{\Omega}$ on the x - y plane, pointing downward. This vector in the $\phi = 0$ direction, \mathbf{q}_1 , is then $1/\sqrt{1-w^2} \langle uw, vw, w^2 - 1 \rangle$. To define the direction of increasing ϕ , the direction of $\phi = \pi/2$, \mathbf{q}_2 , can be chosen such that $\mathbf{q}_2 = \mathbf{\Omega} \times \mathbf{q}_1$. This gives

*E-mail: depeplow@eos.ncsu.edu

$\mathbf{q}_2 = 1/\sqrt{1-w^2} \langle -v, u, 0 \rangle$ and completely defines ϕ for the original photon $\mathbf{\Omega}$. This is shown in Fig. 1. For the special case of $|w| \sim 1$, \mathbf{q}_1 can be defined as $\langle 1, 0, 0 \rangle$ and \mathbf{q}_2 as $\langle 0, 1, 0 \rangle$.

From the foregoing definitions, the new direction $\mathbf{\Omega}'$ can be expressed as a linear combination of the three orthogonal vectors $\mathbf{\Omega}$, \mathbf{q}_1 , and \mathbf{q}_2 :

$$\mathbf{\Omega}' = \mathbf{\Omega} \cos \theta + \mathbf{q}_1 \cos \phi \sin \theta + \mathbf{q}_2 \sin \phi \sin \theta . \quad (2)$$

By inserting the components of \mathbf{q}_1 , \mathbf{q}_2 , and $\mathbf{\Omega}$, the scattered vector is found to be

$$\mathbf{\Omega}' = \begin{bmatrix} u' \\ v' \\ w' \end{bmatrix} = \begin{bmatrix} u \cos \theta + \cos \phi \sin \theta \frac{uw}{\sqrt{1-w^2}} + \sin \phi \sin \theta \frac{-v}{\sqrt{1-w^2}} \\ v \cos \theta + \cos \phi \sin \theta \frac{vw}{\sqrt{1-w^2}} + \sin \phi \sin \theta \frac{u}{\sqrt{1-w^2}} \\ w \cos \theta + \cos \phi \sin \theta \frac{w^2-1}{\sqrt{1-w^2}} + \sin \phi \sin \theta \frac{0}{\sqrt{1-w^2}} \end{bmatrix} \quad (3)$$

$$= \begin{bmatrix} u\mu + (uw \cos \phi - v \sin \phi) \frac{\sqrt{1-\mu^2}}{\sqrt{1-w^2}} \\ v\mu + (vw \cos \phi + u \sin \phi) \frac{\sqrt{1-\mu^2}}{\sqrt{1-w^2}} \\ w\mu - \cos \phi \sqrt{1-\mu^2} \sqrt{1-w^2} \end{bmatrix}, \quad (4)$$

which is a result identical to that of Carter and Cashwell. Using the components of the special case for \mathbf{q}_1 and \mathbf{q}_2 and taking $\mathbf{\Omega} \sim \langle 0, 0, \pm 1 \rangle$ will then give the special case of Carter and Cashwell.

For some routines (for example, biasing routines), the initial and scattered photon directions are known, and the two scatter angles θ and ϕ need to be found. This can be done with

$$\mu = \mathbf{\Omega} \cdot \mathbf{\Omega}' = uu' + vv' + ww' , \quad (5)$$

$$\cos \phi = \frac{\mathbf{q}_1 \cdot \mathbf{\Omega}'}{\sqrt{1-\mu^2}} = \frac{1}{\sqrt{1-\mu^2} \sqrt{1-w^2}} \times (uwu' + vvv' + w'(w^2-1)) , \quad (6)$$

and

$$\sin \phi = \frac{\mathbf{q}_2 \cdot \mathbf{\Omega}'}{\sqrt{1-\mu^2}} = \frac{1}{\sqrt{1-\mu^2} \sqrt{1-w^2}} \times (uv' - vu') , \quad (7)$$

being careful of the special cases of $\mu = \pm 1$ and $w = \pm 1$. Two equations are needed for ϕ so that it may be specified over the entire range of $[-\pi, \pi]$. In ForTran, the dual argument arctangent function $\phi = \text{atan2}[uv' - vu', uwu' + vvv' + w'(w^2-1)]$ will report ϕ over the whole range.

II. A SIMPLIFIED APPROACH

The Carter and Cashwell approach to finding the new direction cosines works but is unnecessarily difficult to

comprehend physically and is somewhat arbitrary in its definition of the azimuthal angle. Coordinate transformations or arbitrarily defining the $\phi = 0$ direction based on the laboratory coordinate system are not easy to understand, and they break down for some initial directions ($w = \pm 1$), which forces the programmer to set up special cases.

When the Carter and Cashwell technique is applied to polarized radiation, extra complications arise in

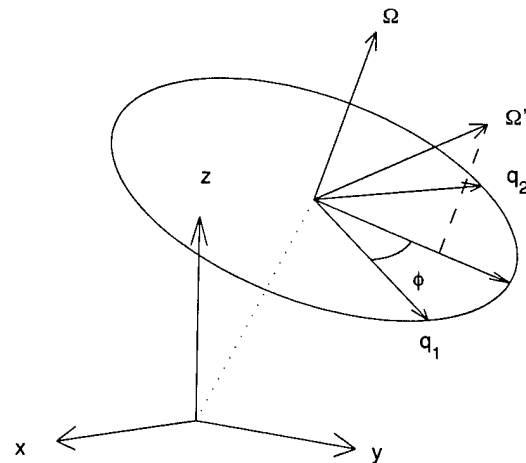


Fig. 1. Geometry of a scatter from direction $\mathbf{\Omega}$ to $\mathbf{\Omega}'$ similar to the Carter and Cashwell approach. The azimuthal angle is in the plane perpendicular to the $\mathbf{\Omega}$ direction, which is shown here by the circle.

calculating the scattered azimuthal angle. Another rotation is required to find where the polarization vector is located in relation to the $\phi = 0$ direction. The scatter angle is then added to that angle.

An alternate approach is to recognize that a photon traveling in direction Ω with an electric field vector p (normal to Ω) is really carrying around its own coordinate system. With the definition of the third vector $t = \Omega \times p$, an orthogonal system of base vectors is complete. The scattered vector Ω' can then be written in terms of these base vectors, the polar scatter angle θ , and the azimuthal angle ϕ , measured in the plane perpendicular to Ω . This gives

$$\Omega' = \Omega \cos \theta + p \cos \phi \sin \theta + t \sin \phi \sin \theta. \quad (8)$$

Note that the $\phi = 0$ direction is aligned with p and ϕ increases toward t . This is quite convenient since differential scattering cross sections are given in terms of ϕ measured from the direction of the polarization vector. This is illustrated in Fig. 2.

Using the notation $\Omega = \langle u, v, w \rangle$ and $p = \langle p_u, p_v, p_w \rangle$, t is easily found to be $\langle vp_w - wp_v, wp_u - up_w, up_v - vp_u \rangle$, and the scattered direction cosines can be written as

$$\Omega' = \begin{bmatrix} u' \\ v' \\ w' \end{bmatrix} = \begin{bmatrix} u \cos \theta + p_u \cos \phi \sin \theta + (vp_w - wp_v) \sin \phi \sin \theta \\ v \cos \theta + p_v \cos \phi \sin \theta + (wp_u - up_w) \sin \phi \sin \theta \\ w \cos \theta + p_w \cos \phi \sin \theta + (up_v - vp_u) \sin \phi \sin \theta \end{bmatrix} \quad (9)$$

$$= \begin{bmatrix} u\mu + (p_u \cos \phi + (vp_w - wp_v) \sin \phi) \sqrt{1 - \mu^2} \\ v\mu + (p_v \cos \phi + (wp_u - up_w) \sin \phi) \sqrt{1 - \mu^2} \\ w\mu + (p_w \cos \phi + (up_v - vp_u) \sin \phi) \sqrt{1 - \mu^2} \end{bmatrix}. \quad (10)$$

Comparing Eqs. (1) and (10), one sees that this photon-coordinate approach has a few more operations but does not contain the "if" logic for the special case. The new approach also has one less square root. When each method was coded in ForTran 77 on a Sun Ultra 2 computer for a polarized photon-slab penetration problem, the new approach was faster than the Carter and Cashwell method by 6%. Of course, in a large code, this small difference probably will not be noticed. Speed is not the attraction of this new approach; its simplicity is.

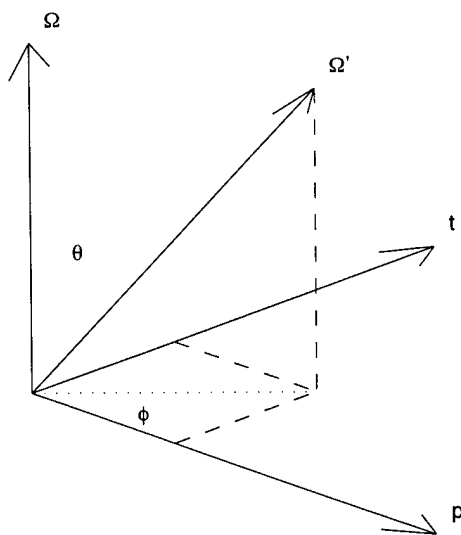


Fig. 2. Geometry of a scatter from direction Ω to Ω' using the photon-coordinate approach. The azimuthal angle is in the plane perpendicular to the Ω direction.

Given the original photon vector Ω and the scattered photon vector Ω' , the angles of scatter can be found by the dot product of each component (Ω, p, t) with the scattered photon vector giving

$$\cos \theta = \Omega \cdot \Omega', \quad (11)$$

$$\cos \phi = \frac{p \cdot \Omega'}{\sqrt{1 - \mu^2}}, \quad (12)$$

and

$$\sin \phi = \frac{t \cdot \Omega'}{\sqrt{1 - \mu^2}}. \quad (13)$$

The only special case here is when $\mu = \pm 1$, where ϕ can be set to 0. In ForTran, again using the dual argument arctangent function, ϕ can be found over the entire range of $[-\pi, \pi]$ with $\phi = \text{atan2}[t \cdot \Omega', p \cdot \Omega']$.

III. POLARIZATION

If the polarization of the photon is being considered, the new electric field vector p' of the scattered photon must be found. Namito, Ban, and Hirayama³ and Vincze et al.⁴ state that p' lies in the plane defined by the electric field vector of the original photon p and the scattered photon direction Ω' . Of course, the new polarization vector p' must also be perpendicular to Ω' . Since these three vectors are all in one plane, the third can be expressed as a combination of the first two:

$$p = p'(p \cdot p') + \Omega'(p \cdot \Omega'). \quad (14)$$

Since everything is in a plane, these are all unit vectors, and $\mathbf{p}' \perp \mathbf{\Omega}'$, then $(\mathbf{p} \cdot \mathbf{p}')^2 + (\mathbf{p} \cdot \mathbf{\Omega}')^2 = 1$. Inserting this and solving for \mathbf{p}' gives

$$\mathbf{p} = \mathbf{p}' \sqrt{1 - (\mathbf{p} \cdot \mathbf{\Omega}')^2} + \mathbf{\Omega}' (\mathbf{p} \cdot \mathbf{\Omega}') \quad (15)$$

$$\mathbf{p}' = \frac{\mathbf{p} - \mathbf{\Omega}' (\mathbf{p} \cdot \mathbf{\Omega}')}{\sqrt{1 - (\mathbf{p} \cdot \mathbf{\Omega}')^2}} \quad (16)$$

Both Namito, Ban, and Hirayama³ and Vincze et al.⁴ describe in words where the polarization vector is located after scatter but neither state the direction mathematically, as is done here.

A coherent scatter maintains the polarization of the photon. An incoherent scatter does not, with a depolarization probability of³

$$(1 - P) = \frac{E/E + E/E' - 2}{E/E + E/E' - 2 \sin^2 \theta \cos^2 \phi} \quad (17)$$

where E is the original photon energy and $E/E' = 1 + (E/mc^2)(1 - \cos \theta)$. Namito, Ban, and Hirayama³ state that when a photon is depolarized, the direction of the polarization vector should be sampled from either \mathbf{p}' or $\mathbf{\Omega}' \times \mathbf{p}'$ (which is equal to $\mathbf{\Omega}' \times \mathbf{p} / \sqrt{1 - (\mathbf{p} \cdot \mathbf{\Omega}')^2}$).

Note that the new electric field direction becomes undefined when $\mathbf{p} \parallel \mathbf{\Omega}'$. This is not a problem since the coherent scatter cross section is zero for scatter in those directions ($\theta = \pi/2$ and $\phi = 0$ or π). The incoherent cross section for scatter in these directions is not zero, but the depolarization probability is one. The new electric field vector direction can be picked as any direction perpendicular to $\mathbf{\Omega}'$.

So, for coherent scatter, the new electric field direction is

$$\mathbf{p}' = \frac{\mathbf{p} - \mathbf{\Omega}' (\mathbf{p} \cdot \mathbf{\Omega}')}{\sqrt{1 - (\mathbf{p} \cdot \mathbf{\Omega}')^2}} \quad (18)$$

For incoherent scatter, a determination by a random variable for depolarization is made first. If the photon will be depolarized, another random number ξ is picked. Then,

$$\mathbf{p}' = \begin{cases} \text{any unit vector } \perp \mathbf{\Omega}' & \text{if } \mathbf{p} \parallel \mathbf{\Omega}' \\ \frac{\mathbf{p} - \mathbf{\Omega}' (\mathbf{p} \cdot \mathbf{\Omega}')}{\sqrt{1 - (\mathbf{p} \cdot \mathbf{\Omega}')^2}} & \text{not depolarized or } \xi > 0.5 \\ \frac{\mathbf{\Omega}' \times \mathbf{p}}{\sqrt{1 - (\mathbf{p} \cdot \mathbf{\Omega}')^2}} & \text{depolarized and } \xi \leq 0.5 \end{cases} \quad (19)$$

IV. UNPOLARIZED PHOTONS

This new approach can also be used in problems involving unpolarized photons. Since there is no electric field vector \mathbf{p} , one has to be picked before the scatter. Any vector perpendicular to $\mathbf{\Omega}$ will suffice; $\mathbf{p} =$

$1/\sqrt{1 - w^2} \langle -v, u, 0 \rangle$ is a simple choice. Of course, one has to check for $|w| \sim 1$ and put in some "if" logic to avoid a division by zero. If this is the case, \mathbf{p} can be defined as $\langle 1, 0, 0 \rangle$.

Now the new method has the problem of the special case, just like the original Carter and Cashwell approach. With a few more operations of Eq. (10) over Eq. (1), combined with the time of finding a new polarization vector, the photon-coordinate approach takes $\sim 8\%$ more time than the Carter and Cashwell approach. However, in a large code, this slight time difference is likely to be insignificant.

This new approach is still easy to understand and has a physical basis: If the radiation is unpolarized, then the electric field vector should be a random direction perpendicular to $\mathbf{\Omega}$ at any given time. Since unpolarized photon scattering cross sections are uniform in ϕ , the direction of $\phi = 0$ is not really important, as shown by the Carter and Cashwell approach. As long as ϕ can be sampled over the entire 2π range for any given direction $\mathbf{\Omega}$, the approach is consistent, and the results will be correct.

The best way to incorporate this new approach for unpolarized radiation may be to pick a random polarization direction ($\perp \mathbf{\Omega}$) after picking the source photon. This \mathbf{p} vector would be updated after each scatter, never bothering to pick whether or not to depolarize. Any code developed with this system for unpolarized radiation would be very easy to upgrade to handle polarized radiation.

V. SUMMARY

This note has done three things. First, a simplified derivation of the Carter and Cashwell formulas for direction cosines showed how arbitrary the approach is. Second, a new approach for direction cosines, which uses the polarization vector and the original direction vector as the base of a coordinate system, was developed and presented. Finally, concise mathematical formulas were presented for calculating the polarization vector after a scatter.

Compared to the transformation of coordinate systems that is used by most Monte Carlo programmers, this new approach for direction cosines is easy to understand, easy to implement, and works very naturally with the angular differential cross sections for polarized photon scattering. For codes that simulate polarized radiation, this new approach offers a small speedup.

ACKNOWLEDGMENTS

The Monte Carlo simulations were performed on a Sun Ultra 2/2200, donated by Sun Microsystems through its Academic Equipment Grant. Many thanks to Sun Microsystems.

Financial support of the author was provided by R. E. Johnston, University of North Carolina, through his Breast Cancer Research Grant from the U.S. Army Medical Research and Material Command.

Special thanks to K. Verghese, J. M. Doster, and R. P. Gardner for their help in preparing this manuscript.

REFERENCES

1. L. L. CARTER and E. D. CASHWELL, "Particle-Transport Simulation with the Monte Carlo Method," Technical Information Center, Office of Public Affairs, U.S. Energy Research and Development Administration (1975).
2. E. D. CASHWELL and C. J. EVERETT, *A Practical Manual on the Monte Carlo Method for Random Walk Problems*, p. 103, Pergamon Press, New York (1959).
3. Y. NAMITO, S. BAN, and H. HIRAYAMA, "Implementation of Linearly-Polarized Photon Scattering Into the EGS4 Code," *Nucl. Instrum. Methods A*, **332**, 277 (1993).
4. L. VINCZE, K. JANSSENS, F. ADAMS, M. L. RIVERS, and K. W. JONES, "A General Monte Carlo Simulation of ED-XRF Spectrometers—II. Polarized Monochromatic Radiation, Homogeneous Samples," *Spectrochi. Acta, Part B*, **50**, 127 (1995).

Appendix

A.10

Chapman D, Thomlinson W, Zhong Z, Johnston RE, Pisano ED, Washburn D, Sayers D, Segre E. Diffraction enhanced imaging applied to materials science and medicine. *Synchrotron Radiation News* 1998;11(2):4-11.

Diffraction Enhanced Imaging Applied to Materials Science and Medicine

D. CHAPMAN¹, W. THOMLINSON², Z. ZHONG², R. E. JOHNSTON³, E. PISANO³, D. WASHBURN³, D. SAYERS⁴ and C. SEGRE

¹CSRR, Illinois Institute of Technology, 3101 South Dearborn, Chicago, IL 60616, USA

²National Synchrotron Light Source, Brookhaven National Laboratory, Upton, NY 11973, USA

³Department of Radiology, University of North Carolina, Chapel Hill, NC 27599, USA

⁴Department of Physics, North Carolina State University, Raleigh, NC 27695, USA

Normal radiography for medical and materials applications uses an area beam which, after traversing and interacting with the subject, is detected by an area detector. The interaction of X-rays with the subject is complex, involving absorption, refraction [1-3] and scattering. The scattering may include small angle scattering [4] (scattering angles less than milliradians) which carries information about the subject's structure

on the length scale up to microns. This information is lost in normal radiography because of its small angle nature. The refraction of X-rays inside the object is also not detectable in conventional radiography due to its small angle nature (on the order of microradians). X-ray diffraction from perfect crystals, with its narrow reflection angular width (on the order of a few microradians) and peak reflectivity of close to unity, provides the tools to analyze X-ray beams traversing an object on the microradian scale. The sides of the reflectivity curve of a crystal (analyzer) placed after the object provide a mechanism to convert the small refraction angles in an object directly into observable intensity variations. The narrow width of the reflectivity curve also provides a high degree of scatter rejection from the object. These two effects, arising from the narrow reflection width of a perfect crystal, create two new sources of image contrast in radiography: refraction contrast and scatter rejection or extinction contrast.

An imaging method called Diffraction Enhanced Imaging (DEI) has been reported [5] which utilizes a perfect crystal analyzer and centers around the concept of taking digital images at different analyzer positions and combining them to produce apparent absorption and refraction images of the object. Apparent absorption is contrast due to a combination of normal absorption in the object and the loss of intensity due to diffraction. This latter effect is commonly referred to as extinction, giving rise to extinction contrast. It was demonstrated in experiments at the National Synchrotron Light Source (NSLS) that one can separate the refraction effects from the apparent absorption by

**Your Partner for
SYNCHROTRON RADIATION
EQUIPMENT**



Diffraction gratings, Mirrors, Mirror Manipulators, Monochromators and Spectrographs (TGM, PGM, SGM,... DRAGON and PADMORE...). Complete Beamlines for the Far UV and Soft X-Ray.

SUPER-ACO - LURE (ORSAY - FRANCE)

**From the OPTICAL COMPONENT
to the COMPLETE BEAMLINE
through dedicated subassemblies...**

 **JOBIN YVON - SPEX**
Groupe HORIBA

16-18 rue du Canal - 91165 Longjumeau Cedex - France
Tel. : (33) 01 64 54 13 00 - Fax : (33) 01 69 09 93 19
In USA call: (1) 908/494 86 60 - In Netherlands call: (31) 172/477 320
In Germany call: (49) 89/46 23 17-0 - In Italy call: (39) 2/57 60 30 50
In UK call: (44) 181/204 81 42

Circle No. 122

taking images on either side of the rocking curve. Objects which have different small angle scattering characteristics from their surroundings can be enhanced by taking images at suitable analyzer positions [6]. These experiments were done with standard mammography phantoms which, although suggesting the potential applicability of DEI to mammography, do not prove this due to differences between the simulated tumors in the phantom and real tumors. Later experiments at the Advanced Photon Source (APS) with biological samples having imbedded tumors showed that DEI may be sensitive to the extinction and refraction contrast in cancerous tissue, and that DEI at appropriate analyzer positions on the rocking curve can enhance different features of the sample [7]. This experiment used embedded tumors which had excessive refraction contrast around the border of the embedded feature. It was concluded that tissues with naturally grown tumors should be used to clearly demonstrate DEI's applicability to cancer detection.

A new set of experiments was performed at APS in September 1997 to study the tissue characterization capability of DEI with clinically relevant biological specimens, and to explore the application of DEI to non-destructive testing. 18 and 30 keV X-rays were used to explore the effect of energy change on DEI, aimed at finding the optimum energy for DEI mammography. Increasing the energy to 30 keV also facilitates the application of DEI to non-destructive testing, which is not realistic with 18 keV photons due to the sample absorption.

Experimental method

The experiments reported here were performed at the Synchrotron Radiation Instrumentation Collaborative Access Team (SRICAT) sector 1-BM-B bending magnet beamline. The setup of the experiment is shown in Figure 1. Perfect silicon crystals in Bragg geometry were used for producing the monochromatic beam and as the analyzer. The first double-crystal monochroma-

PHYSICAL ELECTRONICS

High Voltage — Supply 1 — Display Select

Power — Set Point 1 2 3 4 5 6 7 8 Set Point

High Voltage — Supply 2 — Display Select

DIGITEL MPC—Multiple Pump Control

The **NEW DIGITEL MPC** (Multiple Pump Controller) is intelligent enough to independently operate, monitor and protect as many as two ion pumps and operate a titanium sublimation pump (TSP) or a non-evaporable getter (NEG) for more advanced system control. A full line of standard features include:

- All DIGITEL functions (autostart, autorun, power loss protection, vacuum loss protection and easy to read display)
- Eight process setpoints
- RS-232/422 (485 available)
- Remote TSP/NEG control (current, voltage and power monitoring)
- 5.25" (3 U) X 19" rack mount

The **DIGITEL MPC** – A unique power supply providing maximum reliability, innovative features and exceptional value.

PHYSICAL ELECTRONICS

6509 Flying Cloud Drive, Eden Prairie, MN 55344 Tel: 612-828-6100 FAX: 612-828-6322 e-mail: marketing@phi.com

Circle No. 128

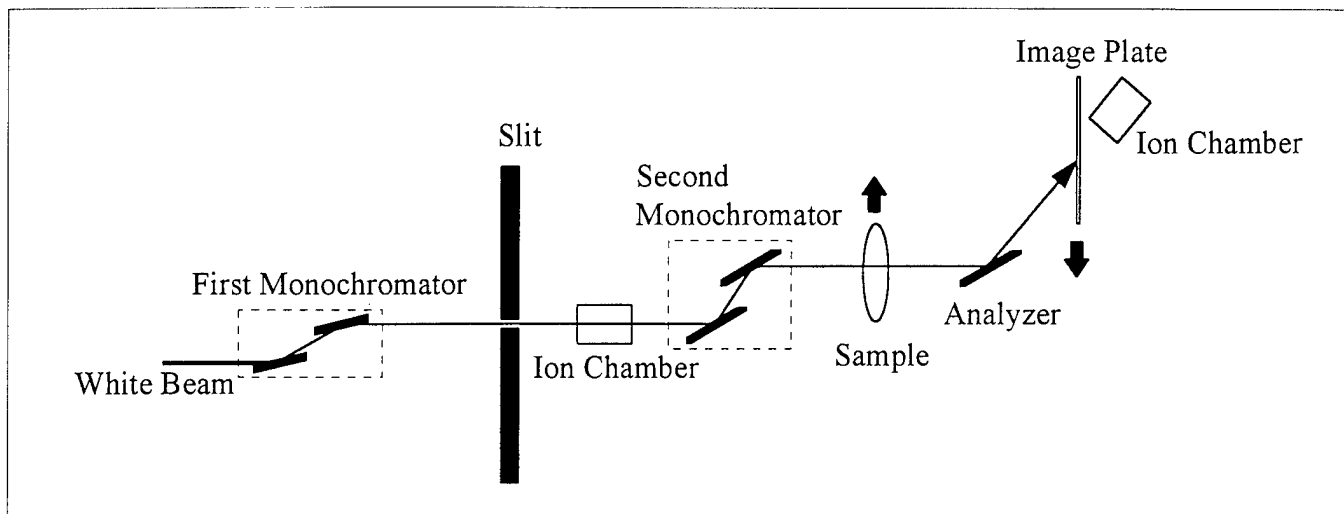
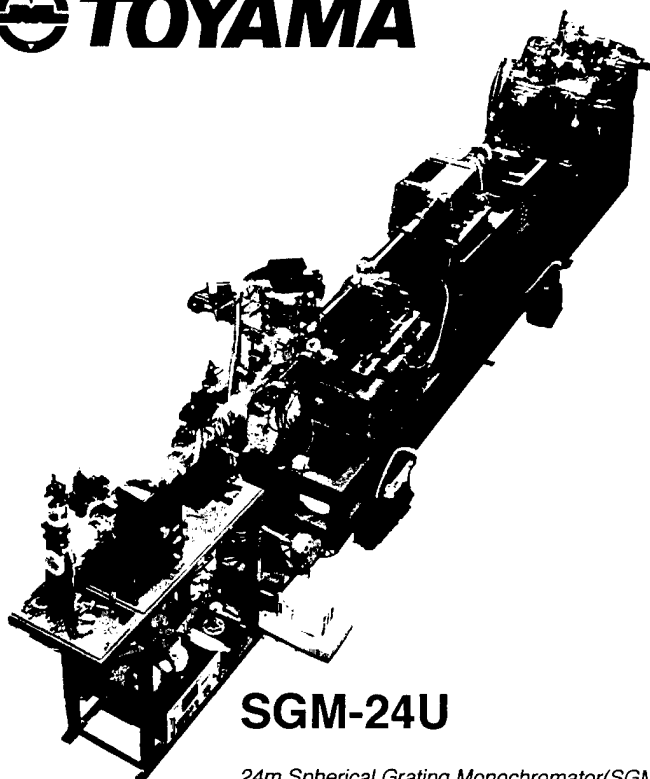


Figure 1. The set-up of the experiment with an analyzer crystal.

tor was the beamline monochromator located upstream of the experimental hutch in the beamline. The [220] reflection was used for this monochromator to pre-monochromize the white

beam to the desired energy (18 keV or 30 keV) and to deliver the beam into the experimental hutch. The second monochromator crystals used the [333] reflection. Due to the dispersion mis-

TOYAMA



SGM-24U

24m Spherical Grating Monochromator(SGM)
for Undulator Beamline
installed at KEK/PF BL-16B, Japan

Supporting cutting-edge science with the best in ultra-high vacuum & precision machining technology.

If you have a good concept that needs to be developed, TOYAMA is the place to come!

We have the technology to turn your ideas into reality.

Main Products:

- Beamline Components
- Monochromators
- Mirror Positioners
- Mirror Bending Mechanisms
- UHV Systems
- Standard Feedthroughs

Pioneering New Horizons in Science

TOYAMA Co., Ltd.

6236, Hibarigaoka 4-chome, Zama-shi,
Kanagawa Prefecture, 228, JAPAN
Tel:+81(462)53-1411 Fax:+81(462)53-1412

E-Mail: salesdept @toyama-jp.com
Internet Home Page: <http://www.toyama-jp.com>

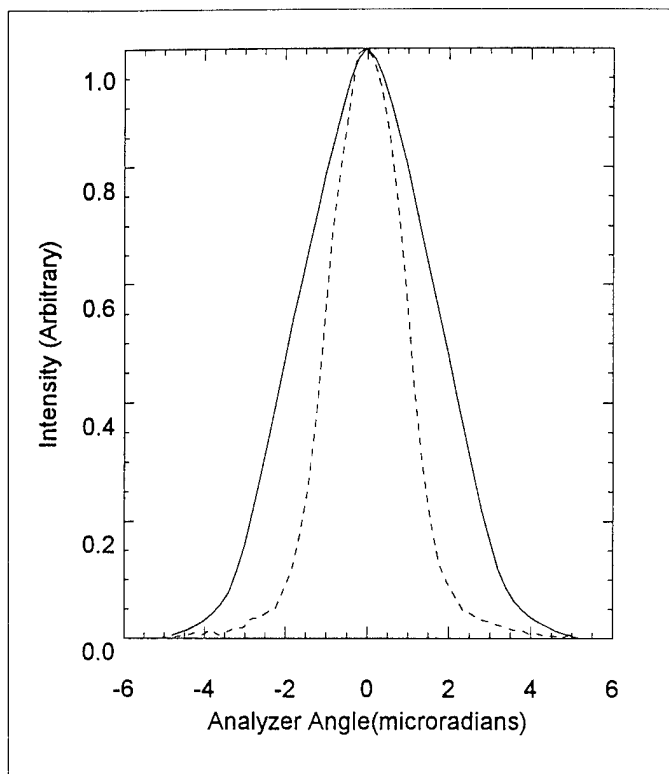


Figure 2. Rocking curves of the analyzer at 18 keV (solid line) and 30 keV (dashed line).

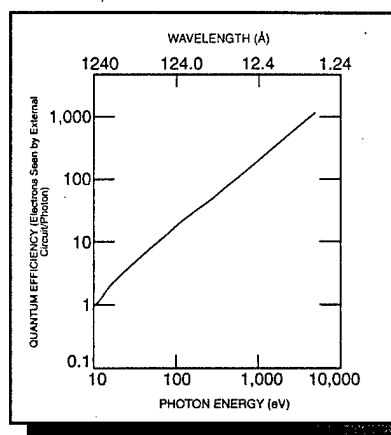
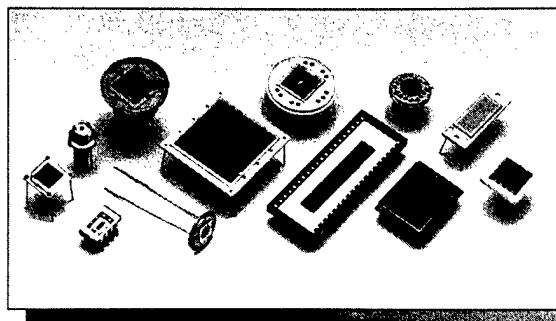
match between the two monochromators and the vertical divergence of the incident beam, the tuning curve of the second monochromator unit with respect to the first monochromator was much wider than the Darwin width of the [333] reflection. Thus the beam intensity on the sample was stable against relative changes of angle between the two monochromators due to vibrations.

The analyzer, also [333], was non-dispersive with respect to the second monochromator. The analyzer was mounted on a tangent arm with 1 meter arm length driven by a linear translator of 0.1 micrometer resolution. This provided an angular resolution of 0.1 microradians, which was sufficient to tune the analyzer to any location on the analyzer rocking curve which had a FWHM of around 2 microradians for 30 keV X-rays. The tangent arm was mounted on the same optical table as the second monochromator.

Figure 2 shows the rocking curves of the analyzer crystal. The FWHM of the rocking curves are 3.9 and 2.1 microradians, respec-

ABSOLUTE

XUV SILICON PHOTODIODES



TYPICAL QUANTUM EFFICIENCY OF
AXUV SILICON PHOTODIODES

Additional Features

- No Change in QE with 100 Mrad (Si) 124 eV Photons
- 8 Decades of Linearity
- May be Operated Without Bias
- Cryogenically and UHV Compatible
- With Integrated Bandwidth Limiting Filters
- 0.27 A/W Responsivity from 100 eV to 12 keV
- Excellent for Low Energy Electrons and Ions Detection

IRD

INTERNATIONAL RADIATION DETECTORS INC.

2545 West 237th Street, Unit I • Torrance, California 90505-5229
(310) 534-3661 • FAX (310) 534-3665 • email: ird@kaiwan.com

DEVELOPED IN COLLABORATION WITH NIST, NIH, LLNL, LANL, NCAR

Circle No. 129

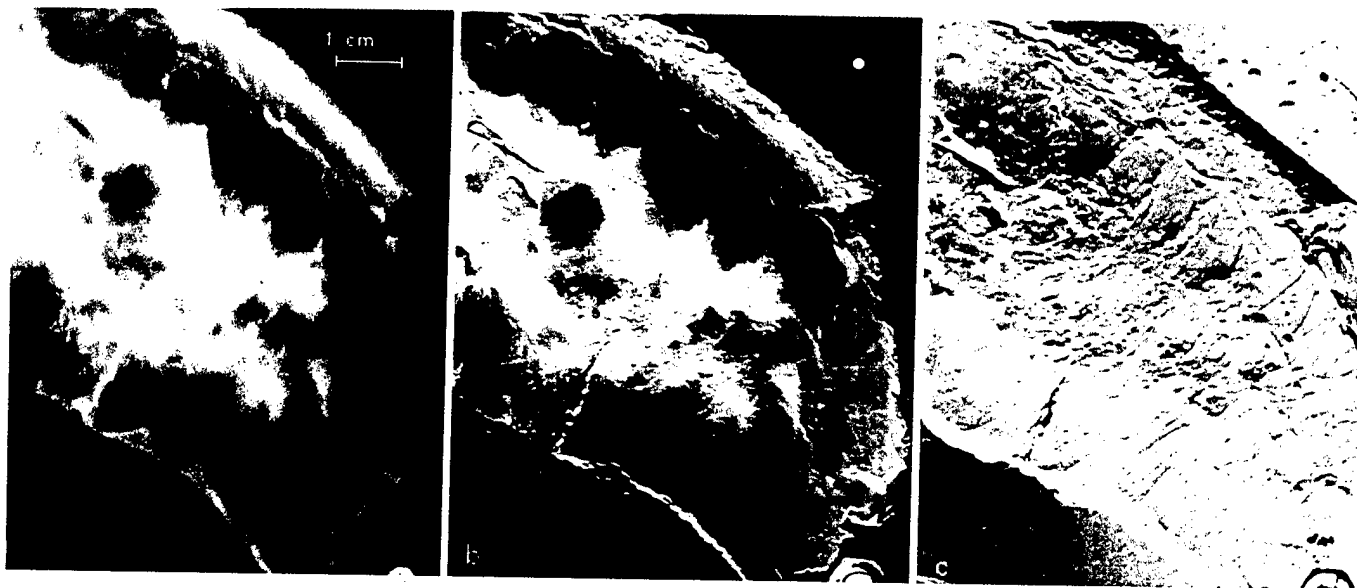


Figure 3. Images of cancerous tissue: (a) "Normal" radiograph taken with a Fischer digital mammography unit with Mo filter operating at 22 kVp. The white region is the tumor with fibrils which indicate the existence of cancer. (b) Apparent absorption image created by summing up the images taken with the analyzer at 1.5 microradians. (c) Refraction image created from the difference of the 1.5 microradians images.

tively, for beam energies of 18 and 30 keV. The theoretical FWHM of the analyzer rocking curves

of the multiple crystal system are 3.57 and 2.06 microradians, respectively, for 18 and 30 keV photons. After preliminary alignment of the analyzer crystal, rocking curves were obtained with two ion chambers monitoring the beam intensity at both ends of the fan beam, and the analyzer tilt angle was adjusted until the peak of the two rocking curves coincided. This ensured that the same DEI characteristics were maintained across the fan beam in terms of position on the rocking curve.

For each sample, a "normal" radiograph with the monochromatic beam was taken by moving the analyzer out of the beam and scanning the image plate and sample through the fan beam in the same direction and at the same speed. DEI images were then acquired with the analyzer tuned to various positions on the rocking curve by translating the sample and the image plate in opposite directions at the same speed through the fan beam. At a scan speed of about 10 mm/s, the surface dose on the sample was a few mGy at 18 keV and tenths of mGy at 30 keV. Rocking curves through a line on the phantom were obtained by fixing the phantom in the fan beam and performing a series of exposures by incrementing the analyzer position and image plate vertical position. The rocking curve is useful for quickly visualizing the optimum analyzer

**We develop,
manufacture and distribute
products for Neutron
and X-ray Spectrometers**

Beam Optics
Multilayer Coatings
Ge Monochromators
Precision Positioning Modules
Electronic Control Systems
Shielding Material

Scientific Instrumentation

GMI GRENOBLE MODULAR INSTRUMENTS

CILAS

Visit our Web site: www.cilas.com
Phone +33 1 64 54 48 96 - Fax +33 1 64 54 48 19

Circle No. 123

position for contrast enhancement of the desired features.

Medical imaging

Various biological samples were imaged. The biological samples were preserved in formalin and included breast tissues with tumors (infiltrating ductal carcinomas). Each biological sample was sealed in a plastic bag and compressed between two Lucite plates. Additional Lucite plates were added during the imaging to make the absorbing thickness on the order of 30–50 mm.

Images of a breast tissue acquired at 18 keV are shown in Figure 3. Figure 3a shows a “normal” radiograph taken at the University of North Carolina. Figure 3b and Figure 3c show the apparent absorption and refraction images, respectively, of the sample. These images are derived from the images taken at 1.5 microradians on each side of the analyzer rocking curve. Compared to the “normal” radiograph, the apparent absorption image (Figure 3b) shows more contrast for the tumor. The DEI apparent absorption image also shows the

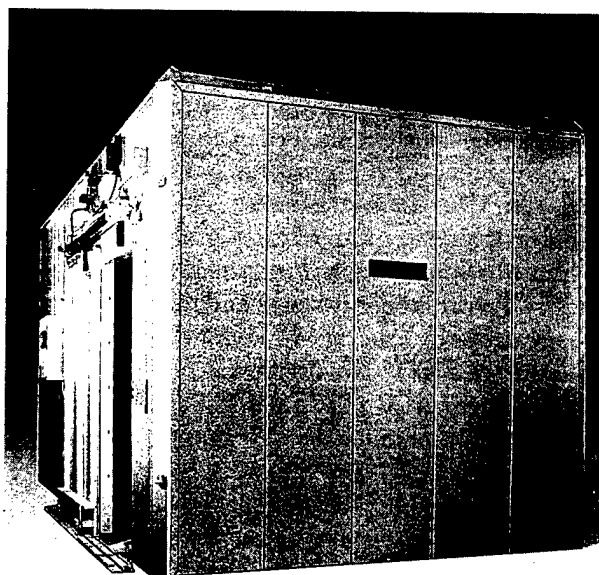
calcifications (clusters of white dots in the image) better than normal radiography. The most striking feature is the refraction image (Figure 3c) which shows small fibrils which are not observable in the conventional image. The presence of radiating fibrils is a possible indication of the presence of a small, unnoticeable tumor.

Conventional radiography depends on the absorption of X-rays by an object to create the radiograph. In DEI, the energy dependence of the refraction and extinction effects differ from that of absorption. Also, the sensitivity of the analyzer crystal to these effects depends on the imaging energy. In general, for a feature in an object which refracts X-rays, the DEI sensitivity will be proportional to $1/E$. For extinction features, the ability of the system to reject scatter will be energy independent. There is a net decrease in sensitivity of the DEI technique as the imaging energy is increased. Since the transmission through an object is a very strong function of imaging energy in the photoelectric range, the net effect is to skew the optimal imaging energy for extinction and refraction to

TECKNIT SHIELDING SYSTEMS, THE FIRST TOTAL ELECTROMAGNETIC SPECTRUM SHIELDING COMPANY

Tecknit Shielding Systems provides a complete line of products and services:

- RADIATION PROTECTION ENCLOSURES
- CUSTOM DESIGNED COLLIMATORS
- RADIO FREQUENCY SHIELDED ENCLOSURES
- MODULAR, WELDED, MAGNETIC ROOMS
- ANECHOIC CHAMBERS
- MAGNETIC SHIELDING ENCLOSURES
- SITE SURVEYS AND FIELD TESTING



MODULAR LEAD SHIELDED ENCLOSURE



TECKNIT®
SHIELDING SYSTEMS

838 MAIN AVENUE, PASSAIC, NJ 07055 / (201) 778-6200 / FAX (201) 778-2177

Circle No. 131

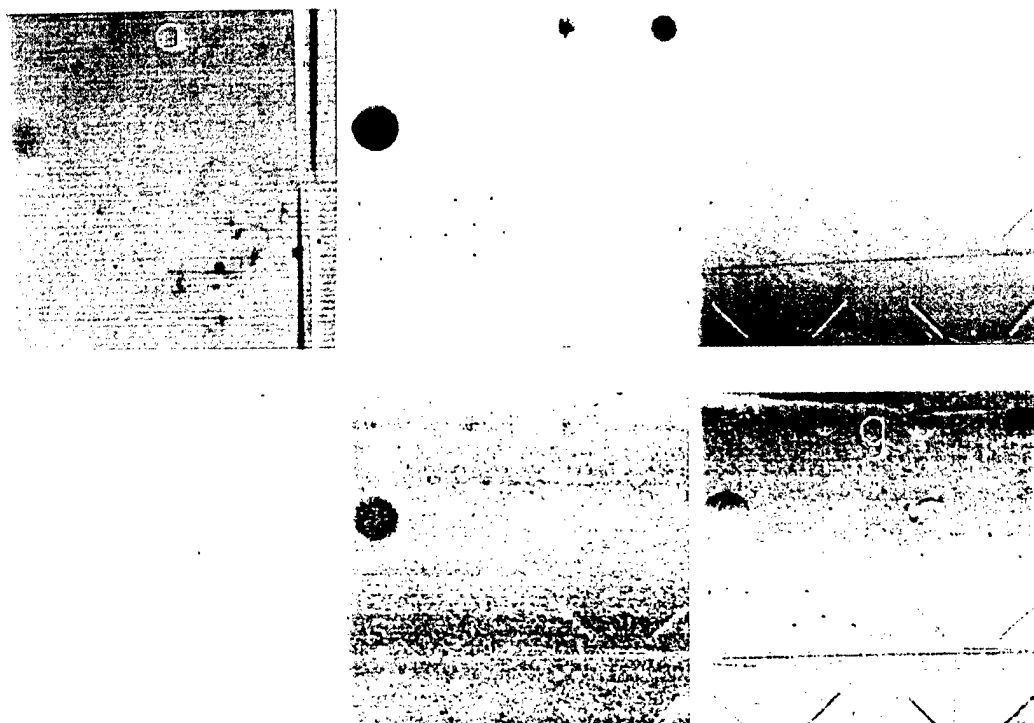


Figure 4. Images of the ACR phantom. The upper row shows images taken at 18 keV, and the lower row shows images taken at 30 keV. (a) and (e) "Normal" radiography. (b) and (f) Apparent absorption images. (c) and (g) Refraction images. (d) and (h) DEI image with analyzer on the peak of the rocking curve. The apparent absorption images and refraction images were derived from DEI images at 1.5 microradians and 1 microradians, respectively, for 18 and 30 keV energies.

higher energies when compared to an optimal absorption contrast energy. For example, in mammography the optimal absorption imaging energy is near 18keV for 5cm of soft tissue. With DEI, the optimal imaging energy for refraction is near 30keV. The transmission through the tissue increases dramatically over this energy range and the skin entry exposure drops by a factor of 15 while maintaining the same exposure to the detector.

Images of the ACR (American College of Radiology) phantom taken at 18 keV (upper row) and 30 keV (lower row) are shown in Figure 4 for comparison. At 30 keV, there is very little contrast in normal radiography due to the low absorption of the phantom. However, the DEI images at this energy show that the apparent absorption and refraction are comparable to those at 18 keV.

Non-Destructive Testing

DEI's sensitivity to refraction and extinction make it an ideal technique for various Non-Destructive Testing (NDT) applications. Refraction contrast arising from abrupt changes in

material density or thickness can be used to visualize cracks and voids in materials. Images of a 1 mm thick steel sample with eight varying depth scribe marks are shown in Figure 5. The contrast of DEI is more than a factor of ten larger than in normal radiography. Note the reversal of the contrast as the analyzer is changed from the peak (Figure 5b) to 2 microradians (Figures 5c, 5d). This is due to the fact that the small angle scattering of the scratched material scatters the intensity away from the peak, resulting in a reduction in intensity when the analyzer is on the peak. This scattered intensity is picked up by the analyzer at 2 microradians.

Future research

This work will be extended to a wide variety of biological and materials samples at the X15A beamline at the NSLS and in future work at the APS. There are many questions to be answered concerning the applicability of DEI to soft-tissue differentiation, optimization of energy and analyzer position, the advantages and disadvantages

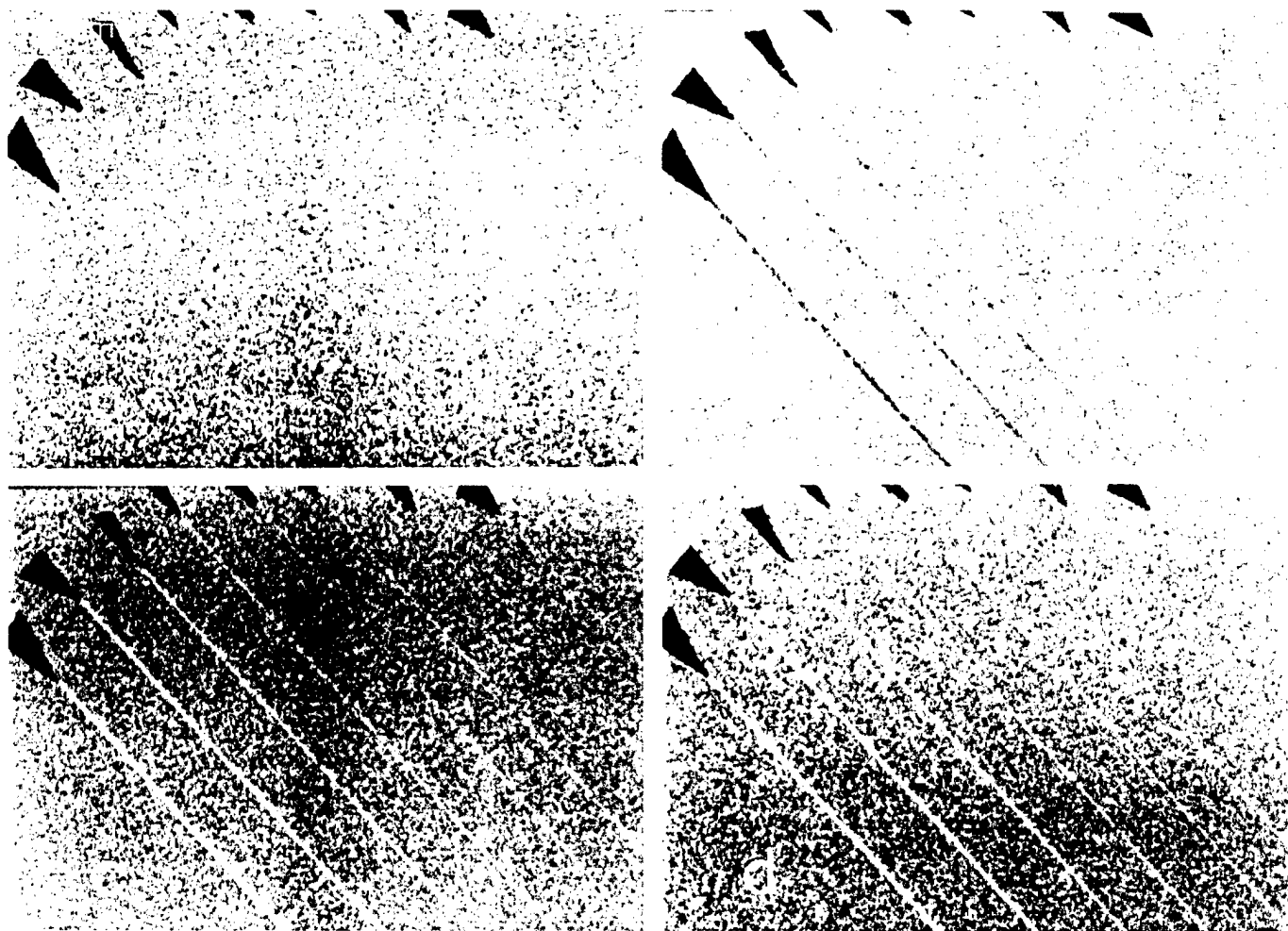


Figure 5. Images of the steel sample acquired at 30 keV. From lower left to upper right, the lines are scratches with decreasing depth and width, the fourth and eighth scratches were measured with a trace profiler as having widths of 200 and 35 microns and depths of 15 and 8 microns, respectively. The black triangles are lead alignment marks. (a) "Normal" Radiograph. (b) DEI with analyzer on the peak of the rocking curve. (c) DEI with the analyzer at -2 microradians. (d) DEI with the analyzer at +2 microradians.

of imaging at higher energies, and the role to be played in non-destructive materials testing. The future of DEI in clinical mammography will depend on the results of the synchrotron-based studies and on the development of compact DEI system for the clinical environment. ■

Acknowledgments

We would like to thank G. Srajer and D. Mills for support and beamtime at APS SRICAT and T. Erber and S. Guralnick for assistance with the materials science project. This work was supported in part by US ARMY grant DAMD17-96-1-6143, US Department of Energy Contract DE-AC02-76CH00016, ARPA contract AOB227 and by the State of Illinois Higher Education Cooperative Agreement.

1. V. A. Bushuev, V. N. Ingal, and E. A. Belyaevskaya, *Crystallography Reports* **41**,766 (1996).
2. V. N. Ingal, and E. A. Belyaevskaya, *Zh. Tekh. Fiz.* **67**, 68 (1997).
3. V. N. Ingal, and E. A. Belyaevskaya, *Physica Medica* **XII**(2), 75 (1996).
4. A. Guinier, G. Fournet, C. B. Walker, and K. L. Yudowitch, *Small-angle Scattering of X-rays* (Wiley, New York, 1955).
5. D. Chapman, W. Thomlinson, F. Arfelli, N. Gmür, Z. Zhong, R. Menk, R. E. Johnston, D. Washburn, E. Pisano, and D. Sayers, *Rev. Sci. Instrum.* **67**(9), CD-ROM (1996).
6. D. Chapman, W. Thomlinson, R. E. Johnston, D. Washburn, E. Pisano, N. Gmür, Z. Zhong, R. Menk, F. Arfelli, and D. Sayers, *Phys. Med. Bio.* **42**, 2015 (1997).
7. W. Thomlinson, D. Chapman, Z. Zhong, R. E. Johnston, and D. Sayers, In: *Proceedings of the International Workshop on Medical Applications Using Synchrotron Radiation HAGA'97*. (Haga, Japan, Aug. 9-10, 1997).

Appendix

A.11

"Preliminary Experience with Monoenergetic Photon Mammography",
Medical Imaging 1995, Physics of Medical Imaging, SPIE Vol. 2432, pp.
434-441, (1996), R. E. Johnston, D. Washburn, E. Pisano, W.C. Thomlinson,
D. Chapman, N.F. Gmür, Z. Zhong, D. Sayers.

Preliminary experience with monoenergetic photon mammography

R.Eugene Johnston¹, David Washburn¹, Etta Pisano¹, William C. Thomlinson², Dean Chapman², Nicholas F. Gmur², Zhong Zhong², Dale Sayers³

1. Department of Radiology, University of North Carolina, Chapel Hill, N.C. 27599
2. NSLS, Brookhaven National Laboratory, Upton, NY, 11973
3. Department of Physics, North Carolina State University, Raleigh, N.C. 27695

ABSTRACT

We are using a beam port at the National Synchrotron Light Source facility at Brookhaven National Laboratory as a source of monoenergetic photons. The photon source is radiation from a bending magnet on the X-ray storage ring and provides a usable X-ray spectrum from 5 keV to over 50 keV. A tunable crystal monochromator is used for energy selection. The beam is 79mm wide and 0.5 mm high.

We imaged the ACR mammography phantom and a contrast-detail phantom using a phosphor plate as the imaging detector. Phantom images were obtained at 16, 18, 20 and 22 keV. Phantom thickness varied from 15 mm to 82 mm. These images were compared to images obtained with a conventional dedicated mammography unit.

Subjective preliminary results show that image contrast of the monoenergetic images is similar to those obtained from the conventional x-ray source with somewhat sharper and cleaner images from the monoenergetic source. Quantitative analysis shows that the monoenergetic images have improved contrast compared to the polyenergetic derived images. Entrance skin dose measurements show a factor of 5 to 10 times less radiation for the monoenergetic images with equivalent or better contrast. Although there remain a number of technical problems to be addressed and much more work to be done, we are encouraged to further explore the use of monoenergetic imaging.

1. INTRODUCTION

The conventional source of x-rays for medical imaging is the x-ray tube which generates a mixture of bremsstrahlung and characteristic x-rays. In modern mammography x-ray tubes, the target material usually used is molybdenum ($Z=43$). The characteristic peaks at 17 and 19 keV are reported to contribute about 25% of the photon flux, the remainder being a continuum of energies¹. Other investigators² have experimented with different target/filter materials, Mo/Mo, Mo/Rh and Rh/Rh to improve the image contrast of the dense breast. However, there are trade offs in contrast and radiation dose as the effective energies are increased for better penetration of dense breast tissues.

Recently Boone and Seibert¹ did a computer simulation to compare performance of monoenergetic x-rays to polyenergetic x-rays from tungsten anode systems with regard to imaging. Their conclusion was that monoenergetic sources exhibited a 40 to 200 % improvement in tissue contrast when imaging the chest with different contrast targets. Admittedly, soft tissue contrast benefited the least. Burattini, et.al,^{3,4} recently published their work using synchrotron radiation to image both breast phantoms and specimens. They conclude that the images obtained with monoenergetic x-rays have higher contrast, better resolution and similar, or less, radiation dose compared to the conventional polyenergetic x-ray images.

We have embarked on a pilot project using a monoenergetic x-ray beam from the National Synchrotron Light Source (NSLS) at Brookhaven National Laboratory to explore the potential of monoenergetic photons for mammographic imaging. The following is a summary of our experience to date.

2. EXPERIMENTAL SET-UP

The National Synchrotron Light Source (NSLS) is an experimental facility consisting of two electron storage rings. The vacuum ultraviolet (VUV) ring stores electrons at 750 MeV to produce infrared, visible and UV light. The x-ray ring stores electrons at 2,500 MeV and extends into a higher energy x-ray region, up to 50 keV.

In conducting these initial studies, we borrowed whatever instrumentation was readily available. The physical arrangement, shown in figure 1, was that of a typical physics experiment and not a polished clinical facility. For our project, we had access to beam port X27C where the x-rays are generated at a main bending magnet on the electron storage ring. The x-ray energies emerging from the beam port range up to 50 keV. The beam is fan shaped with a width of 79 mm and about 0.5mm thickness.

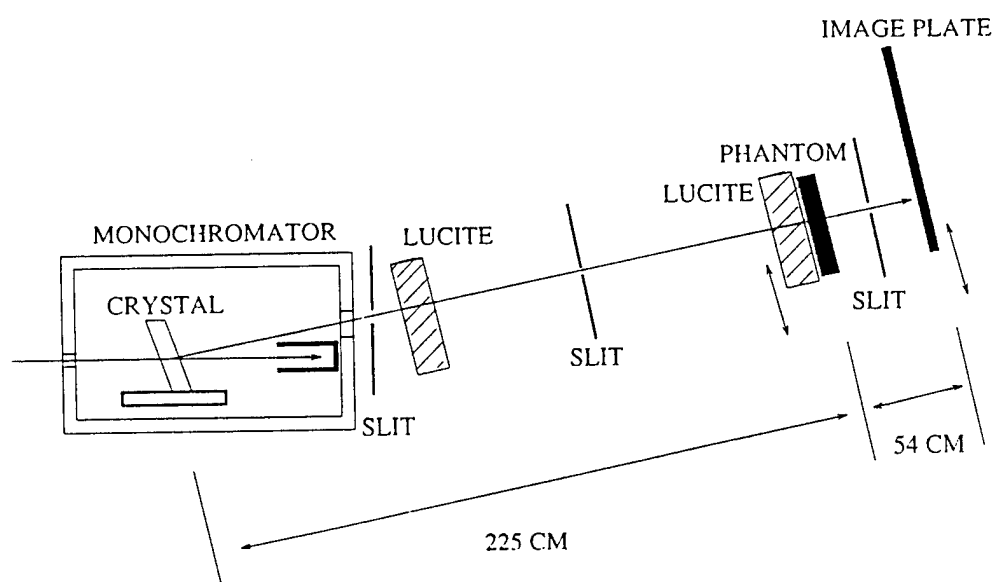


Figure 1. Experimental Setup

2.1 Monochromator/beam scanning system

The monochromator beams are produced by a Si(III) Laue monochromator. This monochromator produces a beam with a bandwidth of about $1.2 \times 10^{-4} \Delta E/E$ in the energy range used here (16 - 22 keV). The energy is set by the angle the crystal makes with the incident synchrotron beam (the Bragg angle). This angle is set remotely by computer to select the desired energy. There is a small contamination of this flux from the monochromator due to harmonics of the fundamental energy. The largest harmonic contribution occurs at 3 times the fundamental energy and is $\sim 0.1\%$ of the fundamental intensity. After passing through the various absorbers used in the experiment, beam hardening effects will increase the relative intensity of the harmonic to the fundamental to only a few percent.

Collimation of the beam was placed at the exit of the monochromator to shield against stray radiation, another slit was located approximately 60 cm in front of the phantom to be imaged, and a final slit between the phantom and the imaging plate serves as an anti-scatter slit. The overall length of the system from monochromator to detector plate was 2.8 meters. To form an image, the imaging plate and the

phantom were scanned through the beam. The total scan field was 79 mm by 87mm. This was large enough to cover about 2/3 of the phantom that we used. The drive system was a stepping motor and the translation speed for most of the images that we obtained was set at 2 mm per second.

2.2 Detector

The detector used to form the image was a Fuji ST3 PSP plate. This is a high sensitivity plate and the only one available for our use that could be read out with the model 2000 Fuji reader. A manual "latitude" control allowed 4 possible selections, from "1", which uses the 10 bits over a narrow window of the dynamic range to "4" which is a wide window and covers the entire range. All the phosphor plate readers installed at NSLS were optimized for x-ray crystallography work with high sensitivity and lower contrast settings than usually used in medical imaging. These plates were read out at a 2000 x 2000 matrix (100 μm /pixel) resolution. Since our interest was contrast resolution, we were not concerned at this point about the lack of spatial resolution, and we felt these plates would be adequate for our preliminary experiments.

2.3 Phantoms

We used two different phantoms for most of the experiments. The ACR phantom, model RMI-156, and a contrast-detail phantom obtained from the Sunnybrook Health Science Center, University of Toronto⁵. The ACR phantom was chosen since it is the standard for comparison of mammography and the accepted phantom for accreditation. The contrast-detail (CD) phantom allows for quantitative measurements of contrast as a function of spatial resolution. Figure 2 shows the detail of the CD phantom.

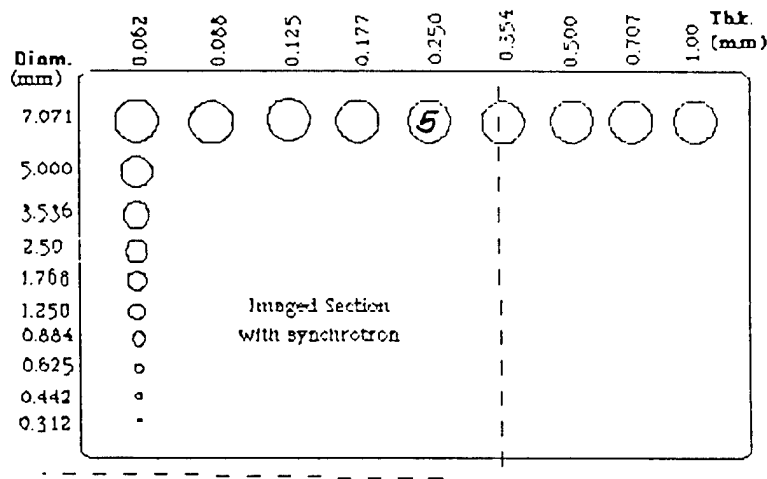


Figure 2. A schematic of the Contrast Detail Phantom used in these experiments.

Note that the portion imaged by the synchrotron beam is indicated by the dotted lines.

Lesion #5 is indicated

To assess the image contrast for different thicknesses of phantom, various layers of Lucite were placed in front of the phantom facing the x-ray beam. In the case of the monoenergetic beam and image plate detector, it was desirable to maintain a constant photon flux at the detector. This was accomplished by placing a total of 67 mm of Lucite absorbers in the beam plus the 15mm thick CD phantom. For a phantom image of 15mm, 67mm of Lucite were placed at the monochromator, and the radiation entrance dose

measured at the front surface of the CD phantom. To create thicker phantoms, a given thickness of absorber was moved from the monochromator to in front of the CD phantom. Under these conditions, excluding variations in scatter, the photon flux should be constant at the imaging plate, the variation being the radiation entrance dose at the surface of the imaged phantom, and the increased scatter generated in the phantom as thickness increased. Figure 1 is a diagram of the experimental setup used with the synchrotron radiation beam.

3. EXPERIMENTAL PROTOCOL

3.1 Conventional x-ray mammography

For comparison to the conventional x-ray source, the CD phantom was placed on the Buckey platform above the film cassette. Additional Lucite thicknesses were added on top of the phantom facing the x-ray tube. To maintain approximately the same photon flux to the film, phototiming was used and the kVp and density control adjusted to provide an average film optical density of 1.2 for all images. Ion chamber measurements were made at the entrance surface of the phantom / absorber combination.

The contrast-detail phantom was imaged with a total phantom thickness of 15mm, 24mm, 44mm, 64mm, and 84mm. The ACR phantom was imaged with no additional Lucite thickness added.

3.2 Synchrotron Images

The beam size of the synchrotron beam was 79 mm wide at the phantom. The CD phantom is 150mm in width. Since we were interested in the most challenging contrast, we scanned the last 5 rows on the low contrast side of the phantom. Phantom thicknesses of 15mm, 24mm, 42mm, 62mm, and 82mm were used. The difference of 2mm between the monoenergetic study and the conventional study was due to the particular combination of Lucite absorbers available at NSLS. Each phantom thickness was imaged at 16 keV, 18.2 keV, 20 keV and 22 keV. The ACR phantom was imaged at each of the above energies with no additional thickness added.

TLD measurements were made at the entrance surface of the phantoms for each phantom thickness and for each energy. Ion chamber measurements were made in the beam as a function of absorber thickness and radiation dose at the surface of each phantom thickness was calculated from these measurements.

4. RESULTS

An example of the conventional x-ray image of the contrast-detail phantom at 44 mm thickness is shown in figure 3. A synchrotron image of the same phantom at 20 keV is shown in figure 4. The largest and most visible target in these images is lesion number 5 as indicated on the phantom schematic. We purposely imaged the low contrast side of the phantom.

Quantitative measurement of contrast over lesion #5 (see diagram of the contrast-detail phantom) show that the contrast in the conventional image is on the order of 0.9%, measured from a digitized version of the film, compared to a contrast of 1.58% measured from the 18.2 keV and 1.12% from the 20 keV synchrotron images. All measurements were for the 42 mm thickness phantom.

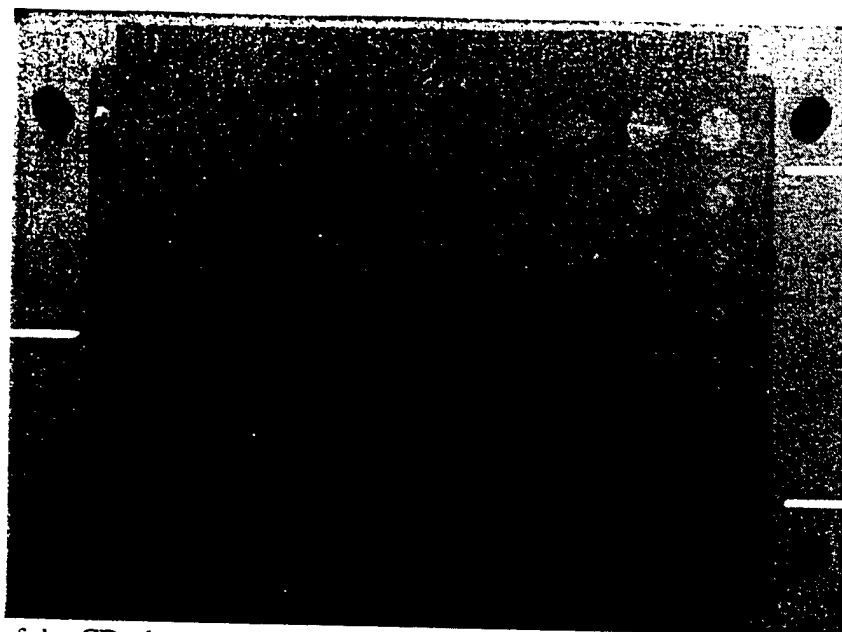


Figure 3. Image of the CD phantom 44 mm thickness at 28 kVp

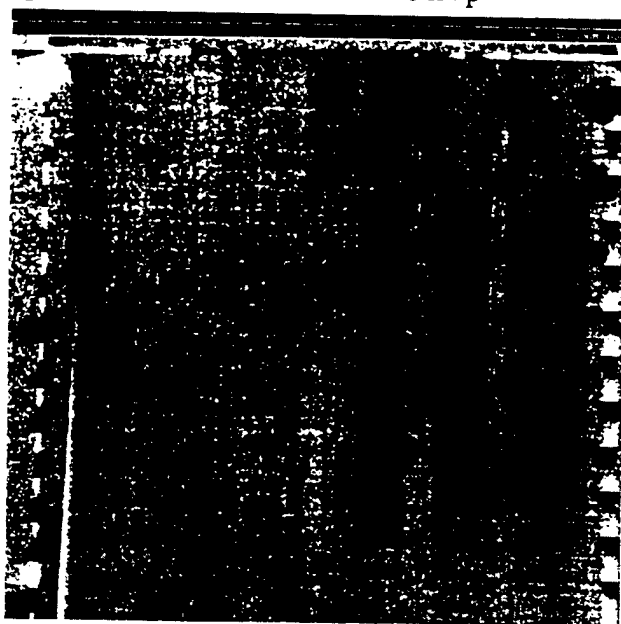


Figure 4. Image of the CD phantom 42 mm thickness with a synchrotron beam of 20 keV.

The radiation entrance dose at the surface of the phantom for various thicknesses and energies for the synchrotron images and the radiation dose for conventional mammography are shown in table 1. In the case of conventional mammography the mAs and kVp were varied to maintain an average optical density of 1.2 on the film. In the case of the synchrotron source, the photon flux at the imaging plate was held approximately constant by maintaining a constant total absorption in the beam path. A characteristic of the synchrotron is that the electron beam current decays with time which also changes the photon flux. The radiation doses reported in table 1 are normalized to a beam current of 75mA.

TABLE 1
Radiation Exposure to the Phantom Surface

Phantom Thickness(mm)	x-ray dose (mR)	Synchrotron radiation dose (mR)			
		16 keV	18.2 keV	20 keV	22 keV
15	78	-	6	-	-
24	158	-	10	-	-
42 (44)	758	108	93	121	38
62 (44)	2400	1080	241	-	-
82 (84)	4460	-	1245	1760	532

Thickness values in parentheses are for the conventional x-ray measurements

5. DISCUSSION:

The goal of these preliminary experiments was to determine if there was any advantage of using monoenergetic photons in imaging low contrast targets in mammography. Theoretically we should be able to improve the visibility of small differences in low Z targets. The properties of the monoenergetic photons, coupled with the beam characteristics that maintain a tightly collimated beam over many meters distance, should show contrast resolution close to the theoretical limit. The few other experiments that have been done confirm that such is the case ^{4,6}.

A calculation of the contrast that should be obtainable for a 0.25mm thick Lucite target imbedded in 42mm of Lucite for different monoenergetic photons is shown in table 2. The contrast is calculated using the measured attenuation coefficients for Lucite at the energies used. Contrast is defined as the difference in measured attenuation coefficients for Lucite at the energies used. Contrast is defined as the difference in attenuation through the target and surround divided by the attenuation through the surround. A calculation for a polychromatic beam of photons with 40% of the photons having 17 and 19 keV, and the remaining 60% of the photon flux spread in 2 keV energy bins from 14 to 28 keV, see figure 5, yields a contrast of 1.35%. The increase in contrast due to the use of monoenergetic beams with a line scanning detector system should yield images with improved contrast.

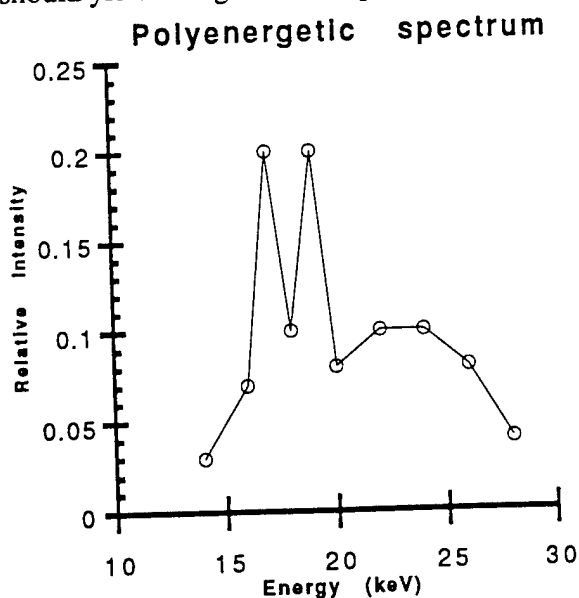


Figure 5. The simulated x-ray spectrum from a Mo target x-ray tube.

TABLE 2

Energy (keV)	16	18.2	20	22	poly-energetic
$\mu \text{ cm}^{-1}$	1.019	0.716	0.648	0.536	--
Measured % contrast		1.58	1.12		0.9
Calculated % contrast	2.4	2.0	1.6	1.4	1.35

Note: % contrast is determined for a Lucite target of 0.25mm thickness in a Lucite phantom of 42mm thickness.

% contrast = $100(I_{41.75}/I_0 - I_{42}/I_0)/(I_{41.75}/I_0)$. Where I_x is the transmitted photon flux through x thickness of Lucite.

Our experiments are encouraging in that we could demonstrate an improvement in contrast in the phantoms. Our preliminary synchrotron images are similar to somewhat better in appearance to those that can be obtained with conventional polyenergetic photons and we expect to be able to improve the image quality with improved instrumentation. The major sources of problems are; 1) the monochromator that we used introduced extraneous streaking and non uniformity into the image data. 2) the Fuji plate/readout system we used was not optimum for low contrast targets resulting in improper scaling of the 10 bits of available data. All the phantom-target data were confined to a small range of data out of the 1024 available.

We propose to carry out additional experiments with an improved monochromator and different detector. Under consideration at this point is the use of mammographic film, or, preferable, a single line scanning digital detector. We are optimistic that with improved instrumentation, coupled with the advantages of the monoenergetic photon beam and the narrow beam geometry, we can show significantly improved contrast images.

6. ACKNOWLEDGMENTS

This research was in part funded by NIH RO1 CA60193 and the Department of Radiology, University of North Carolina. The work at the National Synchrotron Light Source was supported by the U.S. Dept. of Energy under contract # DE-AC02-76CH00016.

7. REFERENCES

1. J.M. Boone and J.A. Seibert, "A Comparison of mono- and poly-energetic x-ray beam performance for radiographic and fluoroscopic imaging," Med. Phys. 21 (12), pp. 1853-1863, December 1994.
2. X. Wu, E.L. Gingold, D.M. Tucker and G.T. Barnes. " X-ray Spectral effects on contrast and dose in mammography," Med. Phys. 21 (6) pp. 1006, June 1994.
3. E. Burattini, M. Gambaccini, P.L. Indovina, M. Pocek, and G. Simonetti. "Synchrotron radiation: A new source in x-ray mammography," Radiol. Med. 4, pp181-188, 1992.

4. E. Burattini, E. Cossu, C. Di Maggio, M. Gambaccini, P. Indovina, M. Maryiani, M. Porek, S. Simeoni, and G. Simonetti. "X-ray Mammography with Synchrotron Radiation: A New High resolution Technique Valid fro Clinical Application," Radiology (to be published), 1994.

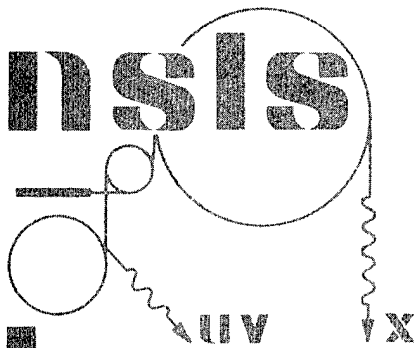
5. Department of Medical Biophysics, University of Toronto. 2075 Bayview Ave. North York, Ontario, Canada.

6.F. Carrol, J. Waters, W. Andrews, R. Price, D. Pickens, R. Wilhott, P. Tompkins, C. Roos, D. Page, G. Reed, A. Veda, R. Bain, P. Wang, and M. Bassinger. "Attenuation of Monochromatic X-Rays by Normal and Abnormal Breast Tissues," Investigative Radiology, 29 (1994), 266-272.

Appendix

A.12.

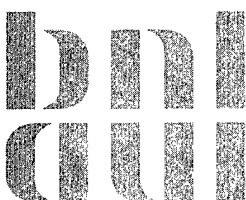
"Data Acquisition and Analysis of Mammography Images at the NSLS",
NSLS, BNL, Upton, NY, BNL Informal Report 62935, (1996), F. Arfelli, C.
Burns, D. Chapman, N. Gmür, R.E. Johnston, R. Menk, E. Pisano, D.
Sayers, W. Thomlinson, D. Washburn, Z. Zhong.



**Data Acquisition and Analysis
of Mammography Images at the NSLS
June - August 1995**

F. Arfelli, C. Burns, D. Chapman, N. Gmur, R. E. Johnston, R. Menk,
E. Pisano, D. Sayers, W. Thomlinson, D. Washburn, Z. Zhong

NATIONAL SYNCHROTRON LIGHT SOURCE



**BROOKHAVEN NATIONAL LABORATORY
ASSOCIATED UNIVERSITIES, INC.**

Under Contract No. DE-AC02-76CH00016 with the

UNITED STATES DEPARTMENT OF ENERGY

Data Acquisition and Analysis of Mammography Images at the NSLS June - August 1995

F.Arfe¹, C.Burns², D.Chapman^{1,4}, N.Gmur¹, R.E.Johnston², R.Menk¹, E.Pisano²,
D.Sayers³, W.Thomlinson¹, D.Washburn², Z.Zhong¹

1. NSLS, Brookhaven National Laboratory, Upton, NY, 11973
2. Department of Radiology, University of North Carolina, Chapel Hill, N.C.27599
3. Department of Physics, North Carolina State University, Raleigh, N.C.27695
4. Illinois Institute of Technology, Chicago, IL 60616

1. Introduction

The display of low-contrast tissue structures and the finest microcalcifications is essential for the early diagnosis of breast cancer (1,2,3). From this requirement, it should be noted that the x-ray imaging beam energy must be matched to the object thickness and the tissue composition of the breast in order to achieve high image quality with minimum radiation exposure to the patient (4-10). With the conventional molybdenum anode x-ray tube, widely used for approximately the last 20 years, the possibilities of adapting the beam energy to the object thickness or the density of the breast tissue are severely limited since the relative energy distribution of the x-ray spectrum changes very little by varying the x-ray tube voltage.

The synchrotron radiation x-ray source provides a high flux over a wide continuous energy spectrum. This presents the possibility of obtaining a monochromatic tunable beam in order to choose the optimal energy that can increase the information content in the images or reduce the patient exposure. The intrinsic vertical collimation of the synchrotron beam may reduce the scattered radiation. Anti-scattering grids used in the conventional mammographic system are not necessary. They may absorb more than 50% of the x-rays exiting from the breast, causing the dose to be more than doubled in order to maintain image quality.

At Brookhaven National Laboratory mammography experiments are being carried out at the X27C R&D beamline of the National Synchrotron Light Source using a monochromatic x-ray beam in order to explore the potential of monoenergetic photons for mammographic imaging. Preliminary reports of some of the work have been submitted for publication as conference proceedings (11,12). Our measurements and results occurred during two separate one week periods of beam time; the first one in June and the second one in August 1995.

The monochromatic x-ray beam used for the imaging was produced by a double crystal Si(111) Bragg monochromator which can select energies from 15 to 25 keV. Conventional mammographic phantoms, including a contrast-detail phantom, the

ACR (American College of Radiology) phantom and an in-vitro excised tissue sample, were imaged. The detector was a Fuji Image plate with a spatial resolution of 100 microns. Many images of the same phantoms were also recorded on a conventional mammographic film-screen system. The images were acquired in a line scan mode simultaneously moving the phantom and the detector through the beam. These images were compared with images produced using a conventional mammographic system at the University of North Carolina. The synchrotron images show a better contrast than the conventional images when compared to the theoretical contrast.

2. Experimental set-up

The experimental set-up is shown in Figure 1. The overall length of the system from the monochromator to the detector is 2.8 meters. The 85 mm wide white beam is provided by the X27C bending magnet source roughly 20 meters from the experimental hutch. The set-up, that is not under vacuum, begins downstream of a beryllium window. At that point a slit provides a 0.5 mm high beam which is incident on a double crystal Si(111) Bragg monochromator. The monochromator consists of two independent crystals 150 mm wide providing complete horizontal acceptance of the beam. The lengths of the first and second crystals are 60 mm and 90 mm, respectively, chosen in order to allow a vertical acceptance up to 3 mm in the energy range from 15 to 25 keV (corresponding to a Bragg angle range from 7.6 to 4.5 degrees). The energy resolution $\Delta E/E$ is 5×10^{-4} at 18 keV. The monochromator aluminum chamber is kept in a He atmosphere. The first water-cooled crystal holder is attached to a Huber rotational stage which allows the Bragg angle to be set with an angular resolution of 2.5×10^{-4} deg. The beam diffracted by the first crystal has another Bragg reflection from the second crystal set in parallel configuration in order to keep the outgoing beam parallel to the incident beam but with an offset in the height which is about 20 mm (about twice the distance of 10 mm between the crystals). There is a slightly variation in the height when changing the Bragg angle but it is negligible for our purposes. The second crystal holder is fixed to the same frame as the first one in order to rotate the two crystals simultaneously. It is provided with fine adjustments by means of three remote-controlled micrometric screws moved by a piezo with a resolution of 0.1 micron (Picomotor driver, New Focus). With these adjustments a good alignment of the two crystals can be achieved. That is fundamental for maximizing the transmitted flux and obtaining a uniform beam over its width. The energy calibration of the monochromator is done by measuring the k-absorption edges of Mo and Rh foils. Each time the working energy is changed the correct position of the second crystal is checked with a fine scan until the maximum flux transmission is reached. That means that a good overlap of the rocking curves of the two crystals exists.

At the exit of the monochromator the beam is collimated by lead shielding. Downstream of the monochromator there is a fast shutter with an ionization chamber in front of it which is used to monitor the strength of the incoming beam before opening the imaging shutter. Another slit is located downstream of the shutter,

approximately 110 cm in front of the object to be imaged. The dose monitor ionization chamber is placed after this slit and is used to measure the entrance dose to the phantom (Section 4). The detector is placed about 100 cm downstream of the phantom with a final slit just in front of it to reduce the scattered radiation from the phantom on the image plate. The detector and phantom are fixed on the same support and are moved vertically by a Klinger stepper motor driver.

3. Method

The detector is a Fuji ST3 PSP image plate used with a Fuji BAS 2000 image plate reader. Typical reading parameters are: sensitivity of 4000 or 400, latitude of 4 and a resolution size of 100 microns. The plates are read out as a 2048x2560 matrix (100 microns/pixel). Conventional mammographic film has also been used to record the images in conjunction with a Film Quick-CT film processor. Since the beam size is 0.5 mm high x 85 mm wide the images were acquired in line scan mode. The phantom and the detector, placed on the same vertical movement stage, were moved simultaneously through the beam by the stepper motor driver with a maximum speed of 16 mm/sec.

Data acquisition software has been developed to automate all the control and scan procedures. The input parameters required are: the beam energy, beam width, the phantom and filter thicknesses, the starting and final positions for the scan and the scan speed. The speed can be set directly or can be automatically chosen by the program for a predetermined detector exposure or, optionally, for a predetermined entrance dose to the phantom. The procedure reads the output current from the monitor ionization chamber (the one upstream of the fast shutter) and calculates the necessary speed. The current from the ionization chamber is amplified by a Keithley amplifier with the gain set at 10^9 and the output voltage is converted into counts/sec by means of a voltage-to-frequency converter which is connected to a scaler. Knowing the current I from the counts/sec, the relationship between the incident photon number/sec N_I and the current I from the ionization chamber is the following:

$$N_I = \frac{I\omega_{ion}}{Ee(1 - e^{-\mu_{en}^{gas}d})}$$

where E is the beam energy, e is the electron charge, ω_{ion} is the ionization energy for the gas in the chamber (nitrogen at atmospheric pressure), μ_{en}^{gas} is the absorption coefficient of the gas and d is the thickness of the ionization chamber.

The total photon number N_{tot} per cm^2 for a translation length h , a beam width w and a translation time ΔT is

$$N_{\text{tot}} = \frac{N_i \Delta T}{w h} = \frac{N_i}{s w}$$

where s is the scan speed. The requirements on detector exposure or phantom entrance dose are correlated to the incident photon number N_{tot} by means of the relationships shown in Section 4. In this way the scan speed is determined from a given N_{tot} . Thus, it is possible to increase or decrease the exposure by controlling the speed. There is, however, an intrinsic limit which is the maximum speed available and this means that the use of lucite and aluminum filters may be necessary directly after the monochromator.

When the scan starts, there is an acceleration phase arranged in such a way that the driver reaches the constant predetermined speed at the starting position at which time the shutter is opened. When the scan is at the end position the shutter is closed and the deceleration phase occurs. In practice, the total translation length is larger than the actual imaged phantom height to allow an imaging scan phase with constant speed and uniform exposure. For each run all the parameters used in the scan and the counts from the first and second ionization chambers are stored in a data file for off-line calculation.

The second ionization chamber (dose monitor chamber), placed after the fast shutter, measures the actual incident photon number on the phantom surface and from this measurement all the actual dose and exposure evaluations are performed, as described in Section 4. A scaler integrates the monitor chamber counts over the whole scan time corresponding to a total charge Q_{tot} produced in the ionization chamber by the incident beam. The actual incident photons/cm² N_{inc} is then given by:

$$N_{\text{inc}} = \frac{1}{hw} \frac{Q_{\text{tot}} \omega_{\text{ion}}}{Ee(1 - e^{-\mu_m d})}$$

where the product $h \cdot w$ represents the imaged area.

4. Dosimetry

Although mammography is uniquely effective in early detection of breast cancer, breast tissue is sensitive to radiation carcinogenesis. Although the resulting benefits of this examination substantially exceed potential risks, the dose must be monitored and minimized. Five major variables affect the breast dose delivered in a mammographic examination: the choice of the imaging system, the x-ray beam energy (HVL), the degree of breast compression employed and the breast size and adiposity.

Various dose parameters that might be considered are the in-air exposure at the position of the entrance surface of the breast (X_a), the dose to the entrance surface of the breast (D_s), the dose to the midline of the breast (D_{mid}), and the mean dose to the glandular tissue of the breast (D_g). In-air surface exposure is easy to measure with an ionization chamber and from this measurement it is easy to determine the surface dose but it gives an overestimation of the cancer risk. Midline dose is difficult to measure

directly (it can represent the risk to the glandular tissue) but it is an underestimation of the risk for the low-energy beams used for film-screen mammography. Mean glandular dose provides the best indicator of the potential carcinogenic radiation risk to the patient from mammographic examination. It commonly is assumed that the cancer risk is linearly related to the dose and that the breast cancers arise in the glandular tissue which is the most vulnerable when compared to adipose, skin and areolar tissues. Mean glandular dose cannot be measured directly but must be calculated from the result of simple measurements and tabulated values. The exposure as a function of the depth may be measured in phantoms using thermoluminescent dosimeters (TLD). Then the doses can be calculated from exposure levels using exposure-to-dose conversion factors.

Although the average glandular dose is the quantity usually reported, dose is sometimes given as the normalized average glandular dose (D_{gN}), which is the dose (D_g) normalized to the unit exposure in air at the entrance surface of the breast (X_a). The value X_a is set depending upon the detection system sensitivity in order to achieve a desired final image density. Once the exposure in air X_a is measured, then it is multiplied by the values of D_{gN} to arrive at reasonably accurate estimates of the average glandular dose (D_g) to the patient. For conventional mammography the normalized dose D_{gN} is determined by the HVL and breast thickness. Tables of values have been provided by a number of sources, including the National Council on Radiation Protection and Measurements (13) and the Center for Devices and Radiological Health (14).

A simplified model for the human breast used for dosimetry is proposed by Hammerstein et al. (15) to compute the average glandular dose in a firmly compressed breast with a rectangular cross section. The assumptions are that there is an outer layer of adipose tissue, not containing glandular tissue, that is roughly 0.5 cm thick on the outer (upper and lower) surfaces of the breast and there is a central portion of breast tissue composed of a uniform mixture of 50% adipose and 50% glandular tissue. Typical breast thickness after firm compression is 45 mm, although thickness can vary in a range from 15 mm to 75 mm.

In our mammographic experiments with synchrotron radiation it has been possible to implement a procedure for dose and exposure evaluations for each acquired image. We use simple relationships which consider the monoenergetic spectrum as well as the good geometric conditions due to the laminar beam and the slit system.

As shown above (Section 3), it is possible to determine the number N_0 of incident photons per surface unit (impinging on the phantom) from the output signal of the second ionization chamber, at a given energy E . The procedure developed for the estimation of dose determines N_0 (ph/cm²), then the entrance dose to the lucite phantom is calculated, using the relationship:

$$D_s = N_0 E \frac{\mu_{en}^{luc}}{\rho^{luc}}$$

where μ_{en}^{luc} is the absorption coefficient of the phantom and ρ^{luc} is its density. In order to have a standard comparison of doses (since the thickness t of lucite can be different

at the different energies to allow a fixed exposure to the detector) the procedure calculates the entrance dose for a 42 mm thick lucite phantom, using $N'_0 = N_0 e^{-\mu_{luc}(t-4.2)}$ instead of N_0 as incident flux, where μ_{luc} is the lucite attenuation coefficient.

The procedure also provides the exposure to the detector, E_D , using the relationship:

$$D_{air}(\text{rad}) = 0.877 E_D(\text{R}) = N_D E \frac{\mu_{en}^{air}}{\rho^{air}}$$

where $N_D = N_0 e^{-\mu_{luc}t}$ is the photon number per surface unit reaching the detector.

Finally, the procedure calculates the average glandular dose that should be delivered to a breast of thickness t in order to obtain an image corresponding to a given exposure to the detector. The breast thickness usually taken into consideration is $t = 45$ mm, which is standard, as well as $t = 20, 40, 42$, and 70 mm.

Considering the standard breast composition described above and the breast thickness t , the photon number on the detector, N_D , for an image is related to the incident photon flux per unit surface area of the breast, N_t , by the relationship

$$N_D = N_t e^{-\mu_{adip}} e^{-\mu_{mix}(t-1)}$$

where μ_{adip} is the adipose tissue attenuation coefficient and μ_{mix} is the glandular-adipose mixture attenuation coefficient. The assumption is that the beam is attenuated by 1 cm of adipose tissue (considering both of the outer adipose layers in the breast) and by $(t-1)$ cm of mixture tissue.

Then the glandular dose $D_g(x)$ at the depth x is calculated to a small mass of glandular tissue embedded in a homogeneous medium with standard composition (50% adipose and 50% glandular tissue):

$$D_g(x) = N_t E \frac{\mu_{en}^{gland}}{\rho^{gland}} e^{-\mu_{adip}0.5} e^{-\mu_{mix}(x-0.5)}$$

where μ_{en}^{gland} and ρ^{gland} are the glandular tissue absorption coefficient and density, respectively.

The beam intensity at the depth x is attenuated by 0.5 cm adipose tissue and $(x-0.5)$ cm mixture tissue. The mean glandular dose \bar{D}_g is now evaluated integrating the glandular dose $D_g(x)$ over the breast mixed tissue region and dividing this number by the thickness:

$$\bar{D}_g = \frac{1}{(t-1)} \int_{0.5}^{t-0.5} D_g(x) dx$$

5. Theoretical considerations

In general the concept of 'image quality' can be considered to indicate the accuracy with which details can be perceived in an image. To avoid confusion about what this means it is necessary to define some terms and relationships which can lead to quantitative evaluation of the visibility of details in an image (16, 17).

A uniform photon fluence N_i (photons per unit area) is incident on a phantom which has two adjacent regions. Region 1 consists of a thickness t of a uniform material in the phantom without details whose total attenuation coefficient is $\mu(E)$. Region 2 is the region which contains the detail and it consists of a thickness $(t-t')$ of the same material plus a thickness t' of a material whose attenuation coefficient is $\mu'(E)$. The transmitted photon fluences for the regions 1 and 2 are labeled N_{T1} and N_{T2} , respectively.

The contrast C in an image can be defined as the difference in x-ray transmission through region 1 and region 2 divided by the average of the two transmitted photon numbers:

$$C = \frac{N_{T1} - N_{T2}}{(N_{T1} + N_{T2}) / 2}$$

For a polychromatic beam we have to integrate over the energy and the contrast is:

$$C = \frac{\int_E N_{T1}(E)dE - \int_E N_{T2}(E)dE}{(\int_E N_{T1}(E)dE + \int_E N_{T2}(E)dE) / 2}$$

The transmitted x-ray fluences, N_{T1} and N_{T2} , consist of a primary (unscattered) component, N_{P1} and N_{P2} , and a scattered component, N_{S1} and N_{S2} , respectively such that

$$N_{T1} = N_{P1} + N_{S1} \quad \text{and} \quad N_{T2} = N_{P2} + N_{S2}$$

In the case of a monochromatic beam at a given energy the primary radiation is

$$N_{P1} = N_i e^{-\mu t}$$

and

$$N_{P2} = N_i e^{-\mu(t-t')} e^{-\mu' t'}$$

Considering an equal contribution of scattered radiation that means $N_{S1} = N_{S2} = N_s$, the contrast becomes

$$C = \frac{2(1 - e^{-\Delta})}{1 + e^{-\Delta} + (2F / (1 - F))}$$

where $\Delta = t'(\mu' - \mu)$ and the factor F is the scatter fraction defined as $F = N_s / N_{T1}$.

If the contribution of scattered radiation is uniform over the image, the number of scattered photons cancels in the numerator but it is present in the denominator, resulting in lower contrast. In the absence of scattered radiation the contrast depends only on the energy and on the absorption differences between the two materials (detail thickness, atomic number and density).

In the absence of scattered radiation and in the case of low contrast, C may be written

$$C \cong (\mu' - \mu)t'$$

In mammography the contrast is an important parameter because of the subtle differences in the transmission properties of the normal soft tissue and pathologic soft tissue masses and because of the importance of detecting minute details such as microcalcifications.

It is important to point out that radiographic contrast is actually influenced by two factors: the subject contrast and the receptor contrast. In the above considerations the concept of contrast refers to the subject contrast in which only the distribution of the photon intensity transmitted through the object is taken into consideration. We can suppose that the photons are counted by an ideal detector with efficiency 100%. The receptor contrast takes into consideration the x-ray intensity pattern related to the image pattern detected by the detector. In this case, instead of the photon numbers N_{T1} and N_{T2} , the corresponding output signal from the detector must be considered. For a film-screen system the x-ray intensity pattern is related to the optical density pattern in the mammogram. The receptor contrast is affected by the film type and the processing conditions. For a digital detector with a simple linear relationship between the incident fluence N_0 and the output signal $N_D = pf\epsilon N_0$, the subject contrast and the receptor contrast are the same. (p is the pixel area, f is the conversion factor of the signal and ϵ is the detector efficiency). This relation holds only for monochromatic photon beams without scattered radiation since, in general, f and ϵ are energy dependent.

Image formation is a statistical process which involves the detection of a large number of photons. The inherent limitation to image information content is the statistical noise. The noise is generated in each component of an image system. It is possible to display all the image information content down to the appearance of "quantum mottle" which is the manifestation of the statistical noise.

A parameter which takes into consideration the effect of the noise on the image quality is the signal-to-noise ratio (SNR). Considering the SNR_{in} at the input to the detector (or considering an ideal detector with efficiency 100%) for a detail with area A , and the photon numbers transmitted in regions 1 and 2 ($n_{T1} = AN_{T1}$ and $n_{T2} = AN_{T2}$), one finds

$$SNR_{in} = \frac{n_{T1} - n_{T2}}{\sqrt{n_{T1} + n_{T2}}} = \frac{C}{2} \sqrt{n_{T1} + n_{T2}}$$

The numbers of photons n_{T1} and n_{T2} vary according to a Poisson distribution with the noise equal to $\sqrt{n_{T1}}$ and $\sqrt{n_{T2}}$ respectively, which is the standard deviation of the photon number.

This equation shows that, unlike the contrast, the signal-to-noise ratio is dependent on the exposure as well as on the size of the detail because it is proportional to $\sqrt{AN_i}$. Scattered radiation, if it is able to enter the detector, produces a reduction of the SNR_{in} .

The SNR_{out} of an image produced by a detector with a given Detective Quantum Efficiency (DQE) is related to the SNR_{in} as following

$$SNR_{out} = \sqrt{DQE} SNR_{in}$$

6. Analysis

The acquired digital images have been processed by means of procedures created using the software "Interactive Data Language" (IDL) (18).

The images to be analyzed were acquired by means of an image plate detector (Section 3). This system is based on a photostimulable phosphor which can temporarily store an x-ray image. The stored x-ray pattern is subsequently read out by a scanning laser beam, which converts the trapped energy into photostimulated luminescence. The emitted luminescence, which is proportional to the absorbed x-ray intensity, is detected by a photomultiplier whose output signal is logarithmically amplified and digitized with a 12-bit A/D converter. The gain of the logarithmic amplifier, which determines the range of the latitude, and the photomultiplier sensitivity (high voltage) are scaled according to the exposure level and the image contrast.

In the first phase of the analysis, the raw data, which are logarithmic values representing the A/D converter, are linearized using the following formula:

$$data_{lin} = \left(\frac{pixelsize}{100} \right)^2 * \frac{4000}{S} * 10^{L \left(\frac{Raw}{G} - \frac{1}{2} \right)}$$

where

L = Latitude (Dynamic Range; 1, 2, 3 or 4)

Raw = raw data value (0-255, 0-1023, or 0-4095)

G = total gradation level (256, 1024, or 4096)

S = sensitivity (400, 1000, 4000, or 10000)

Pixel size = 100 or 200 microns

The parameters used in the June 1995 run were: $L=4$, $G=1024$, $S=4000$ and pixel size=100; in the August 1995 run they were: $L=4$, $G=1024$, $S=400$ and pixel size=100.

The image size was 85 mm (beam width) x 115 mm (translation length) in the June run, while it was 85 mm (beam width) x 95 mm (translation length) in the August run. Considering the pixel size of 100 microns, the number of image plate pixels per image was 850x1150 in the June experiment and 850x950 in the August experiment.

The phantoms used during the two experimental runs were the following: the ACR phantom (American College of Radiology), the CD phantom (Contrast-Detail), an anthropomorphic phantom (which simulates the breast tissue structures) and an excised breast tissue (the tumor was removed). Details of the ACR and CD phantoms are given in Figure 2.

The ACR phantom (Gammex: Model RMI 156) (Fig.2) is designed to attenuate x-ray beams in the same way as a human breast of 50% adipose and 50% glandular tissue compressed down to a thickness of 40 to 45 mm. Test objects of different sizes, shapes and densities are embedded in an insert. These test objects represent simulated malignancies such as micro-calcifications, fibrils and masses.

The CD phantom (Fig.2) is designed to evaluate the visibility limits of low contrast details of different thicknesses and diameter. It consists of a 15 mm thick Lucite background with circular areas of additional thickness. The circles are from 0.062 mm to 1 mm thick and the circle diameters are from about 0.3 to 7 mm. Thus, the two materials which determine the contrast are Lucite and air.

In the June experiment we imaged the CD, ACR and anthropomorphic phantoms using the following energies: 17, 18, 19.3, 20, 22, 24 keV. In the August experiment we imaged the CD and ACR phantom and the excised tissue at 16, 17, 18, 19 keV. In addition, imaging was done for the excised tissue at 20 and 22 keV and for the CD phantom at 24 keV.

The list in Table 1 summarizes the phantom images produced by the image plate in the June and August beamtime at the X27C beamline. It specifies the run number, the energy, the kind of phantom and the corresponding mean glandular dose normalized to a 45 mm thick breast.

The images of the CD and ACR phantoms have been processed in order to achieve a flat background cancelling artifacts due to horizontal and vertical non-uniformities in the incident beam intensity. The horizontal modulations are due essentially to a non-uniform transmission by the monochromator and the Be window, while the vertical modulations are due to periodic oscillations of the translation stage. In the August run the latter problem was nearly completely removed by changing the position of the image plate and phantom to a more stable configuration.

The CD phantom images have been used for contrast and SNR measurements for different detail thicknesses at different energies. The largest diameter details (7 mm) have been analysed. The concept of receptor contrast has been applied and this contrast has been compared with the theoretical subject contrast for a monochromatic beam without scattered radiation using the relationship in Section 5.

In order to calculate the contrast an IDL procedure has been implemented. Once an image is displayed on a screen the procedure draws a circle on same image. It is

possible to drag the circle on the image and change its diameter using the mouse. The first circle allows the selection of the detail area; then, the average value as well as the standard deviation of the pixels included into the circle is calculated. A rectangular box then appears and with the same operation it is possible to select and calculate the average value in a background area close to the detail. The procedure stores the results on a file and calculates the contrast. The SNR_{out} is determined using the photon fluence on the detectors.

The contrast for the same phantom details has been measured in three images of the CD phantom produced by a conventional mammographic x-ray tube at the University of North Carolina using a conventional film-screen as a detector and then digitized. The images were taken for phantoms of 15, 45, 75 mm thickness using 24, 25 and 30 kVp, respectively. The mean glandular dose is normalized to an exposure of 8 mR to the film.

Figure 3 shows the plot of the measured image plate contrast as a function of the detail thickness at 18 keV, along with the theoretical curve. In the same plot the contrast measurements for the digitized film are shown (45 mm thick phantom and 25 kVp). The measured monochromatic beam contrasts are in good agreement with the theoretical values, while the digitized film values are lower than theoretical values. The comparison between experimental and theoretical data for 17, 19.3, 20, 22, 24 keV is shown in Figure 4.

The plots of the measured contrast as a function of energy for three different detail thicknesses are compared with the theoretical curve in Figure 5. Good agreement is also obtained between the theory and experiment for the monochromatic data.

Conclusions

In two different periods of beamtime at the beamline X27C of the National Synchrotron Light Source at Brookhaven National Laboratory, we have performed preliminary studies of mammographic imaging using a monochromatic synchrotron radiation source. We used both phantom objects and real tissue samples.

Qualitative studies with the contrast-detail phantom show good agreement when compared with the theoretical contrast. As expected, the contrast is higher if the energy is lower. The results show an improved contrast with energies 18 keV and lower compared to images obtained from conventional polyenergetic x-ray imaging systems.

The results also show that for similar imaging conditions the monoenergetic mean glandular dose is less than that from polyenergetic sources. This is due both to the increased sensitivity of the image plate detectors and to actual reductions of dose for truly monochromatic beams.

Bibliography

1. L.H. Baker, 'Breast cancer detection demonstration project: five-year summary report,' CA 32(4) (1982) 194-225.
2. S.L. Saltzstein, 'Potential limits of physical examination and breast self-examination in detecting small cancers of the breast: an unselected population-based study of 1302 cases,' Cancer 54 (1984) 1443.
3. S. W. Fletcher, M.S. O'Malley and L.A. Bunce, 'Physicians' abilities to detect lumps in silicone breast models,' JAMA 251 (1984) 1580.
4. P.C. Stomper and R.S. Gelman, 'Mammography in symptomatic and asymptomatic patients,' Hem/Onc clinics NA, 3(4) (1989) 611-640.
5. X. Wu, E.L. Gingold, D.M. Tucker and G.T. Barnes, 'X-ray spectral effects on contrast and dose in mammography,' Med. Phys. 21 (1994) 1006.
6. F. Carrol, J. Waters, W. Andrews, R. Price, D. Pickens, R. Wilhott, P. Tompkins, C. Roos, D. Page, G. Reed, A. Veda, R. Bain, P. Wang and M. Bassinger, 'Attenuation of monochromatic x-rays by normal and abnormal breast tissues,' Investigative Radiology 29 (1994) 266-272.
7. E. Burattini, M. Gambaccini, P.L. Indovina, M. Pock and G. Simonetti, 'Synchrotron radiation: A new source in x-ray mammography,' Radiol. Med. 4 (1992) 181-188.
8. E. Burattini, E. Cossu, C. DiMaggio, M. Gambaccini, P. Indovina, M. Maryianai, M. Porek, S. Simeoni and G. Simonetti, 'X-ray mammography with synchrotron radiation: A new high resolution technique valid for clinical application,' Radiology 195 (1994) 239-244.
9. A. Mantykentta-Pramanick and R. Carr, 'High Resolution mammography with Synchrotron Radiation,' Medical Physics, submitted for publication (1995).
10. J.M. Boone and J.A. Seibert, 'A comparison of mono- and poly-energetic x-ray beam performance for radiographic and fluoroscopic imaging,' Med. Phys. 21 (1994) 1853-1863.
11. R.E. Johnston, D. Washburn, P. Pisano, W.C. Thomlinson, L.D. Chapman, N.F. Gmur, Z. Zhong and D. Sayers, 'Preliminary experience with monoenergetic photon mammography,' Medical Imaging 1995: Physics of Medical Imaging, SPIE 2432 (1995) 434-441.

12. R.E. Johnston, D. Washburn, P. Pisano, C. Burns, W.C. Thomlinson, L.D. Chapman, F. Arfelli, N.F. Gmur, Z. Zhong and D. Sayers, "Mammography phantom studies with synchrotron radiation," Radiology, submitted for publication.
13. "Mammography: a user's guide." NCRP report 85. National Council on Radiation Protection and Measurements (Bethesda, Md, 1986).
14. B.J. Conway, ed. "Nationwide evaluation of x-ray trends (NEXT), tabulation, and graphical summary of surveys, 1984 through 1987." Conference of Radiation Control Program Directors, CRCPD publication 89-3 (Frankfurt, KY, 1989).
15. G.R. Hammerstein, D.W. Miller, D.R. White, M.E. Masterson, H.Q. Woodard and J.S. Laughlin, "Absorbed radiation dose in mammography," Radiology 130 (1979) 485-491.
16. R.J. Jennings, R.J. Eastgate, M.P. Siedband and D.L. Ergun, "Optimal x-ray spectra for screen-film mammography," Med. Phys. 8 (1981) 629-639.
17. J.W. Motz and M. Danos, "Image information content and patient exposure," Med. Phys. 5 (1976) 8-22.
18. Research Systems, Inc., Boulder, Colorado

Table 1a Run List (June 1995)

Run no.	Filename	Energy (keV)	Phantom	Average Glandular Dose(mrad)
1079	cd1.img	19.3	CD	67.9
1096	cd2_1096.img	18	CD	89.2
1118	cd3_1118_17kev.img	17	CD	146.9
1128	cd4_1128_20real.img	20	CD	48.5
1143	cd5_1143_22kev.img	22	CD	27.8
1155	cd6_1155_24kev.img	24	CD	20.4
1201	cd7_1201_18kev.img	18	CD	7.0
1203	cd7_1203_18kev.img	18	CD	21.3
1205	cd7_1205_18kev.img	18	CD	28.4
1207	cd7_1207_18kev.img	18	CD	45.5
1209	cd7_1209_18kev.img	18	CD	51.2
1211	cd7_1211_18kev.img	18	CD	64.1
1213	cd7_1213_18kev.img	18	CD	71.0
1215	cd7_1215_18kev.img	18	CD	99.7
1217	cd7_1217_18kev.img	18	CD	121.2
1090	acr1.img	19.3	ACR	40.1
1109	acr2_1109_18kev.img	18	ACR	67.2
1121	acr3_1121_17kev.img	17	ACR	137.5
1130	acr4_1130_20real.img	20	ACR	46.6
1149	acr5_1149_22kev.img	22	ACR	26.2
1159	acr6_1159_24kev.img	24	ACR	17.0
1080	ant1.img	19.3	ANTR	66.2
1113	ant2_1113_18kev.img	18	ANTR	73.5
1124	ant3_1124_17kev.img	17	ANTR	131.6
1133	ant4_1133_20real.img	20	ANTR	48.5
1151	ant5_1151_22kev.img	22	ANTR	25.8
1162	ant6_1162_24kev.img	24	ANTR	14.2

Table 1b Run List (August 1995)

Run no.	Filename	Energy (keV)	Phantom	Average Glandular Dose(mrad)
7019	cd_7019.img	16	CD	110.3
7026	cd_7026.img	17	CD	68.6
7029	cd_7029.img	18	CD	48.5
7032	cd_7032.img	19	CD	37.1
7034	cd_7034.img	24	CD	18.6
7014	acr_7014.img	16	ACR	105.4
7011	acr_7011.img	17	ACR	65.6
7008	acr_7008.img	18	ACR	45.9
7003	acr_7003.img	19	ACR	34.9
6010	bio_6010.img	18	TISSUE	96.8
6011	bio_6011.img	18	TISSUE	57.9
6012	bio_6011.img	18	TISSUE	155.3
6023	bio_6023.img	16	TISSUE	328.2
6026	bio_6026.img	17	TISSUE	164.6
6031	bio_6031.img	19	TISSUE	64.4
6036	bio_6036.img	20	TISSUE	37.3
6041	bio_6041.img	22	TISSUE	23.1
6106	bio_6106.img	16	TISSUE	106.9
6109	bio_6109.img	17	TISSUE	66.6
6112	bio_6112.img	18	TISSUE	47.1
6115	bio_6115.img	19	TISSUE	35.1

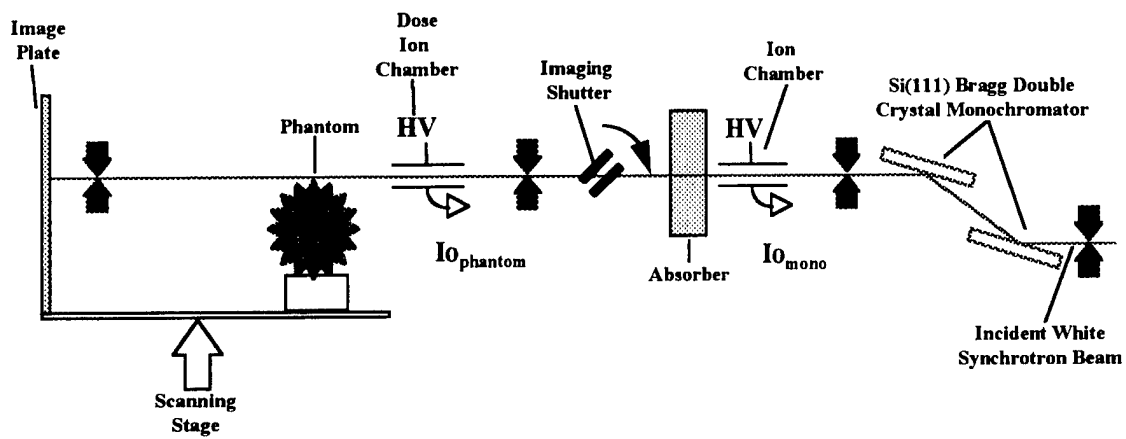


Figure 1: Mammography imaging set-up (not to scale)

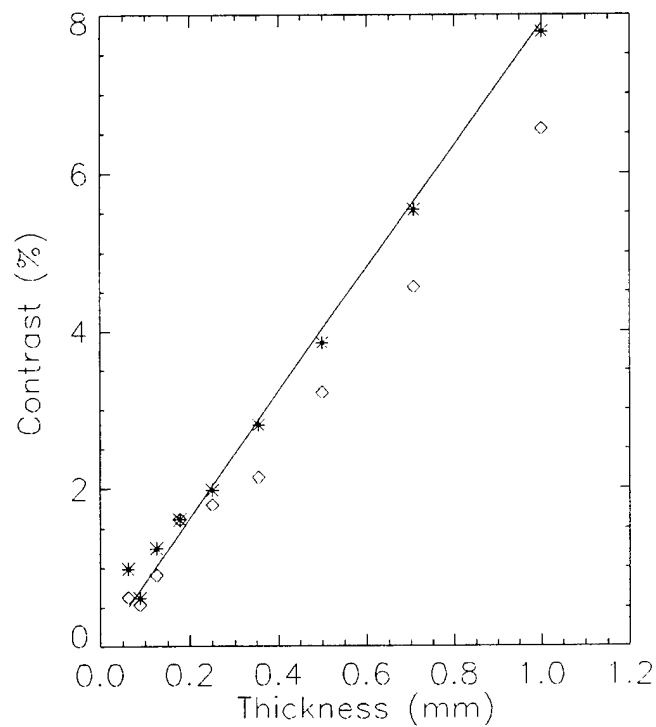


Figure 3: Measured contrast at 18 keV (*). The solid line represents the theoretical contrast. The measured contrast for a conventional film (25kVp) is also plotted (◇).

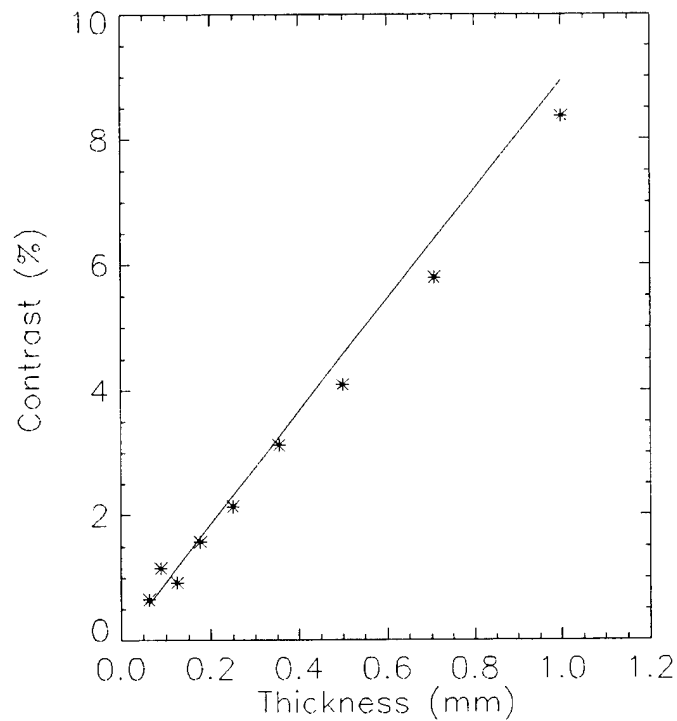


Figure 4a: Measured contrast at 17 keV (*). The solid line represents the theoretical contrast.

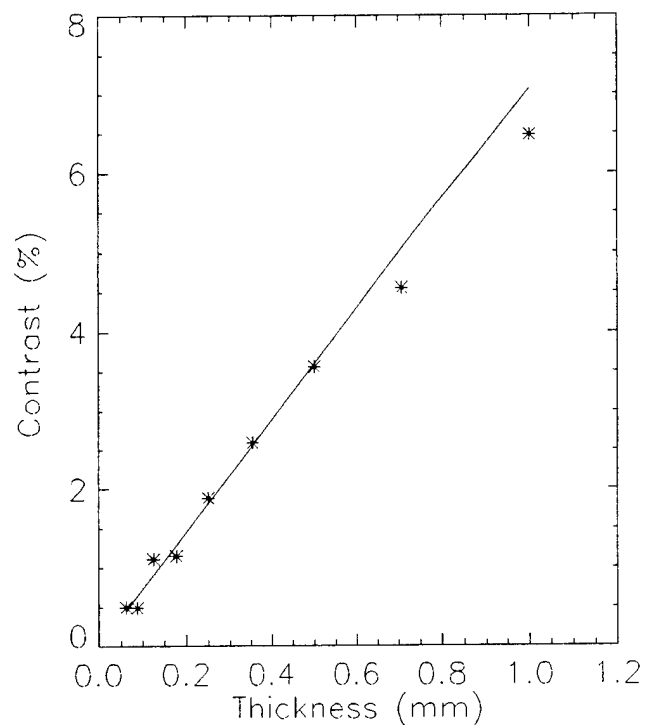


Figure 4b: Measured contrast at 19.3 keV (*). The solid line represents the theoretical contrast.

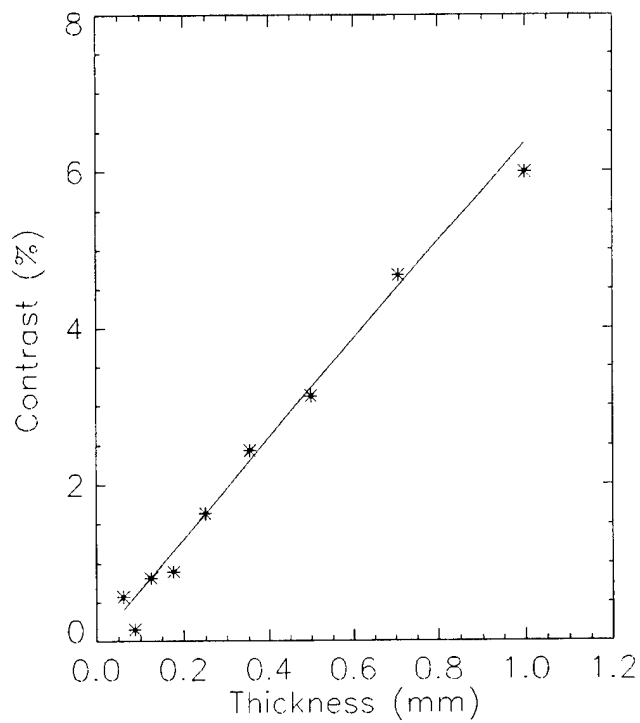


Figure 4c: Measured contrast at 20 keV (*). The solid line represents the theoretical contrast.

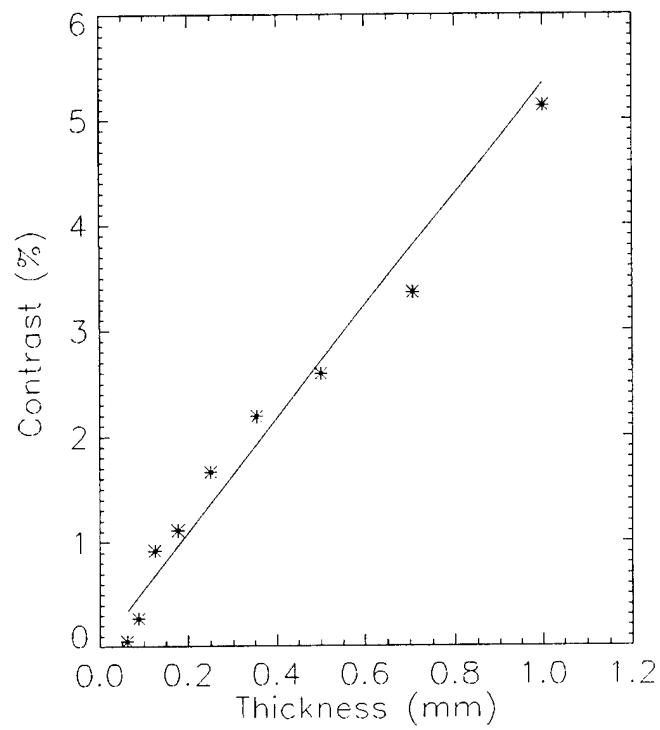


Figure 4d: Measured contrast at 22 keV (*). The solid line represents the theoretical contrast.

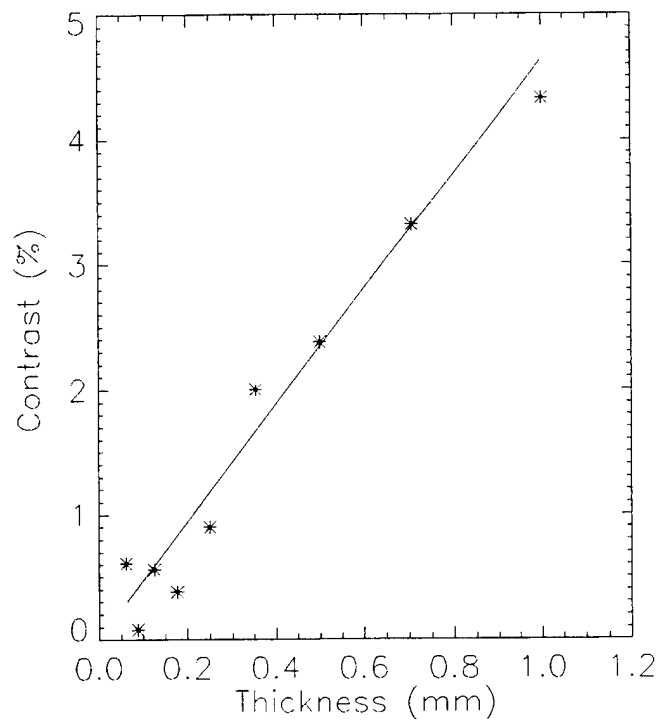


Figure 4e: Measured contrast at 24 keV (*). The solid line represents the theoretical contrast.

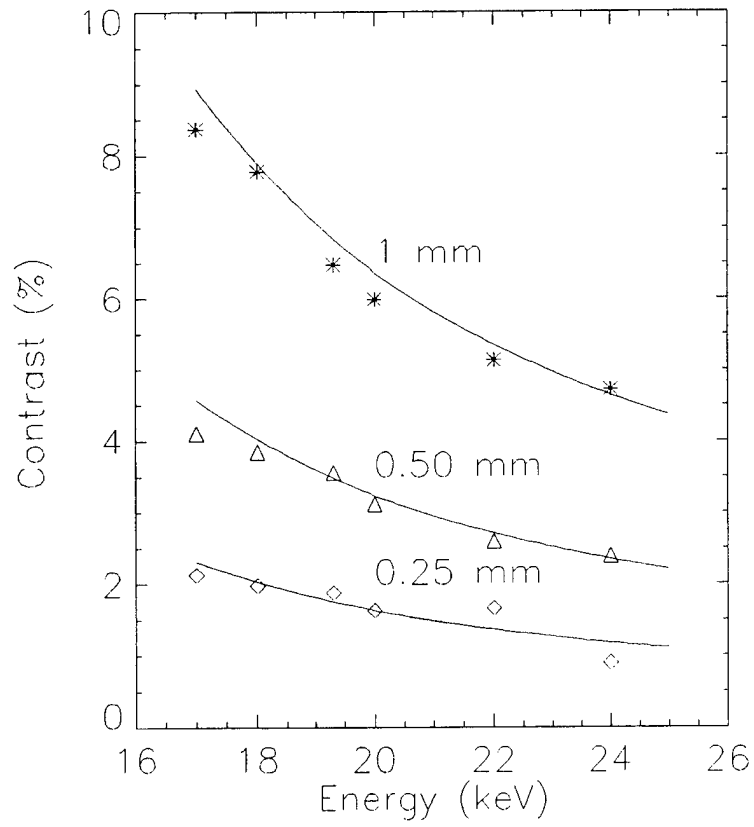


Figure 5: Measured contrast for different detail thicknesses. The solid line represents the theoretical contrast.